



**HAL**  
open science

# Self-polarized magnetic nanocomposites based on ferrimagnetic nanowires for non-reciprocal microwave devices

Labchir Nabil

► **To cite this version:**

Labchir Nabil. Self-polarized magnetic nanocomposites based on ferrimagnetic nanowires for non-reciprocal microwave devices. Material chemistry. Université de Lyon; Université Ibn Zohr (Agadir, Maroc). Faculté des sciences, 2021. English. NNT : 2021LYSES005 . tel-04414716v2

**HAL Id: tel-04414716**

**<https://hal.science/tel-04414716v2>**

Submitted on 22 Aug 2024

**HAL** is a multi-disciplinary open access archive for the deposit and dissemination of scientific research documents, whether they are published or not. The documents may come from teaching and research institutions in France or abroad, or from public or private research centers.

L'archive ouverte pluridisciplinaire **HAL**, est destinée au dépôt et à la diffusion de documents scientifiques de niveau recherche, publiés ou non, émanant des établissements d'enseignement et de recherche français ou étrangers, des laboratoires publics ou privés.



# INTERNATIONAL COTUTELLE OF THESIS

To obtain the Degree of Doctor delivered by

**THE UNIVERSITY OF LYON**

(performed within the University of Jean Monnet)

ED 488: Science, Engineering and Health

Discipline: Microelectronics, Photonics and Microwaves

AND

**THE UNIVERSITY OF IBN ZOHR**

ED: Science, Technology and Engineering

Discipline: Materials science

presented and defended publicly on January 21<sup>th</sup> 2021

by

**LABCHIR Nabil**

---

***Self-polarized magnetic nanocomposites  
based on ferrimagnetic nanowires  
for non-reciprocal microwave devices***

---

*financially supported by PHC Toubkal*

**Supervisors:** VINCENT Didier and IHLAL Ahmed  
**Co-supervisor:** HANNOUR Abdelkrim

**JURY:**

HLIMI Bouchta..... Professor, Faculty of Sciences, Agadir, Morocco..... President  
MATTEI Jean Luc.....Associate Professor HDR, University of ..... Reviewer  
Western Brittany, Brest, France  
PODEVIN Florence.....Associate Professor HDR, Grenoble Institute of Technology, France..... Reviewer  
BENLHACHEMI Abdeljalil.....Professor, Faculty of Sciences, Agadir, Morocco..... Reviewer  
BAYARD Bernard.....Associate Professor HDR, Jean Monnet University, France..... Examiner  
HANNOUR Abdelkrim.....Associate Professor HDR, Faculty of ..... Co-supervisor  
Applied Sciences, Agadir, Morocco.  
IHLAL Ahmed.....Professor, Faculty of Sciences, Agadir, Morocco..... Supervisor  
VINCENT Didier.....Professor, Jean Monnet University, Saint-Etienne, France ..... Supervisor



# Acknowledgments

This work has been carried out with the support of numerous people that I want to acknowledge hereby:

I would like to thank very sincerely the Professor IHLAL Ahmed, Professor VINCENT Didier, and Professor HANNOUR Abdelkrim for their supervision of this work, their availabilities, their scientific competences as well as their human qualities that were the determining factors in the success of this work, I would deeply like to express of my deep gratitude for them. I am also thankful to their many ideas and their criticism and corrections which have been crucial to the project's success. I also would like to acknowledge them for their encouragement and for the trust that they have accorded me, especially by making it possible for me to have a certain autonomy in my work.

My acknowledgements are also addressed to Professor HLIMI Bouchta for accepting to preside the examination jury of my thesis. I would like to acknowledge very sincerely Professor Ms. PODEVIN Florence, Professor BENLHACHEMI Abdeljalil, Professor MATTEI Jean Luc for the honour that they have bestowed to me by accepting to be part of the jury of my thesis as reviewers. I thank them for their pertinent remarks, their corrections and their advices.

I would thank Professor BAYARD Bernard for accepting to judge this work as an examiner.

I would also like to acknowledge Professor CHATELON Jean Pierre for the SQUID magnetometry measurements at the Louis Néel Institut in Grenoble and for the metalization by the rf sputtering at the LHC. I would also like to thank the engineer CELLE Frederic for the technical support in the clean room at LHC and the engineer Ms ROUME Claire for the technical support in electrodeposition at Saint-Étienne School of Mines. I especially thank the engineers Ms. REYNAUD Stéphanie and M. LEFKIR Yaya for the technical support in the images acquisition by the scanning electron microscope and the atomic force microscope.

Many thanks also to all the members of the laboratories (LHC and LMER) for their welcome and their help. I wish good luck to my colleagues, the PhD students of LHC and LMER.

If there is anyone who should see here all my gratitude and appreciation for their love, presence, listening and support in the difficult moments, it should be my parents, Lalla Naima and Sidi Mhammed. May they find here all my gratitude for having taken care of the good progress of my studies. My mother, my father, all these words cannot account

for all that I owe you. Finally, I would like to express my gratitude to my sisters and brothers for their love and support. Thank you to all those who participated in one way or another in the completion of this work.

# Contents

<b>List of Figures</b>	<b>9</b>
<b>List of Tables</b>	<b>10</b>
<b>List of abbreviations</b>	<b>11</b>
<b>General introduction</b>	<b>12</b>
<b>Chapitre 1</b>	<b>14</b>
<b>1 Magnetic materials for microwave applications: State of the art</b>	<b>14</b>
1.1 Introduction . . . . .	14
1.2 Brief history of magnetism . . . . .	14
1.3 Origin of magnetism . . . . .	15
1.4 Types of magnetism in materials and their properties . . . . .	16
1.4.1 Diamagnetism . . . . .	16
1.4.2 Paramagnetism . . . . .	17
1.4.3 Ferromagnetism . . . . .	18
1.4.4 Antiferromagnetism . . . . .	18
1.4.5 Ferrimagnetism . . . . .	19
1.5 Magnetic anisotropy . . . . .	20
1.5.1 Magnetocrystalline anisotropy . . . . .	20
1.5.2 Surface anisotropy . . . . .	21
1.5.3 Magnetoelastic anisotropy . . . . .	21
1.5.4 Shape anisotropy . . . . .	21
1.6 Static properties . . . . .	23
1.6.1 Weiss domains . . . . .	23
1.6.2 Hysteresis phenomenon . . . . .	24
1.6.3 Monodomain state . . . . .	25
1.7 Dynamic properties . . . . .	26
1.7.1 Gyromagnetic resonance . . . . .	26
1.7.2 Non-reciprocity in ferrites . . . . .	27
1.7.2.1 Gyromagnetic resonance ( <i>more detailed in the previous para-</i> <i>graph</i> ) . . . . .	27
1.7.2.2 Faraday effect . . . . .	27
1.7.2.3 Field displacement effect . . . . .	28
1.8 Classes of ferrites . . . . .	28
1.8.1 Garnet . . . . .	28
1.8.2 Hexaferrite . . . . .	29

1.8.3	Spinel . . . . .	29
1.8.4	Nanocomposites . . . . .	30
1.9	Theoretical models of the permeability tensor . . . . .	32
1.9.1	Saturated state: Polder model . . . . .	32
1.9.2	Partially magnetized state . . . . .	34
1.9.3	Demagnetized state . . . . .	35
1.9.4	Any magnetization state . . . . .	35
1.10	Microwave applications of ferrites . . . . .	38
1.10.1	Circulators . . . . .	38
1.10.2	Applications of circulator . . . . .	39
1.10.3	Different topologies of circulators . . . . .	40
1.10.3.1	Faraday rotation-based circulator . . . . .	40
1.10.3.2	Lumped element circulator . . . . .	41
1.10.3.3	Junction circulators . . . . .	42
1.10.4	Self-biased circulator . . . . .	46
<b>Chapitre 2</b>		<b>53</b>
<b>2</b>	<b>Synthesis and characterization techniques</b>	<b>54</b>
2.1	Introduction . . . . .	54
2.2	Electrochemistry: basic concepts . . . . .	54
2.2.1	Metal-solution interface . . . . .	55
2.2.1.1	Double electric layer . . . . .	55
2.2.1.2	Charge transfer mechanism . . . . .	56
2.2.1.3	Electrochemical mass transport . . . . .	56
2.3	Magneto-electrodeposition . . . . .	58
2.3.1	Magneto-induced forces . . . . .	58
2.4	Magneto-electrochemical synthesis of $CoFe_2O_4$ . . . . .	61
2.4.1	Experimental setup . . . . .	61
2.4.2	Electrochemical techniques . . . . .	63
2.5	Characterization techniques . . . . .	65
2.5.1	X-Ray Diffraction (XRD) . . . . .	65
2.5.2	Fourier Transform Infrared (FTIR) spectroscopy . . . . .	67
2.5.3	Atomic Force Microscopy (AFM) . . . . .	68
2.5.4	Scanning Electron Microscope (SEM) . . . . .	69
2.5.5	Stylus Profilometry (SP) . . . . .	71
2.5.6	Vibrating Sample Magnetometer (VSM) . . . . .	72
2.5.7	Superconducting Quantum Interference Device Magnetometer (SQUID) . . . . .	72
<b>Chapitre 3</b>		<b>76</b>
<b>3</b>	<b>Electrochemical synthesis of <math>CoFe_2O_4</math> nanocomposites</b>	<b>77</b>
3.1	Introduction . . . . .	77
3.2	Synthesis and characterization of $CoFe_2O_4$ samples . . . . .	77
3.2.1	$CoFe_2O_4$ thin films . . . . .	77
3.2.1.1	Cyclic Voltammetric study . . . . .	78
3.2.1.2	Chronoamperometry study . . . . .	79
3.2.1.3	Structural properties of $CoFe_2O_4$ thin films . . . . .	80
3.2.2	$CoFe_2O_4$ nanowires . . . . .	81

3.2.2.1	Effects of the pore diameter of the AAO membrane . . . . .	81
3.2.2.2	Effects of the applied potential . . . . .	87
3.2.2.3	Effects of applied magnetic field . . . . .	93
3.2.2.4	Effects of the annealing on the magnetic properties . . . . .	99
3.2.2.5	Magnetic field cooling effects . . . . .	100
3.2.2.6	ZFC-FC studies . . . . .	103
<b>Chapitre 4</b>		<b>109</b>
<b>4</b>	<b>Modeling of <math>CoFe_2O_4</math> nanocomposite permeability - Application to coplanar Y Circulator</b>	<b>110</b>
4.1	Introduction . . . . .	110
4.2	Permeability model of $CoFe_2O_4$ nanocomposite . . . . .	111
4.3	Electromagnetic analysis approaches of the circulator . . . . .	112
4.3.1	Theoretical modeling (Bosma model) . . . . .	112
4.3.2	Electric and magnetic fields . . . . .	113
4.3.3	Analytical calculation of the S-parameters . . . . .	118
4.3.3.1	Loss-related calculation of the S-parameters . . . . .	121
4.3.4	Stripline circulator based on $CoFe_2O_4$ nanocomposite . . . . .	123
4.3.5	Numerical modeling and simulation . . . . .	125
4.3.5.1	The selected numerical simulator . . . . .	125
4.3.5.2	Integration of $CoFe_2O_4$ permeability tensor in HFSS . . . . .	128
4.3.6	Simulation of a coplanar circulator based on $CoFe_2O_4$ nanocomposite . . . . .	130
4.4	Fabrication and microwave characterization of the CPW and Circulator . . . . .	134
4.4.1	Fabrication protocol of the circulator . . . . .	134
4.4.1.1	Deposition of copper and preparation of substrate . . . . .	134
4.4.1.2	Photolithography . . . . .	135
4.4.1.3	Etching and tinning . . . . .	138
4.4.2	Microwave characterization . . . . .	139
4.4.2.1	Characterization bench . . . . .	139
4.4.2.2	Measured S-parameters . . . . .	139
<b>Conclusions and perspectives</b>		<b>143</b>
<b>List of publications</b>		<b>146</b>

# List of Figures

1.1	<i>Electron motion around the nucleus.</i>	15
1.2	<i>Variation of magnetization under magnetic field (a) and thermal variation of the susceptibility (b) for a diamagnetic material.</i>	17
1.3	<i>Paramagnetism in atoms.</i>	17
1.4	<i>Ferromagnetism; (a) Spin arrays, (b) Variation of magnetization as function of field, (c) Thermal variation of <math>1/\chi</math> and spontaneous magnetization.</i>	18
1.5	<i>Antiferromagnetism; (a) Arrays of spins, (b) <math>M(H)</math>, (c) <math>\chi^{-1}(T)</math>.</i>	19
1.6	<i>Ferrimagnetism; (a) spin arrays, (b) variation under field of magnetization, (c) thermal variation of the spontaneous magnetization and <math>\chi^{-1}</math>.</i>	19
1.7	<i>Schematic representation of easy and hard axes of magnetization for cubic symmetry.</i>	20
1.8	<i>Illustration of the demagnetizing field <math>\vec{H}_D</math> in a material with <math>\vec{H}</math> is the applied field and <math>\vec{M}</math> is the magnetization of the material. The dashed lines represent the magnetic field lines.</i>	22
1.9	<i>Weiss domains and Bloch walls in the absence of an applied magnetic field.</i>	24
1.10	<i>Hysteresis loop for a ferrimagnetic material.</i>	25
1.11	<i>Precession of the magnetization with and without damping.</i>	26
1.12	<i>Non-reciprocal Faraday rotation for an EM wave propagating from left to right (red) and from right to left (black).</i>	27
1.13	<i>RF fields mapping for a cross section of the microstrip line; on a dielectric substrate (a), and on a magnetized ferrite (b).</i>	28
1.14	<i>Spinel unit cell structure.</i>	29
1.15	<i>Composite based on magnetic particles.</i>	31
1.16	<i>Definition of effective linewidth <math>\Delta H_{eff}</math>.</i>	33
1.17	<i>Three port circulator.</i>	38
1.18	<i>Some typical applications for the circulator; (a) duplexer; (b) isolator; (c) radar; (d) multiplexer.</i>	40
1.19	<i>Faraday rotation circulator</i>	41
1.20	<i>Lumped element circulator.</i>	41
1.21	<i>Waveguide circulator.</i>	42
1.22	<i>Structure of stripline circulator.</i>	43
1.23	<i>Coplanar circulator's structure</i>	44
1.24	<i>Coplanar structures proposed by Koshiji et al.; (a) and by Ogasawara et al. (b).</i>	44
1.25	<i>The circulator performed by Benevent et al. [53].</i>	44
1.26	<i>The fabricated circulator by Zahwe et al. with <math>6 \times 6 \text{ mm}^2</math> in size [54].</i>	45
1.27	<i>S-parameters of the circulator performed by Zahwe et al. with a YIG substrate [54].</i>	45

1.28	<i>The concept of self-biased circulator [54]. . . . .</i>	46
1.29	<i>Measured transmission parameters between port 1 and port 3 of the circulator fabricated by Saib [59]. . . . .</i>	47
1.30	<i>Measured and simulated performances of the circulator fabricated by Hamoir et al [42]. . . . .</i>	47
1.31	<i>Measured performances of the coplanar circulator investigated by Boyajian et al [60]. . . . .</i>	48
1.32	<i>The experimental parameters of the edge-mode coplanar circulator fabricated by Ardaches [61]. . . . .</i>	48
2.1	<i>Structure of the electric double layer at the electrode-solution interface. The solvent molecules are designated by "S", the anions with "-", and the cations with "+". . . . .</i>	55
2.2	<i>Nernst layer; stationary convective diffusion regime. . . . .</i>	57
2.3	<i>Edge effects according to [12]. . . . .</i>	59
2.4	<i>Configurations of the flows generated at the edges of the circular electrodes; a) Uhlemann et al. [11], b) Sugiyama et al. [18]. . . . .</i>	60
2.5	<i>Image and scheme of the experimental setup of the electrodeposition process. . . . .</i>	61
2.6	<i>Images of the permanent magnets used in the electrodeposition experiments. . . . .</i>	62
2.7	<i>Image of the furnace used for the air annealing treatment of the samples. . . . .</i>	63
2.8	<i>Example of a cyclic voltammetric curve and its characteristic parameters. <math>i_{p,a}</math>, <math>i_{p,c}</math>: anodic and cathodic peak currents; <math>E_{p,a}</math>, <math>E_{p,c}</math>: potentials for anodic and cathodic peaks. . . . .</i>	64
2.9	<i>Theoretical diagram of the current-time curve for three-dimensional germination. . . . .</i>	64
2.10	<i>Picture of X-Ray device used during this work. . . . .</i>	66
2.11	<i>Images of the FTIR spectrophotometer and the mini press used for the preparation of high-quality pellets. . . . .</i>	68
2.12	<i>AFM microscope; (a) agilent 5500 AFM device, (b) scanning operating principle. . . . .</i>	69
2.13	<i>Picture of the used Scanning Electron Microscope "FEI Nova 200". . . . .</i>	70
2.14	<i>Schematic drawing of the typical Scanning Electron Microscope principle and the electron-specimen interactions within a SEM. . . . .</i>	70
2.15	<i>Image of Bruker Dektak XT profilometer. . . . .</i>	71
2.16	<i>VSM instrument: (a) schematic illustration of sample vibration process between the two coils, (b) picture of equipment in a VSM unit. . . . .</i>	72
2.17	<i>MPMS SQUID VSM instrument and its measurement setup. . . . .</i>	73
3.1	<i>J-V characteristic of FTO substrate electrode for the solution containing <math>Co^{2+}</math> and <math>Fe^{2+}</math> at 25 °C. . . . .</i>	78
3.2	<i>Chronoamperogram for the growth of CoFe composite on FTO substrate in an aqueous ionic solution under -1.2 V constant potential for 34 min. . . . .</i>	79
3.3	<i>FTIR spectrum of electrodeposited <math>CoFe_2O_4</math> thin film. . . . .</i>	80
3.4	<i>XRD patterns of electrodeposited-annealed <math>CoFe_2O_4</math> thin films. . . . .</i>	81
3.5	<i>SEM images of AAO membrane; cross sectional view (a,b) and plan view (c). . . . .</i>	82
3.6	<i>Chronoamperograms of CoFe composite growth into AAO membranes at room temperature. . . . .</i>	82

3.7	<i>XRD patterns of the synthesized <math>\text{CoFe}_2\text{O}_4</math> nanowires in different nanoporous AAO membranes.</i>	83
3.8	<i>XRD spectrum of the annealed sample at 850 °C for 24 hours.</i>	84
3.9	<i>Steps of samples preparation for SEM analysis.</i>	84
3.10	<i>SEM images of <math>\text{CoFe}_2\text{O}_4</math> nanowires electrodeposited into various nanoporous AAO membranes; top and cross sectional views for 20 nm (a, d), 100 nm (b, e), and 200 nm (c, f).</i>	85
3.11	<i>EDS spectra of <math>\text{CoFe}_2\text{O}_4</math> nanowires after the dissolution in 0.1 M NaOH.</i>	85
3.12	<i>Hysteresis loops performed at 300 K for <math>\text{CoFe}_2\text{O}_4</math> nanowires with different diameters.</i>	86
3.13	<i>CA curves of electrochemical reduction of CoFe composite into 20 nm-AAO membranes at different applied potentials of -1 V, -1.1 V and -1.2 V.</i>	88
3.14	<i>XRD patterns of the annealed <math>\text{CoFe}_2\text{O}_4</math> nanowires electrodeposited at various applied potentials.</i>	89
3.15	<i>SEM images and corresponding EDS spectra of <math>\text{CoFe}_2\text{O}_4</math> nanowires electrodeposited at various potentials: (a) -1V, b) -1.1 V, and c) -1.2 V.</i>	90
3.16	<i>3D AFM micrographs of electrodeposited-annealed <math>\text{CoFe}_2\text{O}_4</math> nanowires at -1 V (a), -1.1 V (b) and -1.2 V (c).</i>	91
3.17	<i>Hysteresis loops of <math>\text{CoFe}_2\text{O}_4</math> nanowire arrays grown at different deposition potentials. The <math>\parallel</math> and <math>\perp</math> signs indicate the sweeping magnetic field direction parallel and perpendicular to the substrate surface, respectively, during the SQUID-VSM measurement.</i>	92
3.18	<i>CA curves of CoFe composite reduction into AAO membrane under different applied magnetic fields.</i>	94
3.19	<i>MHD effect in electrodeposition under vertical applied magnetic field B.</i>	94
3.20	<i>X-Ray diffraction patterns of the electrodeposited nanowires at various applied magnetic fields.</i>	95
3.21	<i>SEM images and EDX spectra of the magneto-electrodeposited <math>\text{CoFe}_2\text{O}_4</math> nanowires.</i>	96
3.22	<i>AFM 2D surface topography of the magneto-electrodeposited <math>\text{CoFe}_2\text{O}_4</math> nanowires; (a) <math>B=0.4</math> T, b) <math>B=0.5</math> T and (c) <math>B=0.6</math> T.</i>	97
3.23	<i>Hysteresis loops of the electrochemically deposited <math>\text{CoFe}_2\text{O}_4</math> nanowires at various applied magnetic fields.</i>	98
3.24	<i>Hysteresis loops of the annealed <math>\text{CoFe}_2\text{O}_4</math> nanowires at 600 °C and 700 °C.</i>	99
3.25	<i>Field cooling treatment of filled AAO membrane by <math>\text{CoFe}_2\text{O}_4</math> crystallites.</i>	101
3.26	<i>XRD spectrum of field cooled <math>\text{CoFe}_2\text{O}_4</math> nanowires at 0.6 T.</i>	101
3.27	<i>SEM images of field cooled <math>\text{CoFe}_2\text{O}_4</math> nanowires; (a) partial dissolution, (b) total dissolution.</i>	102
3.28	<i>Hysteresis loops of field cooled <math>\text{CoFe}_2\text{O}_4</math> nanowires at 0.6 T.</i>	102
3.29	<i>ZFC-FC magnetization curves for <math>\text{CoFe}_2\text{O}_4</math> nanowires; (a) magneto-electrodeposited at 0.6 T, (b) magneto-electrodeposited at 0.6 T and field cooled at 0.6 T. A magnetic field of 100 Oe is applied along the nanowire axis.</i>	104
3.30	<i>2D surface roughness measurements of filled AAO membrane; (a) as-prepared, (b) after grinding treatment.</i>	105
4.1	<i>Evolution of <math>\mu</math> components as a function of <math>\text{CoFe}_2\text{O}_4</math> nano-crystallites orientation.</i>	111



4.2	<i>Evolution of <math>\kappa</math> components as a function of <math>\text{CoFe}_2\text{O}_4</math> nano-crystallites orientation.</i>	112
4.3	<i>Evolution of <math>\mu_z</math> components as a function of <math>\text{CoFe}_2\text{O}_4</math> nano-crystallites orientation.</i>	112
4.4	<i>Structure of the Y-junction stripline circulator.</i>	113
4.5	<i>Ferrite junction circulation; (a) unmagnetized ferrite, (b) magnetized ferrite.</i>	113
4.6	<i>Design of the central conductor in cylindrical coordinates.</i>	114
4.7	<i>Evolution of the electric field along <math>z</math> for <math>r = R</math> and <math>n = 1</math> as a function of <math>\Phi</math>.</i>	117
4.8	<i>Evolution of the effective permeability for <math>\text{CoFe}_2\text{O}_4</math> nanocomposite as a function of frequency.</i>	123
4.9	<i>The S-parameters as a function of frequency for the stripline circulator; analytical calculation.</i>	124
4.10	<i>Interface of the HFSS simulator.</i>	126
4.11	<i>Example of a meshed structure.</i>	126
4.12	<i>Example of a convergence curve.</i>	127
4.13	<i>Material characteristics-HFSS.</i>	129
4.14	<i>Definition of datasets into HFSS.</i>	129
4.15	<i>Coplanar topology; (a) coplanar circulator with a bottom ground plane, (b) top view of the coplanar circulator, (c) cross sectional view of the CPW of the circulator, (d) A-B cross-sectional view of the circulator with ferrimagnetic substrate, (e) schematic distribution of the RF fields for a CPW line, (f) field displacement in the center of the circulator with coplanar junction.</i>	130
4.16	<i>Simulated CPW based on the ferrimagnetic nanocomposite.</i>	132
4.17	<i>Simulated CPW based on the ferrimagnetic nanocomposite.</i>	132
4.18	<i>Simulated coplanar circulator on HFSS.</i>	133
4.19	<i>Simulated S-parametres of the coplanar circulator.</i>	133
4.20	<i>Frame of TSD350 RF sputtering.</i>	135
4.21	<i>Wet Bench in clean room.</i>	136
4.22	<i>Resin deposition equipment used the clean room.</i>	137
4.23	<i>UV insulation machine.</i>	137
4.24	<i>Technological steps for the fabrication of the circulator.</i>	138
4.25	<i>Printed coplanar circulators on the nanocomposite surface.</i>	139
4.26	<i>Microwave characterization bench; (a) measurement equipment, (b) probes configuration for the CPW structure, (c) probes configuration for the coplanar circulator.</i>	140
4.27	<i>CPW S-parametrs; (a) measured forward <math>S_{12}</math> and reverse <math>S_{21}</math> transmission coefficients, (b) comparison between HFSS and VNA results.</i>	140
4.28	<i>Measured S-parameters of the fabricated coplanar circulator.</i>	141

# List of Tables

1.1	<i>Some magnetic parameters in CGS and SI units.</i>	16
1.2	<i>Susceptibilities of some diamagnetic materials.</i>	17
1.3	<i>Susceptibilities of some paramagnetic materials.</i>	18
1.4	<i>Susceptibilities of some ferromagnetic materials.</i>	18
1.5	<i>Neel temperatures for some antiferromagnetic materials.</i>	19
1.6	<i>Curie temperatures for some ferrimagnetic materials.</i>	20
1.7	<i>Demagnetizing factors for various geometries.</i>	23
3.1	<i>Electrolyte composition.</i>	78
3.2	<i>Squareness ratios and coercive fields for <math>\text{CoFe}_2\text{O}_4</math> nanowires.</i>	87
3.3	<i>Calculated cell parameters and crystallite sizes.</i>	89
3.4	<i>Squareness ratios and coercive fields for <math>\text{CoFe}_2\text{O}_4</math> nanowires.</i>	92
3.5	<i>Measured magnetic properties of <math>\text{CoFe}_2\text{O}_4</math> nanowires grown by magneto-electrodeposition in AAO templates.</i>	97
3.6	<i>Measured magnetic properties of the annealed <math>\text{CoFe}_2\text{O}_4</math> nanowires.</i>	100
4.1	<i>Characteristics of <math>\text{CoFe}_2\text{O}_4</math> nanocomposite.</i>	131

# List of abbreviations

GPS	Global positioning system
$CoFe_2O_4$	Cobalt ferrite
HFSS	High-frequency structure simulator
VNA	Vector network analyzer
FTO	Fluorine-doped tin oxide
AAO	Anodic aluminum oxide
CPW	Coplanar waveguide
EM	Electromagnetic
RF	Radiofrequency
GPT	Generalized permeability tensor
BBG	Bloch-Blombergen-Gilbert
YIG	Yttrium Iron Garnet
BaM	M-hexagonal barium hexaferrite
dB	Decibel
TEM	Transverse electromagnetic
FTIR	Fourier transform infrared
XRD	X-ray Diffraction
SEM	Scanning electron microscope
AFM	Atomic force microscope
SP	Stylus profilometry
VSM	Vibrating sample magnetometer
SQUID	Superconducting quantum interface device
IHP	Inner Helmholtz plane
OHP	Outer Helmholtz plane
MHD	Magnetohydrodynamic
CV	Cyclic voltametry
CA	Chronoamperometry
RE	Reference electrode
CE	Counter electrode
WE	Working electrode
Kbr	Potassium bromide
SPM	Scanning probe microscopy
STM	Scanning tunneling microscope
EDX	Energy-dispersive X-ray
EDS	Energy dispersive spectroscopy
MPMS	Magnetic property measurement system
FC	Field-Cooled
ZFC	Zero-Field-Cooled
DLC	Double layer charging
FWHM	Full width at the half maximum
MFM	Magnetic force microscopy

# General introduction

IN recent years, the market for non-reciprocal passive devices has undergone a remarkable transition due to the development of the wireless telecommunications sector. The miniaturization and performance improvement of these components is partly due to the exploitation of planar technologies, especially to the integration of active circuits on silicon that we find in several devices available to the general public (laptops, GPS, mobile phones and others).

In wireless applications, the circulator, a non-reciprocal passive device made up of at least three ports, allowing signals to be transmitted and received simultaneously using a single antenna, have been the subject of several studies in order to improve its performance. It is characterized by insertion, insulation and reflection losses as well as the operating frequency bandwidth. The conventional circulator operates with ferrite substrates polarized by an external magnetic field to ensure the non-reciprocity of the electromagnetic signals propagation. However, the presence of bulky and heavy permanent magnets that ensures the polarization of the ferrite remains a major obstacle to miniaturize and to integrate this circulator in microelectronic circuit. With the aim of moving to high frequencies and implementing low-cost technologies for commercial applications (satellite links, automotive applications, and collision avoidance radars), the ferrite and permanent magnet must be replaced by a self-polarized magnetic material.

During these last few years, several works on the miniaturization of circulators have been carried out; most of them are based on the idea of the self-orientation of magnetic nanoparticles using different deposition techniques. Indeed, ferrimagnetic nanowires offer an interesting alternative to ferrites, for the synthesis of self-polarized circulators at microwave or millimeter frequencies.

For these reasons, the present thesis is interested in "***Self-polarized magnetic nanocomposites based on ferrimagnetic nanowires for non-reciprocal microwave devices***". This co-supervised thesis is integrated in the PHC (*Hubert Curien Partnership*) "**TOUBKAL**" project, which brings together the Hubert Curien Laboratory (**LHC**) at Jean Monnet University in Saint-Etienne and the Materials and Renewable Energies Laboratory (**LMER**) at Ibn Zohr University in Agadir. This project focused on the fabrication of a self-biased non-reciprocal passive circulator that operates at high frequencies. The originality lies in the synthesis of planar components by using self-polarized ferrimagnetic nanocomposite, embedded in a nanoporous alumina membrane, obtained by electrodeposition under magnetic field.

The objective of this thesis work is to study the effects of the experimental parameters on the physico-chemical properties of cobalt ferrite nanowires ( $CoFe_2O_4$ ) during their

electrochemical deposition. Next, the structure of the microwave circulator has been modeled using an existing mathematical model. Afterwards, the dimensioning rules are developed from the 3-dimensional (3D) electromagnetic simulation of a coplanar structure of the circulator using the ANSYS HFSS software. Finally, prototypes in coplanar topology on the nanocomposite surface by photolithography in a clean room have been printed, in order to experimentally investigate the electromagnetic behavior of the fabricated circulator by a vector network analyzer (VNA).

This work was organized and structured in four chapters.

The first chapter is dedicated to a bibliographic study of the principles relating to magnetic materials which allows us to understand the generalities as well as the different classes of magnetism. The types of ferrites and their physical properties are discussed. Then, the analytical models of permeability tensors are presented according to the shape and the state of magnetization of these materials. Finally, a state of the art is drawn up with the aim of presenting the phenomenon of non-reciprocity which manifests itself in the different types of microwave circulators, as well as their operations, and more particularly the circulators in their coplanar topologies.

The second chapter of this manuscript involves a review of the electrochemistry field. Especially, the influence of the magnetic field during its interaction with an electric current in an electrochemical experiment. A presentation of the experimental setup and the tools used for the electrochemical growth of  $CoFe_2O_4$  will be presented. The different characterization techniques used in this work are the subject of the last part of this chapter.

In the third chapter, an optimisation of the electrochemical conditions of  $CoFe_2O_4$  coating on FTO substrates and porous templates will be performed. Afterwards, a detailed study of the effects of several parameters on the physico-chemical properties of  $CoFe_2O_4$  nanocomposite will be examined. The objective of this study is to fabricate self-polarized ferrimagnetic substrate that can be suitable for microwave application.

The fourth chapter focuses on the modeling and fabrication of CPW and coplanar circulator based on the synthesized ferrimagnetic nanocomposite. Firstly, the permeability tensor model of the nanocomposite will be presented. Afterwards, the analytical modelling of the circulator will be detailed based on the Bosma theory of stripline circulator, followed by a numerical modelling of the coplanar circulator on the HFSS software. Then, several structures will be simulated in order to determine which one gives the best performances. Finally, the manufacturing steps of such component on the nanocomposite surface will be discussed. Afterwards, a microwave characterization, a presentation and interpretation of the obtained results (S-parameters) will be outlined.

The outcome of this work will be summarized in the conclusion in which perspectives will be highlighted.

# Chapter 1

## Magnetic materials for microwave applications: State of the art

### 1.1 Introduction

The microwave devices based on magnetic materials have a specific properties around the gyromagnetic resonance. The most interesting effect is the non-reciprocal propagation of electromagnetic waves, induced by the anisotropic properties of the magnetic material. Indeed, this phenomenon controls the functioning of ferrite circulators in its bulk or thin layer structure. In this chapter we are interested in the theoretical formalism of magnetism in magnetic materials and their microwave behavior. First, we present the different ferrite categories and their physical properties chosen for various technological applications. Within this context, a special attention will be paid to cobalt ferrite ( $CoFe_2O_4$ ) material.

We briefly present the specifications of ferrimagnetic nanoparticles. Next, we describe the magnetization mechanisms in ferrite, and the different models adopted to study the permeability tensor for the saturated, demagnetized, and partially magnetized states. Finally, we discuss the main classes of existing circulators, in order to choice the optimized topology required for the technological application targeted by our project.

### 1.2 Brief history of magnetism

The history of magnetism is very interesting and dating from several centuries ago. Indeed, the first observations of magnetism date back to the exploration of the magnetite  $Fe_3O_4$ , contained in various natural rocks. However, the fundamental comprehension of magnetism started in the 1600s, which initiated the modern treatment of magnetism [1, 2].

The history of magnetism can be resumed as follows:

1600: William Gilbert publishes the first systematic experiments on magnetism of magnetite.

1819: Oersted establishes a fortuitous relationship between magnetism and electricity by discovering that a current carrying wire deviates a compass needle.

1825: Esturgeon discovers the electromagnet.

1880: Warburg obtains the first hysteresis loop for iron.

1895: The Curie law is drawn up.

1905: Langevin explains the theory of the diamagnetism and paramagnetism.

1906: Weiss proposes a theory of ferromagnetism.

1920: The physics of magnetism developed, which included theories based on the electron spin and exchange interactions.

1970: Neel received the Nobel Prize in Physics for his theories of the anti-ferromagnetism (1936) and ferrimagnetism (1948).

### 1.3 Origin of magnetism

A magnetic material is made up of a set of crystals. In the classical physics point of view, each crystal possess a periodic spatial structure of ions and each ion is composed of a nucleus around which revolve a number of electrons (Fig.1.1).

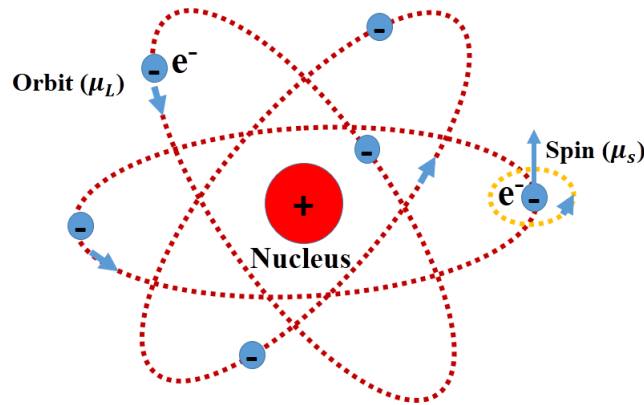


Figure 1.1: *Electron motion around the nucleus.*

The magnetic moment of an ion results from the contribution of its unfilled electronic layers. The electrons explains practically all the magnetic properties of the matter, because the electron is an electric charge in motion, and any movement of electric charge produces a magnetic field. The magnetic moment is originated from the movements of electrons around the nucleus in their orbits and the spin rotation of each electron. This gives rise to an orbital moment ( $\mu_L$ ) and a spin moment ( $\mu_s$ ), respectively. The net magnetic moment of a material is the vector sum of the orbital moments and the spin moments of its peripheral electrons. The application of a magnetic field  $\vec{H}$  modifies the electromagnetic properties of the magnetic medium [3]. The resulting magnetic induction is related to the external magnetic field by the following formula:

$$\vec{B} = \mu_0(\vec{H} + \vec{M}) \quad (1.1)$$

where  $\mu_0 = 4\pi 10^{-7} H/m$ , represents the permeability of free space,  $\vec{M} = \chi \vec{H}$  the magnetization of the magnetic material, i.e. the mean orientation of the magnetic moments, and  $\chi$  is the magnetic susceptibility, defined as the ability of the magnetic material to be magnetized by an external magnetic field.

Thus, the magnetic induction becomes:

$$\vec{B} = \mu_0 \vec{H} (1 + \chi) \quad (1.2)$$

The relative permeability of the material can be expressed from the magnetic susceptibility by the following relationship:

$$\mu_r = 1 + \chi \quad (1.3)$$

which ultimately gives:

$$\vec{B} = \mu \vec{H} \quad (1.4)$$

where  $\mu = \mu_0 \mu_r$  is the magnetic permeability.

These above-mentioned formulas present a collinear dependence of the induction and the magnetization on the applied field, which is the case for an isotropic material. In the general case, the material is anisotropic and the magnetization is not collinear with the magnetic field. Thus, we must introduce the tensors of the susceptibility and permeability. The relationship between certain magnetic parameters in CGS and SI units is summarized in the following table [4]:

Table 1.1: *Some magnetic parameters in CGS and SI units.*

Quantity	CGS	SI	Factor conversion From CGS to SI
Magnetic induction ( $B$ )	Gauss	T	$10^{-4}$
External magnetic field ( $H$ )	Oe	$A.m^{-1}$	$10^3/4\pi$
Magnetization ( $M$ )	$emu.cm^{-3}$	$A.m^{-1}$	$10^3$
Magnetization ( $4\pi M$ )	Gauss	$A.m^{-1}$	$10^3/4\pi$
Susceptibility ( $\chi$ )	$emu.cm^{-3}$	Dimensionless	$4\pi$
Permeability ( $\mu$ )	Dimensionless	$H.m^{-1}$	$4\pi 10^{-7}$

Note that from the values of  $\chi$ , it is possible to classify the main categories of magnetic materials such as:

- **Diamagnetic:**  $\chi < 0$ , around  $-10^{-5}$ ;
- **Paramagnetic:**  $\chi > 0$ , widely dispersed and less than  $10^{-3}$ ;
- **Ferromagnetic:**  $\chi$  is very important and varies with  $H$ . The remanent magnetization is very high;
- **Antiferromagnetic:**  $\chi$  is weakly positive because the moments are balanced in an antiparallel arrangement in two arrays of magnetizations of equal intensities and opposite directions;
- **Ferrimagnetic:** the material has two magnetic moment arrays with different magnetization intensities.

We will briefly detail these magnetism classes of materials in the next paragraph.

## 1.4 Types of magnetism in materials and their properties

### 1.4.1 Diamagnetism

In general, diamagnetism characterizes the materials that contain only non-magnetic atoms. These diamagnetic materials are made up of atoms in which all the electronic



layers are filled. However, under the effect of an external magnetic field, the diamagnetic materials have an induced magnetization opposite to the direction of the magnetic field. In addition, the susceptibility due to diamagnetism is low  $10^{-5}$  and negative; it is independent on the field and the temperature.

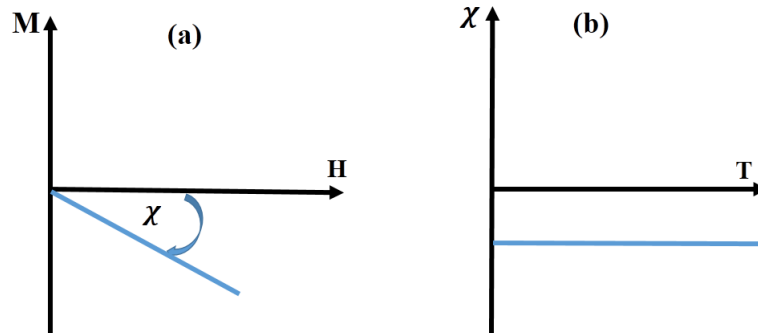


Figure 1.2: Variation of magnetization under magnetic field (a) and thermal variation of the susceptibility (b) for a diamagnetic material.

The diamagnetism exists everywhere in materials but it is negligible compared to the effects of paramagnetism and ferromagnetism when they coexist with it [5].

Table 1.2: Susceptibilities of some diamagnetic materials.

Cu	Ag	Au
$-7 \times 10^{-7}$	$-1.82 \times 10^{-6}$	$-0.1 \times 10^{-6}$

## 1.4.2 Paramagnetism

Paramagnetism occurs when the magnetic moments of atoms practically do not interact with each other and can orient themselves randomly in any direction (Fig.1.3.a).

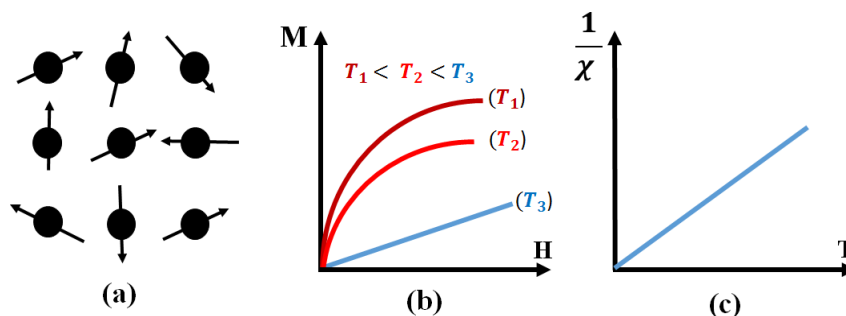


Figure 1.3: Paramagnetism in atoms.

The average sum of the micro-magnetizations is zero, in this case the material is completely demagnetized [6]. However, in the presence of magnetic field, the magnetic moments tend to align in their own direction and an induced magnetization parallel to the field appears. This magnetization becomes weak by increasing the temperature (thermal agitation effect). At high temperature, the magnetization becomes linear as a function of the field (Fig.1.3.b). In addition, the initial magnetic susceptibility, positive, is infinite at absolute zero and decreases as the temperature increases. It is generally around  $10^{-5}$  at room temperature. In the ideal case, the inverse of the susceptibility is proportional

to the temperature as presented by Curie's law, which is valid for not too high magnetic fields and not too low temperatures (Fig.1.3.c):

$$\chi = \frac{C}{T} \quad (1.5)$$

where  $C$  is the Curie constant.

Table 1.3: *Susceptibilities of some paramagnetic materials.*

Al	Na	Li
$1.7 \times 10^{-6}$	$0.7 \times 10^{-6}$	$14.2 \times 10^{-6}$

### 1.4.3 Ferromagnetism

In ferromagnetic materials, the atomic magnetic moments exhibit a strong positive spin exchange, which gives rise to a parallel alignment as described in (Fig.1.4.a) [7].

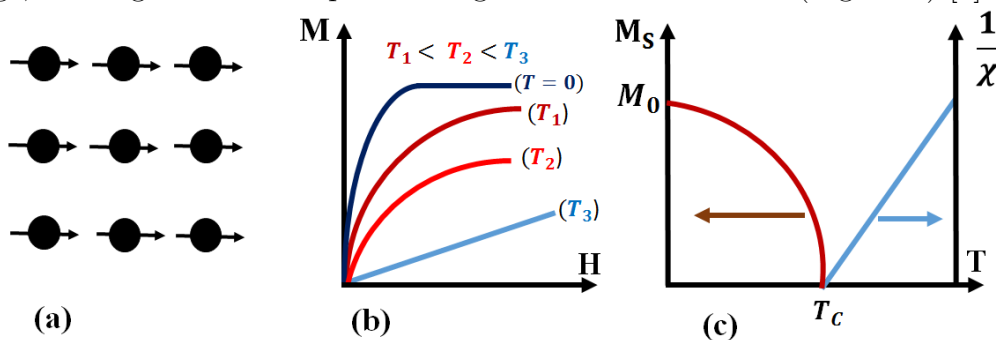


Figure 1.4: *Ferromagnetism; (a) Spin arrays, (b) Variation of magnetization as function of field, (c) Thermal variation of  $1/\chi$  and spontaneous magnetization.*

According to Curie-Weiss law, the thermal agitation induces a paramagnetic behavior (disordered state) beyond Curie temperature  $T_C$ . For temperatures lower than  $T_C$ , the susceptibility  $\chi$  is very high but adopts a paramagnetic behavior above  $T_C$  (Fig.1.4.c). In addition, below  $T_C$ , the interactions dominate the thermal agitation and a spontaneous magnetization  $M_S$  appears in the absence of an applied field, which reaches its maximum value  $M_0$  at zero temperature, corresponding to the parallel arrangement of all the individual moments of the magnetic substance (Fig.1.4.b and c). This phase transition behavior is reversible, and the material regains its ferromagnetic properties when its temperature drops below the Curie temperature  $T_C$ .

Table 1.4: *Susceptibilities of some ferromagnetic materials.*

Co	Ni	Fe
70	110	200

### 1.4.4 Antiferromagnetism

The existence of antiferromagnetic materials corresponds to negative exchange interactions between the spins [8]. The magnetic moments are aligned in antiparallel mode in two arrays of equal and opposite magnetizations (Fig.1.5.a), the mean magnetization being thus generally zero and the susceptibility weakly positive. Consequently, the thermal

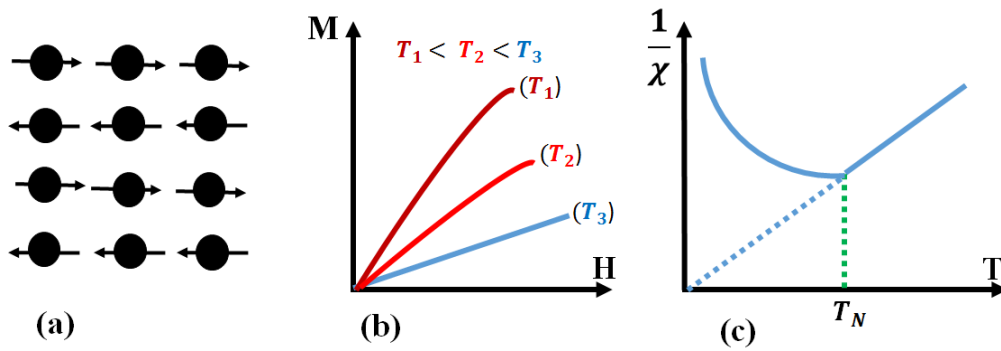


Figure 1.5: *Antiferromagnetism; (a) Arrays of spins, (b)  $M(H)$ , (c)  $\chi^{-1}(T)$ .*

variation of the inverse of the susceptibility exhibits a minimum at the Neel temperature  $T_N$ . Above this temperature, a thermal variation in susceptibility similar to that of a paramagnetic medium is observed, as shown in Fig.1.5.b and c.

Table 1.5: *Neel temperatures for some antiferromagnetic materials.*

NiO	$CoCl_2$	FeO
520 K	25 K	198 K

### 1.4.5 Ferrimagnetism

The ferrimagnetism characterizes a material of the antiferromagnetic type in which the two arrays do not present the same amplitude of magnetization (Fig.1.6.a). As a result, the average magnetization is different to zero [9].

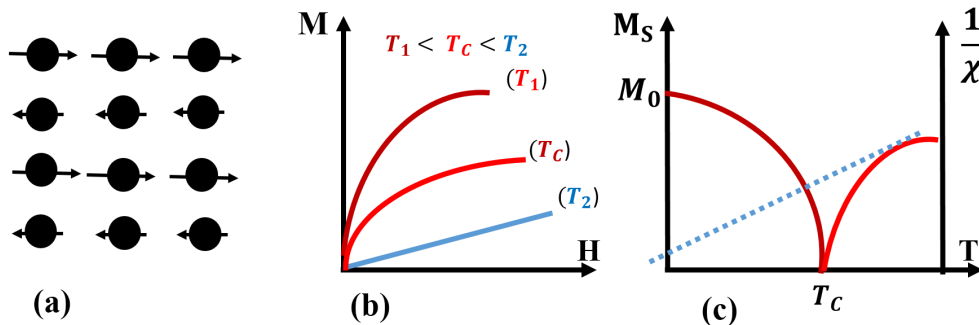


Figure 1.6: *Ferrimagnetism; (a) spin arrays, (b) variation under field of magnetization, (c) thermal variation of the spontaneous magnetization and  $\chi^{-1}$ .*

As shown in Fig.1.6.c, below the Curie temperature  $T_C$ , the spontaneous magnetization is reached, which can explain that one of these sub-arrays is preponderant in front of the other. Consequently, the macroscopic behavior of a ferrimagnetic material in this temperature range can exhibit a close resemblance to that of a ferromagnetic material. The increase in temperature weakens the magnetization. At temperatures above  $T_C$ , they behave like a paramagnetic material (Fig.1.6.b and c). The spinel ferrites ( $MF_e_2O_4$ ) are part of ferrimagnetic materials.

Table 1.6: Curie temperatures for some ferrimagnetic materials.

$CoFe_2O_4$	$NiFe_2O_4$	$Fe_3O_4$
800 K	585 K	955 K

## 1.5 Magnetic anisotropy

The magnetic anisotropy is a fundamental property corresponding to the dependence of energy with the direction of magnetization in magnetic materials [10]. It tends to align the magnetic moments along a preferential direction, where the energy has a minimum value, called axis of easy magnetization. Consequently, the least energetically favorable direction defines the axis of hard magnetization. The anisotropy energy is translated by the difference in energy resulting from the direction change of the magnetization from one axis of easy magnetization to another described as harder. There are different contributions that promote the magnetic anisotropy, of which we can cite:

### 1.5.1 Magnetocrystalline anisotropy

This anisotropy is related to the crystallographic structure in a magnetic crystal [10]. It describes the dependence of internal energy depending on the direction of the spontaneous magnetization. In the case of a cubic symmetry, for example in cobalt ferrite ( $CoFe_2O_4$ ) which crystallizes in a face-centered cubic (fcc) structure, the axes of hard magnetization are the edges [100] of the cube, while the diagonal [111] is easy to be magnetized.

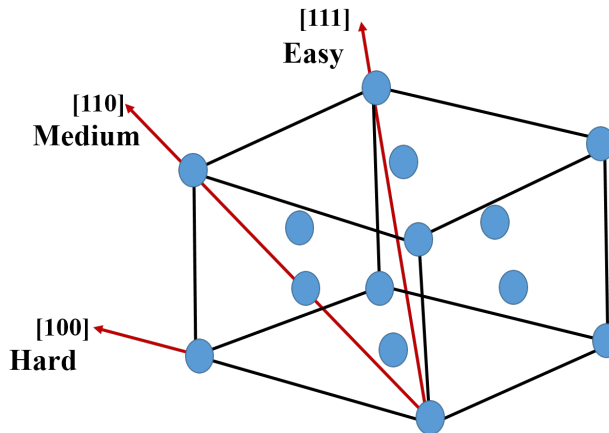


Figure 1.7: Schematic representation of easy and hard axes of magnetization for cubic symmetry.

The magnetocrystalline anisotropy energy can be expressed by the following phenomenological formula:

$$\frac{E_{ma}}{V} = (K_1(\alpha_1^2\alpha_2^2 + \alpha_1^2\alpha_3^2 + \alpha_2^2\alpha_3^2) + K_2(\alpha_1^2\alpha_2^2\alpha_3^2)) \quad (1.6)$$

The coefficients  $K_i$  are the constants of anisotropy. The absolute value of these coefficients decreases sharply when the order increases and we generally take only into account the first constant  $K_1$  in the case of a monodomain particle or sometime  $K_2$ . This quantity can have positive or negative values and it is expressed in  $J/m^3$  or  $erg/cm^3$ . The coefficients

$\alpha_i$  represent the direction cosines of the angles between the magnetization and the axes of the coordinate system. In this context, it is important to define the anisotropy field ( $H_a$ ) oriented along the easy magnetization axis, and for which the magnetization of each domain has become parallel to the applied magnetic field. Indeed, when the magnetization moves easily under the effect of an applied external magnetic field, the anisotropy field becomes weak, and vice versa. For materials with cubic symmetry and which have [111] as an axis of easy magnetization, this field is expressed by:

$$H_a = \frac{4(3K_1 + K_2)}{9\mu_0 M_s} \quad (1.7)$$

where  $M_s$  is the saturation magnetization of the material.

### 1.5.2 Surface anisotropy

On the surface of a magnetic material, the atoms have a more different local environment than those located into the volume. There is a decrease in the number of nearest neighbors and a break in symmetry on the surface will take place, which adds an additional surface anisotropy  $K_s$  term. This type of anisotropy was firstly described by Neel [11]. It has been reported experimentally that this anisotropy exists [12]. In addition, this anisotropy becomes more remarkable for small particles because of the increase of the surface/volume ratio and the magnetization can switch out of the plane when the layer becomes sufficiently thin. The surface anisotropy is expressed as a reduction in planar magnetization.

$$M_{eff} = M_s - \frac{4K_s}{M_s e_F} \quad (1.8)$$

where  $e_F$  is the film thickness.

### 1.5.3 Magnetoelastic anisotropy

The magnetoelastic energy is originated from the magnetostriction, i.e. the deformation of the crystal lattice in size and/or symmetry under the effect of the spin-orbit couplings. Moreover, the magnetoelastic anisotropy is due to the interaction between the magnetization and the mechanical deformations of the crystal lattice. The imposition of an external constraint (*applied stress*) induces a modification of the magnetic properties, since the magnetic moment is strongly linked to the atomic orbitals. In addition, the direction of this constraint makes an angle  $\phi$  with the induced magnetization. The magnetoelastic energy associated with this effect is expressed for a magnetostrictive isotropic material, not subjected to a magnetic field by the following expression [13]:

$$\frac{E_{me}}{V} = K_{me} \cos^2 \phi \quad (1.9)$$

Here  $K_{me} = \frac{3}{2}\lambda_s\sigma$ ,  $\lambda_s$  is the magnetostriction constant, and  $\sigma$  the magnitude of the applied stress.

### 1.5.4 Shape anisotropy

The orientation of the easy axes is conditioned by the shape of the material considered. There is a shape anisotropy resulting from the dipole interaction between the magnetization and the demagnetizing field which opposes the magnetization by closing the magnetic

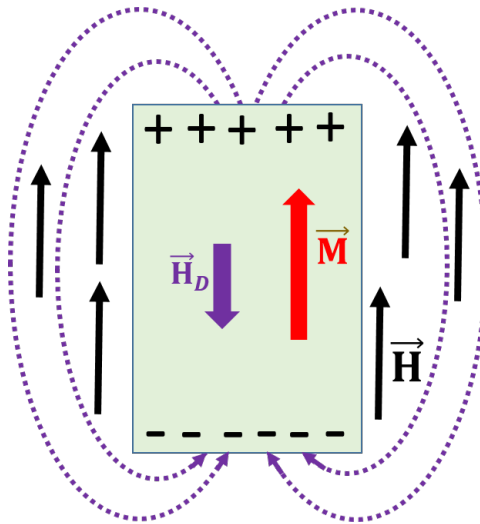


Figure 1.8: Illustration of the demagnetizing field  $\vec{H}_D$  in a material with  $\vec{H}$  is the applied field and  $\vec{M}$  is the magnetization of the material. The dashed lines represent the magnetic field lines.

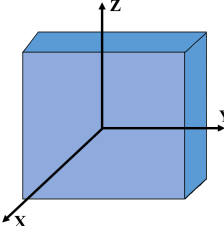
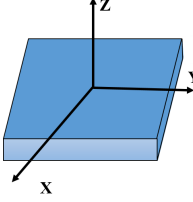
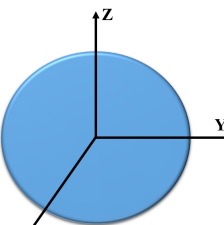
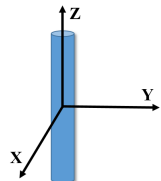
flux loop. By analogy with electrostatics, there will be a production of magnetic virtual charges on the faces of the magnetic material as described in Fig.1.8.

The demagnetizing field  $\vec{H}_D$  is related to the magnetization  $\vec{M}$  by the following formula:

$$\vec{H}_D = -\hat{N}\vec{M} \quad (1.10)$$

where  $\hat{N}$  is a tensor known as the demagnetizing factor. This coefficient depends on the shape of the material and can mainly be presented by three demagnetizing coefficients  $N_X$ ,  $N_Y$ , and  $N_Z$ . The table below gives the form factors of some geometries, the sum must be  $N_X + N_Y + N_Z = 1$ .

Table 1.7: Demagnetizing factors for various geometries.

	$N_X$	$N_Y$	$N_Z$
 <p>Infinite plate in y and z axes</p>	1	0	0
 <p>Infinite plate in x and y axes</p>	0	0	1
 <p>Spherical sample</p>	1/3	1/3	1/3
 <p>Infinite cylinder in z axis</p>	1/2	1/2	0

Finally, the internal magnetic field  $\vec{H}_i$  of a material having dimensions can be presented as a function of the demagnetizing coefficients, the external applied field, and the magnetization, by the following expression:

$$\vec{H}_i = \vec{H}_0 - \hat{N}\vec{M} \quad (1.11)$$

## 1.6 Static properties

### 1.6.1 Weiss domains

At a microscopic level, a ferrimagnetic material is subdivided in regions called Weiss domains (referred to the physicist Pierre Weiss), which are spontaneously magnetized in

random directions, so that their result is statistically zero. These domains are separated by transition zones called Bloch walls, in which the spin orientations rotate gradually. This creates a discontinuity in the magnetic orientation shape from a domain to another (Fig.1.9).

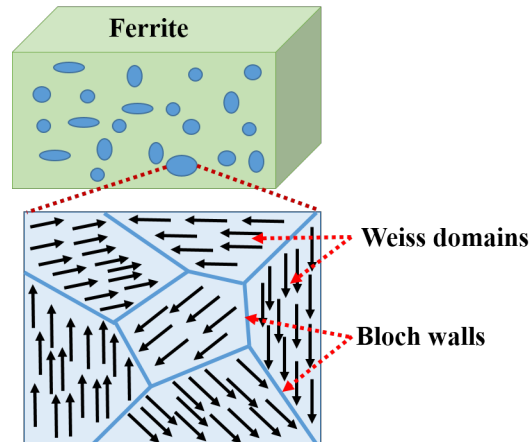


Figure 1.9: *Weiss domains and Bloch walls in the absence of an applied magnetic field.*

In the presence of an external magnetic field, the Weiss domains size increases and decreases reversibly or irreversibly by moving the Bloch walls. If the applied magnetic field is high enough, the material reaches its saturation state in one direction, then in the opposite direction, which gives us finally the hysteresis loop, as detailed in the next paragraph.

## 1.6.2 Hysteresis phenomenon

Another characteristic of ferrimagnetic materials is the hysteresis (a Greek word meaning delay), a phenomenon by which the magnetization  $M$  is not unequivocally determined by the value of the applied field  $H$  but depends on the previous state of the material. When we excite a ferrimagnetic material for the first time, the global magnetization  $M$  first increases in proportion to the field  $H$ , then the increase of  $M$  becomes constant and stable beyond a certain field value, in this zone the saturation magnetization ( $M_s$ ) is reached, corresponding to the maximum magnetization, i.e all the moments are completely parallel to the applied field  $H$  direction. This is the first magnetization curve (see Fig.1.10, dotted curve). If we then decrease the field, we notice that the variation of  $M$  does not have the same profile and that, for  $H = 0$ , preserves a certain value of magnetization, called remanent magnetization  $M_r$ . To suppress the magnetization, it is necessary to alternate the magnetic field to an opposite sign,  $H_c$ , called the coercive field. Two distinct rising and falling curves of  $M(H)$  are obtained, which represents the magnetic response of a material to an applied field. This process thus produces a complete cycle namely the hysteresis loop (*hysteresis cycle*) [14]. The shape of the cycle depends strongly on the chemical composition of the material, the direction of the applied magnetic field, as well as the temperature of the measurement.

By exploiting the coercive field  $H_c$ , we can differentiate between two main classes of magnetic materials:

- **Hard materials:** difficult to magnetize and having a coercive and anisotropic



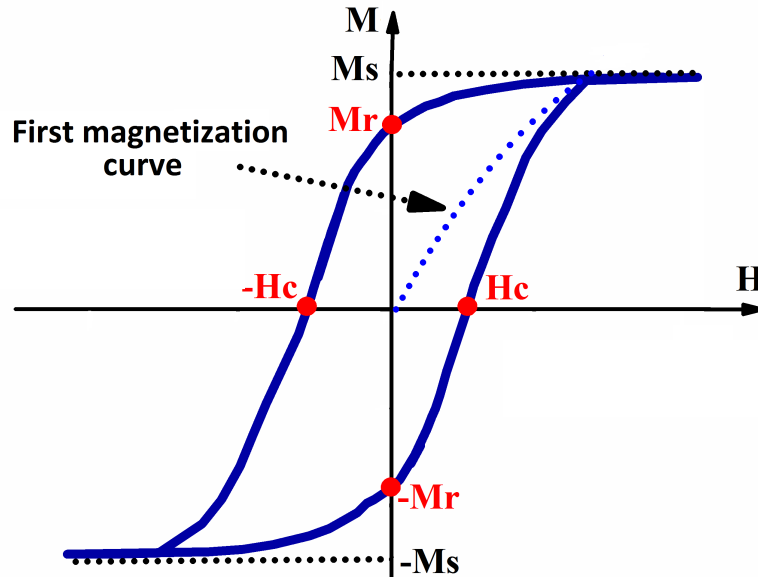


Figure 1.10: *Hysteresis loop for a ferrimagnetic material.*

fields which can reach  $2 \times 10^6 \text{ A/m}$ . They are used to make permanent magnets and self-biased microwave devices.

- **Soft materials:** easy to magnetize and having a weak coercive and anisotropy fields ( $\leq 10^3 \text{ A/m}$ ). They are often used for the design of transformers, motors, inductors and for magnetic shielding.

### 1.6.3 Monodomain state

In the previous paragraph, we have discussed that in the absence of a magnetic field, a ferrimagnetic substance divides into magnetic domains. These domains are very sensitive to the size of the nanoparticles presented inside the material. Generally, the magnetic energy designates the sum of the exchange energy between the spins and the magnetostatic energy originated from the dipolar interaction between the magnetic moments, and which is opposed to the establishment of a macroscopic magnetization. However, below a certain critical diameter, the cost in terms of energy that would have to be paid to create a narrow wall would exceed the gain in the magnetostatic energy related to the formation of two domains. In this case, the monodomain state (all spins are globally aligned in one direction) becomes the most stable magnetization state. A monodomain medium carries a permanent magnetic moment called macrospin, which presents the sum of the individual magnetic moments of the atoms. For an isolated particle, the critical diameter  $D_c$  is given by the following formula [15]:

$$D_c = \frac{9\sigma_w}{2\pi M_s^2} \quad (1.12)$$

where  $\sigma_w = \left(\frac{2k_b T_c K_1}{a}\right)^{1/2}$  is the wall density energy,  $K_1$  the magnetocrystalline anisotropy constant,  $T_c$  the Curie temperature,  $k_b$  the Boltzmann constant, and  $a$  the lattice constant. For  $D > D_c$ , the particles exist in a multidomain structure, while for  $D < D_c$ , the particles exist in a monodomain structure. The critical diameter depends strongly on the type and shape of the sample, and the anisotropy of the particle, it is around 15 nm for the magnetite  $\text{Fe}_3\text{O}_4$ .

## 1.7 Dynamic properties

### 1.7.1 Gyromagnetic resonance

When a ferrimagnetic material with magnetization  $\vec{M}$  is polarized by an external magnetic field  $\vec{H}$ , the magnetization undergoes a torque proportional to  $\vec{M} \wedge \vec{H}$ . This results in a free movement of precession of the magnetization around the direction of the internal field  $\vec{H}_i$  present in the material, which verifies the following equation of motion in an ideal medium (the spins do not interact with each other) [16]:

$$\frac{\partial \vec{M}}{\partial t} = -\mu_0 \gamma \vec{M} \wedge \vec{H} \quad (1.13)$$

Here  $\gamma$  is the gyromagnetic factor taking a positive value and corresponds to the ratio between the magnetic and kinetic moments of spin, with  $\gamma = 2\pi \times 28 \text{ GHz/T}$ . The magnetic moments of the material have an intrinsic frequency of precession called the Larmor frequency, and are characterized by a rotation frequency  $\omega_r$ . Once this frequency becomes equal to the frequency of the excitation field  $\vec{H}$ , the gyromagnetic resonance will take place.

$$\omega_r = \omega_0 = \mu_0 \gamma H_i \quad (1.14)$$

In addition, when the interaction between the moments of spins is not negligible, a damping to this rotational movement (represented by a factor  $\alpha$ ) occurs.

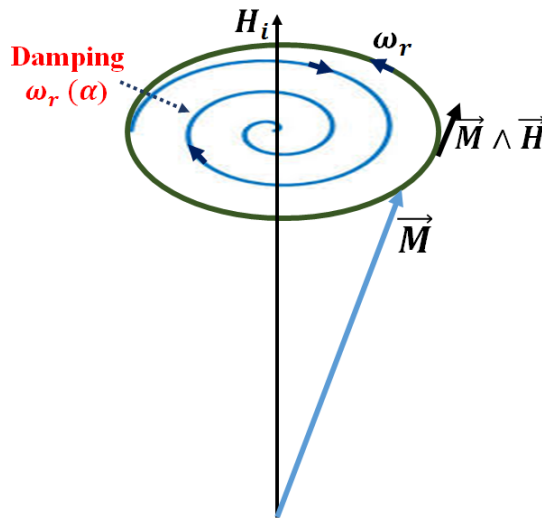


Figure 1.11: *Precession of the magnetization with and without damping.*

$$\omega_r(\alpha) = \omega_0 + j\alpha\omega \quad (1.15)$$

Consequently, the movement is no longer free but it is very quickly absorbed and the magnetization aligns with the internal field after a time of relaxation by describing a spiral. For a ferrimagnetic medium of finite dimensions, the resonance frequency is affected by demagnetizing factors, which depend on the sample shape, so that equation (1.14) can be written as,

$$\omega_r = \omega_0 = \mu_0 \gamma H_i = \mu_0 \gamma [(H - (N_Z - N_X)M_s) \times (H - (N_Z - N_Y)M_s)]^{1/2} \quad (1.16)$$

where  $H$  is the applied external field,  $M_s$  the saturation magnetization of the material, and  $N_X$ ,  $N_Y$ ,  $N_Z$  are the demagnetizing factors (Table.1.7). This relationship is the Kittel formula which is applicable for magnetic media polarized in the Oz direction [17].

## 1.7.2 Non-reciprocity in ferrites

One of the main behaviors of magnetized ferrimagnetic materials is the non-reciprocal propagation of an electromagnetic (EM) wave inside the medium. The non-reciprocity is an important property that controls the proper functioning of the microwave devices (circulators, isolators) [18]. It is based on several physical effects:

### 1.7.2.1 Gyromagnetic resonance (*more detailed in the previous paragraph*)

When an EM wave propagates in a ferrimagnetic medium, it will decompose simultaneously into two types of polarization waves, one right circular or elliptical and the other left circular or elliptical. If the resulting polarization direction is the same as for the gyromagnetic precession, a strong interaction with the ferrimagnetic material which results in a strong absorption of the EM wave will take place. On the other hand, there will be only a weak interaction with the ferrimagnetic material, because the magnetic field rotates in the opposite direction of the gyromagnetic precession.

### 1.7.2.2 Faraday effect

To explain this notion of Faraday effect, we consider a ferrimagnetic material subjected to a rectilinearly polarized EM wave with a propagation direction parallel to  $H$  as displayed in Fig.1.12.

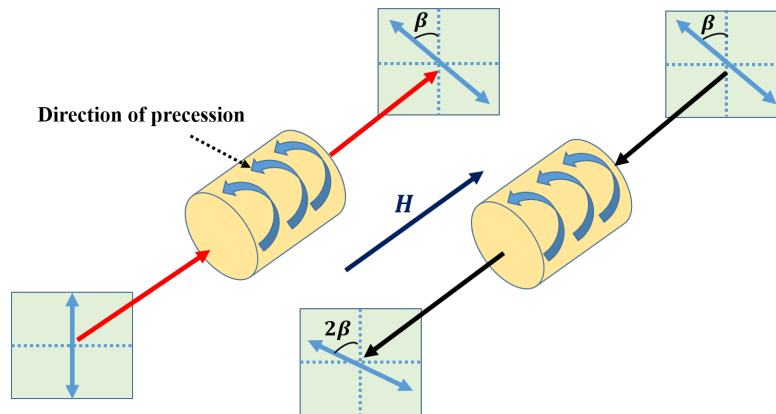


Figure 1.12: *Non-reciprocal Faraday rotation for an EM wave propagating from left to right (red) and from right to left (black).*

Applying a magnetic field on a ferrimagnetic medium in a direction parallel to the direction of light propagation, causes a rotation of the light polarization direction. Indeed, as this phenomenon is due to the gyrotropic movement of the magnetic moments, a wave propagating in the opposite direction sees its polarization turning in the same direction as that of the direct wave, as illustrated in Fig.1.12. This process produces a non-reciprocal rotation known as Faraday rotation [19].

### 1.7.2.3 Field displacement effect

In order to explain this field displacement phenomenon, firstly a microstrip line printed on a dielectric substrate (Fig.1.13.a) is considered. The wave propagation mode has the coordinate system ( $yOz$ ) as the plane of geometric symmetry [20]. In this configuration, the fundamental mode of the wave propagates along the ( $Oz$ ) axis. This results in a mapping of the symmetrical transverse electric and magnetic fields (*RF fields*).

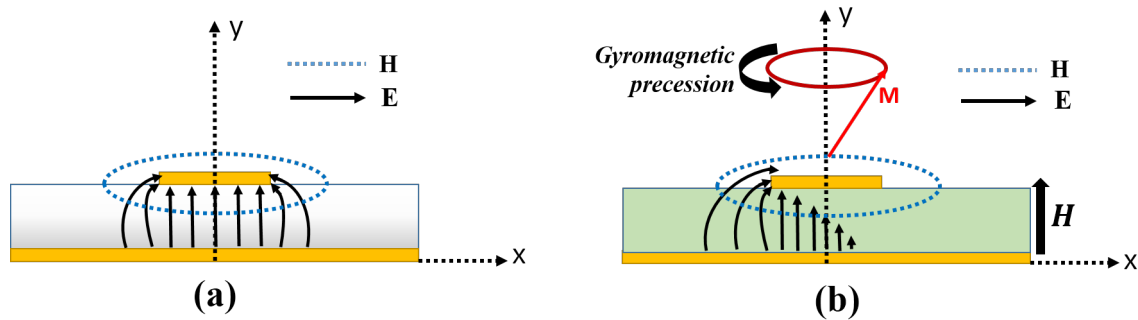


Figure 1.13: *RF fields mapping for a cross section of the microstrip line; on a dielectric substrate (a), and on a magnetized ferrite (b).*

In the other configuration, if the dielectric is replaced by a ferrimagnetic material magnetized along ( $Oy$ ) (Fig.1.13.b), a modification in the distribution of the transverse fields to the direction of the EM wave propagation in the ferrimagnetic medium can be noticed. Consequently, the plane ( $yOz$ ) is no longer a plane of geometric symmetry and we have an electric field displacement along ( $Ox$ ). Therefore, the structure undergoes the field displacement phenomenon. The ferrites, which are typical of ferrimagnetic materials, are characterized by a high resistivity ( $10^5 \Omega.m$ ), which promotes the penetration of electromagnetic waves. They are intensively used in high frequency electronics. We will detail the different classes of these ferrites in the next section.

## 1.8 Classes of ferrites

The ferrites are generally classified according to their crystallographic structures. Indeed, ferrites with garnet, hexagonal and spinel structure can be found.

### 1.8.1 Garnet

The ferrites with a garnet structure are composed of  $R^{3+}$  rare earth elements [21], such as  $Gd^{3+}$  (Gadolinium),  $Tb^{3+}$  (Terbium),  $Y^{3+}$  (Yttrium), and have the general chemical formula  $R_3Fe_5O_{12}$ . The garnet crystallizes in a cubic structure and the most common garnet-material is the garnet of iron and yttrium  $Y_3Fe_5O_{12}$ , known as *YIG* (Yttrium Iron Garnet). Moreover, the garnets have low saturation magnetization  $M_s$  and a low Curie temperature, e.g. the Curie temperature of the *YIG* is 560 K, which limits their use in the frequency range from 10 MHz to 10 GHz. They also have low magnetic losses ( $\Delta H$  and  $\Delta H_{eff}$ ). This type of ferrite is generally used in different applications such as filters and oscillators.

## 1.8.2 Hexaferrite

The most common structure of hexaferrite is type M with the chemical stoichiometric formula  $BaFe_{12}O_{19}$ . This structure has a "hard" magnetic behavior. In practice, the permanent magnets are generally based on the M-hexagonal barium ferrite ( $BaM$ ). Another main application of this material is the high density magnetic recording medias [22]. Other structures like type Z, type W or type Y, have a planar anisotropy which is mild, and presenting a high permeability in the microwave range. In fact, the high value of the anisotropy in M-type hexaferrite makes it possible to design some millimeter devices in the frequency range from 30  $GHz$  to approximately 100  $GHz$ . This property makes them attractive for the manufacture of miniaturized devices which can be operated without the presence of any external polarization (*self-polarized mode*). They have a strong axial magnetic anisotropy up to 2800  $kA/m$ , greater than that of garnet, i.e. a saturation magnetization and Curie temperature of around 400  $kA/m$  and 723  $K$ , respectively.

## 1.8.3 Spinel

Spinel ferrite has a  $MFe_2O_4$  structure, where  $M$  represents a metal ( $Co$ ,  $Ni$ ,  $Li$ , etc.). The spinel materials crystallize in a face-centered cubic (fcc) structure, where the cations are located on two different crystallographic sites. As shown in Fig.1.14, there are two kinds of sites in the crystal cell of the spinel phase [23]:

- **Tetrahedral site (T)**: a bivalent cation is coordinated with four oxygen ions;
- **Octahedral site (O)**: a trivalent cation is coordinated with six oxygen ions.

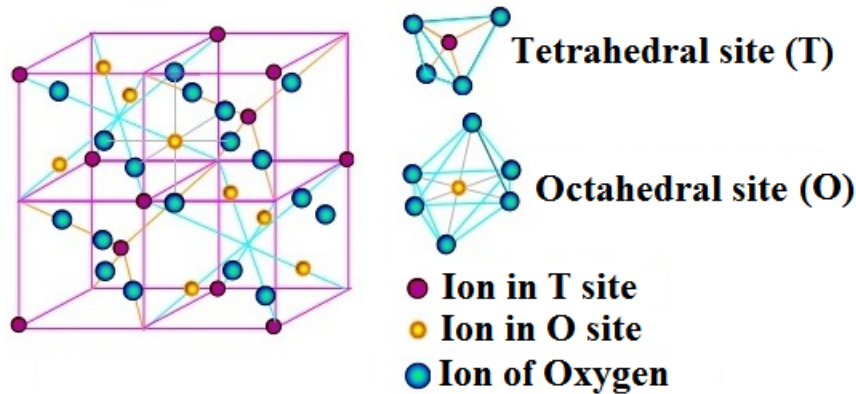


Figure 1.14: Spinel unit cell structure.

The distribution of the individual cations in the unit cell can be described by the following chemical formula:

$$(Co_{1-i}^{2+}Fe_i^{3+})[Co_i^{2+}Fe_{2-i}^{3+}]O_4^{2-} \quad (1.17)$$

where  $i$  is the degree of inversion. The ideal inverse spinel structures have  $i = 1$  and  $i = 0$  for the normal spinel and the mixed spinel structures, with the value of  $i$  varying between 0 and 1. The ions within square brackets are located in the octahedral sites and the ions within brackets are located in the tetrahedral sites.

In a normal spinel structure, all  $Fe^{3+}$  cations are placed in the octahedral sites and all  $Me^{2+}$  cations are located in the tetrahedral sites. In the case of a completely reverse spinel

structure, the  $Me^{2+}$  cations are located in octahedral sites, while the  $Fe^{3+}$  are distributed equally between the octahedral and tetrahedral sites. Consequently, the lattice parameter of the spinel is higher. The majority of ferrites used at high frequencies have an inverse spinel structure. The magnetic properties of ferrites depend strongly on the ions located in the interstices as well as on their distribution. However, the coefficient  $i$  may depend on the heat treatment and physical forces applied to the ferrite material. Each change in the parameter  $i$  creates a modification in the magnetic response of the spinel ferrite.

$CoFe_2O_4$  is one of the spinel-group and adopts an inverse spinel structure. It has  $a = 8.39 \text{ \AA}$ . From a magnetic point of view (at room temperature),  $CoFe_2O_4$  has a saturation magnetization which can vary from 1200 to 2800 Gauss depending on the chemical composition. It has a Curie temperature of 800 K and a magnetostriction coefficient close to  $-200 \times 10^{-6}$ , a relative dielectric permittivity  $\epsilon_r$  ranging from 10 to 15. In addition, the magnetocrystalline anisotropy constant  $K_1$  of  $CoFe_2O_4$  is about  $2 \times 10^5 \text{ J.m}^{-3}$  (30 times higher than that of  $NiFe_2O_4$ ) [24], which results in a large coercive field values, up to 2500 Oe. From a dynamic point of view, the full-width at half-maximum  $\Delta H$  of  $CoFe_2O_4$ , defined from the resonance of the permeability as a function of the external applied field is directly coupled to the magnetic losses induced by the magnetic anisotropy. It is characterized by dielectric and magnetic loss, which varies between  $10^{-1}$  and  $10^{-2}$ . The resonance frequency varies according to the value of the internal field present in the  $CoFe_2O_4$ ; it is often around 40 GHz. These properties discussed above, and especially the resonance frequency, made  $CoFe_2O_4$  very attractive for the microwave applications such as the miniaturized self-biased circulators.

## 1.8.4 Nanocomposites

All classes of ferrite discussed above, can be introduced into dielectric carrier (matrix) in order to fabricate nanocomposites with a reduced size, which is necessary for the miniaturization of the non-reciprocal components.

### Nanocomposite structure

Generally, a nanocomposite is an assembly of at least two materials with a strong adhesion capacity, which creates a material with different properties. For thousands of years, scientists and experimenters have investigated the nanocomposite materials, and they have used these materials in various fields such as construction, electronics, chemicals, biomedical and others. As shown in Fig.1.15, this nanocomposite consists of the matrix that ensures the cohesion of the structure of the composite material and in which the particles are included. It also contains the reinforcement which plays the role of a structural support. However, to have a magnetic nanocomposite with specific dielectric or magnetic properties, magnetic particles can be incorporated. The properties of the composite material will depend on the nature of the particles incorporated, their size, their shape, as well as their orientation.

### Magnetic nanocomposites

The magnetic particles provide the magnetic properties of the nanocomposite material. The reduction in the particle diameter leads to an improvement in the magnetic properties. Several studies have been performed to develop some methods to elaborate the magnetic nanocomposites, study the influence of the magnetic nanoparticles in specific matrices and their behavior under the effect of an applied magnetic field.

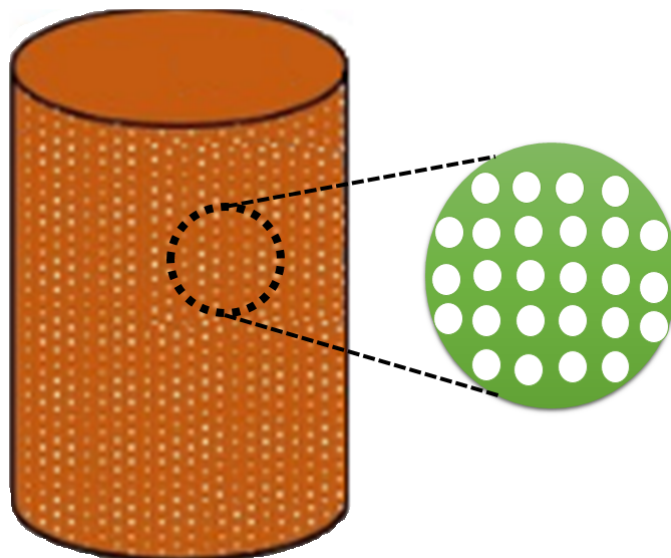


Figure 1.15: *Composite based on magnetic particles.*

Among these works, we can cite the work carried out by Zhang et al. [25], in which a new type of a nanocomposite based on barium hexaferrite has been produced. In this work, the variation of the morphology of the particles and of the ferrite phase as a function of the temperature treatment was studied. The permeability of composites at high frequency was also investigated. In the same context, Ramprasad et al. [26] reported the limits of nanocomposites using particles of soft magnetic materials for high frequency applications. He also exposes the magnetic properties of composites with ferromagnetic metallic nanoparticles.

Wu et al. studied the complex permeability of iron nanoparticles in a non-magnetic matrix using Bruggman's theory of effective media and considering each grain as a single magnetic domain [27, 28]. He also studied magnetic permeability in high frequency of ferromagnetic nanoparticles of cylindrical chromium dioxide. He was especially interested in the influence of the particle size on the microwave properties of magnetic composites based on iron nanoparticles.

Dong et al [29] have developed cobalt ferrite nanocomposites for potential applications in the ultra-high frequency domain. He studied the dynamic properties, especially the permeability and permittivity of nanocomposites.

During the experimental investigations of Boyajian et al. [30], barium hexaferrite nanoparticles were inserted into a host matrix formed by the SU-8 resin used in the field of microelectronics. This step has contributed to better integration of the magnetic powder inside an organic resin. Then, the microwave characterizations have shown the non-reciprocal effect of the composite material and materialized the possibility of producing a microwave component based on a magnetic nanocomposite.

In his work, Tchanguoulian et al. synthesized a polymeric silica material ( $SiO_2$ ) which plays the role of the matrix in which particles of cobalt ferrite with average size of 20 nm have been incorporated using the dip coating technique in presence of an applied magnetic field [31]. The inserted nanoparticles will assign to the nanocomposite material its magnetic properties. He also used a nanoporous matrix with micrometric thickness to fabricate nanowires from a cobalt ferrite that can be exploited to fabricate self-biased microwave devices.

To theoretically investigate the microwave devices based on ferrite composites, it is essential to understand the physical mechanisms which govern the behavior of the magnetic media and to propose theoretical models that predict their permeability tensor.

## 1.9 Theoretical models of the permeability tensor

In this section, we describe existing models in the literature to theoretically determine the permeability tensor according to the magnetization state of the medium (saturated, partially magnetized, demagnetized, and any state of magnetization).

### 1.9.1 Saturated state: Polder model

When an intense external magnetic field  $H$  is applied on a ferrimagnetic medium, the alignment of all the dipolar moments in its direction appears. Thus causing the disappearance of the domains and Bloch walls. This case corresponds to a totally magnetized medium. Thus, it is possible to consider, for this state, a single moment of magnetization  $M_s$ , called saturation magnetization. In the small signal approximation, where a weak microwave magnetic field  $\vec{h}_r$  is applied perpendicular to  $H$ , Polder's model is to solve the motion equation of the magnetic moment [32]. The solution leads to an anisotropic relationship between the magnetic induction vector  $\vec{b}$  and the magnetic field  $\vec{h}$  via a tensor permeability proposed by the Gilbert equation:

$$\vec{b} = \mu_0 \hat{\mu} \vec{h} \quad (1.18)$$

where

$$\hat{\mu} = \begin{pmatrix} \mu & -j\kappa & 0 \\ +j\kappa & \mu & 0 \\ 0 & 0 & 1 \end{pmatrix} \quad (1.19)$$

$$\mu = 1 + \frac{\omega_m \omega_0}{\omega_0^2 - \omega^2} \quad (1.20)$$

$$\kappa = \frac{\omega_m \omega}{\omega_0^2 - \omega^2} \quad (1.21)$$

In the tensor (Eq.1.18) appear extra-diagonal terms noted  $\pm j\kappa$ . These terms represent the anisotropy induced by the medium under control of the external magnetic field, and indicate the mathematical origin of the non-reciprocity of the EM signal propagation in a ferrimagnetic material.

The Eq.1.20 and Eq.1.21 describe the frequency response of the components of the Polder tensor. To take into account the magnetic losses, it is necessary to introduce the damping factor ( $\alpha$ ) mentioned in section 1.7. Thus the expressions of  $\omega_0$  and  $\omega_m$  become:  $\omega_0 = \mu_0 \gamma H_i + j\omega\alpha$  and  $\omega_m = \mu_0 \gamma M_s$ . In this case, the elements  $\mu$  and  $\kappa$  of the Polder tensor adopt real and imaginary components:

$$\mu = \mu' - j\mu'' \quad (1.22)$$

$$\kappa = \kappa' - j\kappa'' \quad (1.23)$$

Here,

$$\mu' = 1 + \frac{\omega_m \omega_0 (\omega_0^2 + \omega^2 (1 - \alpha^2))}{(\omega_0^2 - \omega^2 (1 + \alpha^2))^2 + 4\alpha^2 \omega^2 \omega_0^2} \quad (1.24)$$



$$\mu'' = \frac{\alpha\omega_m\omega(\omega_0^2 + \omega^2(1 + \alpha^2))}{(\omega_0^2 - \omega^2(1 + \alpha^2))^2 + 4\alpha^2\omega^2\omega_0^2} \quad (1.25)$$

$$\kappa' = \frac{\omega_m\omega(\omega_0^2 - \omega^2(1 + \alpha^2))}{(\omega_0^2 - \omega^2(1 + \alpha^2))^2 + 4\alpha^2\omega^2\omega_0^2} \quad (1.26)$$

$$\kappa'' = \frac{2\alpha\omega^2\omega_m\omega_0}{(\omega_0^2 - \omega^2(1 + \alpha^2))^2 + 4\alpha^2\omega^2\omega_0^2} \quad (1.27)$$

The elements of the Polder tensor presented above can be plotted either as a function of the frequency for a given internal field, or as a function of the internal field for a fixed frequency. The representation of the imaginary part of  $\mu$  (or  $\kappa$ ) as a function of the internal magnetic field makes it possible to define the linewidth  $\Delta H$  or effective linewidth  $\Delta H_{eff}$  of the gyromagnetic resonance, as shown in Fig.1.16. These parameters depend directly on the damping term  $\alpha$  by the following relationship:

$$\Delta H_{eff} = \frac{2\alpha\omega}{\mu_0\gamma} \quad (1.28)$$

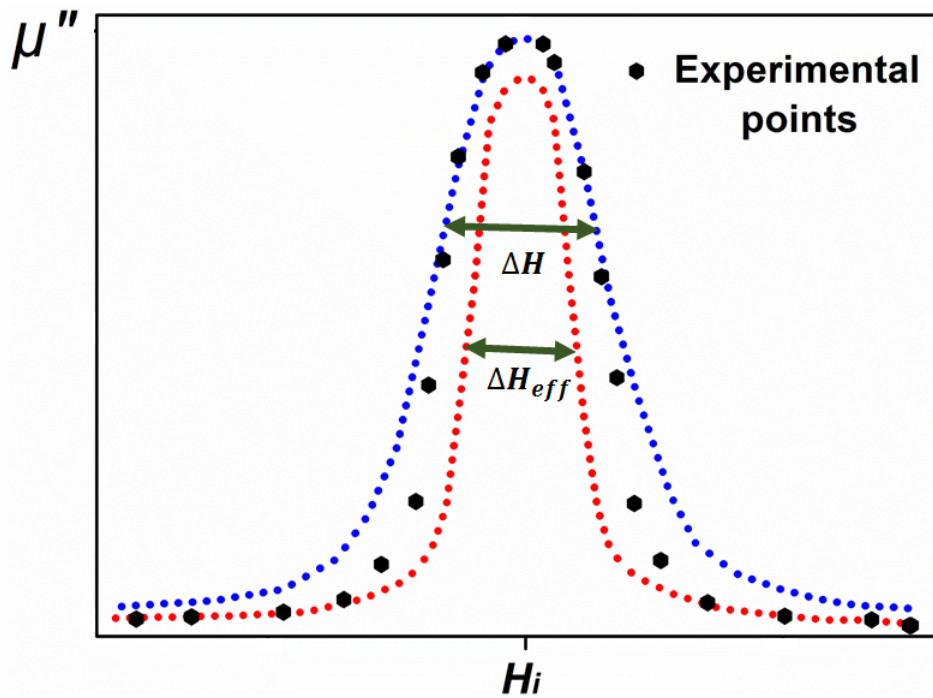


Figure 1.16: Definition of effective linewidth  $\Delta H_{eff}$ .

Depending on the material used for a specific application of a microwave device at a given frequency, the choice between  $\Delta H_{eff}$  and  $\Delta H$  depends strictly on the external magnetic excitation point. Indeed,  $\Delta H$  is taken into consideration to quantify the magnetic losses of the material at the gyromagnetic resonance (the  $H$  field equivalent to the resonance field), when all the magnetic moments precess in a single phase. In the other case,  $\Delta H_{eff}$  is exploited to determine the magnetic losses outside the resonance, when the excitation field  $H$  defers the resonance field.

In these studies, Schloemann et al. [33] described that the resonance width can be influenced by the magnetocrystalline anisotropy and the porosity of the studied material.

## 1.9.2 Partially magnetized state

### Green and Sandy model

Based on the analysis of the experimental results, Green and Sandy [34] proposed an empirical model for the components of the permeability tensor  $\hat{\mu}$ . They have developed a method for direct measurement of permeability as a function of the material state of magnetization. These measurements were carried out with a cylindrical cavity into which ferrite rod was introduced. The permeability was then calculated as a function of the evolution of the resonance frequency and of the quality factor ( $Q$ ) of the cavity. The ferrite rod was magnetized using an electromagnet and the poles of the electromagnet are in contact with the edges of the ferrite rod to close the magnetic flux, thus ensuring uniformity of the magnetization. From the experimental results, Green and Sandy proposed the following empirical expressions for the diagonal terms of the permeability tensor:

$$\mu = \mu_{(H=0)} + (1 - \mu_{(H=0)}) \left( \frac{M}{M_s} \right)^{3/2} \quad (1.29)$$

$$\mu_z = \mu_{(H=0)} \left( 1 - \frac{M}{M_s} \right)^{5/2} \quad (1.30)$$

$$\mu_{(H=0)} = \frac{2}{3} \left[ 1 - \left( \frac{\gamma 4\pi M_s}{\omega} \right)^2 \right]^{1/2} \quad (1.31)$$

It should be noted that in magnetized state, this model is not very accurate. In addition, it does not give access to the magnetic losses of the material.

### Rado model

In 1953, Rado [35] published a theory based on microscopic phenomena of magnetization which allowed him to deduce the permeability tensor in partially magnetized state. By making a statistical average over all the directions of easy magnetization of the domains, this theory takes into account the heterogeneous factor of medium. In his model, Rado considers an isotropic and random distribution of magnetic moments around the direction of the static magnetic field. By performing a spatial average, the following expressions are obtained for the tensor components of permeability:

$$\mu = \mu_z = 1 \quad (1.32)$$

$$\kappa = -\gamma \frac{M}{\omega} = -\frac{M}{M_s} \frac{\omega_m}{\omega} \quad (1.33)$$

Here,  $\omega_m = \gamma M_s$ .

This model is only valid far from the gyromagnetic resonance since Rado assumed that  $\gamma H \ll \omega$ , where  $H$  is the applied static field that saturates the material and compensates the demagnetizing effects. In addition, the experimental results show that after the gyromagnetic resonance the component of the permeability in the direction of the static field is less than 1. As a matter of fact, the model presented here is no longer valid.

## Igarashi and Naito model

Igarashi and Naito [36] have considered in their paper a partially magnetized material with a random orientation of the magnetic domains. They have semiempirically determined the expression of the diagonal term of the effective permeability tensor  $\hat{\mu}_e$ . These formulations are obtained using spatial averages and experimental results.

$$\mu_e = \frac{1}{3} + \frac{2}{3} \left[ \sqrt{\mu^2 - \kappa^2} \left( 1 - \left( \frac{M}{M_s} \right)^2 \right) + \mu \left( \frac{M}{M_s} \right)^2 \right] \quad (1.34)$$

where,

$$\mu = 1 + \frac{(\omega_e + j\alpha\omega)\omega_m}{(\omega_e + j\alpha\omega)^2 - \omega^2} \quad (1.35)$$

$$\kappa = \frac{-\omega\omega_m}{(\omega_e + j\alpha\omega)^2 - \omega^2} \quad (1.36)$$

Later, these authors [37] will propose an expression for the element  $\mu_z$  of the effective permeability tensor using the same approach as the one used by Rado:

$$\mu_z = 1 + \frac{(\omega_e + j\alpha\omega)\omega_m}{(\omega_e + j\alpha\omega)^2 - \omega^2} \left[ 1 - \left( \frac{M}{M_s} \right)^2 \right] \quad (1.37)$$

with  $\omega_e = \gamma H$

To be accurate, this model requires preliminary measurements, in order to fix the parameter  $\omega_e$  which is different from  $\gamma H$  for relatively strong applied fields.

### 1.9.3 Demagnetized state

#### Schlömann model

Schlömann [38] developed a theory based on a magnetostatic approximation, which takes into account the interactions between domains with opposite magnetizations. In a completely demagnetized state, an average value of the three diagonal components of the permeability tensor gives an accurate value of the isotropic permeability.

$$\mu = \frac{2}{3} \left[ \frac{\left( \frac{\omega}{\gamma} \right)^2 - (H_a + 4\pi M_s)^2}{\left( \frac{\omega}{\gamma} \right)^2 - H_a^2} \right]^{1/2} + \frac{1}{3} \quad (1.38)$$

where  $\omega$  is the frequency,  $H_a$  the anisotropy field, and  $M_s$  the saturation magnetization. The average permeability of a random orientation can be obtained approximately by the average permeability applicable in the three main directions. Schlömann considered that the applied field is completely compensated by the static demagnetizing fields. In Eq.1.38, the field that appears is the anisotropy field which is the same as the internal field of the material.

### 1.9.4 Any magnetization state

#### Generalized Permeability Tensor (GPT) model

The GPT model is based on the average responses of the randomly oriented domains, which take into account the interactions between the adjacent domains and the Polder-Smith effect that occurs between the magnetic domains [39]. In this model, each region is characterized by its angle between the direction of magnetization and the direction ( $Oz$ ) where the magnetic field is applied. This theory is established in two essential stages; the calculation of static fields and the calculation of the dynamic response of the magnetic moments. The evolution of the magnetization vector of a domain is governed by the Landau-Lifshitz-Gilbert equation:

$$\frac{\partial \vec{M}}{\partial t} = -\gamma \vec{M} \times (\vec{H}_i + \vec{h}_d) + \frac{\alpha}{M_s} \vec{M} \times \frac{\partial \vec{M}}{\partial t} \quad (1.39)$$

where,  $\gamma$  is the gyromagnetic factor and  $M_s$  the saturation magnetization. To solve this equation, it is essential to determine  $\vec{H}_i$  and  $\vec{h}_d$ .  $\vec{h}_d$  is the demagnetizing *RF* magnetic field which depends on the shape of the domain. The presence of the demagnetizing fields can be explained by the presence of the magnetic dipole charges at the periphery of the domain. When the dipole charges of two adjacent domains tend to add up, they can double the value of the demagnetizing field, this is the Polder-Smith phenomenon. This can be expressed mathematically by two coupled Gilbert equations coupling two adjacent domains:

$$\begin{aligned} \frac{\partial \vec{M}_1}{\partial t} &= -\gamma \vec{M}_1 \times (\vec{H}_1 + \vec{h} - n(\vec{m}_1 - \vec{m}_2)) + \frac{\alpha}{M_s} \vec{M}_1 \times \frac{\partial \vec{M}_1}{\partial t} \\ \frac{\partial \vec{M}_2}{\partial t} &= -\gamma \vec{M}_2 \times (\vec{H}_2 + \vec{h} - n(\vec{m}_2 - \vec{m}_1)) + \frac{\alpha}{M_s} \vec{M}_2 \times \frac{\partial \vec{M}_2}{\partial t} \end{aligned} \quad (1.40)$$

where  $\vec{M}_1$ , ( $\vec{M}_2$ ) and  $\vec{H}_1$ , ( $\vec{H}_2$ ) are the magnetic moments and the internal magnetic fields in the domains 1, (2), respectively.  $n$  is the demagnetizing coefficient which depends on the shape of the domain,  $\vec{m}_1$  and  $\vec{m}_2$  are the dynamic parts of  $\vec{M}_1$  and ( $\vec{M}_2$ ), and  $n(\vec{m}_2 - \vec{m}_1)$  represents the dynamic demagnetizing field of the domain 1 (including the Polder-Smith effect). This model has been improved by taking into account the shape of the grains, the shape of the domains, their statistical distribution in space and the hysteresis loop of the material.

### Bloch-Blombergen-Gilbert (BBG) model

The BBG model was developed by Carignan [40] to determine the effective permeability of nanowire arrays embedded in an alumina matrix. The mathematical formulation of this model is inspired from GPT model. In the course of their work, they studied the quasi-static response of the ferromagnetic nanowire arrays by taking into account the different magnetic energy terms of nanowires.

Based on MFM images for nickel nanowires, they observed that the surface presents a homogeneity of up and down oriented domains. Consequently, they proposed to subdivide the array of wires into two populations 1 and 2 in proportion  $f_1$  and  $f_2$ , respectively, with the condition  $f_1 + f_2 = 1$  is satisfied. In order to accurately predict their microwave response, they introduced the relaxation of the magnetization discussed in detail in the reference [41]. The magnetization dynamics will be a coupling of the BBG equations of

these two populations:

$$\begin{aligned}\frac{\partial \vec{M}_1}{\partial t} &= -\gamma \vec{M}_1 \times \vec{H}_{tot,1} + \frac{\alpha}{M_s} \vec{M}_1 \times \frac{\partial \vec{M}_1}{\partial t} - \frac{\vec{m}_1}{T_1} \\ \frac{\partial \vec{M}_2}{\partial t} &= -\gamma \vec{M}_2 \times \vec{H}_{tot,2} + \frac{\alpha}{M_s} \vec{M}_2 \times \frac{\partial \vec{M}_2}{\partial t} - \frac{\vec{m}_2}{T_1}\end{aligned}\quad (1.41)$$

where  $T_1$  is the relaxation time of the magnetization in the transverse direction.  $H_{tot,1,2}$  is the total field acting on the wires of population 1 and 2, respectively. This total field includes the static external field, the dynamic external field, the static and dynamic dipolar field coming from the shape of the wires and the static and dynamic dipolar field interwires of population 1 and 2. Moreover, the BBG model makes it possible to determine the dynamic susceptibility of nanowires, in order to deduce the effective permeability as a function of  $f_1$  and  $f_2$ . It also gives access to calculate the ferromagnetic resonance of the nanowires. Consequently, this frequency of resonance is very important to select the frequency band desired by the user who exploits the non-reciprocal microwave device.

### Modified Igarashi model

Hamoir et al. [42] and Spiegel et al. [43] developed a simplified model for the permeability of nanowired magnetic substrate based on Igarashi theory. The mathematical formalism of this model takes into account the geometric parameters of the substrate such as the porosity  $p$  of the membrane used as a matrix of nanowires growth, the filling ratio  $h_w$  of the pores by the magnetic matter, the magnetic losses presented by the damping factor  $\alpha$  and the measured squareness ratio  $m$  for the nanowires. The permeability of the nanowires is determined by the following tensor:

$$\hat{\mu}_{wire} = \begin{pmatrix} \mu_{wire} & -j\kappa_{wire} & 0 \\ +j\kappa_{wire} & \mu & 0 \\ 0 & 0 & \mu_{zwire} \end{pmatrix}\quad (1.42)$$

where

$$\mu_{wire} = 1 + 2\pi M_s \gamma P h_w (f_r + j f \alpha) ((f_r + j f \alpha)^2 - f^2)^{-1} (m^2 + 1)\quad (1.43)$$

$$\kappa_{wire} = 4\pi M_s \gamma P h_w f ((f_r + j f \alpha)^2 - f^2)^{-1} m\quad (1.44)$$

$$\mu_{zwire} = 1 + 2\pi M_s \gamma P h_w (f_r + j f \alpha) ((f_r + j f \alpha)^2 - f^2)^{-1} (1 - m^2)\quad (1.45)$$

Here

$m = \frac{M_r}{M_s}$ ; where  $M_r$ ,  $M_s$ ,  $f_r$  and  $\gamma$  are the remanent and saturation magnetization, the resonance frequency and the gyromagnetic factor, respectively.

The model presented here gives us the possibility to globally model the permeability behavior for unbiased nanowire arrays. Moreover, it is possible in the calculation to control the dependence of the microwave behavior on the nanowires length and the orientation of the magnetic moments inside the pores of the nanowired substrate. Although many physical parameters are not taken into account as in the previous model, this model will be use in our work because it is easy to compute and to enter in a simulation software. The results are sufficiently accurate for a first approach.

## 1.10 Microwave applications of ferrites

Currently, most telecommunication systems operating at high frequencies are based on microwave circuit technology. To satisfy the development needs of consumer and scientific applications, the signal transceivers must both transmit and receive an EM wave on the same antenna. In other words, it is necessary to separate simultaneous signals that differ only in their direction of propagation, which requires the presence of non-reciprocal passive components, such as circulators. These devices currently operate at bulk state based on a ferrite subjected to a static magnetic field, obtained by heavy and bulky magnets. It is indeed the intrinsic properties of magnetically polarized ferrite materials that control the separation of the transmission and reception channels of telecommunication systems.

These non-reciprocal passive components use the ferrite magnetic materials which gives them their non-reciprocal behavior. The spinel structure ferrites were the first to be used, then appeared garnet structure ferrites (YIG) and hexagonal structure ferrites (barium, strontium). These materials are, in general, polarized by external magnets providing an external field perpendicular or parallel to the plane of the ferrite depending on the application.

### 1.10.1 Circulators

These are non-reciprocal passive devices made up of at least three ports oriented at  $120^\circ$  from each other. A circulator is known to be non-reciprocal if the EM wave transmission differs according to the directions of propagation of the device. The non-reciprocity of the circulator is ensured by a ferrite disc placed under the central circular conductor. The ideal circulator is characterized by an EM wave transmission from one port to another, in the clockwise ( $1 \rightarrow 2 \rightarrow 3 \rightarrow 1$ ) or anti-clockwise ( $1 \rightarrow 3 \rightarrow 2 \rightarrow 1$ ). The EM wave propagation direction inside the circulator depends on the orientation of the applied magnetic field to the device.

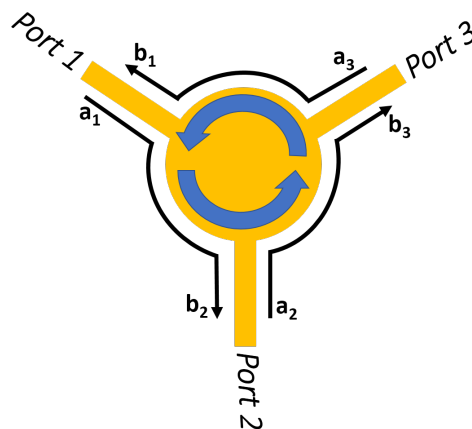


Figure 1.17: *Three port circulator.*

These passive circulators known for fifty years are still the subject of research to improve their performance and make them miniaturized. These performances are investigated by the insertion loss, isolation, reflection and bandwidth. The insertion losses have several origins: the dielectric and magnetic losses, and the losses in the conductors. The circulator

is characterized by its scattering parameters (S-matrix):

$$b = S \times a \iff \begin{bmatrix} b_1 \\ b_2 \\ b_3 \end{bmatrix} = \begin{bmatrix} S_{11} & S_{12} & S_{13} \\ S_{21} & S_{22} & S_{23} \\ S_{31} & S_{32} & S_{33} \end{bmatrix} \times \begin{bmatrix} a_1 \\ a_2 \\ a_3 \end{bmatrix} \quad (1.46)$$

Note that  $a_1$ ,  $a_2$  and  $a_3$  are the amplitudes of the incoming EM reduced waves in a three-port circulator and  $b_1$ ,  $b_2$  and  $b_3$  are the amplitudes of EM outgoing reduced waves.

$S_{11}$ ,  $S_{22}$  and  $S_{33}$  are the reflection coefficients at port 1, 2 and 3 and are exploited to evaluate the device mismatch.  $S_{21}$ ,  $S_{32}$  and  $S_{13}$  are the transmission coefficients of the circulator. Finally,  $S_{12}$ ,  $S_{23}$  and  $S_{31}$  are the inverse transmission coefficients (*isolation between the ports*). A circulator must present lower insertion losses than 1 dB to have application interest and an isolation less than -20 dB. The reflection must be weak, around -20 dB, which means that there is no reflected EM wave at each port (designated by  $S_{ii}$ ).

An ideal circulator transmits without losses in the direction of circulation and perfectly absorbs EM signals in the opposite direction. Therefore, the dispersion matrix of a perfect circulator, when the waves circulate in clockwise, is written as follows:

$$S = \begin{bmatrix} 0 & 0 & 1 \\ 1 & 0 & 0 \\ 0 & 1 & 0 \end{bmatrix} \quad (1.47)$$

The fact that this matrix is non-symmetrical, translates clearly the non-reciprocity of the component. This non-reciprocity makes all the interest of the device and which explains that this function is used in many telecommunication applications.

## 1.10.2 Applications of circulator

### Duplexer

The first example, which is the most common, corresponds to the broadcast in an antenna circuit (duplexer)(Fig.1.18.a). In this circuit, the circulator orients the signals from the transmitter to the antenna without any interference with the receiver (isolated port). The signal received by the antenna springs on the receiver without interacting with the transmitter. The circulation direction of the EM signal inside the circulator is related to the orientation of the applied magnetic field on the ferrite.

### Isolator

In other microwave applications, it is necessary to protect the energy source from the reflected energy. The circulator is then used in isolator mode as a protector. In this case, the circulator is inserted between the source and the load, the third port being connected to a suitable load which absorbs the energy transmitted to it (Fig.1.18.b). Thus the source emits its signal on port 1 of the circulator, which transmits it to the load connected to port 2. If there is any mismatch in the load, the signal reflected by the load due to this mismatch will be transmitted by the circulator to port 3, where it will be absorbed by the adapted load. In this way, no signal has the possibility of returning to the source and damaging it.

## Radar

The circulator thus occupies an important place in monostatic radar circuits (which involves only one antenna) (Fig.1.18.c). Its role is then to separate transmission and reception signals transiting through this unique antenna. The isolation in this case is an essential parameter that takes into account the very significant differences in power between the transmission and reception circuits.

## Multiplexer

The non-reciprocity of the circulator makes it able to split the spectrum received into several frequency channels with bandwidths and spaces varying according to the intended application. In this configuration, the circulator is considered as a multiplexer (Fig.1.18.d).

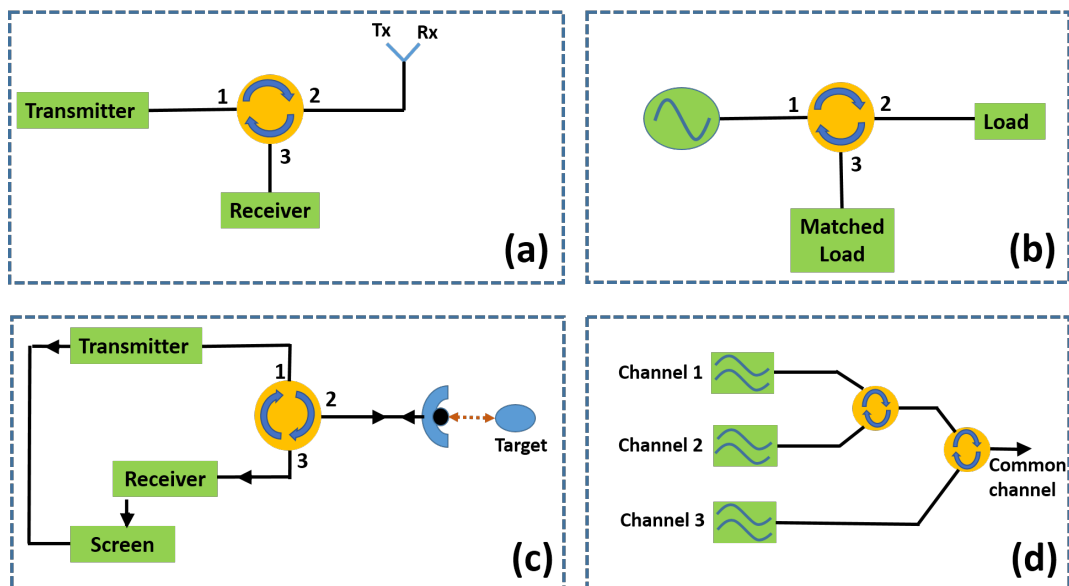


Figure 1.18: *Some typical applications for the circulator; (a) duplexer; (b) isolator; (c) radar; (d) multiplexer.*

There are different kinds of circulators which are generally distinguished according to the transmission frequency band, the physical operating principle, the fabrication technology used, the type of connection, etc. These different topologies obviously have advantages and disadvantages in terms of cost, simplicity of fabrication, size, as well as performances. The majority of telecommunication systems are based on active or passive circulators. The configuration and the design of active circulators are well detailed in the bibliography study carried out in 2000 by Bayard [44].

In this manuscript, we will be interested in passive circulators. This category of circulators is characterized by the non-reciprocity property provided by the ferrimagnetic materials.

### 1.10.3 Different topologies of circulators

#### 1.10.3.1 Faraday rotation-based circulator

The Faraday rotation circulator consists of circular to rectangular waveguide transitions. A cylindrical ferrite is positioned inside the central circular waveguide. Then, the ferrite



is polarized along the axis of the cylinder. The length of the ferrite and the magnetic polarization field are dimensioned so that the EM wave is rotated of  $45^\circ$  [45]. An EM wave entering port 1 is transmitted to port 2, an EM wave entering in port 2 comes out on port 3 and so forth. It is a four port circulator as shown in Fig.1.19. The rotation depends directly on the applied field direction. In fact, this field is applied using a magnet surrounding the ferrite. When it is applied in the opposite direction, the flow of energy is performed from port 1 to 4 instead of 1 to 2.

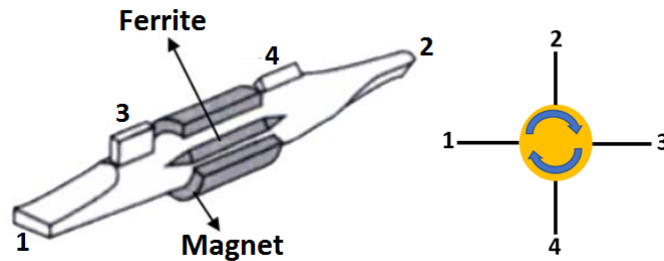


Figure 1.19: *Faraday rotation circulator* .

The Faraday rotation circulators have been used at very high frequencies and in the optical sector since the emergence of the optical fiber.

### 1.10.3.2 Lumped element circulator

The Lumped element circulator operating at low frequencies (MHz) has large dimensions. The miniaturization being a challenge and the lumped element circulator turns out to be interesting. Indeed, the size of these devices is reduced because the size of the ferrite disc is independent of the working frequency. The lumped element circulator was firstly proposed by Kionishi [46]. Its topology consists of three conductors crossing over each other and oriented by an angle of  $120^\circ$ . They are all connected to the same outer conductors at the other end.

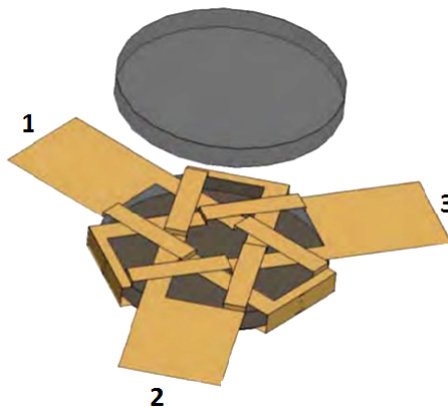


Figure 1.20: *Lumped element circulator*.

The signal flow occurs when the ferrite material is polarized by an external magnetic field. The dimensions of the conductors, their spacings and their positions as well as the ferrite must be chosen so as to obtain the best performances. A study of the influence of each of these parameters has shown that, unlike most circulators that operate above

or below resonance, the lumped element circulator works optimally near to the ferromagnetic resonance. It is to remember that such a circulator is not suitable for the millimeter wavelengths.

### 1.10.3.3 Junction circulators

The junction circulators are relatively bulky at microwave frequencies and it is easy to fabricate them.

#### Waveguide Y-junction circulator

The waveguide Y-junction circulator has three ports at  $120^\circ$  from each other and located around a central body containing the ferrite element responsible for non-reciprocity effect (Fig.1.21).

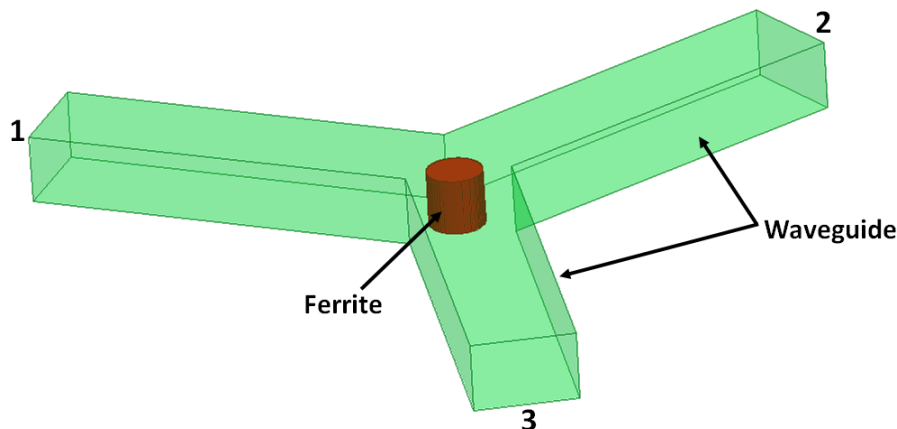


Figure 1.21: *Waveguide circulator.*

These circulators generally operate by the field displacement process. The dimensions of the ferrite element and of the guide as well as the value of the external polarizing magnetic field are such that an EM signal entering on port 1 is received on the port 2, that a EM signal present on port 2 is transmitted to the port 3 and that an incoming EM signal on port 3 is transmitted to the port 1.

Many different studies have been carried out by changing the geometries and the dimensions of the ferrite in order to improve the performance and reduce the complexity of the fabrication technology of this circulator type. One such study was that of Che et al. [47], who analyzed and developed a waveguide junction circulator with a spherical ferrite. Also, Helszajn [48] studied several composite structures of the central ferrite cylinder: (i) bordered ferrite disc on both sides of two dielectric discs, (ii) a ferrite cylinder coated with a dielectric.

The waveguides must respect very specific dimensions depending on the frequency. So this type of circulator will meet millimeter wavelength difficulties. Indeed, it becomes difficult to precisely manufacture the ferrite elements because these must then have diameters less than a millimeter.

#### Stripline circulator

The Y-junction stripline circulator presents a simple geometrical arrangement which makes its analytical study fairly simple. It is technically exploited for signal type applica-

tions, i.e. for the cases where the power levels are modest. The topology of this stripline circulator consists of three oriented access lines at  $120^\circ$  from each other and connected to a central metallic disk as displayed in Fig.1.22.

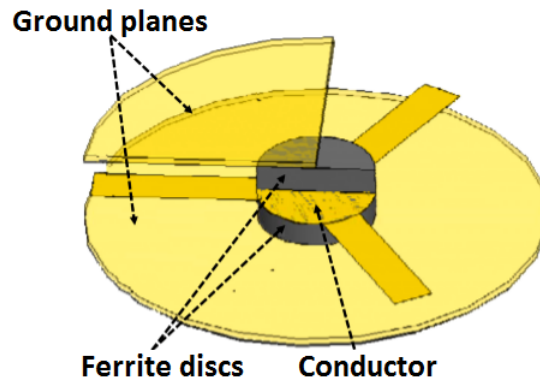


Figure 1.22: *Structure of stripline circulator.*

This conductor is inserted between two ferrite discs of identical shape to that of the central disc. Two ground planes are located on either side of the structure, the space between the two ground planes is a dielectric material. Then, two magnets on each side of the structure create a static magnetic field which polarizes the central disc in the perpendicular direction. The idea of a three-port junction circulator was considered by Carlin [49] on the theoretical bases for the treatment of the S-parameters matrix. Moreover, the operating principle of a ferrite Y-junction circulator, described by Bosma [50], is based on the resonance of two eigenmodes of ferrite discs, which are considered to have electrical walls at the top and the bottom faces. So the access lines are assumed to transport only transverse electromagnetic (TEM) modes, and the periphery of the disk is considered to form a magnetic wall except for access lines. Thus, this study has become an important reference for the work carried out on this type of circulator. We will discuss its theoretical operating principle as well as its dimensioning in Chapter 4 of this manuscript.

### Coplanar circulator

Finally, the Y-junction circulator can be fabricated in the coplanar technology. This is an unusual structure for which we have only few scientific articles. The coplanar Y-junction circulator is however well suited to microwave integrated circuits, its main advantage being that the conductor and the ground planes are at the same level. This facilitates the manufacturing process by reducing the steps of the photolithography and reducing the fabrication cost. The structure illustrated in Fig.1.23 shows the arrangement of the different planes: the dielectric, the ferrite, the central conductor formed by a circular central part and three access lines forming  $120^\circ$ . The ground planes are laterally placed in the spaces between the access lines. Note that the ferrite material is either in the form of a disk placed into the dielectric located below the central conductor (Fig.1.23.a), or is as an entire layer placed between the dielectric and the conductor (Fig.1.23.b).

Ogasawara et al.[51] investigated different coplanar structures. Better performance has been obtained for the configuration consisting of a ferrite plane and a conductive plane which are placed on the coplanar line (conductive and dielectric plane) as shown in Fig.1.24.a. Fig.1.24.b presents the topology tested by Koshiji et al. [52], which consists on

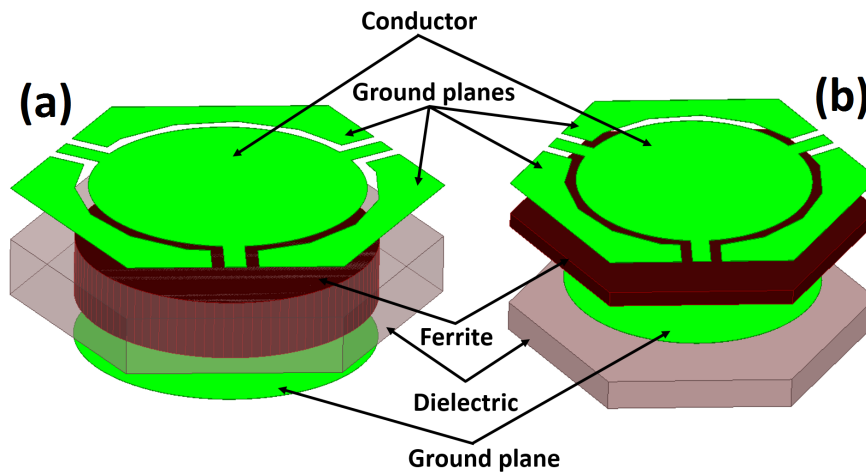


Figure 1.23: *Coplanar circulator's structure .*

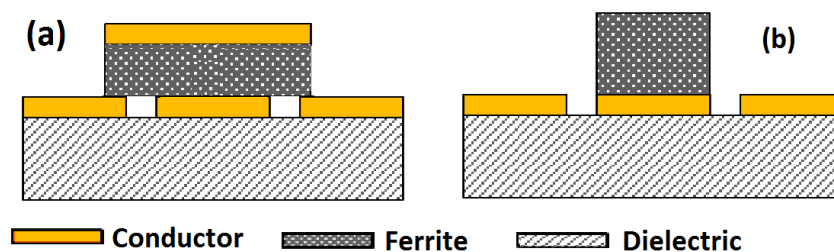


Figure 1.24: *Coplanar structures proposed by Koshiji et al.; (a) and by Ogasawara et al. (b).*

the integration of a ferrite disc on the central conductor. The experimental measurements have shown better performance, i.e. an isolation of  $-19\text{ dB}$  and insertion losses of  $-0.8\text{ dB}$  for an operating frequency of  $9.5\text{ GHz}$ .

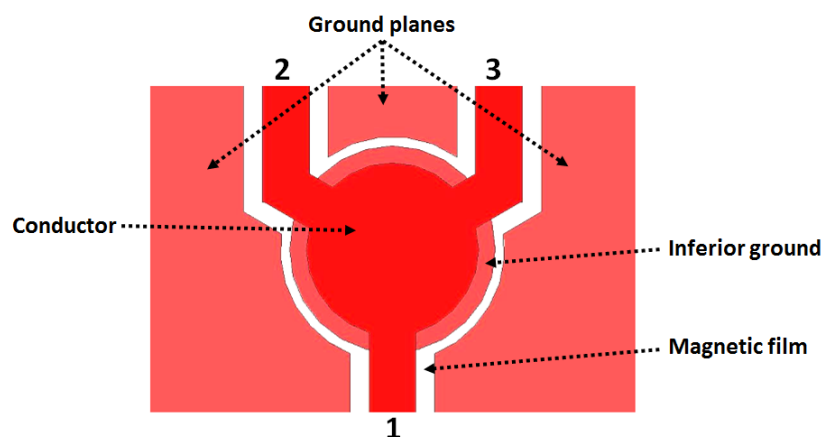


Figure 1.25: *The circulator performed by Benevent et al. [53].*

Recently, a work has been carried out by Benevent et al. [53] on the coplanar circulator with angled access lines and based on magnetic thin layers of barium hexaferrite (BaM) greater than  $10\text{ }\mu\text{m}$  as displayed in Fig.1.25. He modeled a miniaturized coplanar struc-

ture to make it operative between 40 and 50  $GHz$ . The observation of a non-reciprocal effect made it possible to validate this work. However, further processing steps will be necessary to improve the crystal orientation of the magnetic moments of barium hexaferrite in a direction perpendicular to the plane of the thin layer.

Moreover, Zahwe et al. [54] studied the feasibility of coplanar circulator based on a thin layer of YIG (thickness varies from 1 mm to 16  $\mu m$ ) operating around 10  $GHz$  (Fig.1.26).

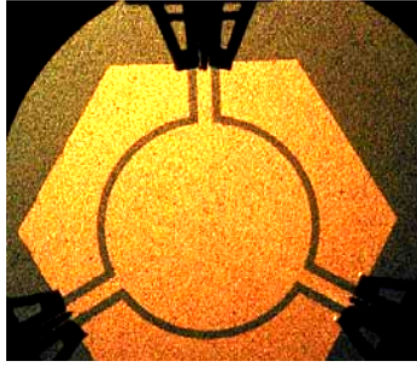


Figure 1.26: The fabricated circulator by Zahwe et al. with  $6 \times 6 \text{ mm}^2$  in size [54].

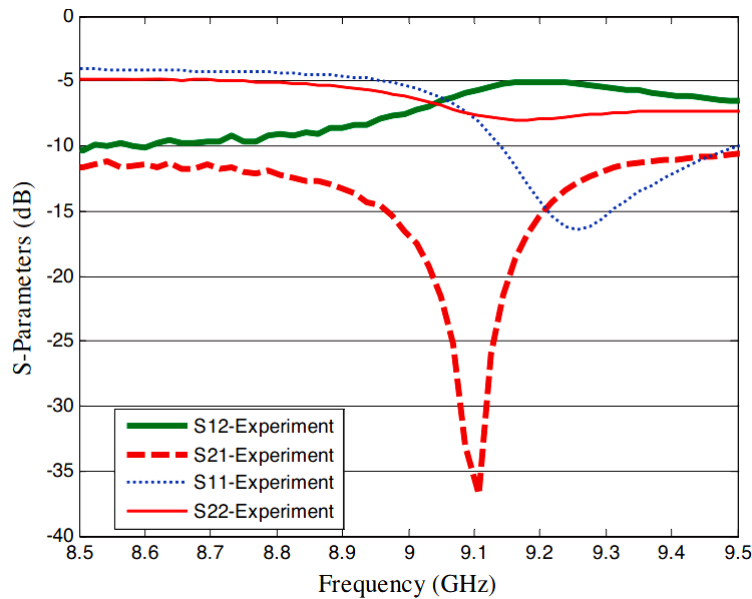


Figure 1.27:  $S$ -parameters of the circulator performed by Zahwe et al. with a YIG substrate [54].

Indeed, the layers of large thickness consisted of commercial brochures and the thin layers were deposited by RF sputtering. The fabricated structure has geometric dimensions of  $6 \times 6 \text{ mm}^2$  and a YIG magnetic layer with a thickness of 65  $\mu m$ . The experimental measurements report an insertion of 5  $dB$  at 9.2  $GHz$  frequency, a reflection and isolation of around 16  $dB$  and 15  $dB$ , respectively, as shown in Fig.1.27. The simplicity of the manufacturing process saves the fabrication technology cost. The studies on this type of Y-junction circulators using ferrite materials are becoming more and more frequent [55-57]. For the reasons of simplicity, miniaturization, rapid prototyping process and higher

operating frequency band, we are interested in our work in the self-biased circulators in the coplanar topology.

#### 1.10.4 Self-biased circulator

Fig.1.28 displays the technological concept of self-biased circulator for a microstrip topology. In order to avoid the use of a permanent magnet and to ensure the integration of these circulators, it is necessary to replace the ferrite-magnet assembly by a self-polarized material, i.e. their magnetic moments are intrinsically oriented in a direction perpendicular to the substrate plane.

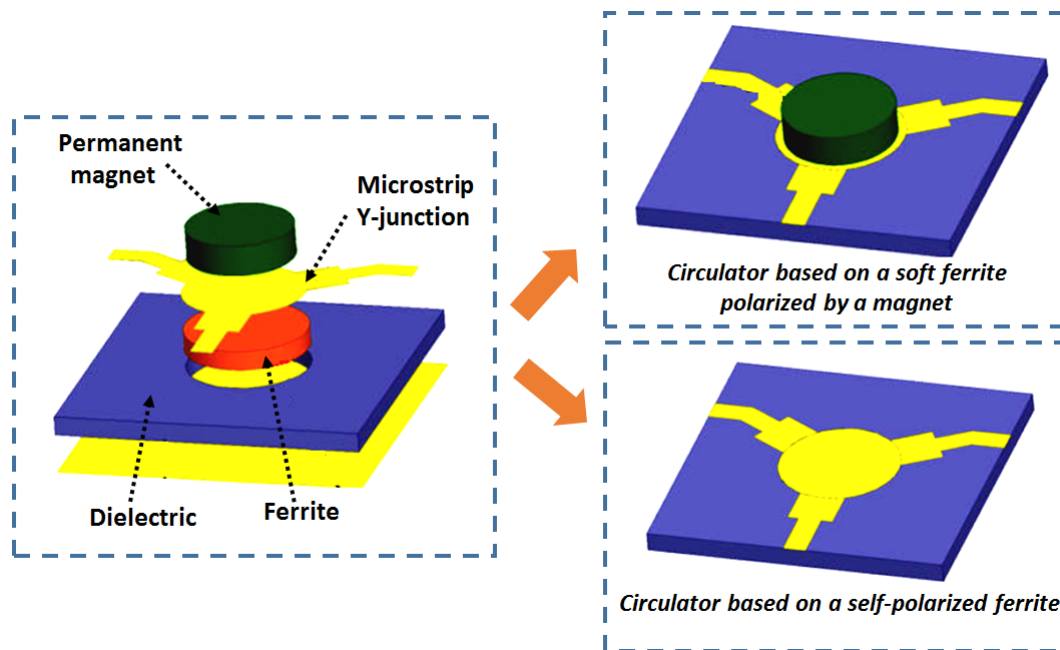


Figure 1.28: *The concept of self-biased circulator [54].*

From a magnetic point of view, this property is characterized by a ratio between the zero field magnetization ( $M_r$ ) and the magnetization ( $M_s$ ) at strong field close to the unit. In addition, a high coercive field ( $H_c$ ) makes it possible to guarantee the stability of the magnetization and is thus a characteristic also sought.

Among the techniques for synthesizing magnetic thin layers, we can cite RF sputtering, plasma vapor deposition, laser pulse deposition, etc [58]. These techniques, which are still under development, are very expensive, require sophisticated equipment and still have not produced the expected properties of crystallization or orientation of the magnetic moments of the material. Many research centers are interested in processes to obtain low-cost self-polarized materials. Faced with these technological limitations, the ferrimagnetic nanocomposites seem to be a promising solution. These materials have the magnetization of ferrimagnetic media and the low conductivity of dielectric media. Several works have been carried out on this subject with different magnetic materials in the microstrip and coplanar structures.

In 2000, Saib et al.[59] investigated a circulator in microstrip topology based on magnetic CoNiFe nanowires embedded electrochemically in a nanoporous polycarbonate ma-

trix. He has shown a significant non-reciprocal effect in his performed simulation, then

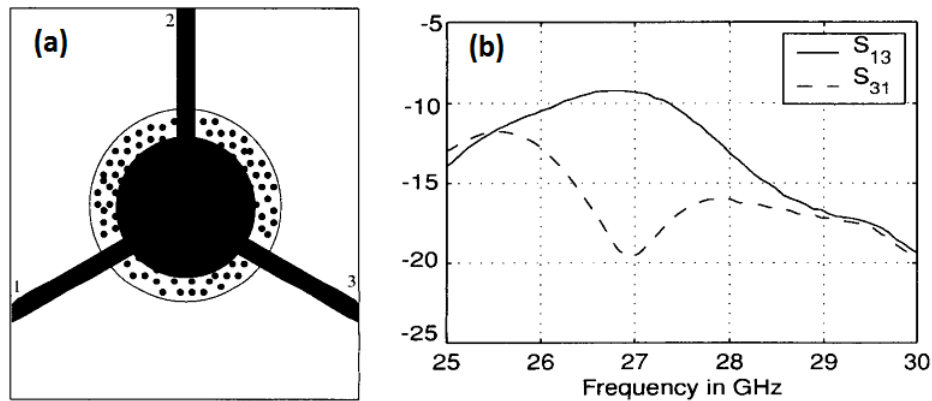


Figure 1.29: Measured transmission parameters between port 1 and port 3 of the circulator fabricated by Saib [59].

fabricated a circulator composed of nanowired ferrimagnetic substrates with low losses as shown in Fig.1.29. He highlighted the phenomenon of circulation. However, the structure produced presents a losses ( $> -9$  dB) as displayed in Fig.1.29. The obtained performance has not presented an application interest in the microwave industry.

Hamoir et al. studied in 2013 circulators based on electrodeposited NiFe onto AAO membranes and showed the dependence of the length of these nanowires in order to control the frequency of circulation [42], as shown in Fig.1.30. By adjusting this parameter,

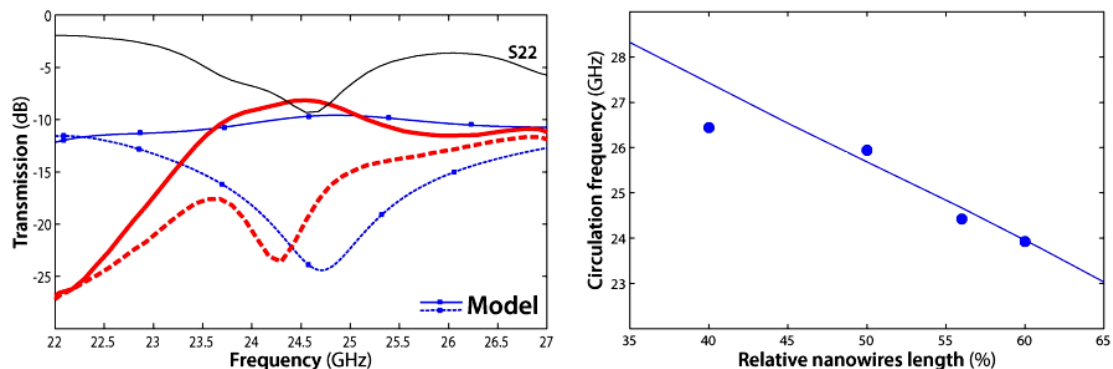


Figure 1.30: Measured and simulated performances of the circulator fabricated by Hamoir et al [42].

Hamoir worked in the frequency band from 22 to 27 GHz and made an optimization of the S-parameters of the circulator by the bosma model in order to experimentally achieve the desired structure.

Concerning the circulator in coplanar topology, the spinel ferrite and hexaferrite being hard materials with high remanence, they have strong anisotropies and are good candidates for this type of application. In this area, we try to obtain self-polarized thin magnetic layers to ensure the miniaturization of the circulator.



In 2011, Boyajian et al. [60] produced a prototype of a coplanar circulator. The magnetic substrate which has been used consists of magnetic particles of barium hexaferrite mixed in SU-8 resin matrix deposited by technical spin coating on an alumina substrate. During the magnetic substrate growth process, a permanent magnet was placed under the alumina substrate in order to orient the magnetic moments of the particles. After engraving the circulator, the performances were evaluated as shown in Fig.1.31.

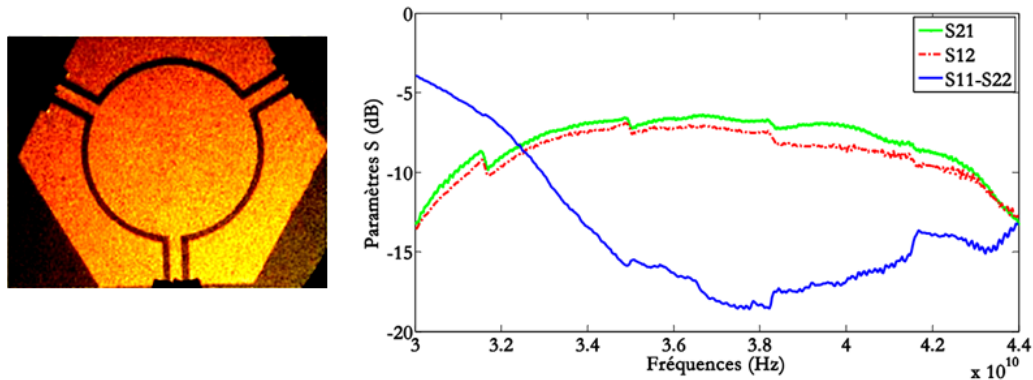


Figure 1.31: *Measured performances of the coplanar circulator investigated by Boyajian et al [60].*

The measurements showed a transmission at 39.34 GHz with insertion losses of -6.9 dB and with low reciprocity caused by wrong orientation particles and lower concentration.

In the same context, Ardaches [61] tried to develop a self-biased coplanar circulator. The approach chosen is based on the synthesis of nano-ferrimagnetic composite substrates. It consists of making a deposit by dip-coating under magnetic field of  $CoFe_2O_4$  nanoparticles into porous alumina membranes. Several prototypes of circulators were designed, modeled and simulated using the HFSS software. Following interesting simulation results; a first prototype was manufactured and characterized in high frequencies. The measure-

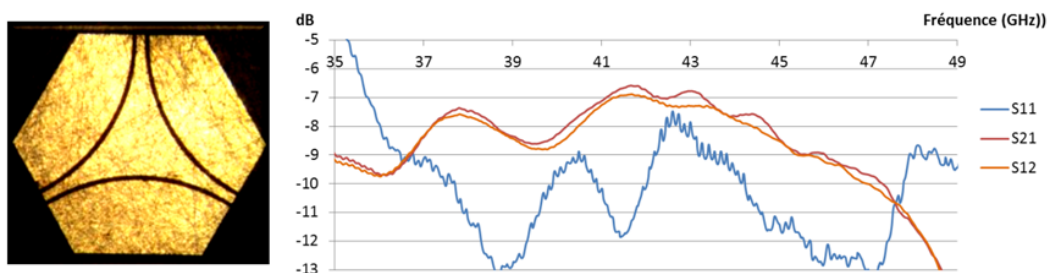


Figure 1.32: *The experimental parameters of the edge-mode coplanar circulator fabricated by Ardaches [61].*

ment results (Fig.1.32) have shown a circulation phenomenon, which remains very low due to the small concentration percentage of the magnetic nanoparticles in the composite. This type of circulator is still under study because it should allow to avoid using permanent magnets and to reduce the costs with simple and collective manufacturing techniques. These composite magnetic materials have many advantages, and can have a wide operating frequency band. In the context of this thesis, to get around these technological



obstacles, we are interested in the technological potential of self-polarized ferrimagnetic nanowire arrays for non-reciprocal microwave devices.

Thus, we decided to move towards the electrochemical deposits of ferrite spinel materials ( $CoFe_2O_4$ ), recognized for their strong magnetic anisotropy, into nanoporous membranes under an intense magnetic field. In this context, many studies of magneto-electrodeposition (electrodeposition under magnetic field) of alloys and oxides have shown the influence of the magnetic field on the morphology, the crystallographic structure and the physical properties of the material. The magnetic field favors generally denser and more homogeneous deposits with very small crystallite sizes. In the case of magnetic materials, the magnetic field influences the coercive field and the saturation magnetization, which offers the possibility to realize a self-polarized magnetic nanocomposite with very strong spontaneous magnetization.

The circulator studied in this thesis belongs to the family of coplanar circulators based on  $CoFe_2O_4$  nanowires, whose different parts will be discussed in detail in the next chapters.

## Chapter 1: Summary

This first introductory chapter was devoted to present the different classes of magnetism and the different theoretical models of the permeability tensor for massive ferrites with different magnetization states. Moreover, this chapter has highlighted the different types of circulators, their functions, structures and field applications. In addition, a state of the art was drawn up on the different materials exploited to fabricate the passive circulators in their stripline and coplanar topology. This non-reciprocal component is widely used in telecommunication systems and a greater performance is required to ensure the development of this sector. Its miniaturization, low manufacturing cost, low losses and increasingly high operating frequencies remain the basis of the desired properties. The coplanar circulator based on self-polarized nanocomposite material, such as  $CoFe_2O_4$  electrochemically embedded in a dielectric alumina template, seems to be an attractive alternative to overcome these technological limitations.

# Bibliography

- [1] D. C. Mattis, History of Magnetism. In: The Theory of Magnetism I. Springer Series in Solid-State Sciences, Springer, (1981) 1-38.
- [2] K. H. J. Buschow, New developments in hard magnetic materials. *Rep. Prog. Phys.*, 54(9) (1991) 1123.
- [3] D. Jiles, Introduction to magnetism and magnetic materials. CRC press, Iowa, 2nd ed, (2015) 1-529.
- [4] C. P. Slichter, Principles of magnetic resonance . Science and Business Media, Springer, (1990) 1-651.
- [5] N. A. Spaldin, Magnetic materials: fundamentals and applications. Cambridge university press, 2nd ed, (2010) 1-270.
- [6] R. C. O'handley, Modern magnetic materials: principles and applications. Wiley, 2nd ed, (2000) 1-768.
- [7] R. A. MacCurrie, Ferromagnetic materials. Acad. Press, 2nd ed, (1994) 1-292.
- [8] T. Nagamiya, K. Yosida, R. F. Kubo, Antiferromagnetism. *Adv. Phys*, 4(13) (1955) 1-112.
- [9] D. S. Mathew, R. S. Juang, An overview of the structure and magnetism of spinel ferrite nanoparticles and their synthesis in microemulsions. *Int. J. Chem. Eng*, 129 (2007) 51-65.
- [10] B. D. Cullity, C. D. Graham, Introduction to magnetic materials. John Wiley and Sons, 2nd ed, (2011) 197-239.
- [11] L. Néel, Magnetic surface anisotropy and superlattice formation by orientation, *J. Phys. Radium*, 15 (1954) 225-239.
- [12] J. P. Nibarger, R. Lopusnik, Z. Celinski, T. J. Silva, Variation of magnetization and the Landé g factor with thickness in Ni-Fe films, *Appl. Phys. Lett*, 83 (2003) 93
- [13] C. Kittel, Physical Theory of Ferromagnetic Domains, *Rev. Mod. Phys*, 21 (1949) 541-583.
- [14] L. F. Chen, C. K. Ong, C. P. Neo, V. V. Varadan, V. K. Varadan, Microwave Electronics: Measurement and Materials Characterization. John Wiley and Sons, (2004) 15-22.
- [15] J. Smit, H.P.J. Wijn, Ferrites, Dunod, Paris, (1961) 61-65.

- [16] R. alenzuela, Novel applications of ferrites. *phys. res. int*, (2012) 1-9, doi:10.1155/2012/591839.
- [17] B. Lax, K. J. Button, Microwave ferrites and ferrimagnetics. *Literary Licensing*,(2012) 768.
- [18] N. R. Bernier, L.D. Tóth, A. Koottandavida, M. A. Ioannou, D. Malz, A. Nuppenkamp, A. K. Feofanov, T. J. Kippenberg, Nonreciprocal reconfigurable microwave optomechanical circuit. *Nat. Commun*, 8 (2017) 1-8.
- [19] P. N. Schatz, A. J. McCaffery, The faraday effect. *Q. Rev. Chem. Soc*, 23 (1969) 552-584.
- [20] R. Carey, B. W. J. Thomas, The theory of the voigt effect in ferromagnetic materials. *J. Appl. Phys*, 7 (1974) 2362.
- [21] S. Geller, M. A. Gilleo, The crystal structure and ferrimagnetism of yttrium-iron garnet,  $Y_3Fe_2(FeO_4)_3$ . *J. Phys. Chem. Solids*, 3 (1957) 30-36.
- [22] K. K. Mallick, P. Shepherd, R. J. Green, . Magnetic properties of cobalt substituted M-type barium hexaferrite prepared by co-precipitation. *J. Magn. Magn.Mater*, 312 (2007) 418-429.
- [23] D. S. Mathew, R. S. Juang, An overview of the structure and magnetism of spinel ferrite nanoparticles and their synthesis in microemulsions. *J. Chem. eng*,129 (2007) 51-65.
- [24] T. E. Torres, E. Lima Jr, A. Mayoral, A. Ibarra, C. Marquina, M. R. Ibarra, G. F. Goya, Validity of the Néel-Arrhenius model for highly anisotropic  $Co_xFe_{3-x}O_4$  nanoparticles. *J. Appl. Phys*, 118 (2015) 183902.
- [25] L. Zhang, L. Deng, P. Zhou, Synthesis and microwave magnetic properties of a Fe/ferrite composites with sandwich structure. *J. Magn. Magn. Mater*, 312 (2007) 224-227.
- [26] R. Ramprasad, P. Zurcher, M. Petras, M. Miller, P. Renaud , Fundamental limits of soft magnetic particle composites for high frequency applications. *Phys. Status-Solidi*, 233 (2002) 31-38.
- [27] L. Wu, J. Ding, H. B. Jiang, L. F. Chen, C. K. Ong, Particle size influence to the microwave properties of iron based magnetic particulate composites. *J. Magn. Magn. Mater*, 285 (2005) 233-239.
- [28] L. Wu, J. Ding, , H. B. Jiang, C. P. Neo, High frequency complex permeability of iron particles in a nonmagnetic matrix. *J. Appl. Phys*, 99 (2006) 083905.
- [29] H. Dong, A. Meininger, H. Jiang, K. S. Moon, C. P. Wong, Magnetic nanocomposite for potential ultrahigh frequency microelectronic application, *J. Electron. Mater*, 36 (2007) 593-597.
- [30] T. Boyajian, D. Vincent, M. Le Berre, S. Neveu, Magnetic Behavior of Barium Hexaferrite Nanoparticles, *Adv. Mater. Res*, 324 (2011) 286-289.

- [31] A.Tchangoulian, E. A. Diwan, D. Vincent, S. Neveu, F. Royer, J. P. Chatelon, C. Nader, R. Habchy, Realization of Unbiased Ferrite Cobalt Nano-Composite for Non-Reciprocal Microwave Components. *J. Mater. Sci. Eng*, 3 (2013) 751.
- [32] D. Polder, On the theory of ferromagnetic resonance. *Physica*, 15 (1949) 253–255.
- [33] E. Schloemann, Spin-wave analysis of ferromagnetic resonance in polycrystalline ferrites. *J. Phys. Chem. Solids*, 6 (1958) 242-256.
- [34] J.J. Green, F. Sandy, Microwave characterization of partially magnetized ferrites. *IEEE Trans. Microwave Theory Tech*, 6 (1974) 641-645.
- [35] G.T. Rado, Magnetic Spectra of Ferrites. *Rev. Mod. Phys*, 25 (1953) 81-89.
- [36] M. Igarashi, Y. Naito, Tensor permeability of partially magnetized ferrites. *IEEE. Trans. Magn*, 13 (1977) 1664-1668.
- [37] M. Igarashi, Y. Naito, Parallel Component  $\mu_z$  of Partially Magnetized Microwave Ferrites. *IEEE. Trans. Microw. Theory. Tech*, 29 (1981) 568-571.
- [38] E. Schlomann, Microwave behavior of partially magnetized ferrites. *J. Appl. Phys*, 41 (1970) 204-214.
- [39] P. Gelin, P. Queffelec, F. Le Pennec, Effect of domain and grain shapes on the dynamical behavior of polycrystalline ferrites : Application to the initial permeability. *J. Appl. Phys*, 98 (2005) 053906.
- [40] L. P. Carignan, Thesis report: Modélisation, développement et caractérisation de matériaux magnétiques à base de nanofils ferromagnétiques pour les technologies hyperfréquences, (2012) 92-96, Polytechnic School of Montreal, Canada.
- [41] C. E. PATTON, Microwave resonance and relaxation. *In Magn. oxides*, 10 (1975) 575–648.
- [42] G. Hamoir, L. Piraux, I. Huynen, Control of microwave circulation using unbiased ferromagnetic nanowires arrays. *IEEE Trans. Magn*, 49 (2013) 4261-4264.
- [43] J. Spiegel, J. De La Torre, L. Piraux, I. Huynen, (2009, June). Isolator concept based on ferromagnetic nanowired substrates. *In IEEE MTT-S International Microwave Symposium Digest*, (2009) 29-32.
- [44] B. Bayard, Thesis report, Contribution au développement de composants passifs magnétiques pour l'électronique hyperfréquence, (2000) 30-32, Université Jean Monnet, Saint-Etienne, France.
- [45] P. J. Allen, The turnstile circulator. *IEEE. Trans. Microw. Theory. Tech*, 4 (1956) 223-227.
- [46] Y. Konishi, Lumped Element Y Circulator, *IEEE. Trans. Microw. Theory. Tech*, 13 (1965) 852-864.
- [47] W. Q. Che, E. N. Yung, Temperature compensation of VHF-band lumped-element ferrite circulator for wireless communication application. *J. Electromagnet. Wave*, 19 (2005) 1125-1135.

- [48] J. Helszajn, Complex gyrator circuit of a three-port circulator using a planar resonator composed of a gyromagnetic disk, a triplet of UEs and a triplet of single radial magnetic walls. *IET. Microw. Antennas. Propag*, 3 (2009) 281-287.
- [49] H. J. Carlin, Principles of gyrator networks. In: Proceedings of the symposium on modern advances in microwave techniques, (1954) 175-203.
- [50] H. Bosma, On the principle of stripline circulation. *IEEE. B: Electron. Commun. Eng*, 109 (1962) 137-146.
- [51] N. Ogasawara, M. Kaji, Coplanar-guide and slot-guide junction circulators, *Electron. Lett*, 7 (1971) 220–221.
- [52] K. Koshiji, E. Shu, Circulators using coplanar waveguide, *Electron. Lett*, 22 (1986) 1000–1002.
- [53] E. Benevent, T. Rouiller, B. Sauviac, V. Larrey, D. Vincent and A. Madelaine, Stripline Y-junction circulator using barium hexagonal ferrite thin films. *IEEE International Symposium on Industrial Electronics*, 1 (2004) 15-18.
- [54] O. Zahwe, B. Sauviac, J. J. Rousseau, Fabrication and Measurement of a Coplanar Circulator with 65 m Yig thin Film. *Prog. Electromagn. Res*, 8 (2009) 35-41.
- [55] Y. Wang, B. Peng, W. L. Zhang, K. Tan, CPW Circulators with Barium Ferrite Thin Films. *J.E.S.T.C*, 8 (2010) 351-355.
- [56] O. Zahwe, B. Sauviac, B. Abdel Samad, J. P. Chatelon, J. J. Rousseau, Numerical study of a circulator using yig thin film with a coplanar structure. *Prog. Electromagn. Res. C*, 6 (2009) 193-207.
- [57] O. Zahwe, B. Abdel Samad, B. Sauviac, J. P. Chatelon, M. F. Blanc Mignon, J. J. Rousseau, D. Givord, YIG thin film used to miniaturize a coplanar junction circulator. *J. Electromagn. Waves Appl*, 24 (2010) 25-32.
- [58] A. Jilani, M. S. Abdel-Wahab, A. H. Hammad, Advance deposition techniques for thin film and coating. *Modern Technologies for Creating the Thin-film Systems and Coatings*, 2 (2017) 137-149.
- [59] A. Saib, D. Vanhoenacker-Janvier, J. P. Raskin, A. Crahay, L. Huynen, Microwave tunable filters and nonreciprocal devices using magnetic nanowires. *1st IEEE Conference on Nanotechnology. IEEE-NANO*, (2001) 260-265.
- [60] T. Boyajian, D. Vincent, S. Neveu, M. LeBerre, J. J. Rousseau, Coplanar circulator made from composite magnetic material. *In International Microwave Symposium, IEEE MTT-S* (2011) 1-4.
- [61] A. Tchangoulian, Thesis report: Utilisation de matériaux composites magnétiques à nanoparticules pour la réalisation de composants passifs non réciproques micro-ondes, (2014) 144-147, Jean Monnet University Saint-Etienne, France.

# Chapter 2

## Synthesis and characterization techniques

### Contents

---

1.1	Introduction . . . . .	14
1.2	Brief history of magnetism . . . . .	14
1.3	Origin of magnetism . . . . .	15
1.4	Types of magnetism in materials and their properties . . . . .	16
1.5	Magnetic anisotropy . . . . .	20
1.6	Static properties . . . . .	23
1.7	Dynamic properties . . . . .	26
1.8	Classes of ferrites . . . . .	28
1.9	Theoretical models of the permeability tensor . . . . .	32
1.10	Microwave applications of ferrites . . . . .	38

---

### 2.1 Introduction

This chapter is divided in two parts. The first part will be devoted to the basics of electrochemistry and a state of art on the work presenting the influence of the presence of a magnetic field on the electrochemical behavior and the physico-chemical properties of the elaborated deposits. It will also present the experimental setup used for the magneto-electrodeposition of  $CoFe_2O_4$  thin films and nanowires on different substrates. The second part reviews the characterization techniques used during this thesis: Fourier Transform Infrared (FTIR) Spectroscopy, X-Ray Diffraction (XRD), Scanning Electron Microscope (SEM), Atomic Force Microscope (AFM), Stylus Profilometry (SP), Vibrating Sample Magnetometer (VSM) and Superconducting Quantum Interface Device Magnetometer (SQUID-VSM).

### 2.2 Electrochemistry: basic concepts

The electrochemistry is the study of structural properties of the media containing metallic species in a solution (electrolyte), as well as the phenomena taking place at the in-

interfaces between these electrolytes or between an electronic conductive medium and an electrolyte.

## 2.2.1 Metal-solution interface

### 2.2.1.1 Double electric layer

At the interface between a charged surface and an electrolytic solution, there is a layer of solution, denoted double electric layer that has different properties from those of the solution. Due to the potential difference between the charged surface (electrode in the case of an electrochemical cell) and the interior of the solution, a load transport takes place during a transient phenomenon, which produces an excess charge on the surface of the electrode and around it in the solution. The charges located on the electrode surface are due to an excess or a deficit of electrons in a very small zone ( $\simeq 1 \text{ nm}$ ). On the side of the solution, the compact layer of nanometric thickness, called Helmholtz layer [1], contains solvent molecules oriented in contact with metal and sometimes certain species (ions or molecules) that are specifically adsorbed on the interface. The location of the electrical centers of the specifically adsorbed ions is called the Inner Helmholtz Plane (IHP) (Fig.2.1). Indeed, the non-specifically adsorbed ions are solvated and cannot approach the surface at a distance less than the radius of their solvation sphere. The plane passing through the center of these non-specifically adsorbed ions closest to the surface is called the Outer Helmholtz layer (OHL).

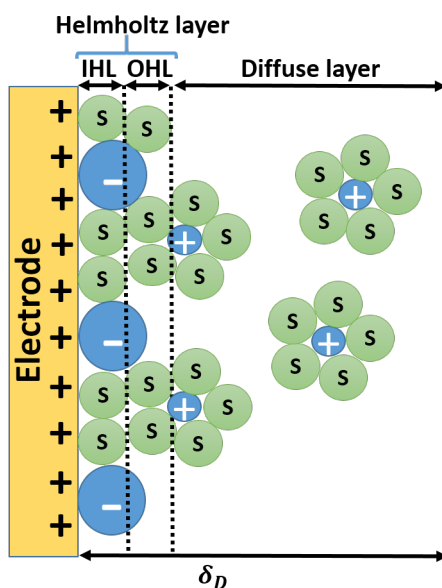


Figure 2.1: Structure of the electric double layer at the electrode-solution interface. The solvent molecules are designated by "S", the anions with "-", and the cations with "+".

Then, due to their brownian motion, the non-specifically adsorbed ions are not fixed in the Helmholtz plane. Their distribution near the electrode results from the competition between the electrostatic interactions that attract them towards the interface, and the thermal agitation that is tending to disperse them in the solution. These interactions make then the ion concentration near the interface differs from its value far from the electrode (within the solution). This excess of ions is localized in a stationary layer near the electrode, called diffuse layer whose thickness varies from a few nanometers to a few

tens of nanometers. According to Nernst theoretical model, the Helmholtz and diffuse layers constitute the double electrochemical layer [2]. The thickness of this layer is given by the following expression:

$$\delta_D = \sqrt{\pi Dt} \quad (2.1)$$

where  $t$  is the mass transfer time and  $D$  the electrolyte diffusivity.

### 2.2.1.2 Charge transfer mechanism

In the case of a metallic deposition performed via the electrochemical route, the metal is deposited on the cathode according to the simplified equation reaction:



where  $M^{n+}$  is the metallic ion and  $e^-$  the electron.

The electrochemical equilibrium calculations can be used to determine the concentration of free metal ions  $M^{n+}$  and consequently the reduction-oxidation (Redox) potential  $E_{eq}$  of the reaction, which is given by the Nernst equation:

$$E_{eq}(A) = E_{\frac{M^{n+}}{M}}^0 + \left(\frac{RT}{nF}\right) \ln\left(\frac{a_{M^{n+}}}{a_M}\right) \quad (2.2)$$

where

$E_{\frac{M^{n+}}{M}}^0$  is the standard Redox potential for M;

$R = 8.314 \text{ J/mol.K}$ , is the gas constant;

$T$  is the absolute temperature;

$n$  is the number of the exchanged electrons;

$F = 96485 \text{ C/mol}$ , is the Faraday constant;

$a_{M^{n+}}$  is the activity of the ion  $M^{n+}$ ;

A metal can be reduced from such solution when the applied potential ( $E_{ap}$ ) is more negative than  $E_{eq}(A)$  [3]. The charge transfer during the electrocrystallization process corresponds to the association of electrons from metal to metallic ions located in the electric double layer. This electrochemical reaction is characterized by a charge transfer resistance  $R_{tc}$  that indicates the ease with which the electronic transfer of  $M^{n+}$  to the electrode takes place. Consequently, easier transfer, weaker  $R_{tc}$  and therefore faster electrochemical reaction.

### 2.2.1.3 Electrochemical mass transport

In addition to the electrochemical charge transfer reaction, the mass transport phenomenon can happen and regulate the movement of the species towards the electrochemical interface. This mass transport can be done by migration, convection and diffusion as described in Fig.2.2. Most often, one of the three modes prevails over the other, which simplifies its study [3].

## Migration



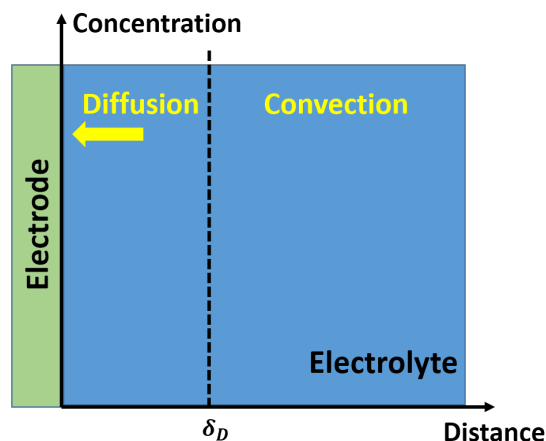


Figure 2.2: *Nernst layer; stationary convective diffusion regime.*

The displacement of the chemical species under the effect of the electric field is called migration. Within the electrolytic solution, the migration ensures the passage of the electric current during the electrolysis. As a matter of fact, it is important to have in the solution species of high electrical conductivity in order to increase this current. When the electrolytic solution is weakly concentrated in electroactive species, the supporting electrolyte ensures the transport of chemical species to the surface of the electrodes; it is very often the case for fundamental studies [3].

### Diffusion

The diffusion appears as the result of the lack of homogeneity in the composition of a system, i.e. in the case where different portions of this system contain either different species, or the same species in different concentrations [3]. When a reaction takes place at the interface of an electrode, the transformation of the reagents and the simultaneous appearance of products on the electrode surface naturally create differences in the concentrations in an area close to the electrode surface: the concentration of the electroactive species varies with their distances from the electrode. The resulting concentration gradient makes the transport of matter by diffusion predominant in the region near to the electrode called the diffusion limit layer of thickness  $\delta_D$ . The other species present in solution which do not react, also undergo a much smaller relative variation in order to ensure the neutrality of the solution in the diffusion layer.

### Convection

The convection of an ionic solution corresponds to the movement taken by this solution under the influence of variations of certain factors [4]:

- The convection is considered free or natural, when the movement is not produced by an expense of mechanical energy (agitation, pumping, etc.) but through local variations in density, resulting from local variations in temperature, and above all differences in concentration from reactions;
- The convection is considered forced, when the ionic solution is set in motion by an externally controlled mechanism such as the magnetic field.

## 2.3 Magneto-electrodeposition

The electrodeposition under a magnetic field is called magneto-electrodeposition. It presents the formation of a deposit by the electrolysis process with the superimposition of a magnetic field on the electrochemical cell. This is an example of research that mixes experimentation and theory (physics and electrochemistry). The effects of the magnetic field are numerous on the electrochemical kinetics, the morphology, and the magnetic properties of the formed deposit. The coupling between these two disciplines in the magneto-electrodeposition process, as well as the promising technological applications have been studied in various works, at different scales and with different points of view [5-7]. In this context, review papers have been proposed in this context by Fahidy et al. [8] and more recently by Mogi et al. [9].

### 2.3.1 Magneto-induced forces

During the application of a magnetic field in the electrodeposition process, different forces occur which can be at the origin of the effects observed on the crystallography and the kinetics discussed later. Two of them depending on the magnetic properties of the electrolyte are described below.

The magnetic energy of the electrolyte under magnetic field is written in the following form [10]:

$$E_m = -\frac{1}{2}MB \quad (2.3)$$

where  $M$  the magnetization induced by the magnetic field  $B$ .

The magnetization is given as a function of the molar susceptibility  $\chi_M$  of the species present in solution of concentration  $C$  by:

$$M = \chi_M CB \quad (2.4)$$

The expression of  $E_m$  becomes:

$$E_m = -\frac{1}{2}\chi_M CB^2 \quad (2.5)$$

Thus, as the magnetic force is equal to  $-\vec{\nabla}E_m$ , we deduce that this force is decomposed according to two terms: the first corresponds to the paramagnetic force  $\vec{F}_p$ , whose originated from the variation of the magnetic susceptibility in the diffusion layer due to the ion concentration gradient [11].

$$\vec{F}_p = -\frac{\chi_M B^2 \vec{\nabla}C}{2} \quad (2.6)$$

The second term  $\vec{F}_B$ , corresponds to the strength of the magnetic field gradient in the solution.

$$\vec{F}_B = -\frac{\chi_M CB \vec{\nabla}B}{2} \quad (2.7)$$

In the case of homogeneous magnetic field, this term is almost negligible. On the other hand, the first term highlights the expression of a force resulting solely from the concentration gradient of the electroactive species in the diffusion layer.

Moreover, there is another force that appears during the movement of electric charges in

the electrolytic solution, it is the Lorentz force ( $\vec{F}_L$ ). This electromagnetic force is responsible for the phenomena of the classic magnetohydrodynamic (MHD) convection. This force is generated by the interaction of the magnetic field  $\vec{B}$  with the electric current density  $j$ , and can be expressed in the phenomenological form [10]:

$$\vec{F}_L = \vec{j} \wedge \vec{B} \quad (2.8)$$

When a magnetic field  $\vec{B}$  is imposed on an electrochemical cell, several interactions can occur depending on the adopted configuration (parallel or perpendicular magnetic field to the reactive surface). In addition to the effects that a magnetic field can present by its amplitude, its orientation allowed to deepen the study of changes made within the obtained deposit. The researchers are divided on the explanations of the effects generated by the magnetic field. When the applied magnetic field  $\vec{B}$  is perpendicular to the surface of the cathode, the current lines are parallel to the magnetic field and the  $\vec{F}_L$  vanishes. Otherwise, when the magnetic field is parallel to the cathode, this force appears within the solution. The relationship between the orientation of the magnetic field and its effects is investigated in several studies, which have shown that the role of the  $\vec{F}_L$  are not negligible even for a magnetic field perpendicular to the reactive surface.

On the other hand, by working under a uniform magnetic field  $\vec{B}$  perpendicular to the used microelectrodes, they do not raise the effect of a paramagnetic force but they talk about residues of the Lorentz force on the electrode edges [12-14]. Because the current lines do not all come perpendicular to the electrode surface, especially on the edges, some are found to be perpendicular to the applied magnetic field and therefore, a Lorentz force appears around the electrode (Fig.2.3.b). The real-time video images show that there is a rotation of the solution around the axis of the electrode, i.e. helical vortex formation (Fig.2.3.a).

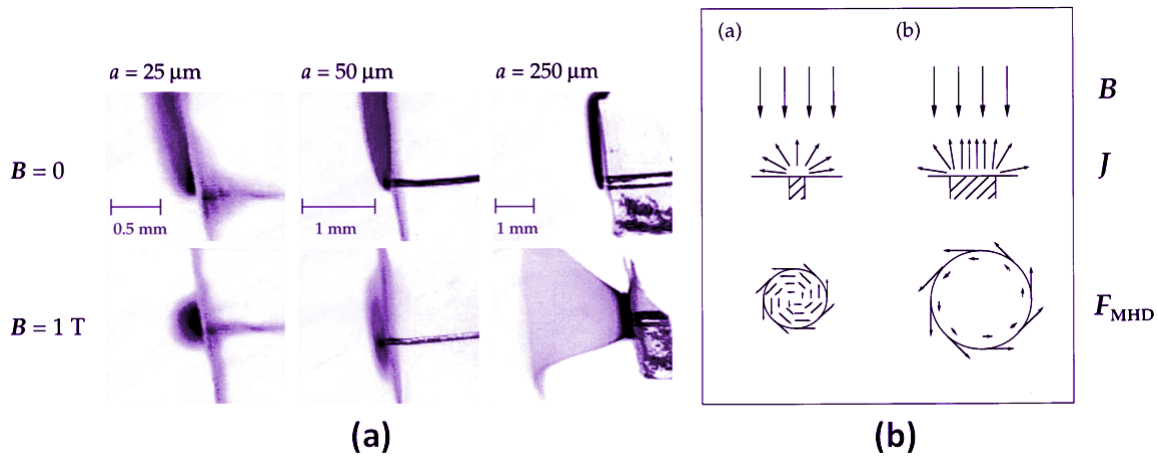


Figure 2.3: *Edge effects according to [12].*

In addition, the edge effects in the electrochemical process are always present. As a result, the current density is not uniform and therefore has at least two components.

$$\vec{j}_L = j_x \vec{e}_x + j_y \vec{e}_y \quad (2.9)$$

The component parallel to the surface is naturally more important near the edges than in the central region. In these conditions, if the magnetic field  $\vec{B}$  is perpendicular to

the electrode ( $\vec{B} = B\vec{e}_y$ ), the interaction of  $\vec{B}$  and  $\vec{j}_L$  generates a movement in the third direction at the edges, i.e. tangential in the case of circular electrodes. Under these conditions, a mathematical analysis of the mode that controls the transfer must take into account this MHD convection due to the  $\vec{F}_L$  at the edges.

$$\vec{F}_L^{edges} = j_x \vec{e}_x \wedge B \vec{e}_y = j_x B \vec{e}_z \quad (2.10)$$

This recirculation convection has been observed by Levintis et al. [15-17]. By changing the diameter of the micro electrodes, they observed this phenomenon, and emphasized the same recirculations above the surface of the electrodes. Uhlemann et al. [11] and Sugiyama et al. [18] have published their works on the possible hydrodynamic configurations in the presence of the edge effects generated by the  $\vec{F}_L$ . The authors propose an interpretation of the residual movement presented in Fig.2.4 based on the edge effects generated by a magnetic field perpendicular to the electrode surface.

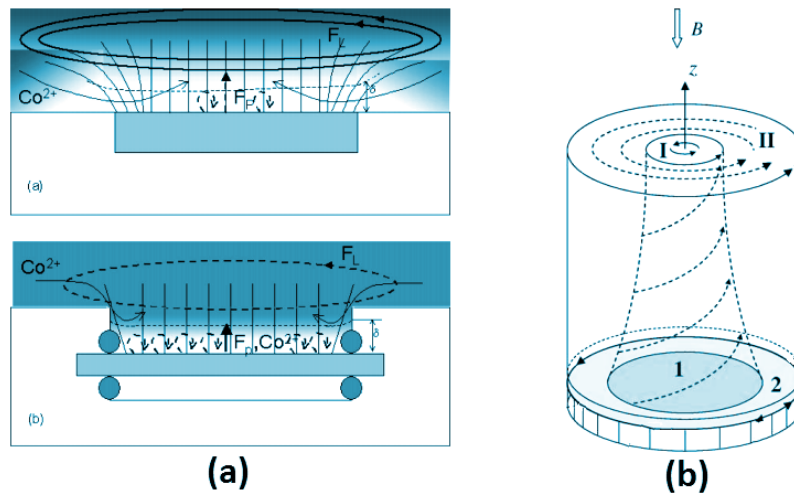


Figure 2.4: Configurations of the flows generated at the edges of the circular electrodes; a) Uhlemann et al. [11], b) Sugiyama et al. [18].

In this context, the thickness of Nernst diffusion layer  $\delta_D$  decreases with the magnetic field  $B$  according to the following phenomenological law [19] :

$$\delta_D = 1.59(\rho R \nu^{2/3} D^{1/3})^{1/3} (nFC)^{-1/3} B^{-1/3} \quad (2.11)$$

where  $R$  is the radius of the working electrode,  $\rho$  the density of electrolyte,  $\nu$  the bulk flow velocity,  $n$  the electron number,  $F$  the Faraday constant,  $D$  the diffusion coefficient, and  $C$  the concentration of electroactive ions in the electrolyte.

Moreover, Sugiyama et al. [18] reported a general expression for the total diffusion current density of the inner region of the Nernst diffusion layer as a function of the magnetic field and the average concentration difference  $\Delta C$  between bulk concentration and surface concentration:

$$j = 0.451 R \pi^{-1} \gamma (nFD)^2 (\nu/D)^{2/3} (\nu\eta)^{-1} B \Delta C^2 \quad (2.12)$$

where  $\gamma$  is the rotation efficiency introduced by the deviation from the ideal parallel arrangement of current lines, and  $\eta$  the dynamic viscosity.

On the other hand, in recent work [20], Coey et al. justified the effects observed by others researchers either to small gradients of magnetic field  $B$  created in the cell or to the effects of the  $F_L$  on the edges.

The entire bibliography reports that the magnetic field can be used in order to control the electrochemical response and the physico-chemical properties of the deposit. The originality of our work is to use a static uniform magnetic field to electrochemically grow self-polarized  $CoFe_2O_4$  nanocomposites.

## 2.4 Magneto-electrochemical synthesis of $CoFe_2O_4$

To start, we are brought to present the experimental setup used for the electrochemical deposition of  $CoFe_2O_4$ . This can be achieved only by the procedure of optimization of the experimental conditions of electrodeposition such as the potential, the pH and the concentrations of species. Thus, we will briefly describe the two main techniques for studying the electrochemical deposition process: Cyclic Voltametry (CV) and Chronoamperometry (CA).

### 2.4.1 Experimental setup

In order to perform the electrochemical growth, a classical three-electrode system was used. The experimental setup is shown in the Fig.2.5.

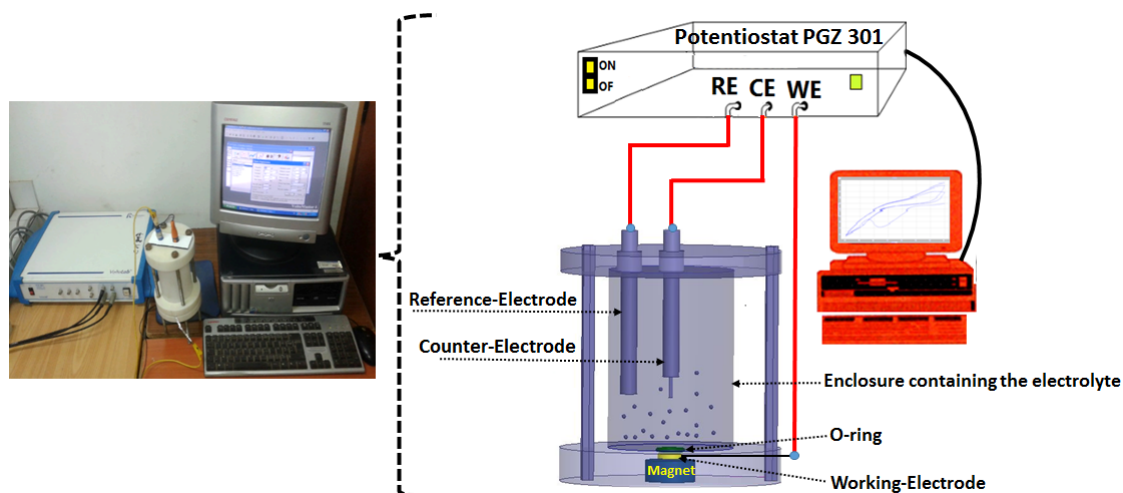


Figure 2.5: *Image and scheme of the experimental setup of the electrodeposition process.*

It consists of an electrochemical cell, made of Teflon, with three electrodes: the Reference Electrode (RE), a Counter Electrode (CE) and a Working Electrode (WE). They are connected to a Potentiostat PGZ 301, which is controlled by a computer using the "VoltaMaster4" software.

#### Reference Electrode (RE)

This electrode allows to compare the potentials of the studied reactions. The value of its potential must be reproducible and stable over time during the electrochemical growth. The reference electrode used during the experiments is the silver/silver chloride (Ag/AgCl) electrode.

## Counter Electrode (CE)

It ensures the passage of current in the circuit and gives its measure. It can be in platinum, carbon, or made from the material that we are trying to deposit. The counter electrode must be placed opposite the working electrode to obtain a good distribution of the current lines. In our case, we used a cylindrical rod of platinum with a surface area of  $1 \text{ mm}^2$  and is located at a distance of  $1.2 \text{ cm}$  from the substrate surface.

## Working Electrode (WE)

It is the electrode whose surface serves as a site for the electrochemical reduction of the metallic ions that are present in electrolyte. The working electrodes used in our study are purchased from Sigma Aldrich company:

- Fluorine-doped Tin Oxide (FTO) coated glass substrate with surface resistivity of  $7 \Omega/\text{sq}$ .
- Anodic Aluminum Oxide (AAO) membrane with a thickness of  $60 \mu\text{m}$  and a porosity of 50%. We used three types of AAO membranes with an average pore diameter of 20 nm, 100 nm and 200 nm. The working electrode is obtained by RF sputtering of a thin layer ( $3 \mu\text{m}$ ) of copper on one side of the AAO membrane.

## Applied magnetic field B

Circular permanent magnets based on NdFeB material (Fig.2.6), which generate a magnetic field ranging from 0.4 to 0.6 T, have been used in the electrodeposition experiments. Their diameters and thickness varies between 20 mm and 30 mm. During the electrodeposition experiments, each magnet is placed under the WE as shown in Fig.2.5.



Figure 2.6: Images of the permanent magnets used in the electrodeposition experiments.

In addition, each magnet produces a static homogeneous magnetic field perpendicular to the WE surface.

## Substrates cleaning

Before starting the electrodeposition and in order to eliminate any kind of impurity on the surface of the substrate, FTO-coated glass and AAO membranes were cleaned in an ultrasonic bath with acetone, ethanol, and distilled water (10 min for each step).

## Reagents

The samples are elaborated from analytical grade precursors purchased from Sigma Aldrich company. Electrochemical bath components were consisted of cobalt sulphate heptahydrate ( $CoSO_4 \cdot 7H_2O$ , 97%), ammonium sulphate ( $(NH_4)_2SO_4$ , 99%), ferrous sulphate heptahydrate ( $FeSO_4 \cdot 7H_2O$ , 99%). Sulfuric acid ( $H_2SO_4$ , 99%) and boric acid ( $H_3BO_3$ , 99%) were used in order to adjust the pH of the ionic solution and keep the value of pH more stable at the electrolyte-WE interface, respectively. Distilled water was used to prepare all aqueous solutions.

## Air annealing

The deposited samples may contain many defects such as voids, pinhole, etc. Annealing in air reduces these defects. The electrochemically grown samples onto various substrates were annealed in air by using a NABERTHERM furnace equipped with P 320 Controller (Fig.2.7).



Figure 2.7: Image of the furnace used for the air annealing treatment of the samples.

The main of this air annealing was to complete the desired physical and chemical processes within the materials.

### 2.4.2 Electrochemical techniques

During this section, we will present some electrochemical techniques. They can be used both for the study of the reaction mechanisms involved in an electrodeposition process and for the formation of the deposit itself. The main methods used are cyclic voltammetry and chronoamperometry.

#### Cyclic Voltammetry (CV)

The CV is an electroanalysis technique based on the measurement of the current flow resulting from the electrochemical phenomena that occur on the surface of the electrode under the effect of a controlled variation of the potential difference between two specific electrodes. The CV is based on forward and reverse linear scans of the potential, allowing the measurement of the curves  $i = f(E)$  for the oxidation and reduction of the compound [21]. Thus, a negative current, recorded by convention, designates the cathodic current,



while a positive one represents the anodic current. The main characteristic quantities of a voltammogram are given in Fig.2.8.

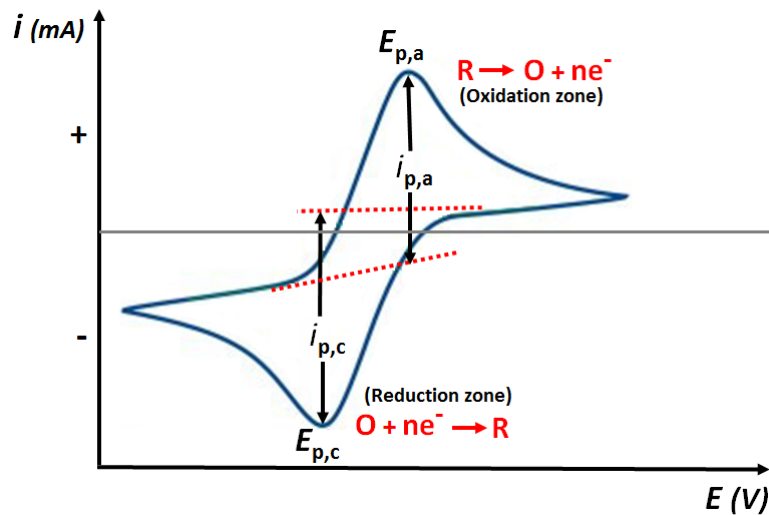


Figure 2.8: Example of a cyclic voltammetric curve and its characteristic parameters.  $i_{p,a}$ ,  $i_{p,c}$ : anodic and cathodic peak currents;  $E_{p,a}$ ,  $E_{p,c}$ : potentials for anodic and cathodic peaks.

### Chronoamperometry (CA)

The CA is an electrochemical method, which consists of imposing or fixing a potential and varying the current as a function of time [22]. This method is of main interest in the case of processes with the formation of a new phase, and in particular in the case of metallic deposits. Consequently, we can quantitatively demonstrate via theoretical models, the transient phenomena of nucleation and then of crystal growth.

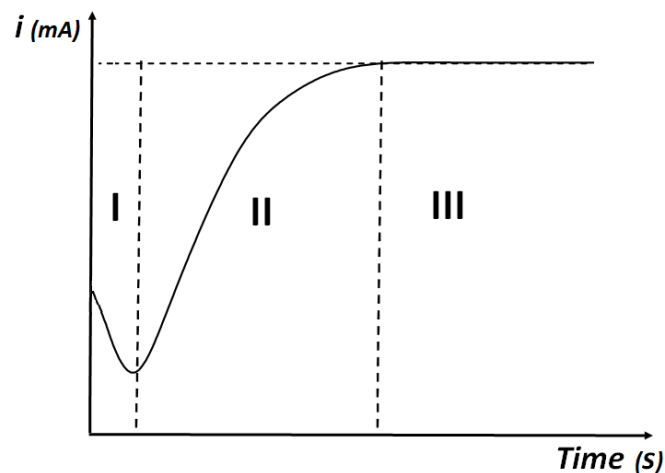


Figure 2.9: Theoretical diagram of the current-time curve for three-dimensional germination.

The theoretical diagram (Fig.2.9) of the current-time curve for three-dimensional germination includes three distinct areas:

- **Zone I**: corresponds to the charge of the electric double layer and the time required to form the germs;



- **Zone II**: reflects the growth of germs and the increase in the active surface on the electrode;
- **Zone III**: displays the fact that the diffusion of ions in the solution becomes the limiting factor for the growth reaction of the deposited film.

The electrodeposition process is generally influenced by the following parameters:

- The concentration of metal ions in the electrolyte;
- The pH of the solution;
- The bath temperature;
- The applied potential for deposition;
- The applied current.

### Faraday's Law and deposit thickness

When an electrochemical deposition is done under a potential that reduces the desired metal, the recorded response  $i = f(t)$  during a deposition is integrated to calculate the total charge  $Q$  that passes through the electrolyte in order to deduce the mass and thickness of the deposit.

$$Q = \int_0^t i dt \quad (2.13)$$

According to Faraday's law, the quantity of charge passing through the electrolyte is expressed as follows:

$$Q = it = nNF \quad (2.14)$$

where  $n$  is the number of the exchanged electrons in the studied reaction,  $N$  the number of the reduced moles during the reaction,  $F$  the Faraday constant,  $t$  the deposition time. The parameter  $N$  can be written:

$$N = \frac{m}{M} = \frac{\rho V}{M} = \frac{\rho Sh}{M} \implies m = \rho Sh \quad (2.15)$$

where  $m$  is the deposited mass ( $g$ ),  $M$  the molar mass ( $g/mol$ ),  $\rho$  the volumetric mass density ( $g/cm^3$ ),  $V$  the deposited volume ( $cm^3$ ),  $S$  the deposition area ( $cm^2$ ),  $h$  the thickness of the deposit ( $cm$ ).

Using Eq.2.14 and Eq.2.15, the expression of the deposited thickness can be deduced as follows:

$$h = \frac{QM}{n\rho SF} = \frac{itM}{n\rho SF} \quad (2.16)$$

## 2.5 Characterization techniques

### 2.5.1 X-Ray Diffraction (XRD)

X-ray diffraction is the basic material characterization technique allowing the determination of the mineral phases of crystals; it is based on the ability of matter to deflect

X-ray beams. Indeed, this technique provides access the type of geometric arrangement, the lattice parameter and the crystallite size concerning a crystallized material. The principle consists of projecting an X-ray beam on an array made up of the atomic planes of a crystal. This beam is diffracted by the sample at a specific angle, according to Bragg's law [23].

$$\lambda_x = 2d \sin(\theta) \quad (2.17)$$

where  $d$  is the inter-plane distance and  $\lambda_x$  the wavelength of the incident beam. The variation of the angle  $\theta$  makes it possible to obtain a XRD pattern whose the peak positions and heights depend on the crystallographic structure and the nature of the analyzed compound. The diagram is actually resulting from the Fourier transform of the crystallographic planes. If the rays are very fine for a uniform and infinite crystal structure, they can be enlarged by a finite structure (case of nanoparticle) or by a variation of the interplane distance inside the crystallite (case of a distortion of the lattice). The study of the peak width in XRD spectrum allows therefore to determine the average size of the crystallite as well as the distortion rate of a material, while the position of these lines gives access to the inter-plane distance, i.e. the lattice parameter of the synthesized crystal. In this study, the XRD pattern of the samples were obtained on a XPERTPRO X-Ray

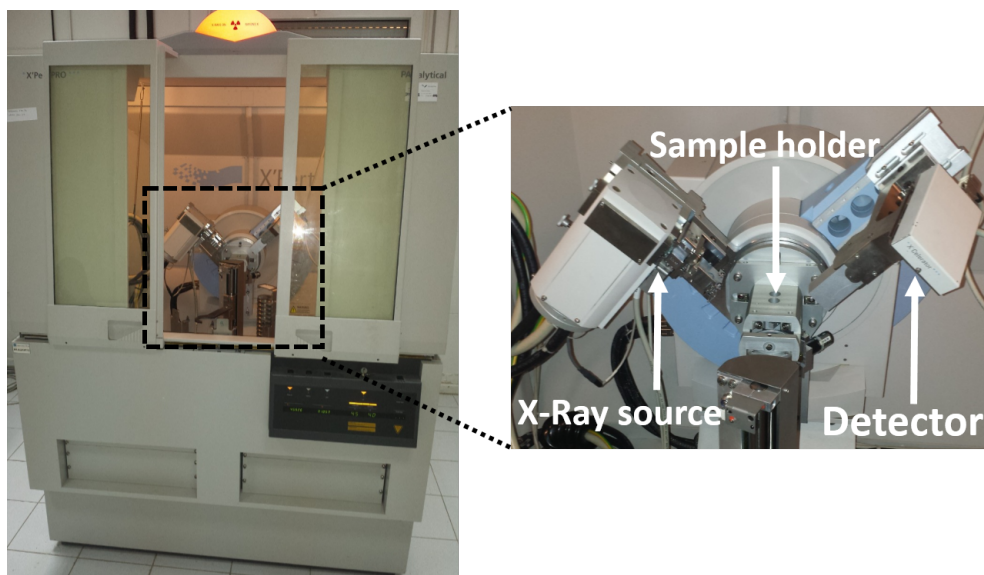


Figure 2.10: *Picture of X-Ray device used during this work.*

diffractometer using Cu radiation ( $\lambda = 1.5407 \text{ \AA}$ ) in the  $2\theta$  range  $15 - 83^\circ$ , with a step size of  $0.03^\circ$ . The data acquisition is done at room temperature ( $25^\circ \text{C}$ ). The objective of the analysis is the determination of the phases present in the synthesized samples, the verification of the absence of secondary phases, calculation of the lattice parameter as well as the estimation of the crystallite size.

### Lattice parameter calculation

The studied material in our study adopts a cubic symmetry relative to the spinel structure. The lattice parameter in this case depends on the Miller indices ( $h, k, l$ ) of the reticular planes, the wavelength ( $\lambda$ ) of the X-ray beam, and the angle ( $\theta$ ) of incidence in

degrees. It is given by the following expression:

$$a = \frac{\lambda \times \sqrt{h^2 + k^2 + l^2}}{2 \sin(\theta)} \quad (2.18)$$

### Crystallite size calculation (Williamson-Hall plot)

Williamson and Hall proposed in 1953 that the total enlargement of XRD peaks is originated from the sum of the enlargement due to the size and to the defects, with the simplifying assumption that all the contributions have a lorentzian character [23], they established the following equation:

$$\beta_{hkl} \cos \theta = \frac{0.9\lambda}{D} + 4\epsilon \sin \theta \quad (2.19)$$

The instrumental broadening  $\beta_{hkl}$  is corrected from the adjustment of the XRD peaks by using the following equation:

$$\beta_{hkl} = \sqrt{(\beta_{hkl})_{Measured}^2 - (\beta_{hkl})_{Standard}^2} \quad (2.20)$$

where  $\epsilon$  is the mean strain (due to atomic scale defects) within the material. The best approach to make this correction and determine the standard broadening is to anneal the sample at high-temperature ( $>800$  °C). This heat treatment will remove not only the stored strain energy, but also the broadening associated to small crystallites. As a result, a deposit consisting of large crystallites can be obtained. Then, the Williamson-Hall standard formula is used to extract the corrected values of  $\beta_{hkl}$  from the sample without large crystallites.

Therefore, Eq.2.19 is a straight-line equation. Accordingly, the Williamson-Hall plot consists of plotting the points on a graph, with known coordinates, on a graph. A linear regression and Y-Intercept extrapolation of the experimental points allow to obtain the parameters of the line and deduce the value of the crystallite size  $D$  and the slope  $\epsilon$ .

$$D = \frac{0.9\lambda}{Y_{Intercept}} \quad (2.21)$$

$$\epsilon = slope \quad (2.22)$$

### 2.5.2 Fourier Transform Infrared (FTIR) spectroscopy

The FTIR spectroscopy is based on the absorption of infrared radiation by the analyzed material. It allows, by detecting the characteristic vibrations of chemical bonds, to perform the analysis of the chemical functions present in the sample. When the wavelength (energy) supplied by the light beam is close to the vibration energy of the molecule, the latter will absorb the radiation and we will record a decrease in the reflected or transmitted intensity. As a matter of fact, the obtained spectra correspond to a set of characteristic absorption bands, which will facilitate the identification of the material nature [24].

The analysis is performed in LMER using IRAffinity-1 SHIMADZU FTIR spectrophotometer (Fig.2.11). In order to avoid signal saturation; the powders studied are diluted in anhydrous KBr (transparent to infrared radiation), in the form of pellets consisting of 150 mg of KBr and 5 mg of powder of the synthesized material. The spectra are recorded between 300 and 3500  $cm^{-1}$  and processed using the Win-IR software.



Figure 2.11: Images of the FTIR spectrophotometer and the mini press used for the preparation of high-quality pellets.

### 2.5.3 Atomic Force Microscopy (AFM)

The AFM belongs to a larger family of surface analysis techniques called scanning probe microscopy (SPM). Most of these techniques are derived from the invention of the Scanning Tunneling Microscope (STM) in 1981. Four years later, Binnig et al. [25] accessed the first atomic force microscope by adapting one of these microscopes.

The principle of the AFM is based on the measurement of different interaction forces (repulsion and attraction forces, van der Waals forces, electrostatic forces, friction forces, magnetic forces, etc.) between an ideally atomic probe attached to a cantilever and the surface of a material. The rigid probe shape can be tetrahedral or triangular, with a length varying from 14 to 16  $\mu\text{m}$ , and a radius of curvature of 6  $\text{nm}$ . The most commonly used probes are those based on silicon nitride ( $\text{Si}_3\text{N}_4$ ) or silicon. It implements the Hellmann-Feynman theorem, which highlights the repulsion and attraction forces occur at the probe-surface interface. The sample is fixed on a sample holder and it is magnetically plated on piezoelectric ceramic providing displacements in the three directions of space (XYZ). During the scanning of the sample surface, the interaction forces induce the deflection of the cantilever. This deflection is tracked by reflecting a laser beam on the upper side of the cantilever to a photodiode divided into four quadrants, which simultaneously records the light signal of deflection movements and friction perpendicular to each other. Each AFM image is recorded by scanning the surface in X and Y directions.

The AFM microscope operates in several modes, depending on the forces involved between the probe and the surface behavior of the analyzed sample (smooth, rough, solid, liquid, soft, etc.). The contact mode will be used for rigid materials while the non-contact mode will be used to study soft and porous materials. To prevent any kind of surface deterioration, for example by the probe, it is preferable to proceed by tapping mode. The mode is intermediate between contact and non-contact modes. The principle of measurement in this mode consists of oscillating the cantilever near to its resonance frequency that ranging from 50  $\text{kHz}$  to 500  $\text{kHz}$  and with a sufficiently high amplitude (typically greater than 20  $\text{nm}$  but in practice rather than 100  $\text{nm}$  to 200  $\text{nm}$ ). The probe touches periodically the sample surface by tapping it punctually. This allows to switch from attractive to repellent regime and vice versa, and frictional forces are thus avoided. This mode is widely used because there is no risk of damage of the sample surface and the probe.

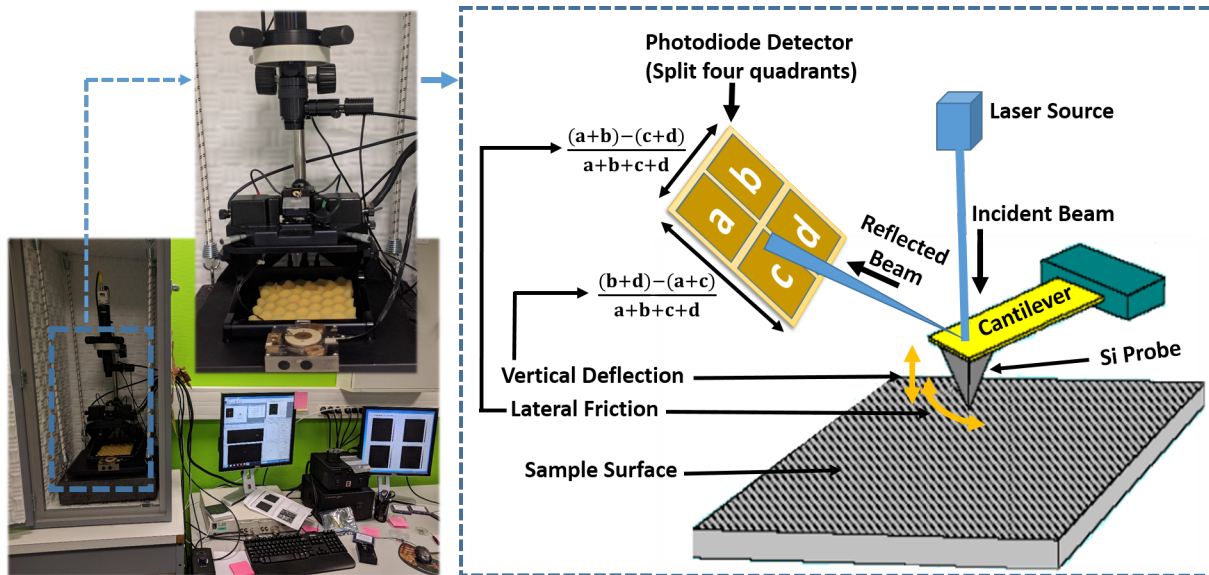


Figure 2.12: *AFM microscope; (a) agilent 5500 AFM device, (b) scanning operating principle.*

In these cases, the AFM analyses were performed in tapping mode with Silicon (*Si*) probes using the Agilent 5500 AFM device available at the Hubert Curien laboratory.

#### 2.5.4 Scanning Electron Microscope (SEM)

The SEM instrument was conceived for the first time in Germany, in the 1930s, by Knoll and Von Ardenne and developed by Zworykin Hillier and Snyder in RCA laboratories in the United States (1940). However, the SEM has known a real improvement between 1948 and 1965, as a result of technical advances in television and electron detectors. This powerful technology is used as a technique for observation and chemical analysis of materials [26].

The one available at the LHC is a *FEI Nova 200* equipped with a (FEG) Schottky electron gun operating between 50 V and 30 kV (Fig.2.13).

The electron gun emits a beam of electrons, which will be accelerated and focused in secondary vacuum by electromagnetic lenses in a fine probe, and interact with the sample as shown schematically in Fig.2.14. The sample is placed in the specimen room on a motorized stage enabling movement in three directions of space. Turbo-molecular pumps serve a pumping chamber in order to obtain a high vacuum ( $10^{-9}$  mbar) at the tip and a secondary vacuum at the column ( $10^{-7}$  mbar) and the analysis chamber ( $10^{-5}$  mbar). A software provided by its manufacturer controls the SEM device.

A SEM is equipped with the specific detectors necessary to detect each radiation and can exploit the radiation and particles result from elastic and inelastic interactions between the electron beam and the material (sample). By scanning the surface of the sample, an image is formed on the screen in data acquisition. The main images produced by the SEM are of three types: images formed by secondary electrons, backscattered electrons, emitted X-ray, and Auger electrons. These do not concern the present study.

- **Backscattered electrons:** are electrons of the primary beam, which react, in quasi-elastic mode with the atoms of the sample. They are returned in a direction



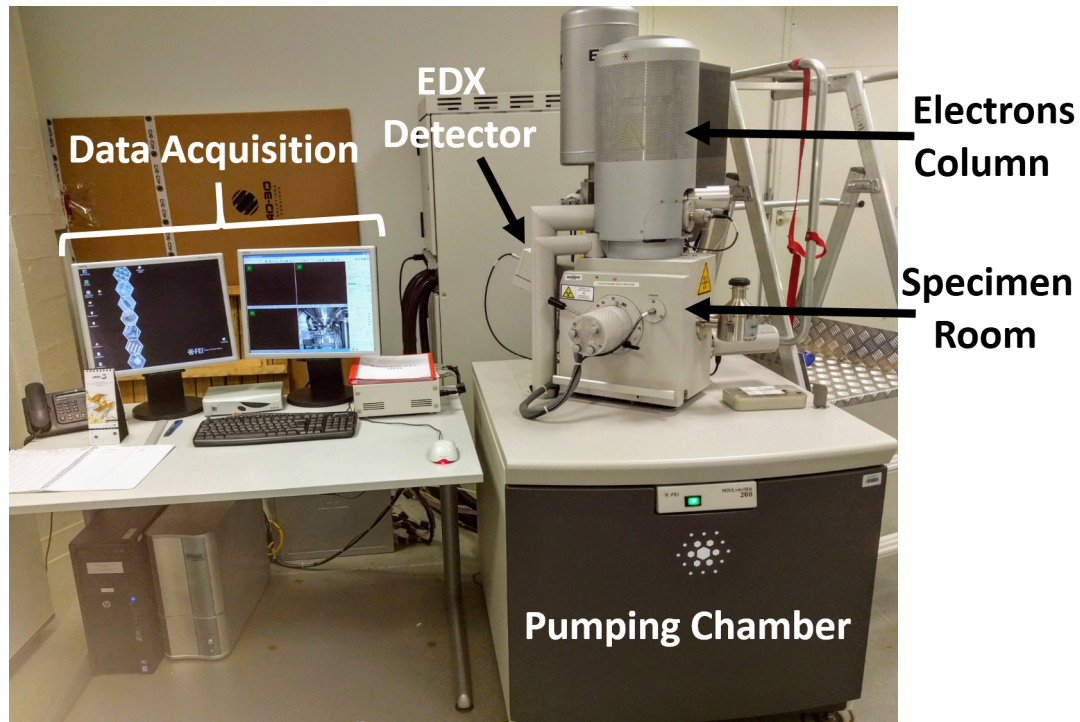


Figure 2.13: Picture of the used Scanning Electron Microscope "FEI Nova 200".

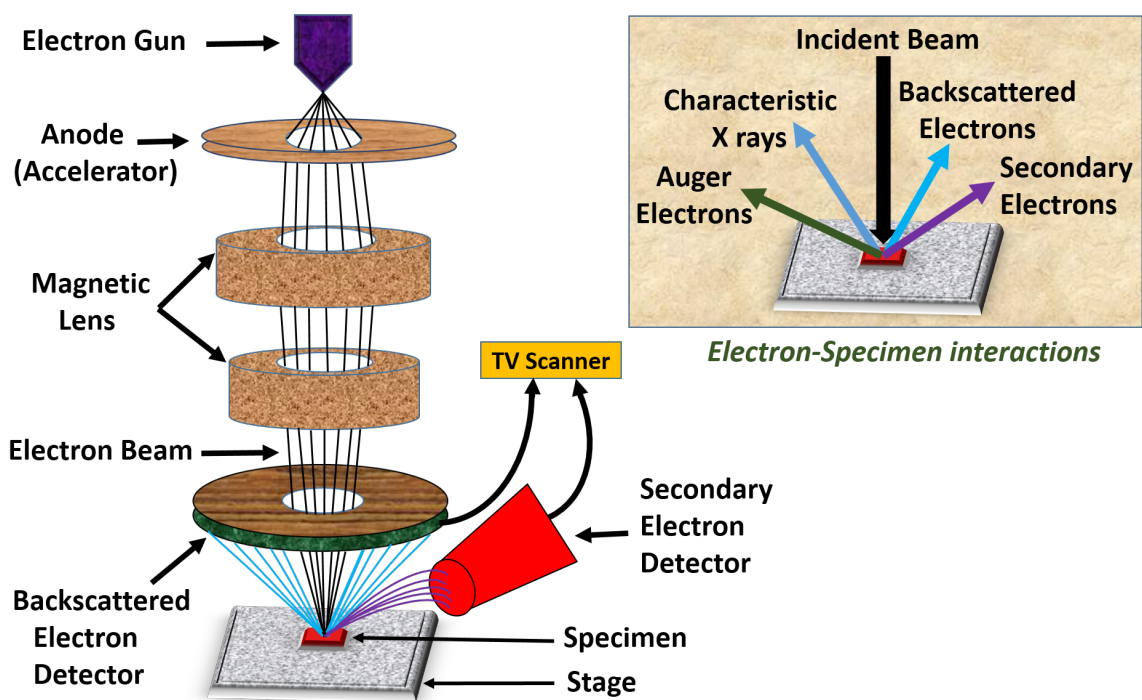


Figure 2.14: Schematic drawing of the typical Scanning Electron Microscope principle and the electron-specimen interactions within a SEM.

close to their original direction with low loss of energy. A detector generally placed vertically on the sample, i.e. in the beam axis, attracts them.

- **Secondary electrons:** are low energy emitted electrons when the primary beam,

that lost a part of its energy, excites the atoms of the sample. This low energy electrons cannot be extracted if they occurred very close to the surface;

- **X-rays:** the inelastic interaction with emission of an electron leads to the ionization of the atom, it is then excited. It can be de-excited by emission of X-rays (spectrum of rays).

The formation of high-resolution SEM images is produced by the emission of secondary and backscattered electrons. The contrast of the image is then mainly given by the relief of the sample. However, this is a 2D photograph of the sample surface unlike the AFM that gives a 3D image. For our study, the advantage of SEM lies in its chemical analysis capacity and wide angle photographs that it can provide.

### Energy Dispersive X-ray analysis (EDX)

During the SEM scanning, the incident electron beam has enough energy to ionize the atoms of the deep layers and thus causes the emission of X-rays, which are collected using a lithium doped silicon (*Si/Li*) detector (Fig.2.13). Each element emits X photons, corresponding to an electronic transition between the core levels of the atom. This technique is called Energy-Dispersive X-Ray Analysis (EDX) or Energy Dispersive Spectroscopy (EDS). It makes it possible to establish a map of distribution of the individual elements present in an area of the analyzed sample. In this work, all SEM-EDS experiments for imaging and elemental analysis have been performed in backscattered electrons mode.

### 2.5.5 Stylus Profilometry (SP)

The SP technique serves to characterize the surface of materials. The profilometer used in our work is *Bruker DektakXT* available at the OPC (Optical and Photonic Characterization) platform of LHC (Fig.2.15).

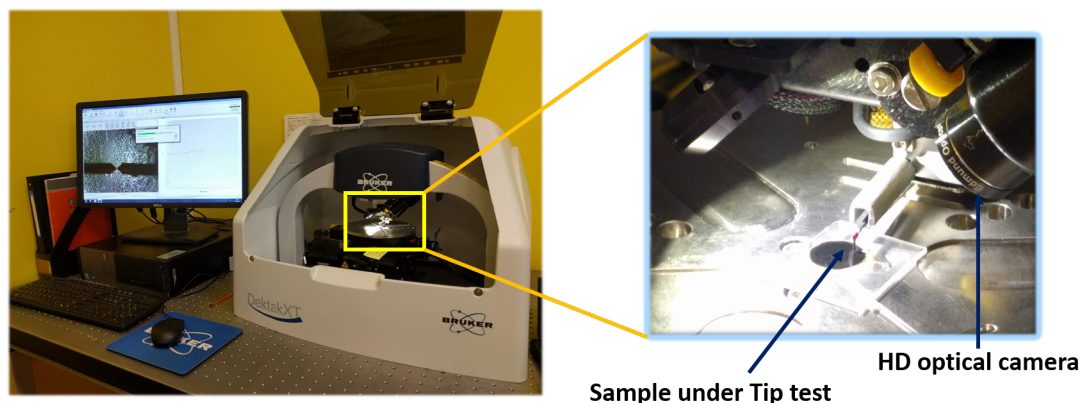


Figure 2.15: Image of Bruker Dektak XT profilometer.

It is a powerful tool for measuring roughness and thickness of thin layers, and it is able to measure and detect deviations from 500 Å to 1 mm. It contains a stylus tip of diamond which encounters the sample surface. A spring system maintains a constant force on the stylus. The sample is moved under the tip with the control of an HD optical camera, in order to trace the topography of the surface. This tool can profile the topography and surface ripple. The Dektak XT profilometer has also thin layer stress analysis software and a 3D mapping capacity [27].

## 2.5.6 Vibrating Sample Magnetometer (VSM)

The study of the magnetic properties of cobalt ferrite nanocomposites constitutes the important part of this work. The VSM instrument enables the determination of the magnetic properties of materials as a function of the applied field (*hysteresis loop*). It measures the flux induced in a coils system by periodic vertical vibration of the sample. The measurement principle consists of placing the sample in a mobile holder that is connected to the vibration unit that enables to vibrate the sample along  $z$  direction. The sample with size of  $3\text{ mm} \times 3\text{ mm}$  is located inside the two detection coils at the level  $z = 0$  and vibrates in the  $\pm z$  directions during the measurement process (Fig.2.16). This vibration creates a variation of flux as a function of  $z$ .

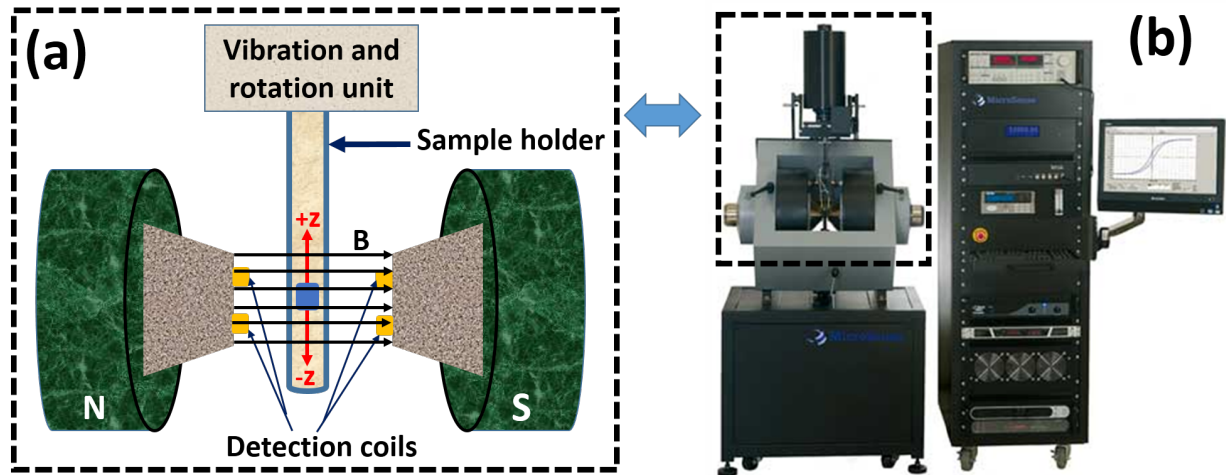


Figure 2.16: VSM instrument: (a) schematic illustration of sample vibration process between the two coils, (b) picture of equipment in a VSM unit.

The induced flux  $\Phi$  created by the sample of magnetic moment  $m$  is determined from the reciprocity theorem:

$$\Phi = \frac{B}{I} m \quad (2.23)$$

where  $B$  is the magnetic field created by a fictitious current  $I$  flowing in the detection coils.

The induced tension is expressed as:

$$V_{coils} = \frac{\partial \Phi}{\partial t} = m \frac{\partial(B/I)}{\partial z} \frac{\partial z}{\partial t} \quad (2.24)$$

In this study, some hysteresis loops are measured at room temperature ( $300\text{ K}$ ) using the vibrating sample magnetometer (VSM) in STICC Laboratory (*Lab – STICC*) at Brest University.

## 2.5.7 Superconducting Quantum Interference Device Magnetometer (SQUID)

Other hysteresis loops of  $\text{CoFe}_2\text{O}_4$  nanowires were made using an *MPMS SQUID VSM* magnetometer installed at the institute of Neel in Grenoble (Fig.2.17). The magnetic



measurements can be done in a wide temperature range from 1.8  $K$  to 400  $K$  and for a magnetic field up to 5  $Tesla$ .

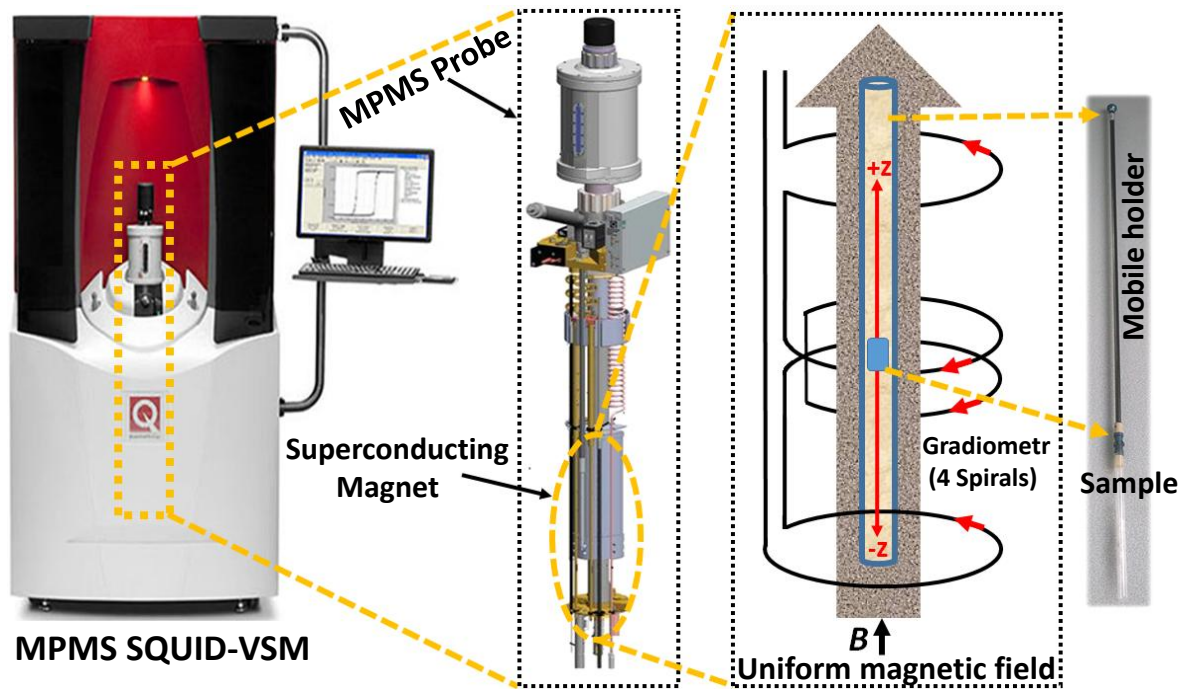


Figure 2.17: *MPMS SQUID VSM instrument and its measurement setup.*

The operating principle is based on the detection of magnetic flux variations when a magnetic sample passes through the superconducting detection coil (Gradientmeter of 4 spirals) during its vibration in  $\pm z$  directions at a fixed temperature. This coil is surrounded by a superconducting magnet that produces a homogeneous and intense magnetic field. The coil is located inside a cryogenic probe (MPMS probe) as shown in Fig.2.17. The SQUID VSM is the most sensitive magnetic field detection system that exists; it is a current-voltage converter extremely accurate. The amplitude of the measured signal is directly proportional to the magnetic moment of the sample. This instrument allows the measurement of hysteresis loops of samples with very low magnetization, up to some  $10^{-8}$  emu. In addition, a RSO system (Reciprocating Sample Option) oscillating around a measuring point, can increase this sensitivity. In this case, the measurements are faster and the signal processing is better [28].

Moreover, we have carried out magnetic measurements according to the procedures known as Field-Cooled (FC) and Zero-Field-Cooled (ZFC) in the presence of a low applied field. These measurements reveal the irreversibility properties below a so-called blocking temperature  $T_b$  which is correlated to the characteristic measurement time [29]. The protocol employed for ZFC-FC measurements consists of measuring two magnetization curves as follows:

- The sample is cooled in the absence of a magnetic field from room temperature, where all particles are in the superparamagnetic state, to a temperature  $T_{min}$  below the blocking temperature. Then a weak magnetic field (100  $Oe$ ) is applied and the magnetic moment of the sample is measured by increasing the temperature from  $T_{min}$ . The ZFC curve is then obtained;

- For FC measurement, the protocol is the same as that used for ZFC measurements except that the cooling takes place in the presence of a magnetic field (100 *Oe*).

## Chapter 2: Summary

In this chapter, we have discussed reminders of electrochemistry and the influence of applying a magnetic field on the electrochemical reactions during the elaboration of metallic deposits. Then, we presented the experimental set-up and the techniques used to electrochemically synthesize cobalt ferrite thin films and nanowires on FTO and into AAO membranes, respectively.

The characterization techniques have been subsequently exposed starting with spectroscopic (FTIR) and structural (XRD) analysis followed by morphological imaging (SEM) and surface topography (AFM, SP) up to the magnetic measurements by a simple VSM and coupled SQUID-VSM instruments.

The next chapters deal the different obtained results and their interpretations.

# Bibliography

- [1] B. Bhattacharyya, Electrochemical micromachining for nanofabrication, MEMS and nanotechnology, William Andrew, Elsevier, (2015) 25-52.
- [2] R. Rousseau, M. L. Délia, A. Bergel, A theoretical model of transient cyclic voltammetry for electroactive biofilms. *Energ. Environ. Sci*, 7 (2014) 1079-1094.
- [3] A. J. Bard, L. R. Faulkner, Fundamentals and applications. Electrochemical Methods, Wiley, 2nd ed, (2000) 580-632.
- [4] D. Brunner, M. Boldrini, G. K. Boiger, Model based analysis of forced and natural convection effects in an electrochemical cell. *Int. J. Multiphys*, 11 (2017) 97-111.
- [5] A. L. Daltin, M. Benaissa, J. P. Chopart, Nucleation and crystal growth in magneto-electrodeposition. *IOP. Conf. Ser. Mater. Sci. Eng*, 424 (2018) 012022.
- [6] A. Fattahi, M. E. Bahrololoom, Investigating the effect of magnetic field on pulse electrodeposition of magnetic and non-magnetic nanostructured metals. *Surf. Coat. Technol*, 261 (2015) 426-435.
- [7] I. Mogi, R. Morimoto, R. Aogaki, K. Takahashi, Surface Chirality in Rotational Magneto-electrodeposition of Copper Films. *Magnetochemistry*, 5 (2019) 53.
- [8] T. Z. FAHIDY, Magneto-electrolysis. *J. Appl. Electrochem*, 13 (1983) 553-563,
- [9] I. Mogi, R. Morimoto, R. Aogaki, Surface chirality effects induced by magnetic fields. *Curr. Opin. Electrochem*, 7 (2018) 1-6.
- [10] J. R. Reitz, F. J. Milford, R. W. Christy, Foundations of electromagnetic theory, Addison-Wesley, 4th Ed, (2008) 1-630.
- [11] M. Uhlemann, A. Krause, J. P. Chopart, A. Gebert, Electrochemical deposition of Co under the influence of high magnetic fields. *J. Electrochem. Soc*, 152 (2005) C817.
- [12] K. M. Grant, J. W. Hemmert, H. S. White, Magnetic field driven convective transport at inlaid disk microelectrodes: The dependence of flow patterns on electrode radius. *J. Electroanal. Chem*, 500 (2001) 95-99.
- [13] K. M. Grant, J. W. Hemmert, H. S. White, Magnetic field-controlled microfluidic transport. *J. Am. Chem. Soc*, 124 (2002) 462-467.
- [14] D. Mehta, H. S. White, Finite-Element Analysis of Magnetic Field Driven Transport at Inlaid Platinum Microdisk Electrodes. *Chem. Phys. Chem*, 4 (2003) 212-214.

- [15] N. Leventis, M. Chen, X. Gao, M. Canlas, P. Zhang, Electrochemistry with stationary disk and ring-disk millielectrode in magnetic fields. *J. Phys. Chem. B*, 102 (1998) 3512.
- [16] N. Leventis et X. Gao, Steady state voltammetry with stationary disc millielectrodes in magnetic fields. *J. Phys. Chem. B*, 103 (1999) 5832.
- [17] N. Leventis, A. Dass, Demonstration of the Elusive concentration gradient paramagnetic force. *J. Am. Chem. Soc.*, 127 (2005) 4988.
- [18] A. Sugiyama, M. Hashiride, R. Morimoto, Y. Nagai, R. Aogaki, Application of vertical micro-disk MHD electrode to the analysis of heterogeneous magneto-convection. *Electrochim. Acta*, 49 (2004) 5115-5124.
- [19] M. Zieliński, E. Miękoś, Influence of constant magnetic field on the electrodeposition of Co–Mo–W alloys. *J. Appl. Electrochem*, 38 (2008) 1771.
- [20] J. M. D. Coey, F. M. F. Rhen, P. Dunne, S. McMurry, The magnetic concentration gradient force—Is it real ?. *J. Solid. State. Electrochem*, 11 (2007) 711-717.
- [21] P. Allongue, F. Maroun, Self-ordered electrochemical growth on single-crystal electrode surfaces. *J. Phys. Condens. Mat*, 18 (2006) S97.
- [22] F. Lantelme, A. Seghioer, A. Derja, Model of nickel electrodeposition from acidic medium. *J. Appl. Electrochem*, 28(9) (1998) 907-913.
- [23] G. Williamson, W. Hall, X-Ray Line Broadening from Filed Aluminium and Wolfram. *Acta. Metall*, 1 (1953) 22-31.
- [24] N. Labchir, E. Amaterz, A. Hannour, A. A. Hssi, D. Vincent, A. Ihlal, M. Sajieddine, (2019). Highly efficient nanostructured  $CoFe_2O_4$  thin film electrodes for electrochemical degradation of rhodamine B. *Water. Environ. Res*, <https://doi.org/10.1002/wer.1272>.
- [25] G. Binnig, C. Gerber, E. Stoll, T. R. Albrecht, C. F. Quate, Atomic resolution with atomic force microscope. *E.P.L.(Europhysics Letters)*, 3 (1987) 1281.
- [26] A. Bogner, P. H. Jouneau, G. Thollet, D. Basset, C. Gauthier, A history of scanning electron microscopy developments: towards “wet-STEM” imaging. *Micron*, 38 (2007) 390-401.
- [27] M. Merola, A. Ruggiero, J. S. De Mattia, S. Affatato, On the tribological behavior of retrieved hip femoral heads affected by metallic debris. A comparative investigation by stylus and optical profilometer for a new roughness measurement protocol. *Measurement*, 90 (2016) 365-371.
- [28] D. Hurt, S. Li, A. Amann, Versatile SQUID susceptometer with multiple measurement modes. *IEEE Trans. Magn*, 49(7) (2013) 3541-3544.
- [29] K. L. Livesey, S. Ruta, N. R. Anderson, D. Baldomir, R. W. Chantrell, D. Serantes, Beyond the blocking model to fit nanoparticle ZFC/FC magnetisation curves. *Scientific reports*, 8(1) (2018) 1-9.

# Chapter 3

## Electrochemical synthesis of $CoFe_2O_4$ nanocomposites

### 3.1 Introduction

In this chapter, we will present the results corresponding to the electrochemical synthesis of  $CoFe_2O_4$  nanocomposites from aqueous ionic solutions. As a preliminary step, the composition of the electrolytic bath and the formation of the spinel phase of  $CoFe_2O_4$  were electrochemically optimized onto FTO coated glass substrates. Then, we will focus on the electrodeposition of  $CoFe_2O_4$  nanowires in AAO nanoporous membranes. The effects of experimental parameters such as AAO membrane pore diameter, applied potential, magnetic field and annealing temperature on the electrochemical, structural, morphological, elementary composition and magnetic properties will be discussed.

### 3.2 Synthesis and characterization of $CoFe_2O_4$ samples

Before deposition of  $CoFe_2O_4$  into AAO templates, it was necessary to verify the possibility of obtaining the spinel phase of  $CoFe_2O_4$  from an aqueous solution containing  $CoSO_4$ ,  $(NH_4)_2SO_4$ ,  $FeSO_4$ . For this reason, the choice of the FTO substrate is justified by its simplicity of manipulation and the transparency, which makes it well suited for FTIR spectroscopic analysis. In addition, the electrodeposition tasks require a very short time.

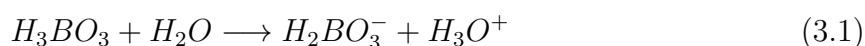
#### 3.2.1 $CoFe_2O_4$ thin films

In order to find the right optimal electrochemical synthesis protocol for  $CoFe_2O_4$ , several concentrations and pH values have been systematically tested at room temperature (25 °C). The working concentrations adopted for a 100 mL of an electrolyte are:

Table 3.1: *Electrolyte composition.*

Chemical species	Concentrations in M
$FeSO_4$	0.06
$CoSO_4$	0.04
$(NH_4)_2SO_4$	0.12
$H_3BO_3$	0.4
$H_2SO_4$	0.08

During the cathodic reaction, the evolution of hydrogen can lead to the precipitation of hydroxides (if the pH is not maintained constant at the solution-electrode interface). To avoid this harmful phenomenon for the quality of the deposit, the bath pH is adjusted to 3 by  $H_2SO_4$  and stabilized by the addition of boric acid ( $H_3BO_3$ ) which compensates for the loss of protons according to the following reaction:



According to the literature, its action is being important at about pH of 4 and is very commonly used as a buffering agent in electrodeposition baths [1].

### 3.2.1.1 Cyclic Voltammetric study

The CV is an electrochemical technique used in order to evaluate the suitable region of growth potential of metals. The CV curve of the precursor solution has been performed directly on the FTO substrate. The potential sweep was ranged from 0 to -1.4 V with a scan rate of 30 mV/s. Therefore, for simultaneous co-deposition of Co and Fe metals,

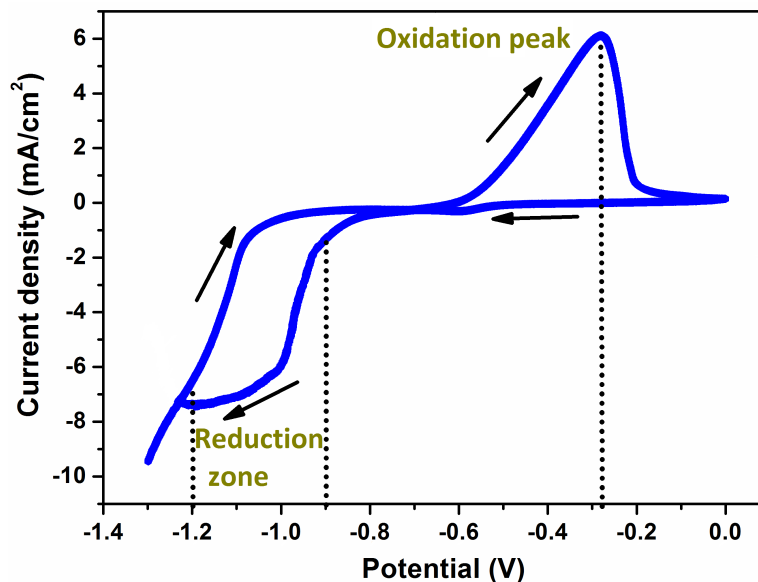


Figure 3.1:  $J$ - $V$  characteristic of FTO substrate electrode for the solution containing  $Co^{2+}$  and  $Fe^{2+}$  at 25 °C.

the deposition potential should be such that the deposition potential of individual metals comes closer to each other. Indeed, it is well known that the standard reduction potentials at room temperature for the Fe and Co metals are -0.44 V and -0.28 V, respectively

[1]. According to Fig.3.1, the oxidation peak of CoFe alloy is observed at -0.28 V. The singular peaks of  $Co^{2+}$  and  $Fe^{2+}$  reduction are masked by the reduction of water which is kinetically more favorable on aqueous bath. Moreover, the voltammogram shows an increase of the cathodic current with negative scan of the electrode potential from -0.9 to -1.2 V, which might be related to the reduction of Co and Fe ions as described by the following equations:



From -1.2 down to -1.3 V, the current density increases rapidly, indicating the occurrence of another reaction except for the reduction of ions. Indeed, in the case of an applied potential more than -1.2 V, large bubbles appeared on the FTO surface which can significantly affect the electrochemical growth of CoFe composite. As a matter of fact, in order to deposit the CoFe composite without hydrogen bubble generation, it is necessary to choose a potential value less than -1.3 V.

### 3.2.1.2 Chronoamperometry study

A CA curve was recorded at room temperature for an applied potential of -1.2 V. In order to study the nucleation and growth mechanism behavior of CoFe onto  $1\text{ cm}^2$  of FTO substrate (Fig.3.2).

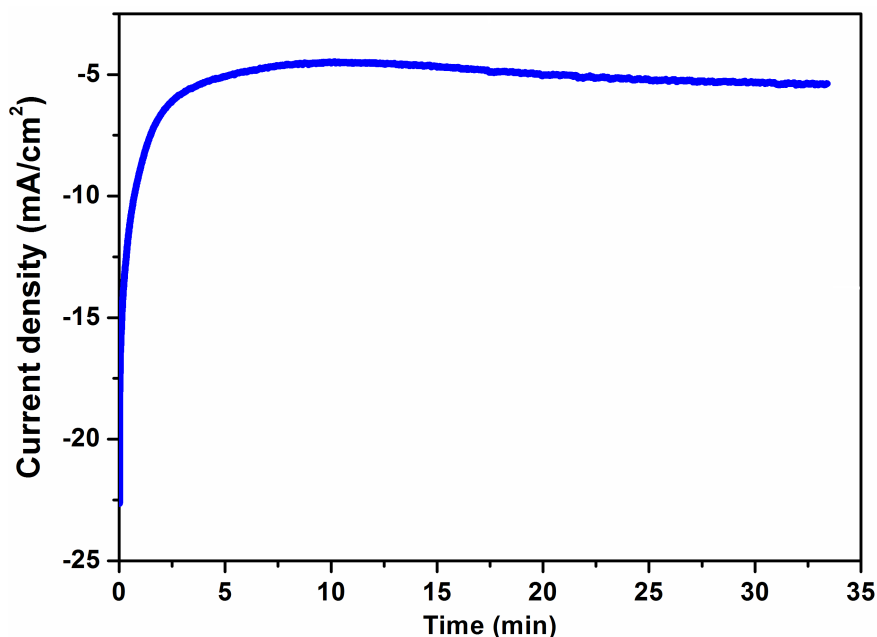


Figure 3.2: Chronoamperogram for the growth of CoFe composite on FTO substrate in an aqueous ionic solution under -1.2 V constant potential for 34 min.

It was observed at the beginning of the electrochemical growth that a non-faradaic process is involve. In the case of this phenomenon, known as double layer charging (DLC), the Co and Fe ions were arranged at the FTO surface [3]. Then, a stable faradaic current flows after 5 minutes, and a newly formed phase appears, indicating the growth and the nucleation of CoFe composite under diffusion controlled reaction. After this first deposition step, the electrodeposited sample was annealed at  $500\text{ }^{\circ}C$  in air for 24 hours.

The aim of this heat treatment was to complete the desired physical and chemical processes in order to obtain the phase-pure  $CoFe_2O_4$  spinel.

### 3.2.1.3 Structural properties of $CoFe_2O_4$ thin films

The FTIR spectrum was recorded into absorbance mode in the range  $300 - 3250\text{ cm}^{-1}$ .

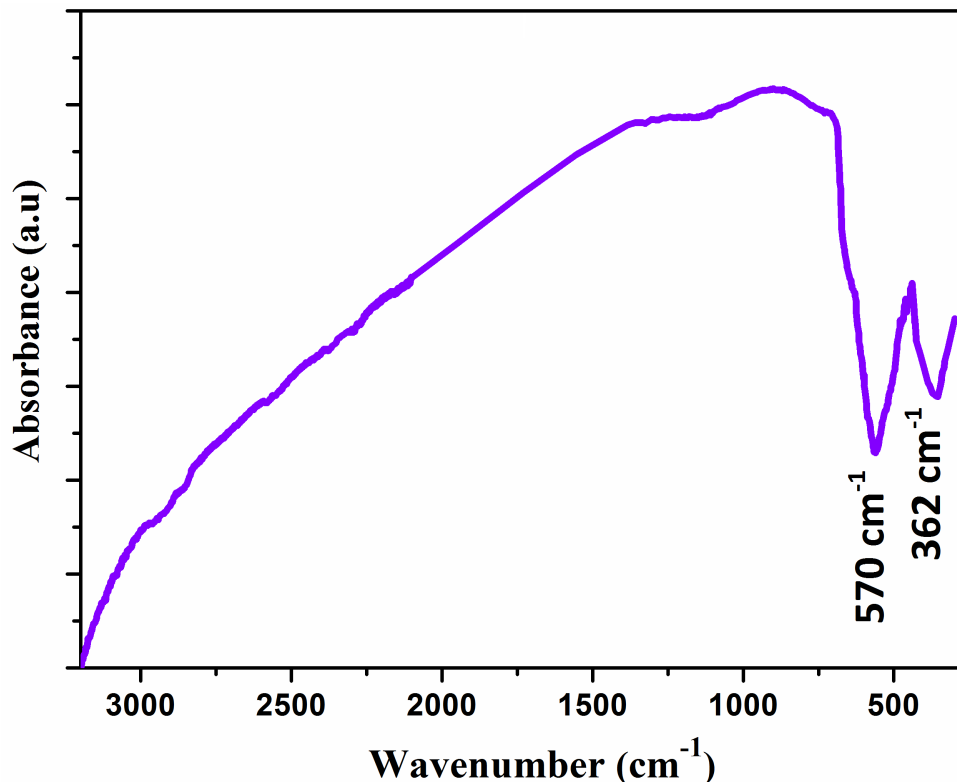


Figure 3.3: FTIR spectrum of electrodeposited  $CoFe_2O_4$  thin film.

From Fig.3.3, we notice the appearance of two characteristic absorption bands of  $CoFe_2O_4$  in the range  $350-600\text{ cm}^{-1}$ . The first band at  $362\text{ cm}^{-1}$  and the other at  $570\text{ cm}^{-1}$ . These bands are attributed to the stretching vibrations of Co–O and Fe–O in the octahedral and tetrahedral sites. This confirms the presence of the spinel phase in the elaborated thin film [4].

The X-ray diffraction (XRD) patterns of the thin films synthesized by electrodeposition technique onto FTO substrates before and after annealing treatment are displayed in Fig.3.4. As shown in the XRD spectrum of the as-prepared film, the first electrochemical deposition step leads to the growth of CoFe composite (*JCPDS*  $n^\circ$ . 10717173). Moreover, the spectrum for the sample annealed at  $500\text{ }^\circ\text{C}$  during 24 hours revealed the complete formation of the cubic spinel phase (*JCPDS*  $n^\circ$ . 22 – 1086), with higher intensity along (311) plane compared with the others peaks. The calculated value of the lattice constant parameter for the  $CoFe_2O_4$  film ( $a = 8.37\text{ \AA}$ ) is in good agreement with the standard lattice constant value reported in the literature [5].

Once the electrodeposition conditions of  $CoFe_2O_4$  crystallites growth are optimized on FTO substrates, we have decided to orient towards the growth of  $CoFe_2O_4$  nanowires into AAO membranes.



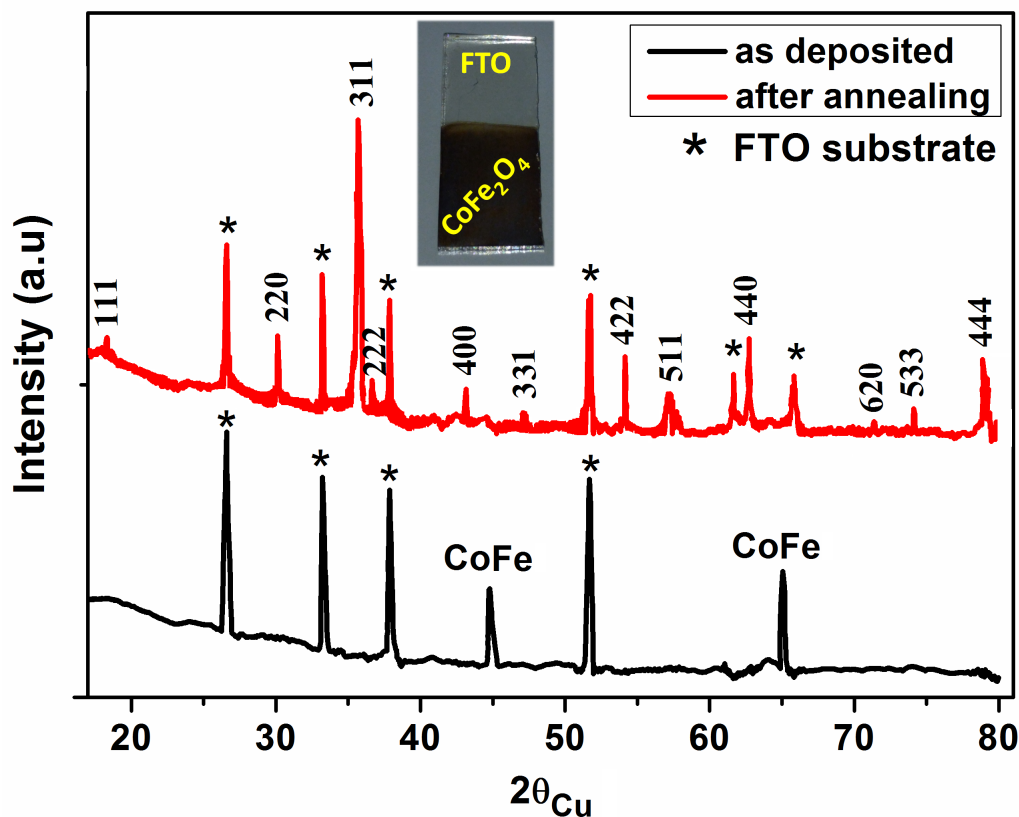


Figure 3.4: XRD patterns of electrodeposited-annealed  $CoFe_2O_4$  thin films.

### 3.2.2 $CoFe_2O_4$ nanowires

The growth of  $CoFe_2O_4$  nanowires was performed using metallized AAO membranes with a copper layer of  $3\ \mu m$ , deposited on one side of the template (Fig.3.5). This layer is used as working electrode required for the electrodeposition process. During the electrochemical deposition, the same electrolytic bath and electrochemical conditions used for the growth of  $CoFe_2O_4$  film have been preserved.

#### 3.2.2.1 Effects of the pore diameter of the AAO membrane

##### Chronoamperometry study

The chronoamperogram analysis provides various informations of the nucleation and growth mechanisms. Especially, the synthesis duration and the critical overflow time of the deposit from the pores. Fig.3.6 shows the chronoamperograms resulting from the synthesis of CoFe composite into AAO membranes of different nominal diameters (20 nm, 100 nm, 200 nm). The synthesis conditions are the same for every sample, i.e. an applied potential of  $-1.2\ V$  and an identical surface growth with  $1\ cm$  in diameter.

As shown in Fig.3.6, in the early stages of the electrochemical growth, the establishment of the diffusion layer contributes to the decrease of the current density. Once the diffusion layer is occurred, the growth of the wires takes place inside the porous AAO membrane. The current density is quasi-static during the pore filling (zone 1), after the pores become completely filled (zone 2). In addition, hemispherical overflow caps are starting to be formed (zone 3) on the outer face of the AAO membrane, which increases deposition area and thus, the current density. Finally, in the last phase (zone 4), the current density

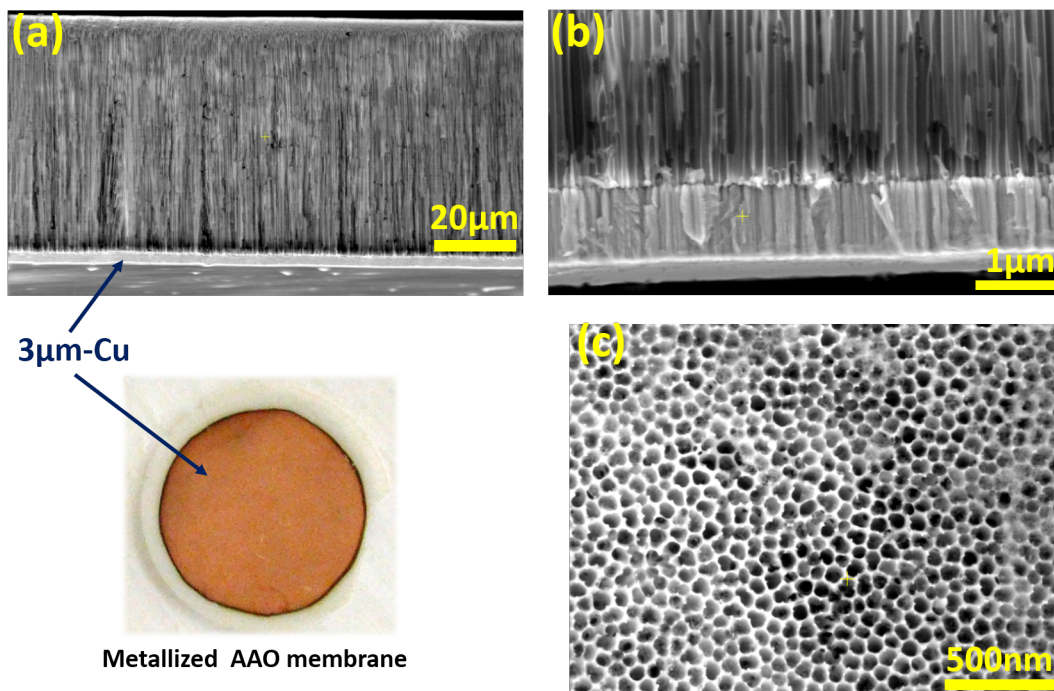


Figure 3.5: SEM images of AAO membrane; cross sectional view (a,b) and plan view (c).

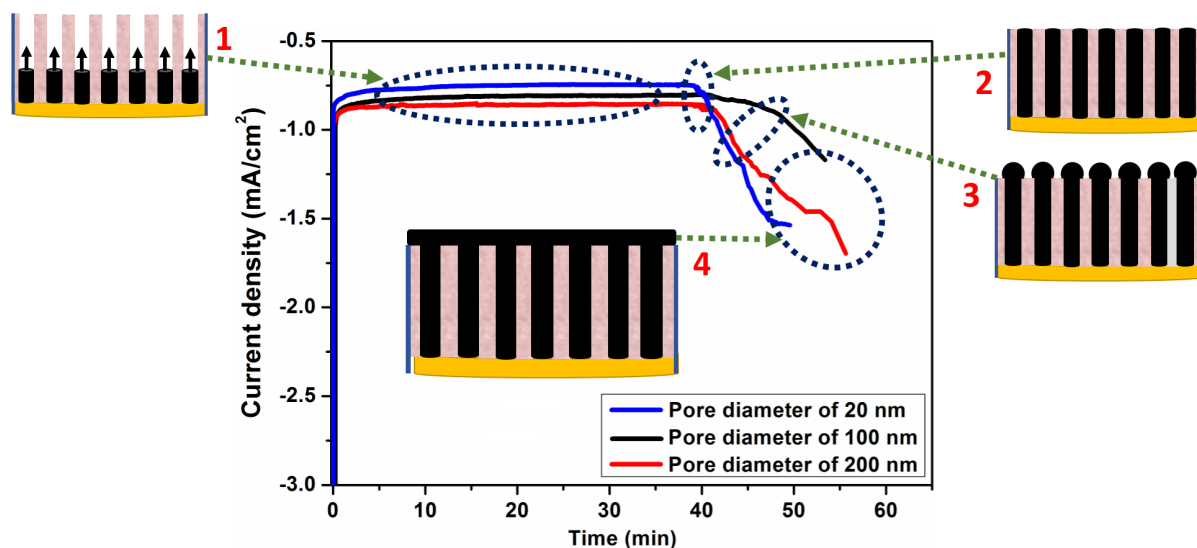


Figure 3.6: Chronoamperograms of  $\text{CoFe}$  composite growth into AAO membranes at room temperature.

continues to rise when the entire upper surface of the membrane is covered and a thin film is growing. Similar behaviors have been reported by Riveros et al. [6].

Moreover, we noticed that the current density of the electrochemical reduction of  $\text{Co}$  and  $\text{Fe}$  ions during the phase 1 is more important as the pore diameter increases. Indeed a very close current density values of  $-0.74 \text{ mA}$ ,  $-0.80 \text{ mA}$ , and  $-0.85 \text{ mA}$  for AAO membranes with 20, 100, and 200 nm in diameter pore, respectively, were observed. This small difference in the resulting current density is explained by the difference in the electrochemically active surface of the working electrode, which can be related to the geometry defects of

the wires after the copper deposition. Moreover, we can see that the synthesis time that is required to fill the AAO membrane pores is almost the same, i.e. around 40 min.

### Structural and morphological properties

Fig.3.7 shows the X-ray diffractograms of the samples electrodeposited at -1.2 V into various nanoporous AAO membranes and annealed at 500 °C for 24 hours.

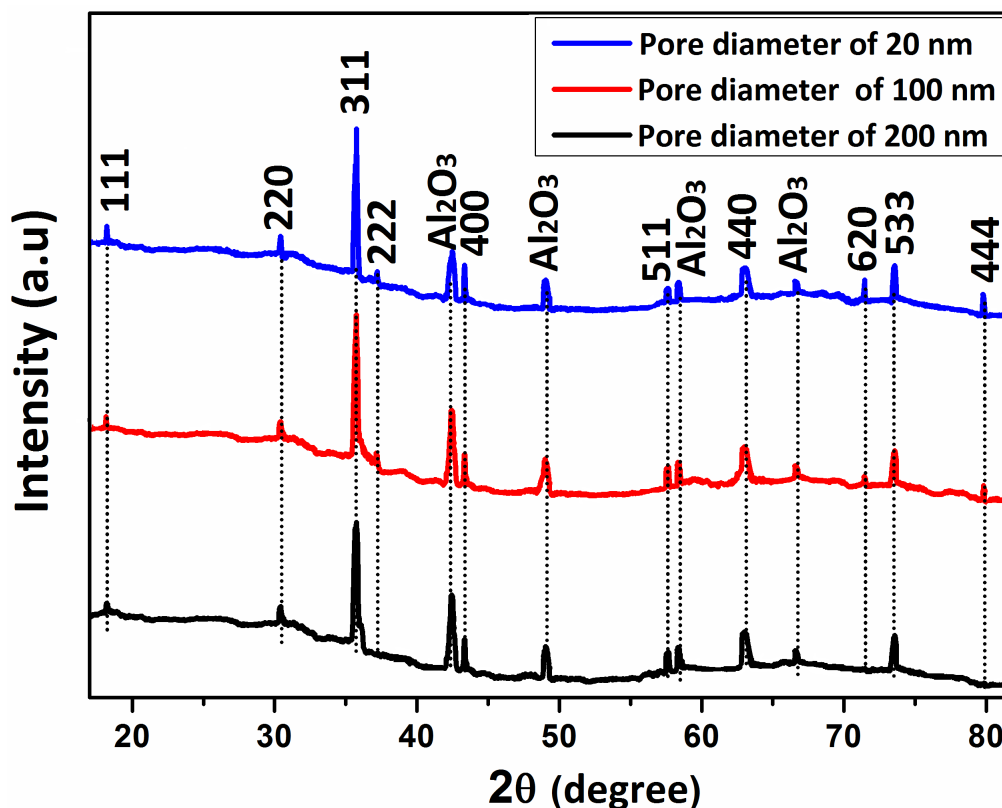


Figure 3.7: XRD patterns of the synthesized  $CoFe_2O_4$  nanowires in different nanoporous AAO membranes.

The formation of the spinel phase of  $CoFe_2O_4$  on the AAO membranes was confirmed by the appearance of these characteristic peaks in the XRD patterns (JCPDS  $n^\circ$ . 22–1086). The spectra obtained for the  $CoFe_2O_4$  nanowires indicate that the samples are well crystallized and polycrystalline. Moreover, the analyses show the birth of three other peaks located at  $2\theta = 37.11^\circ$ ,  $2\theta = 71.5^\circ$  and  $2\theta = 79.8^\circ$  which are assigned respectively to the plans (222), (620) and (444). In addition, XRD spectra revealed the presence of a strong diffraction intensity of the plane (311) for all samples, indicating the presence of a partial orientation along this reflection. The AAO membrane peaks were designated by  $Al_2O_3$ . The crystallographic lattice parameter  $a$  of the spinel phase of  $CoFe_2O_4$  crystallized in face-centred cubic (fcc), was estimated and averaged for the three intense peaks (311), (400) and (533) in all XRD spectra using Eq.2.18. The calculated values are 8.378 Å, 8.382 Å and 8.386 Å for the  $CoFe_2O_4$  nanowires prepared in AAO membranes of 200, 100 and 20 nm in pore diameter, respectively. The calculated value for  $a$  is in good agreement with the standard lattice constant value reported in the literature [7].

The significance of the full width at the half maximum (FWHM)  $\beta_{hkl}$  of the peaks evidences crystallite refinement with a large strain inside the  $CoFe_2O_4$  crystal. The in-

strumental broadening corresponding to each X-ray diffraction peak of the  $CoFe_2O_4$  was corrected by annealing the sample at  $850\text{ }^\circ C$  for 24 hours as detailed in Chapter 2, Section 2. This protocol has been adopted for all the synthesized samples in this work. Fig.3.8 shows the XRD spectrum of the annealed nanowired composite of 20 nm in the pore diameter at  $850\text{ }^\circ C$ .

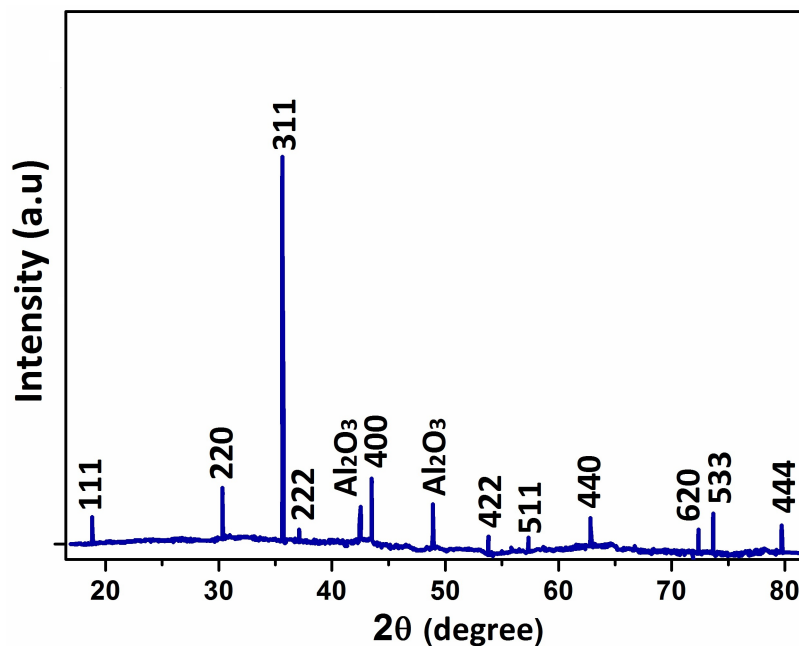


Figure 3.8: XRD spectrum of the annealed sample at  $850\text{ }^\circ C$  for 24 hours.

It can be noticed that the peaks become very fine which indicates the formation of large crystallites inside the AAO membrane pores. The crystallite size of  $CoFe_2O_4$  nanowires was evaluated from the XRD line broadening using the Williamson-Hall method. The result shows that  $CoFe_2O_4$  nanowires grown into AAO membranes of 200 and 100 nm in pore diameter have approximately 40.25 and 32.21 nm in crystallite size, respectively. However, the sample grown into AAO membrane of 20 nm in pore diameter has 14.05 nm in crystallite size.

Moreover, the morphology of the nanowires embedded electrochemically at  $-1.2\text{ V}$  into AAO membranes with different pore sizes has been studied using SEM microscopy. To do this, all membranes are firstly immersed for a duration of 30 s in a diluted iron perchloride solution for removing the copper serving as cathode. Next, the samples are then dissolved in 1 M of sodium hydroxide (NaOH) for 40 min in order to remove the alumina from the elaborated nanocomposites. This protocol is illustrated in Fig.3.9.

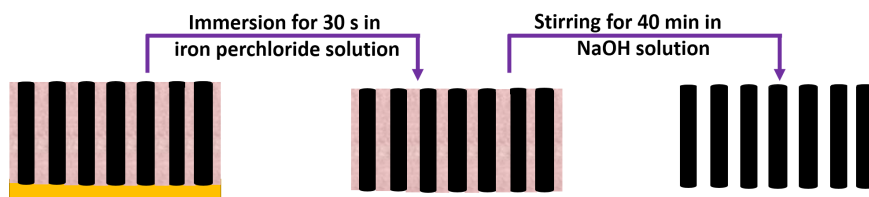


Figure 3.9: Steps of samples preparation for SEM analysis.

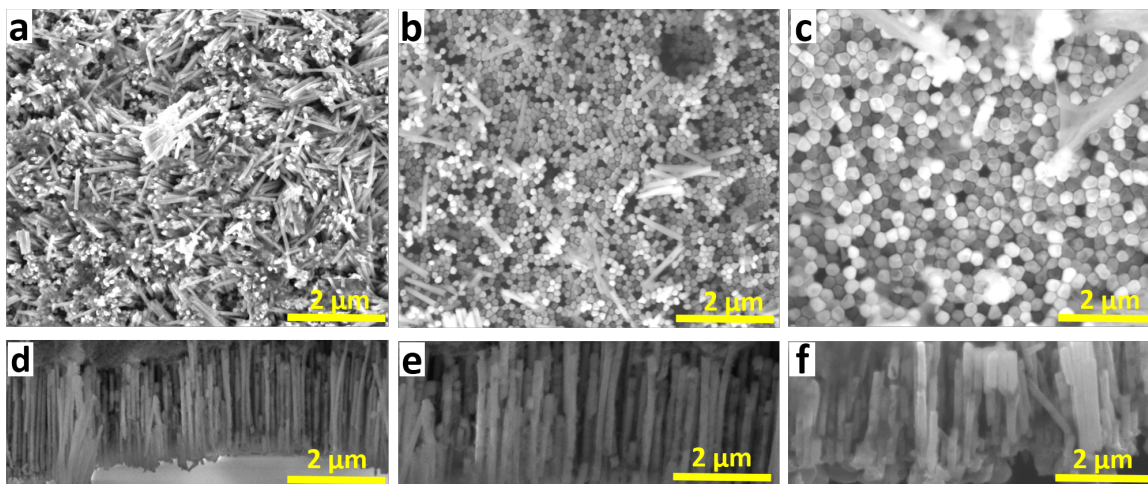


Figure 3.10: SEM images of  $CoFe_2O_4$  nanowires electrodeposited into various nanoporous AAO membranes; top and cross sectional views for 20 nm (a, d), 100 nm (b, e), and 200 nm (c, f).

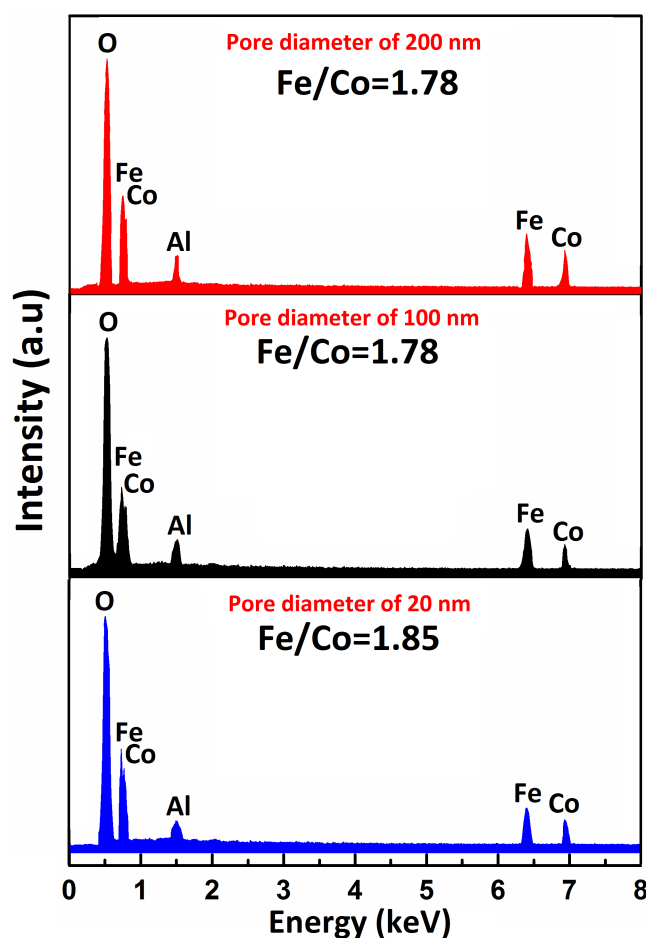


Figure 3.11: EDS spectra of  $CoFe_2O_4$  nanowires after the dissolution in 0.1 M NaOH.

As shown in Fig.3.10.a, b and c, the top view images revealed that the electrodeposited  $CoFe_2O_4$  nanowires are completely filled and have average diameters of 200, 100 and 20 nm, respectively. These values are approximately equal to the pore diameters of the AAO



templates. The cross-sectional images of the nanowires are shown in Fig.3.10.d, e and f. They show that the nanowires are well filled and oriented after the dissolution process.

On the other hand, the chemical composition was examined in various zones of the samples in order to study the effect of the pore diameter variation on the stoichiometry of the electrodeposited nanowires (Fig.3.11). The EDS spectra indicate the existence of peaks corresponding to Co, Fe and O. The Al peaks originate from the residues of the alumina membranes. In addition, no copper peak is detected, confirming that 30 s of sample immersion in the iron perchloride solution is sufficient to completely remove the copper film. Indeed, the purity of the synthesized samples could be confirmed by the absence of any impurities in the EDS spectra. From Fig.3.11, it can be concluded that the average atomic ratios of O, Co and Fe vary as the pore diameter decreasing from 200 to 20 nm. This enhancement could be justified by the fact that the decreasing pore diameter promotes the formation of a pure  $CoFe_2O_4$  spinel phase. As a result, the nanowires deposited in AAO membranes of 20 nm in pore diameter possess a high stoichiometry of Co and Fe elements.

### Magnetic properties

The magnetic properties of the developed nanowires were measured using a SQUID magnetometer. The electrochemical synthesis was interrupted before the deposition overflow from the pores of AAO membranes to avoid any kind of thin layer on the surface of the nanowires. During the measurement, the magnetic field was systematically applied parallel to the nanowires, as shown in Fig.3.12.

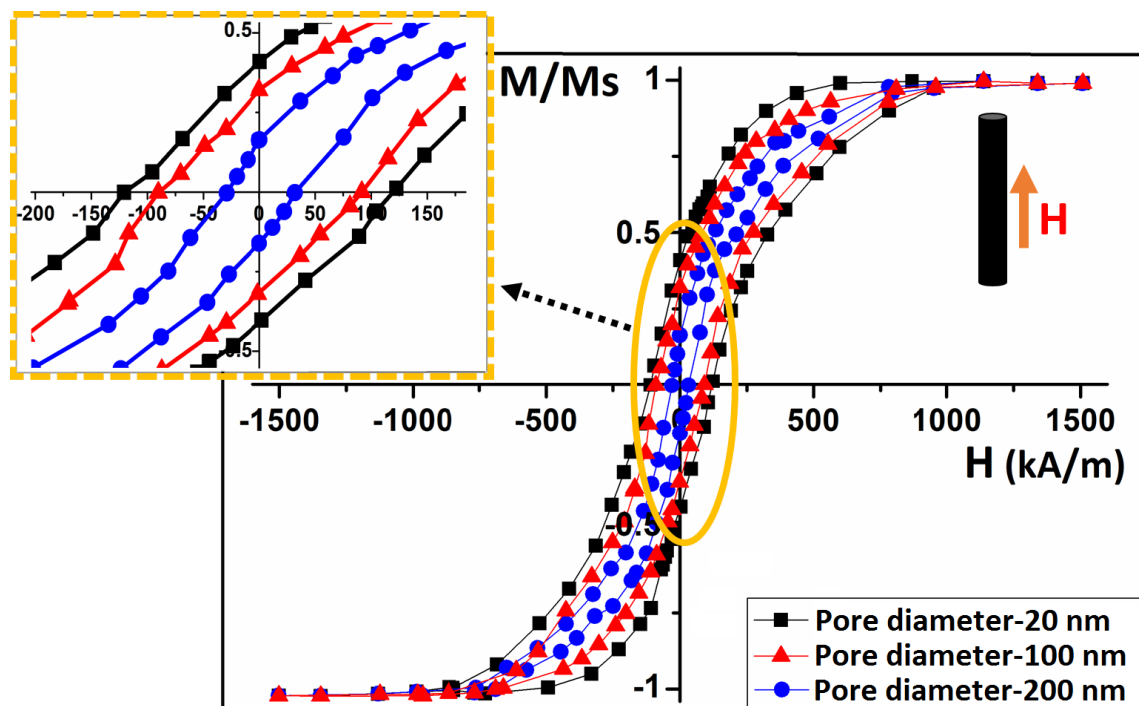


Figure 3.12: *Hysteresis loops performed at 300 K for  $CoFe_2O_4$  nanowires with different diameters.*

Fig.3.12 shows the hysteresis loops measured at 300 K for  $CoFe_2O_4$  nanowires with different pore diameters of AAO membranes (200, 100, and 20 nm). The hysteresis loops have

been normalized to the saturation magnetization for each sample. This saturation magnetization was determined using Eq.3.4, which allows to convert the measured saturation magnetization in *emu* to the saturation magnetization in Tesla (*T*);

$$M_s (T) = \frac{4\pi 10^{-4}}{V_{sample}} \times M_s(emu) \quad (3.4)$$

where  $V_{sample} = (width \times length \times height) \text{ cm}^3$  is the volume of the measured sample. Table.3.2 summarizes the estimated magnetic parameters characterizing the  $CoFe_2O_4$  nanowire arrays. The measurements reveal that the nanowires array is ferrimagnetic.

Table 3.2: *Squareness ratios and coercive fields for  $CoFe_2O_4$  nanowires.*

	200 nm	100 nm	20 nm
$M_r/M_s$	0.16	0.32	0.4
$H_c$ (kA/m)	32	96	110

Moreover, it is noted that the squareness ratio ( $M_r/M_s$ ) and the coercive field ( $H_c$ ) increase as the diameter of the nanowires decreases (pore diameter) from 200 to 20 nm. This enhancement is generally attributed to the transition from a dominated mode with magnetic domains in large diameter nanowires (200 nm) towards a monodomain mode in small diameter nanowires. The critical diameter ( $D_c$ ) that produced the mono-domain structure of  $CoFe_2O_4$  is estimated using Eq.1.12 by exploiting these characteristics reported in chapter 2 and the calculated saturation magnetization. The estimated value of ( $D_c$ ) is about 14.47 nm, which is comparable to the average diameter (14.05 nm) of the synthesized  $CoFe_2O_4$  crystallite. So the grown  $CoFe_2O_4$  crystallites into the pores of 20-nm-diameter exhibit a monodomain behavior. This result indicates the dominance of the shape anisotropy for the nanowires inside the pores of 20-nm-diameter. Furthermore, the EDS measurements (Fig.3.11) emphasized that the chemical stoichiometry of the spinel structure is better for the nanowires of 20 nm. In this case, the reduction of the crystallite size confirmed by the XRD analyses can be considered as an additional reason to explain the modification of the magnetic properties. The obtained results are in good agreement with previous literature reports [8-10]. Therefore, for the rest of the manuscript, we have decided to work with the membrane in 20 nm of pore diameter due to the best magnetic response.

### 3.2.2.2 Effects of the applied potential

#### Chronoamperometry study

Fig.3.13 shows the CA curves obtained during the deposition of the CoFe composite into AAO membranes of 20 nm in the pore diameter, at different applied potentials. From the recorded CA curves, it was observed at the early stages of the electrochemical reduction that a non-faradaic process is involved resulting from the DLC in which Co and Fe ions migrate to the bottom of the AAO membrane pores [11]. Then, a new phase of stable current, reflecting the growth of CoFe in the nanopores, appears. Moreover, the current density was clearly increased negatively with the rising of the applied deposition potential, which justifies the difference and the delay in the starting increase of the current density for the potentials -1.1 and -1 V. In addition, the CA results indicate that the pore filling time tends towards 55 and 70 min for the applied potentials -1.1 and -1 V, respectively.

On the other hand, a duration of 40 min is sufficient for a total pore filling in the case of -1.2 V, which corroborates the enhanced nucleation efficiency of the CoFe composite. The observations of the pore-filling time drop is in accordance with Faraday's law (Eq.2.14), which suggests that the bigger reduction current of ions gives the smaller pore filling time. In this context, a good reproducibility is achieved in the different electrodeposition experiments.

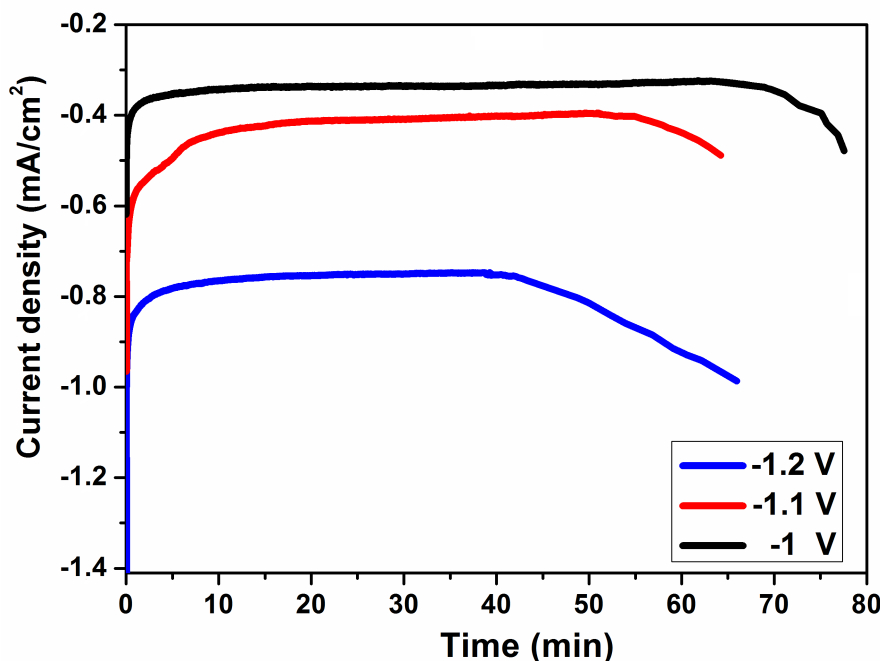


Figure 3.13: CA curves of electrochemical reduction of CoFe composite into 20 nm-AAO membranes at different applied potentials of -1 V, -1.1 V and -1.2 V.

After this first deposition step, all the electrodeposited samples were annealed at 500 °C in air for 24 hours in order to promote the formation of the  $CoFe_2O_4$  spinel phase and also to keep the AAO membrane more thermally stable.

### Structural and morphological properties

The crystalline structure of the nanowires electrodeposited into 20nm-membranes at various potentials was explored by XRD as shown in Fig.3.14. The XRD spectra suggest that all the prepared nanowires possess a spinel phase, confirming the formation of  $CoFe_2O_4$  into the AAO membranes according to the JCPDS standard data ( $n^\circ$ . 22–1086). The XRD patterns revealed that all the nanowires exhibited a partial orientation along the reflection (311). However, we can note the appearance of a new peak of  $CoFe_2O_4$  at  $2\theta = 79.8^\circ$  for the sample deposited at -1.1 V. Furthermore, for the sample electrodeposited at -1.2 V, the XRD spectra emphasized the birth of two new peaks, (620) at  $2\theta = 71.62^\circ$  and (444) at  $2\theta = 37.36^\circ$ , corresponding to spinel  $CoFe_2O_4$  phase. The cell parameters were determined by a refinement procedure for the reflections (311), (400) and (533). As a consequence, the lattice parameter was found to be 8.32 Å, 8.33 Å and 8.35 Å for the nanowires electrodeposited at -1, -1.1 and -1.2 V, respectively. Indeed, the obtained values are in good agreement with that corresponding to  $CoFe_2O_4$  single-crystal ( $a = 8.394$  Å). The average crystallite size (D) for each  $CoFe_2O_4$  samples



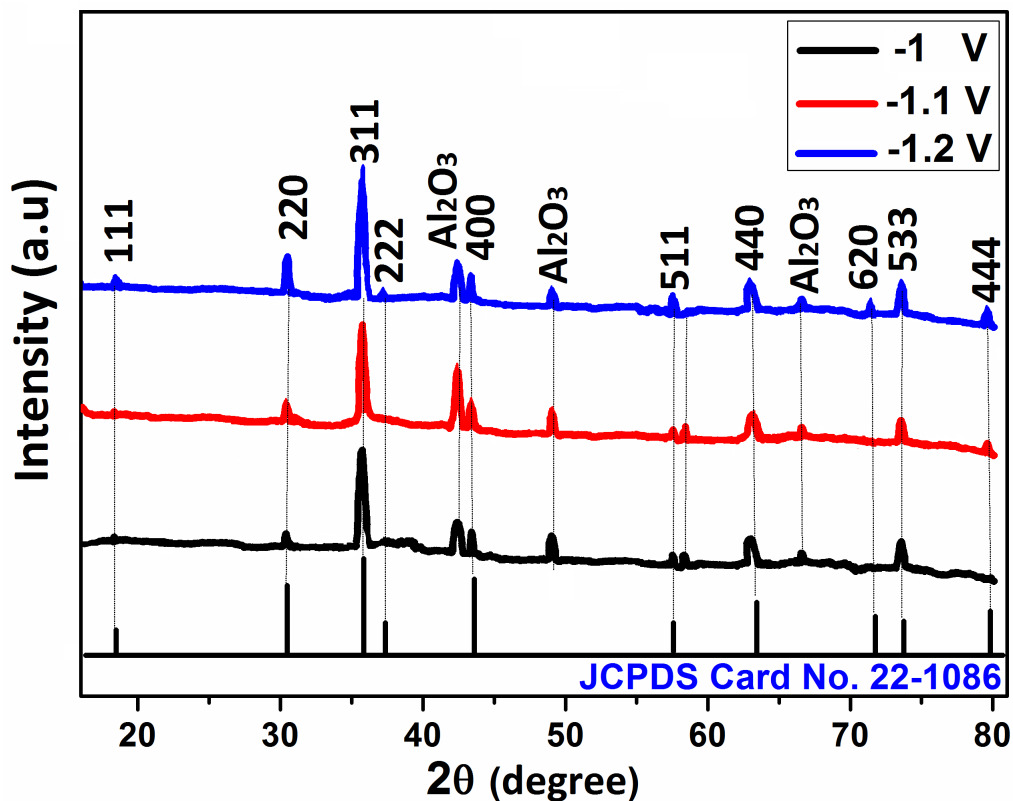


Figure 3.14: XRD patterns of the annealed  $CoFe_2O_4$  nanowires electrodeposited at various applied potentials.

Table 3.3: Calculated cell parameters and crystallite sizes.

Applied potential (V)	Cell parameter ( $\text{\AA}$ )	Crystallite size (nm)
-1	8.32	15.17
-1.1	8.33	14.76
-1.2	8.35	14.04

is also calculated from XRD data using the Williamson-Hall method. The calculations revealed that the crystallite size of  $CoFe_2O_4$  depends on the applied potential. In fact, the average crystallite size decreases from 15.17 to 14.04 nm for the applied potentials of -1 and -1.2 V, respectively. Moreover, the XRD results show globally that the degree of crystallinity is improved as the applied potential becomes more negative. The evolution of lattice parameter and crystallite size is explained by the fact that agglomerations of crystallites become smaller by varying the applied potential from -1 to -1.2 V. Within this context, similar results are reported recently by Franco et al. [12].

Fig.3.15 shows the SEM images that evaluated the effect of the potential variation on the morphology and the ratio of pore-filling. The electrodeposition time was interrupted at 40 min in order to evaluate the difference in the pore filling of the 20nm-AAO membranes. As shown in Fig.3.15.a, b and c, the pore-filling ratio strongly depends on the deposition voltage. Fig.3.15.c reveals that a total and uniform pore-filling with  $CoFe_2O_4$  crystallites is reached at -1.2 V for 40 min, unlike the samples deposited at -1 and -1.1 V, contain unfilled pores as observed in Fig.3.15.a and b. In this case, the samples need more

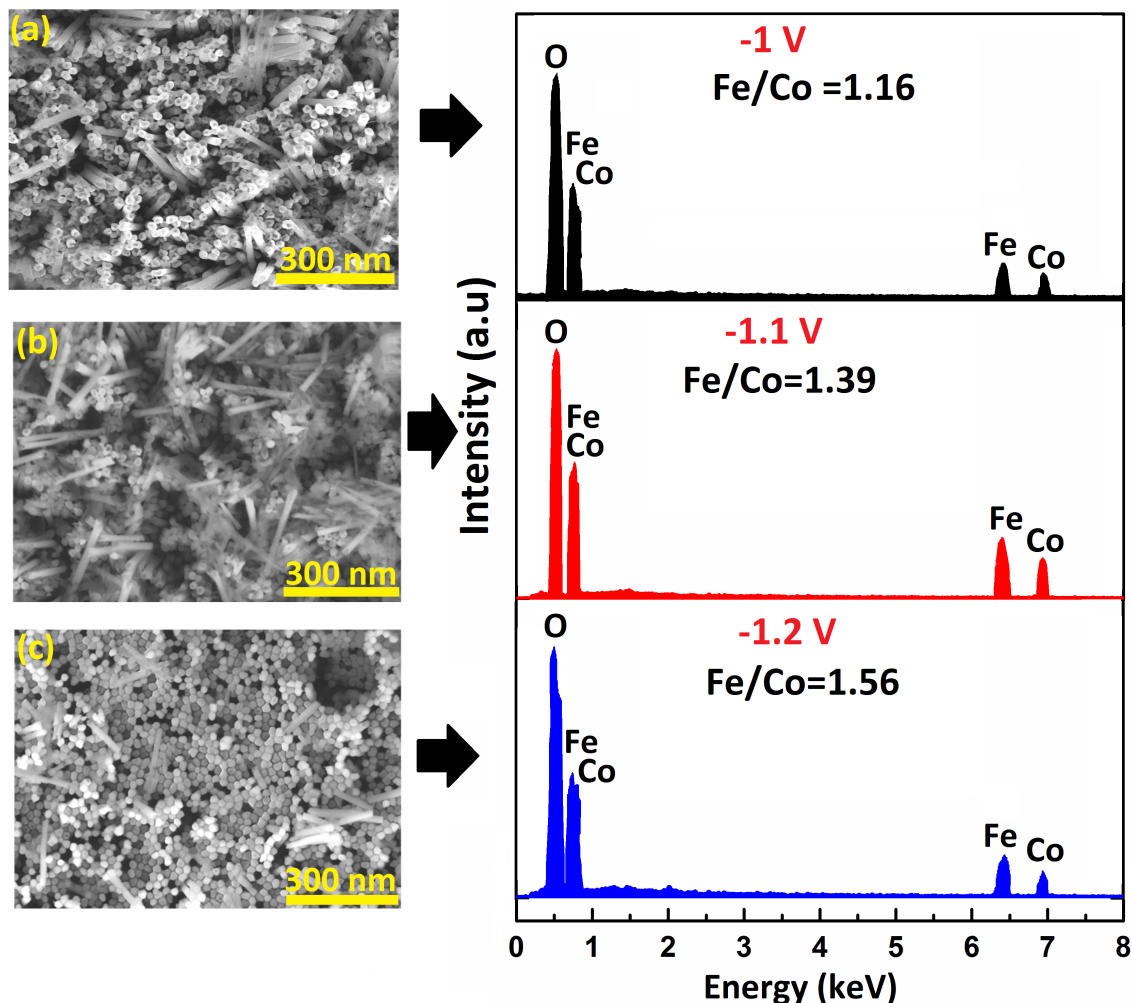


Figure 3.15: SEM images and corresponding EDS spectra of  $CoFe_2O_4$  nanowires electrodeposited at various potentials: (a)  $-1V$ , b)  $-1.1V$ , and c)  $-1.2V$ .

time to reach the total filling of the pores as indicated in the CA curves (Fig.3.13). This change in pore-filling ratio arises from many phenomena that have occurred during the electrochemical reduction of metal ions into the AAO membranes. However, the thickness reduction of the diffusion layer (i.e. where the ions dynamic is controlled), can drastically change the kinetics of ions diffused from the solution to the pores, thus modifying the nucleation and the growth rate. Consequently, the structure and the composition of the  $CoFe_2O_4$  nanowires showed a noticeable modification. The diameter of the elaborated nanowires is ranging from 20 to 23 nm, which is equivalent to the nominal diameter of the used AAO membranes.

In addition, the elementary composition of the synthesized nanowires investigated by the EDS analysis (Fig.3.15), confirms that no relevant impurities are detected inside the  $CoFe_2O_4$  nanowires. Moreover, the EDS analysis revealed a better stoichiometry of the  $CoFe_2O_4$  nanowires electrochemically grown at an applied potential of  $-1.2V$ . This result indicates the good arrangement of the Co, Fe cations in the tetrahedral and octahedral sites of the elementary lattice of  $CoFe_2O_4$  and confirms the good formation of the spinel phase for the  $CoFe_2O_4$  nanowires. As a matter of fact, the obtained stoichiometry degree reconfirms the birth of the new peaks observed in the XRD spectrum for a pure spinel

phase.

As shown in Fig.3.16, the AFM probing technique was used to characterize the surface topography of  $CoFe_2O_4$  nanowires elaborated by electrodeposition at various applied potentials.

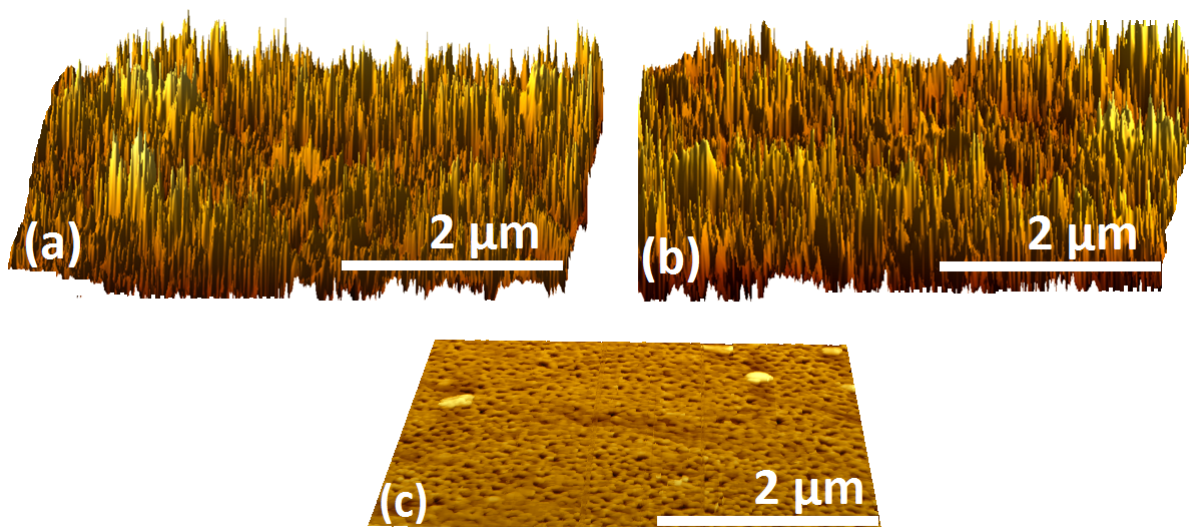


Figure 3.16: 3D AFM micrographs of electrodeposited-annealed  $CoFe_2O_4$  nanowires at -1 V (a), -1.1 V (b) and -1.2 V (c).

As a preliminary step, the 3D AFM images are recorded in tapping mode in order to determine the surface topography of the different samples. AFM images of the  $CoFe_2O_4$  nanowires deposited at -1 and -1.1 V clearly confirm the absence of total pore-filling. The surface of both samples is generally rough and contains many areas with different levels and lengths of nanowires. In addition, the surface of the nanowires deposited at -1.2 V shows a total pore filling. The surface is very homogeneous and compact, which confirms that the pores are completely filled by the  $CoFe_2O_4$  crystal. The AFM results reproduced greatly the SEM observations discussed in the previous paragraph.

### Magnetic properties

The magnetic properties of the  $CoFe_2O_4$  nanowire arrays performed at different deposition potentials have been measured at room temperature under an applied field up to 1500 kA/m. Fig.3.17 displays the variation of squareness ratio  $M/M_s$  as a function of the applied field  $H$ . Their corresponding magnetic parameters are listed in Table.3.4. We have investigated the evolution of the magnetic properties of  $CoFe_2O_4$  nanowire arrays as a function of their average chemical composition. Thus, within the elementary composition ranges between 28.39% and 16.44% of Co as shown in EDS spectra (Fig.3.15) for the applied potential varying from -1 to -1.2 V, it was found that the nanowires grown at -1.2 V exhibit a quasi-perfect stoichiometry. Table.3.4 reveals that the squareness ratio and coercive field are enhanced in both parallel and perpendicular orientations as the applied field negatively increases. Therefore, the  $CoFe_2O_4$  nanowires electrodeposited at -1.2 V exhibited high squareness ratio of 0.41 and coercivity  $H_c$  of 118 kA/m along the wire axis, in comparison to a squareness ratio of 0.36 and coercivity of 111 kA/m in the

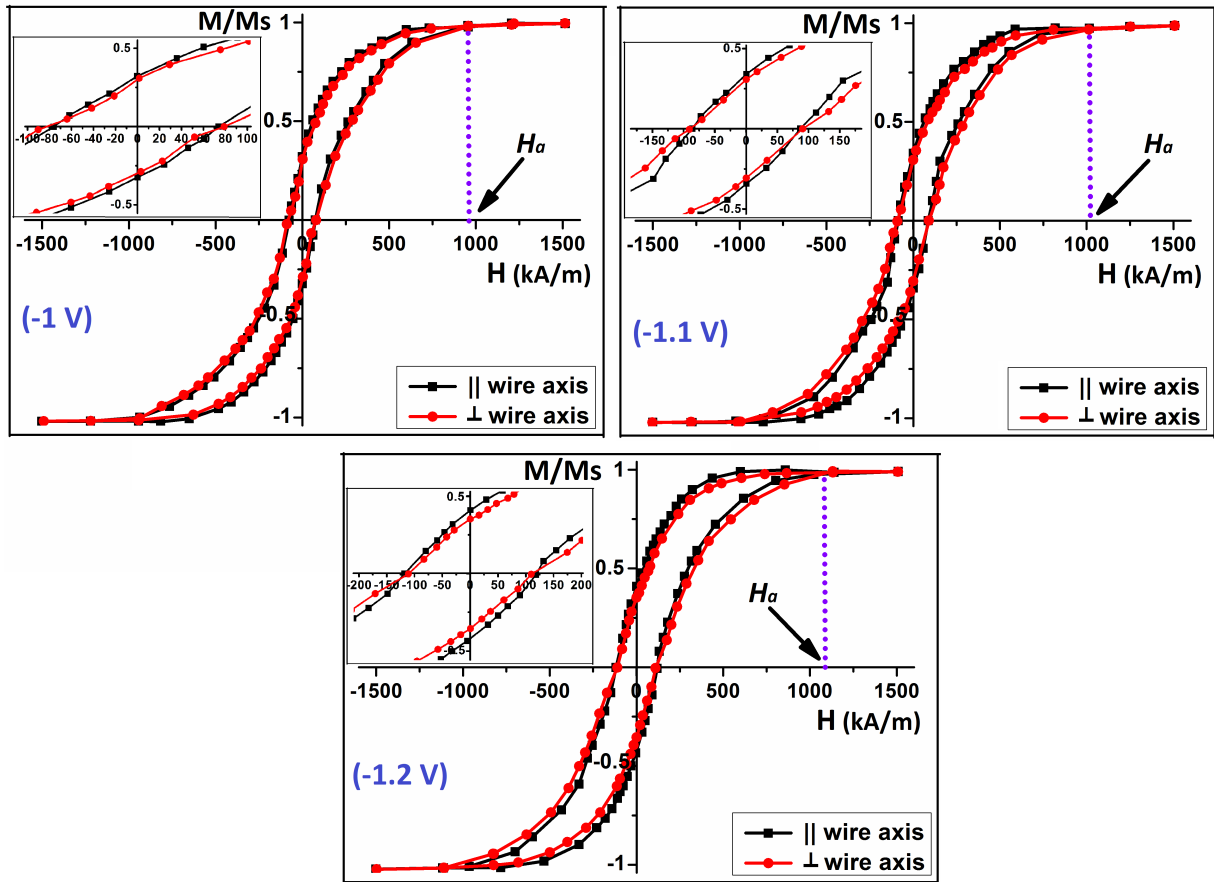


Figure 3.17: *Hysteresis loops of  $CoFe_2O_4$  nanowire arrays grown at different deposition potentials. The  $\parallel$  and  $\perp$  signs indicate the sweeping magnetic field direction parallel and perpendicular to the substrate surface, respectively, during the SQUID-VSM measurement.*

perpendicular configuration. It is obvious that the squareness ratio and the coercivity are highly affected by the elementary composition of  $CoFe_2O_4$  into AAO membrane.

Table 3.4: *Squareness ratios and coercive fields for  $CoFe_2O_4$  nanowires.*

	-1 V	-1.1 V	-1.2 V
$M_r/M_s (\parallel)$	0.32	0.34	0.41
$H_c$ (kA/m) ( $\parallel$ )	73	86	118
$M_r/M_s (\perp)$	0.30	0.31	0.36
$H_c$ (kA/m) ( $\perp$ )	79	90	111
$\mu_o H_a$ (T)	1.12	1.25	1.4

The magnetic response of the  $CoFe_2O_4$  nanowires is closely related to the cation distribution in tetrahedral and octahedral sites of spinel phase and also the crystallographic microstructure [13]. Due to the rapid deposition of  $Fe^{2+}$  and  $Co^{2+}$  ions into the pores with the variation of the applied potentials from -1 to -1.2 V, the intrinsic defects and stress increase with the decrease of Co atoms in the nanopores. As a consequence, these factors could improve the crystallographic structure to obtain a pure spinel phase. It has been observed from the hysteresis loops that at -1.2 V, the easy axis is slightly controlled

by the shape anisotropy of  $CoFe_2O_4$  crystallites into the nanopores. Indeed, there is a significant enhancement in the coercivity parallel and perpendicular to the wire axis when the applied potential is fixed at -1.2 V. Indeed, this effect is expected due to the decrease in the crystallite size as shown in XRD analysis (i.e. transition from multidomain state to monodomain one), as well as the more reduction of  $Fe^{2+}$  and  $Co^{2+}$  metallic ions. It has been reported that the crystallites deposited at -1 and -1.1 V possess comparable sizes (15.17 nm, 14.76 nm) with the monodomain size (14.47 nm). On the other hand, the crystallite deposited at -1.2 V has a size of 14.04 nm, so the formation of the monodomain state is ensured. Within this context, similar findings have been reported by Wu et al. [14]. Moreover, the internal magnetic field ( $H_i$ ) acting inside the  $CoFe_2O_4$  nanowires, can be expressed at the remanent state by the following formula [15]:

$$H_i = H_a - NM_r \quad (3.5)$$

where  $H_a$  is the anisotropy field of  $CoFe_2O_4$  nanowires, and  $N$  represents the demagnetizing factor, which is approximatively equal to 0 in the case of an elongated magnetic cylinder polarized vertically along the  $z$  axis. The  $H_a$  value is determined experimentally by the intersection between the edges of the hysteresis loops in the two measurement directions (parallel and perpendicular) as described in Fig.3.17. Table.3.4 summarizes the values collected for  $H_a$ . As expected, the nanowires elaborated electrochemically at -1.2 V have an anisotropy field of 1.4 T. In this case, the internal magnetic field  $H_i$  of the  $CoFe_2O_4$  nanowires is proportional to the anisotropy field, and we can approximatively write  $H_i \cong H_a$ .

The results reached in this section are encouraged to maintain -1.2 V as a reduction potential for Co and Fe ions in the future electrodeposition experiments of this work.

### 3.2.2.3 Effects of applied magnetic field

#### Chronoamperometry study

To investigate the effect of the magnetic field on the electrochemical growth of Co and Fe elements within AAO membranes, chronoamperometric curves were recorded during the electrodeposition process (Fig.3.18). The CoFe nanowires were electrodeposited at room temperature in potentiostatic mode (deposition potential fixed at -1.2 V). As shown in Fig.3.18, the resulting current density of CoFe reduction into AAO membranes increases when the applied magnetic field  $B$  ranges from 0.4 to 0.6 T. As more detailed in section 2 of chapter 2, the current density enhancement is mainly explained by the fact that the migration of the electroactive species towards the bottom of the nanopores becomes faster with the magnetic field, which decreases the thickness of the DLC according to the following formula (Eq.2.11):  $\delta_D = 1.59 (\rho R \nu^{2/3} D^{1/3})^{1/3} (nFC)^{-1/3} B^{-1/3}$ . Indeed, in the case of the system with mass transport control, the limiting current density of diffusion increases with  $B$  and the species concentration gradient following the law (Eq.2.12):  $j = 0.451 R \pi^{-1} \gamma (nFD)^2 (\nu/D)^{2/3} (\nu\eta)^{-1} B \Delta C^2$ . Thus, the amount deposited increased with the magnetic field. As a result, the total filling time of the AAO membrane nanopores is reduced from 37 to 30 min as displayed in Fig.3.18, which confirms our results. During the electrochemical investigations for the deposition of CoNiMo alloys, Aaboubi et al. [16] revealed that the presence of a magnetic field affects the polarization curves and increases clearly the resulting current density of growth. Such result is obtained in our work, indicating the presence of the MHD convection responsible for improving the rate of ions transferred to the deposition surface. This phenomenon is

illustrated in Fig.3.19.

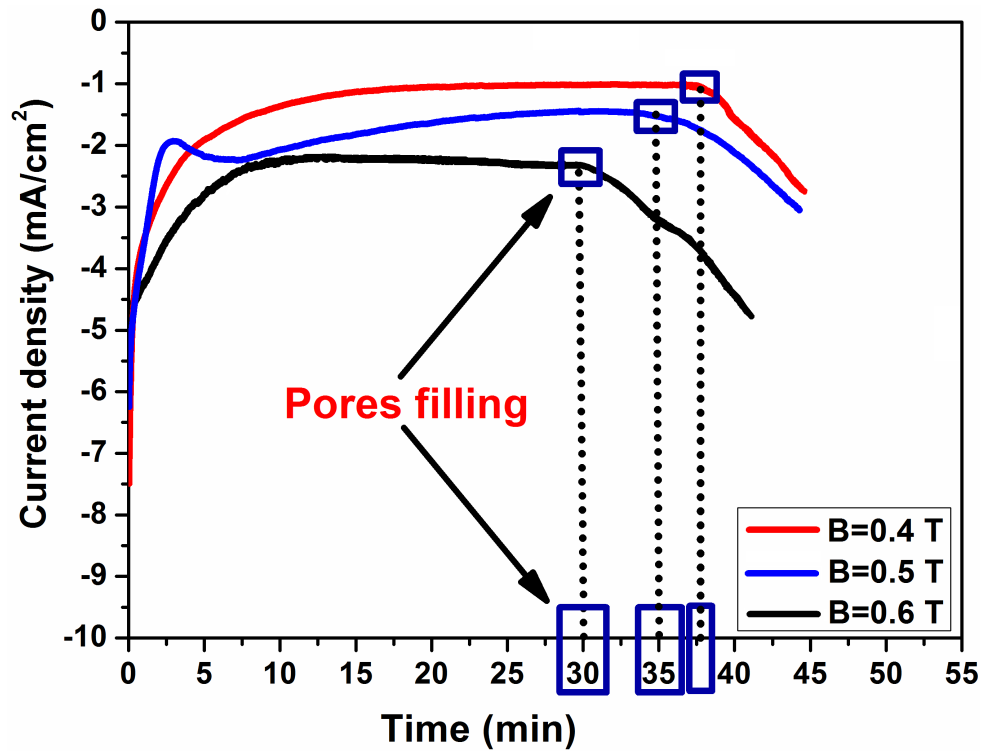


Figure 3.18: CA curves of CoFe composite reduction into AAO membrane under different applied magnetic fields.

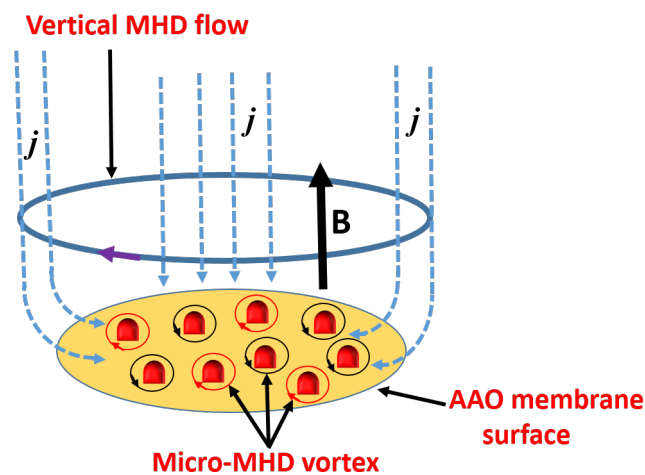


Figure 3.19: MHD effect in electrodeposition under vertical applied magnetic field  $B$ .

From the adopted scheme, two types of MHD flows are produced by the action of Lorentz force: (i) a vertical macroscopic MHD flow around the AAO membrane edges, and (ii) a micro-MHD vortices around the nonequilibrium fluctuations such as hemispherical diffusion zones around each pore.



## Structural and morphological properties

In order to determine the effect of the applied magnetic field on the  $CoFe_2O_4$  nanowires microstructure, the X-ray diffraction technique was employed. Fig.3.20 shows three diffractograms obtained for the magneto-electrodeposited nanowires at -1.2 V with  $B = 0.4$  T, 0.5 T and 0.6 T, after an annealing for 24 hours at 500 °C.

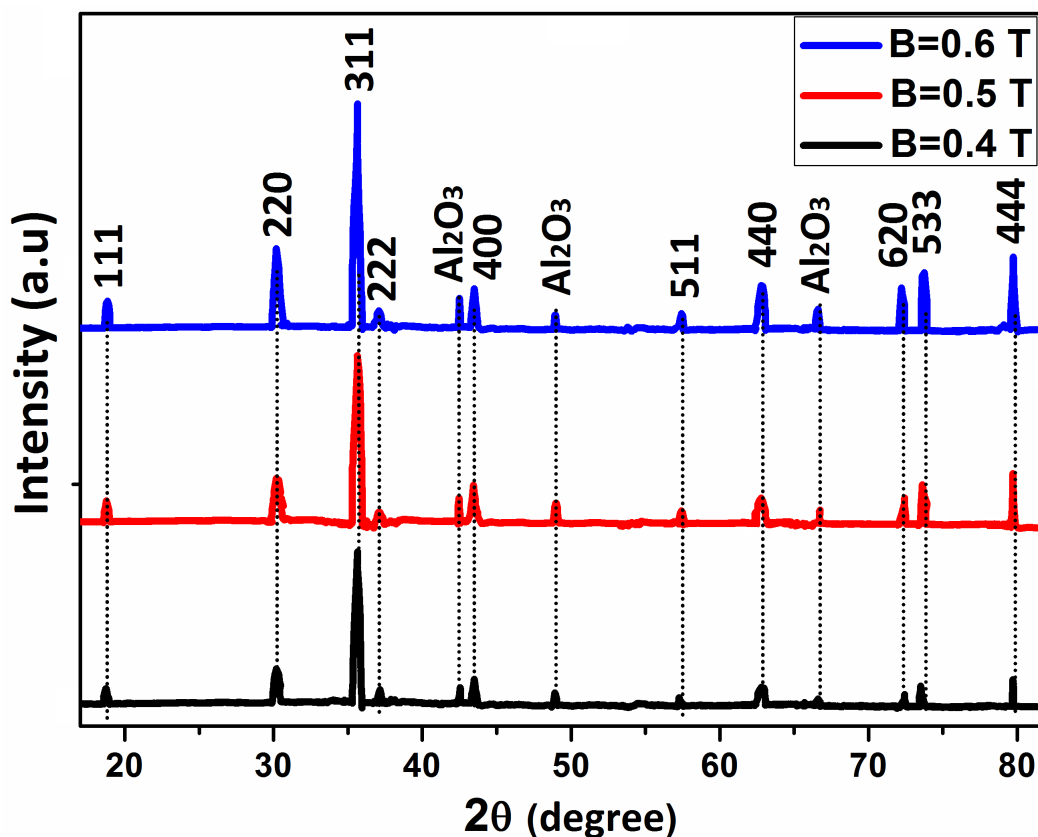


Figure 3.20: X-Ray diffraction patterns of the electrodeposited nanowires at various applied magnetic fields.

As displayed in the recorded diffractograms, the formation of the spinel phase of cobalt ferrite was confirmed by the presence of these characteristic peaks with a partial texture along the crystallographic direction (311). Moreover, the XRD spectra demonstrate that the magnetic field qualitatively increases the enlargement of some peaks. The shown result reveals that the  $CoFe_2O_4$  nanowires exhibit a higher degree of crystallinity. Quantitatively, the lattice parameter ( $a$ ) and the average crystallite size ( $D$ ) have been evaluated by exploiting the XRD data. The calculations have revealed that the magneto-electrodeposition decreases the crystallite size within the nanopores from 12.82 nm to 10.54 nm, and also shifted the lattice parameter from 8.36 Å to 8.38 Å, which approaches to the value of bulk cobalt ferrite (8.39 Å). In conclusion, the growth is strongly affected by the action of the magnetic field. This effect is attributed to the micro-MHD convection acting on the ions during the cathodic reaction. The magnetic field controls and enhances the current density (Fig.3.18), thus promoting a constant growth of the germs. This would explain the modifications of the  $CoFe_2O_4$  crystalline properties such as texture and structure [17]. The observed XRD results are in good agreement with those reported by Ganesh et al. [18].

Moreover, the morphologies of the magneto-electrodeposited  $CoFe_2O_4$  samples were examined using SEM analysis after the samples dissolution in 1 M of NaOH for 40 min. Fig.3.21 shows the nanowires deposited for various filling times (30, 35 and 37 min), corresponding to each value of the applied magnetic field as described in Fig.3.18.

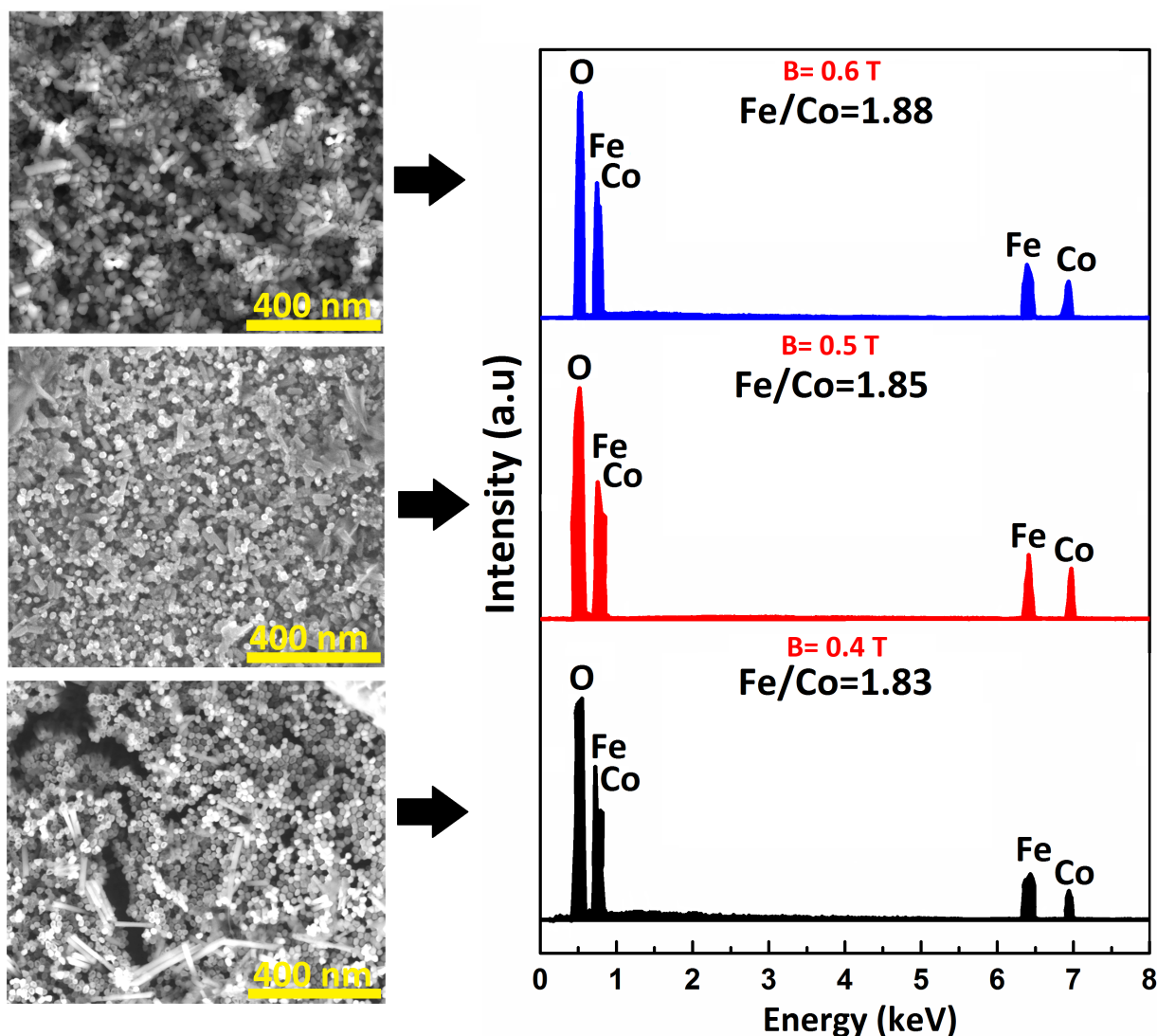


Figure 3.21: SEM images and EDX spectra of the magneto-electrodeposited  $CoFe_2O_4$  nanowires.

As observed in the top SEM images, the pores of the AAO membranes are well filled by the  $CoFe_2O_4$  nano-crystallites. The diameter of the nanowires is ranging from 20 to 22 nm, which is nearly equivalent to the nominal diameter of the used AAO membrane. The elementary composition of  $CoFe_2O_4$  nanowires was investigated by the EDX spectra (Fig.3.21). As indicated by the collected data in the tables, the nanocomposite consisted only of Fe, Co and O, which confirms its purity. Moreover, it was observed that the nanocomposite magneto-electrochemically grown at 0.6 T presents a great stoichiometry (15.15%-Co, 28.54%-Fe and 56.31%-O). In addition, this stoichiometry confirms the higher crystallinity of  $CoFe_2O_4$  and the formation of the spinel phase with regular occupation of the octahedral and tetrahedral sites by Co and Fe ions. Moreover, this result can explain the enlargement enhancement of XRD reflections shown in Fig.3.20. It is quite conceivable that for the ferromagnetic ions, the induced magnetic dipolar effects



can have significant influence on the crystallographic distribution within the spinel structure of  $CoFe_2O_4$  [19].

The AFM technique was used to investigate the surface uniformity. Fig.3.22 shows the AFM 2D surface topography of the  $CoFe_2O_4$  nanowires deposited at different applied magnetic fields. The samples present uniform and well-filled nanopores, especially for the sample deposited at 0.6 T, as shown by SEM analysis. Basically, under the effect of the increasing of the applied magnetic field on the AAO membrane, the movement of ions in the electrolyte, the mass transport speed towards the electrochemically active surface and the magnetohydrodynamic convection generated from Lorentz force (Eq.2.10) reach their maximum levels. This is reflected by a remarkable enhancement of the reduction current (Eq.2.12), which corresponding to the formation of deposit inside the AAO membrane pores.

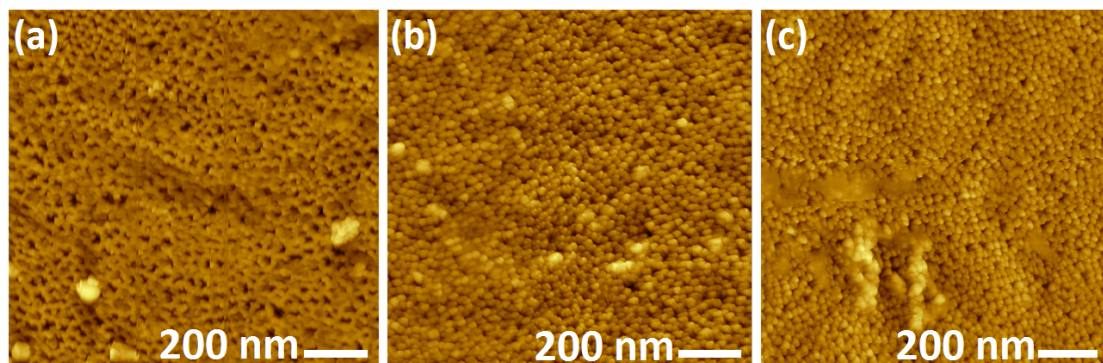


Figure 3.22: AFM 2D surface topography of the magneto-electrodeposited  $CoFe_2O_4$  nanowires; (a)  $B=0.4$  T, b)  $B=0.5$  T and (c)  $B=0.6$  T.

As a result, the surface of the deposit becomes more compact and homogeneous as the magnetic field increases Fig.3.22.a,b and c.

### Magnetic properties

The normalized M–H curves of  $CoFe_2O_4$  nanowires magneto-electrochemically grown in the AAO membranes are obtained at 300 K for an applied scanning field parallel and perpendicular to the wire axis. Fig.3.23 shows the hysteresis loops of the annealed samples, and Table.3.5 summarizes the estimated magnetic parameters characterizing the  $CoFe_2O_4$  nanowire arrays.

Table 3.5: Measured magnetic properties of  $CoFe_2O_4$  nanowires grown by magneto-electrodeposition in AAO templates.

	B=0.4 T	B=0.5 T	B=0.6 T
$M_r/M_s$ ( $\parallel$ )	0.47	0.5	0.55
$H_c$ (kA/m) ( $\parallel$ )	120	116	131
$M_r/M_s$ ( $\perp$ )	0.42	0.44	0.46
$H_c$ (kA/m) ( $\perp$ )	121	125	140
$\mu_o H_a$ (T)	1.42	1.44	1.5

The measurements reveal that the application of the magnetic field modifies the magnetic

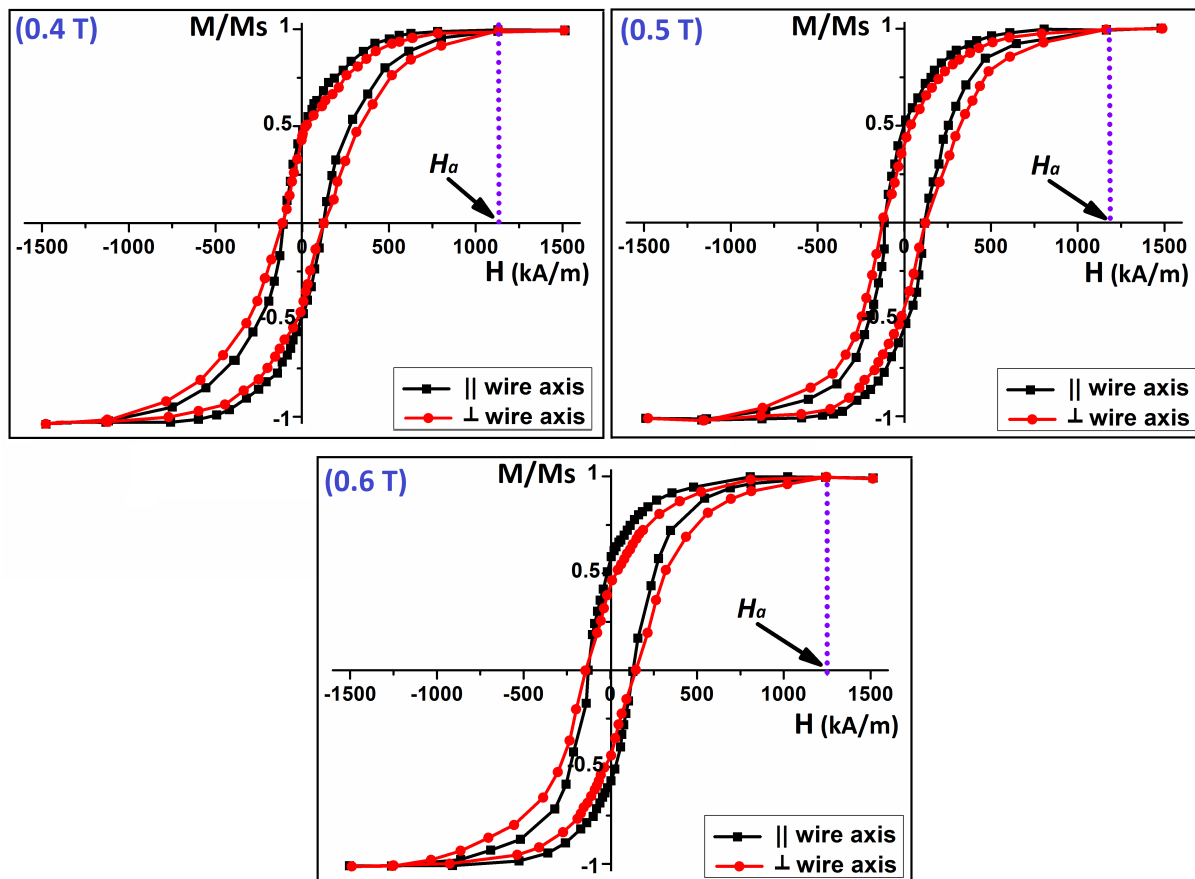


Figure 3.23: Hysteresis loops of the electrochemically deposited  $CoFe_2O_4$  nanowires at various applied magnetic fields.

properties by enhancing the squareness ratio, the coercive field, and the anisotropy field in both scanning directions (Table.3.5). They report a remarkable shifting from 0.47, 120 kA/m and 1.4 T to 0.55, 130 kA/m and 1.5 T for  $M/M_s$ ,  $H_c$  and  $\mu_0 H_a$  of the magneto-electrodeposited nanowires at 0.4 and 0.6 T, respectively.

From an electrochemical and microstructural point of view, the observed enhancement of the magnetic response for the  $CoFe_2O_4$  nanowires can be related to the mechanism of the reduction of Fe and Co ions, and also to the process of growth during the electrodeposition. The electrodeposition growth in the magnetic field is influenced by an additional convection and the crystallite growth is favorable in the direction of the easiest magnetization. The nucleation rate is increased and small crystallites can uniformly grow since the convection near the interface provides sufficient magnetic ions to each crystallite. In this case, the reduction of the crystallite size in the presence of the magnetic field is essentially due to the increase of the nucleation rate, as confirmed by the XRD analysis, and can be considered as a key point to tailor the magnetic properties of the cobalt ferrite nanocomposites. Furthermore, the EDX measurements emphasize that the chemical composition of nanowires is enriched in cobalt as the applied magnetic field increases from 0.4 to 0.6 T, which eventually forms a highly pure spinel phase inside the nanopores.

These results could be explained by the dominance of an uniaxial magnetic anisotropy and the appearance of the single magnetic domain structure, i.e. induced by the walls displacement of the local domains formed between the clusters of crystallites, leading to a partial orientation on the magnetic moments into the AAO membranes. Moreover, its

shape anisotropy favors the alignment of the easy axis along the nanowires. Consequently, these mentioned factors enhance the internal magnetic field  $H_i$  that greatly depends on the anisotropy field  $H_a$  estimated from the measured hysteresis loops. The current results of the magnetic measurements of our samples have shown a great similarity with those previously reported [19-21].

In conclusion, we have demonstrated a significant improvement in the magnetic properties of the  $CoFe_2O_4$  nanowires by applying an external magnetic field during the growth of the nanowires in 20 nm-AAO porous templates.

### 3.2.2.4 Effects of the annealing on the magnetic properties

Fig.3.24 presents the room-temperature hysteresis curves for the magneto-electrodeposited  $CoFe_2O_4$  nanowires at 0.6 T/-1.2 V and annealed at two different temperatures.

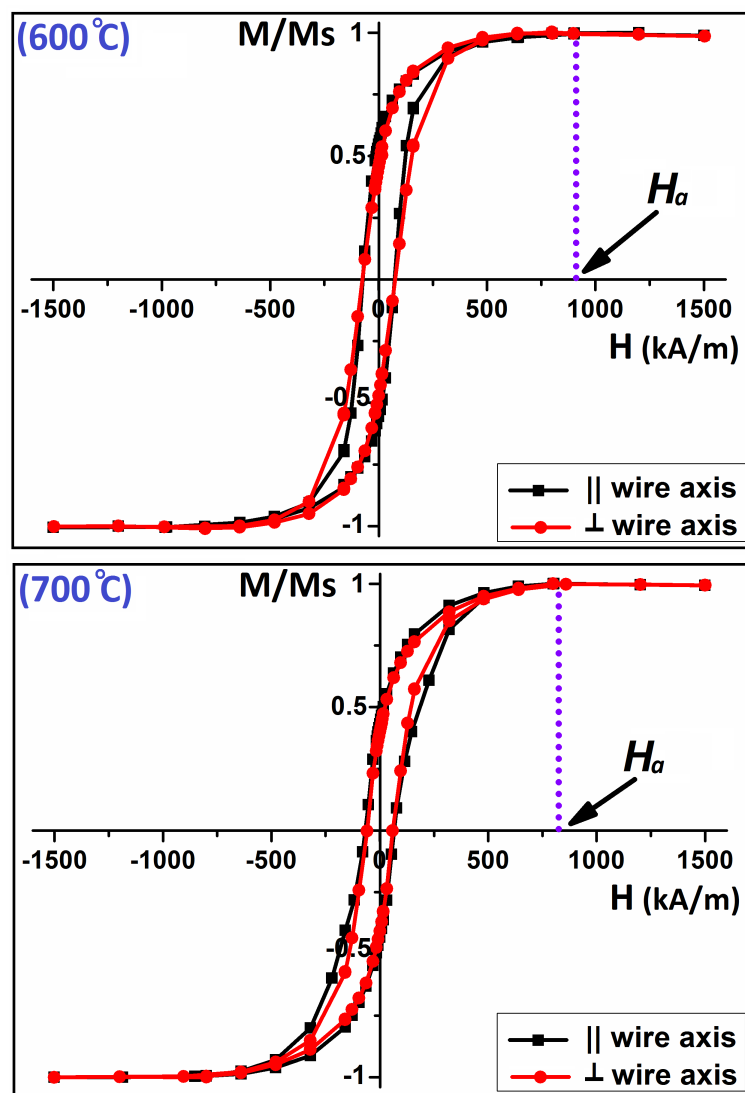


Figure 3.24: Hysteresis loops of the annealed  $CoFe_2O_4$  nanowires at 600 °C and 700 °C.

The experimental data of the hysteresis loops, i.e. squareness ratio  $M_r/M_s$ , coercive field  $H_c$  and anisotropy field  $H_a$  are displayed in Table.3.6. Accordingly, there is a significant difference in the magnetic response of the annealed nanowires. The nanowires correspond-

Table 3.6: Measured magnetic properties of the annealed  $CoFe_2O_4$  nanowires.

	600 °C	700 °C
$M_r/M_s$ (  )	0.52	0.43
$H_c$ (kA/m) (  )	73	60
$M_r/M_s$ ( $\perp$ )	0.46	0.41
$H_c$ (kA/m) ( $\perp$ )	76	61
$\mu_o H_a$ (T)	1.12	1.06

ing to the annealing temperature (600 °C) have a  $M_r/M_s$  of 0.52,  $H_c$  of 73 kA/m and 1.12 T for  $\mu_o H_a$ . On the other hand, the nanowires annealed at 700 °C possess a  $M_r/M_s$  of 0.43, 60 kA/m for  $H_c$  and 1.01 T for  $\mu_o H_a$ . In principle, the magnetic properties are highly sensitive to the crystallite size, microstructures and distributions of cations into tetrahedral and octahedral sites in the spinel structure [22]. The cations distribution is influenced by various parameters such as the ionic radius of the cation, the stabilization energy in the crystalline field, the electronic configuration, etc. In this context, the shown decrease of  $M_r/M_s$  with the increase of the annealing temperature can be attributed to the cations redistribution where  $Co^{2+}$  ions migrate from tetrahedral to octahedral sites and  $Fe^{3+}$  cations migrate from octahedral to tetrahedral sites with the increase of temperature from 600 °C to 700 °C. These phenomena will be responsible for a change in the degree of inversion  $i$  (Eq.1.17) and therefore the formation of structural distortions leading to a structural disorder. This structural disorder will be accompanied by a magnetic disorder due to a non-alignment of the spins with the global magnetization direction of the crystal. Accordingly, the net magnetic moment will be affected.

The preference of the net magnetic moment of  $CoFe_2O_4$  crystallites with the spinel structure is presented as [23,24]:  $m = \sum m_{octahedral} - \sum m_{tetrahedral}$ . It should be noted that the magnetic moment of  $Fe^{3+}$  ions is greater than that of  $Co^{2+}$  ions. As a matter of fact, the redistribution of  $Fe^{3+}$  ions at octahedral sites will increase the total number of the magnetic moment which appears as the decrease of  $M_r/M_s$  in the  $CoFe_2O_4$  nanowires in parallel and perpendicular orientations.

Moreover, the reduction in coercivity and anisotropy field as the annealing temperature shifting from 600 °C to 700 °C can be associated with the increase in  $CoFe_2O_4$  crystallite size inside the AAO membrane pores and the drop in the anisotropy constant of the samples. This weakening was corroborated by the finding that the XRD peaks become very fine and have small FWHM ( $\beta_{hkl}$ ) (Fig.3.8), which indicates such shape modification of the produced nanocrystallite, i.e. the transition from single separated nanocrystallite to compact nanocrystallite granules. Our findings are in agreement with those reported by Ajroudi et al.[25]

As a conclusion, the obtained results confirm that the optimal temperature that provides the best magnetic properties for  $CoFe_2O_4$  nanocomposite is around of 500 °C. This annealing temperature will be kept in the next examinations.

### 3.2.2.5 Magnetic field cooling effects

In this study, a lower rate cooling under magnetic field was performed in order to investigate its effect on the structural and magnetic properties of  $CoFe_2O_4$  nanowires. Fig.3.26 shows the XRD patterns of the magneto-electrodeposited  $CoFe_2O_4$  nanowires at

-1.2 V/0.6 T and then annealed for 24 hours at 500 °C. After this first step of synthesis, the sample was cooled under uniform static magnetic field (0.6 T) by placing it on the upper side of a permanent magnet, which is the same used during the electrochemical deposition, as shown in Fig.3.25.

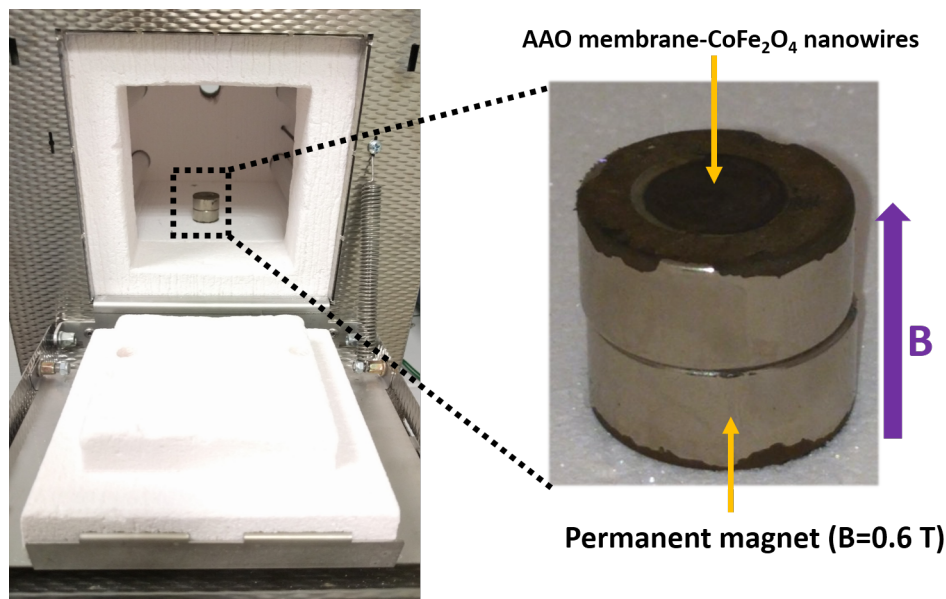


Figure 3.25: Field cooling treatment of filled AAO membrane by  $CoFe_2O_4$  crystallites.

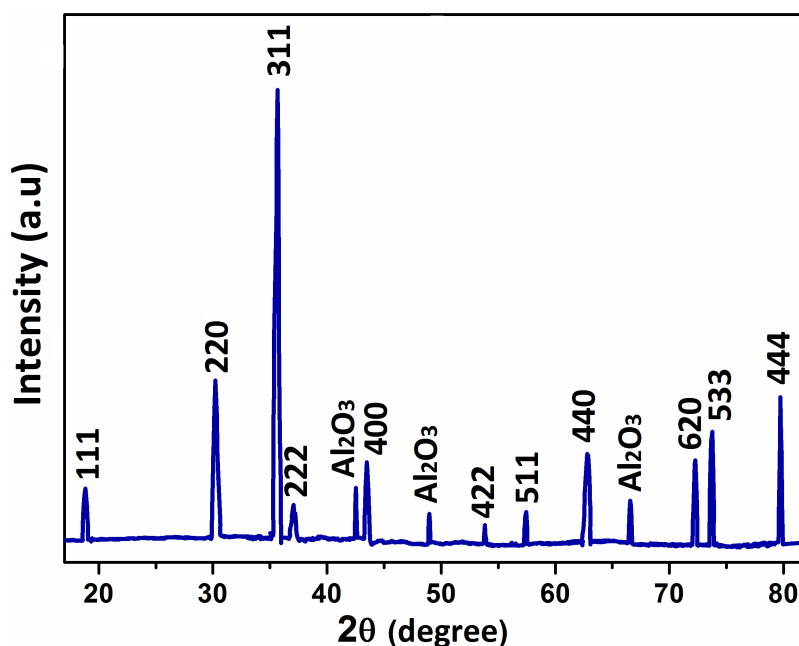


Figure 3.26: XRD spectrum of field cooled  $CoFe_2O_4$  nanowires at 0.6 T.

The XRD reflections correspond to cobalt ferrite (spinel structure). It can be noted that the cooling under magnetic field induces a new XRD reflection (422) of  $CoFe_2O_4$  at  $2\theta = 53.7^\circ$ , which indicates the possible effect of the field cooling on the internal microstructure of nanowires. The calculated lattice parameter has a value of 8.389 Å. In addition, the Williamson-Hall calculation provides a crystallite size of 9.06 nm, which is

smaller than those reported in the previously discussed studies of our work.

Fig.3.27 presents SEM observations of field cooled nanowires at 0.6 T after their dissolution in NaOH solution. The images confirm that the AAO membrane pores are completely filled by the  $CoFe_2O_4$  crystallites, as well as the presence of high density of nanowires.

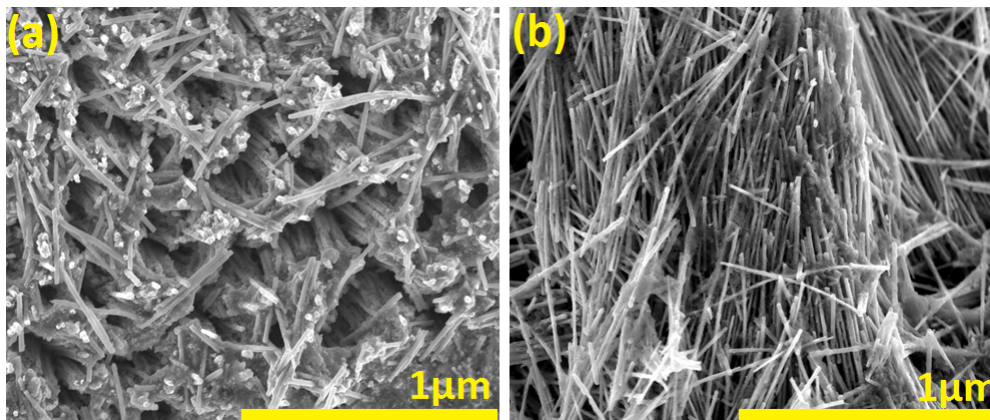


Figure 3.27: SEM images of field cooled  $CoFe_2O_4$  nanowires; (a) partial dissolution, (b) total dissolution.

In order to investigate the influence of the field cooling effect on the magnetic response of  $CoFe_2O_4$  nanowires, hysteresis loops were measured at room temperature in the parallel and perpendicular orientations.

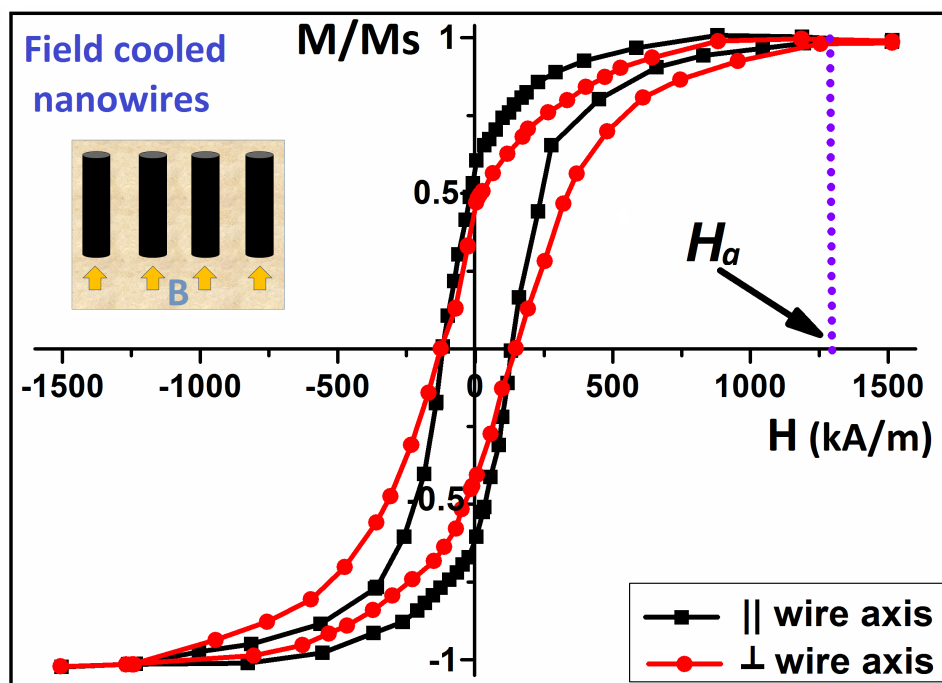


Figure 3.28: Hysteresis loops of field cooled  $CoFe_2O_4$  nanowires at 0.6 T.

During the magnetic field cooling, the nano-crystallites were aligned in the direction of the



magnetic field. From the recorded curves, the easy axis is parallel to the nanowire axis and the perpendicular direction represents the hard axis. An interesting result was observed in the hysteresis loops when the nanocrystals are aligned along the easy axis. This configuration promotes the spin order of the  $CoFe_2O_4$  nano-crystallites, which increases the coercivity and remanent magnetization of the nanowire arrays. The increase in coercivity  $H_c$  (141 kA/m) and squareness ratio  $M_r/M_s$  (0.6) is attributed to the magnetocrystalline and shape anisotropies induced by the imposition of the magnetic field during the cooling process. Along the easy axis, the  $CoFe_2O_4$  nanowires exhibit a large magnetic anisotropy due to magnetocrystalline anisotropy superimposed on the shape one. Moreover, the uniformity of nanowire length, reflected by the total filling of the AAO membrane pores, is a key parameter in the magnetic inversion process. A closely distributed nanowire length can lead to a coherent magnetization reversal process and results in enhanced coercivity and squareness of the loops. Generally, when the nanowires are aligned in the direction of the magnetic field, all the spins of the  $CoFe_2O_4$  crystallites being parallel to the easy axis. Thus, aligned nanowires may exhibit a partially square hysteresis loops. As a matter of fact, the higher  $M_r/M_s$  and  $H_c$  ratio might be attributed to two possible reasons: (i) the sizes of all nano-crystallites are smaller, i.e. single domain regime, and (ii) magnetization curve are governed by coherent rotation of magnetic moments. As a result, partially auto-polarized ferrimagnetic  $CoFe_2O_4$  nanowires that present magnetic response of hard material with an internal magnetic field of 1.52 T were obtained.

### 3.2.2.6 ZFC-FC studies

Fig.3.29 shows the zero-field-cooled (ZFC) and field-cooled (FC) dc magnetization curves for  $CoFe_2O_4$  nanowires magneto-electrodeposited at 0.6 T/-1.2 V and annealed at 500 °C for 24 hours, and the nanowires performed in the same conditions but cooled under magnetic field of 0.6 T. These two samples have been selected for these tests since they exhibit the best magnetic properties.

The ZFC measurements were made after cooling the sample down to 5 K in zero field and measuring up to 300 K in a field of 100 Oe parallel to the wire axis. The FC measurements have been made by cooling the sample in the same field [26]. Thus, the magnetic response of  $CoFe_2O_4$  nanowires revealed an irreversibility between the variations of ZFC and FC curves. Consequently, in nanogranular composite, upon increasing the temperature (ZFC curve), the measured magnetic moment increases and reaches a maximum. The corresponding temperature is referred to the blocking temperature  $T_b$ . This temperature globally depends on the applied field and the typical measurement scale. It can be estimated using the following expression:

$$T_b = \frac{K_s V}{K_B \ln(\frac{\tau}{\tau_0})} \quad (3.6)$$

where  $\tau = 100$  s represents the relaxation time (SQUID magnetometer measuring time),  $\tau_0 \approx 10^{-9}$  s the characteristic time of the system,  $K_s$  the bulk magnetic anisotropy constant,  $V$  the volume of the particle, and  $k_B$  the Boltzmann constant. In our case, the  $CoFe_2O_4$  nanowires have no clear peak from the recorded ZFC-FC curves, an increase is observed at low temperature, and a slight and progressive increase up to room temperature. Fig.3.29 clearly shows that the blocking temperature shifted from 308 to 300 K with decreasing the crystallite size from 10.54 to 9.06 nm for magneto-electrodeposited (Fig.3.29.a) and magneto-electrodeposited and field cooled (Fig.3.29.b) nanowires, respectively.

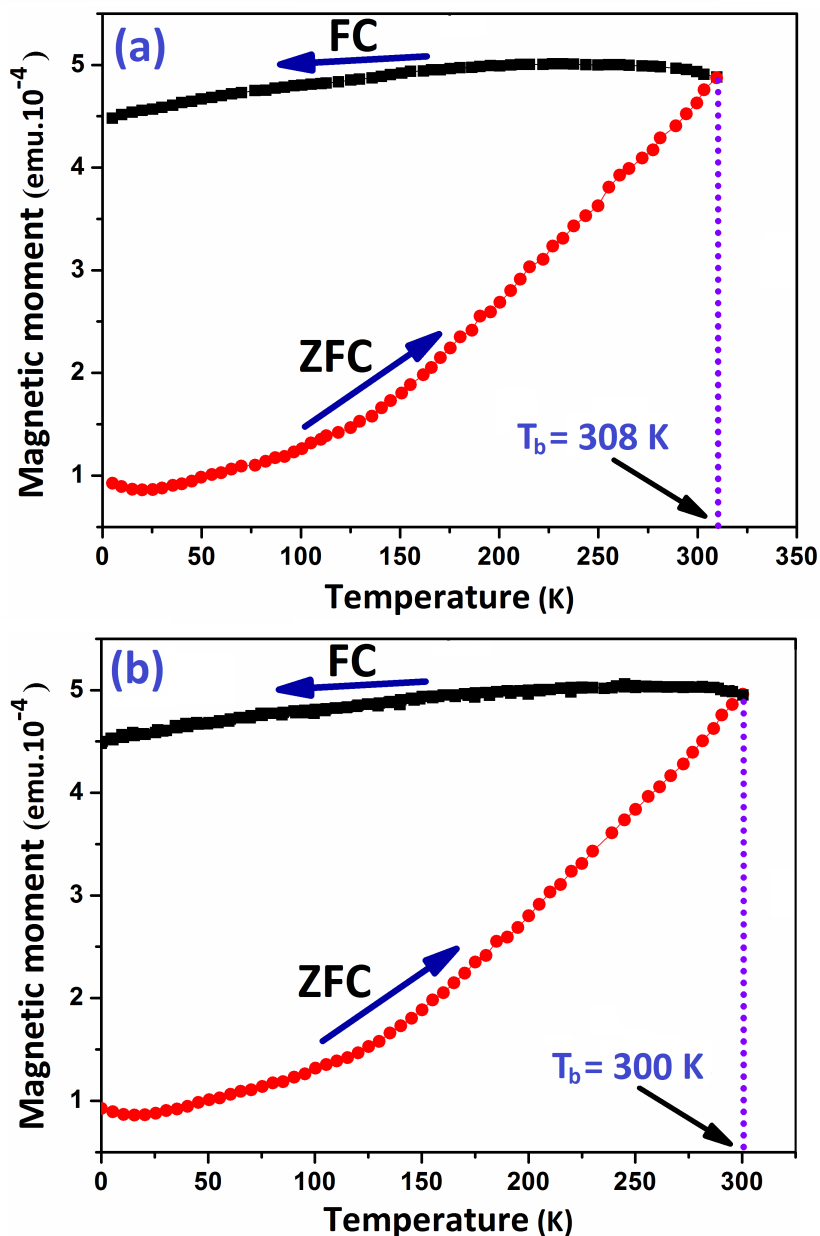


Figure 3.29: ZFC–FC magnetization curves for  $CoFe_2O_4$  nanowires; (a) magneto-electrodeposited at 0.6 T, (b) magneto-electrodeposited at 0.6 T and field cooled at 0.6 T. A magnetic field of 100 Oe is applied along the nanowire axis.

The anisotropy energy rises for higher volumes of crystallites, which results in a lower probability of jumping through the anisotropy barrier. Consequently, the blocking phenomenon is shifted to a higher temperature [27, 28]. The effect of crystallite size is highly considerable in the present study. Several studies mainly focusing on  $CoFe_2O_4$  have shown that  $T_b$  also depends on the synthesis technique [29]. Our results are in good agreement with those corresponding to Tomita et al. [30], where they revealed that the increase in  $T_b$  is assigned to the increase in the crystallite size. Besides the particle size, blocking temperature can also be affected by several other factors like the magnetocrystalline and shape anisotropies.

As a consequence, the magneto-electrodeposition can be used as a powerful method for



growing ferrimagnetic nanowires with tailored properties, which could be a promising material for the fabrication of magneto-optical and non-reciprocal microwave devices (circulators, insulators, etc.).

## Surface roughness

Due to the technological challenges of copper deposition, a surface roughness investigation is required. Before the copper deposition on the  $CoFe_2O_4$  composite magnetic substrate, it was necessary to verify that the surface flatness was acceptable. Roughness measurements were performed with a profilometer device to decide on a grinding and polishing of the surface (Fig.3.30).

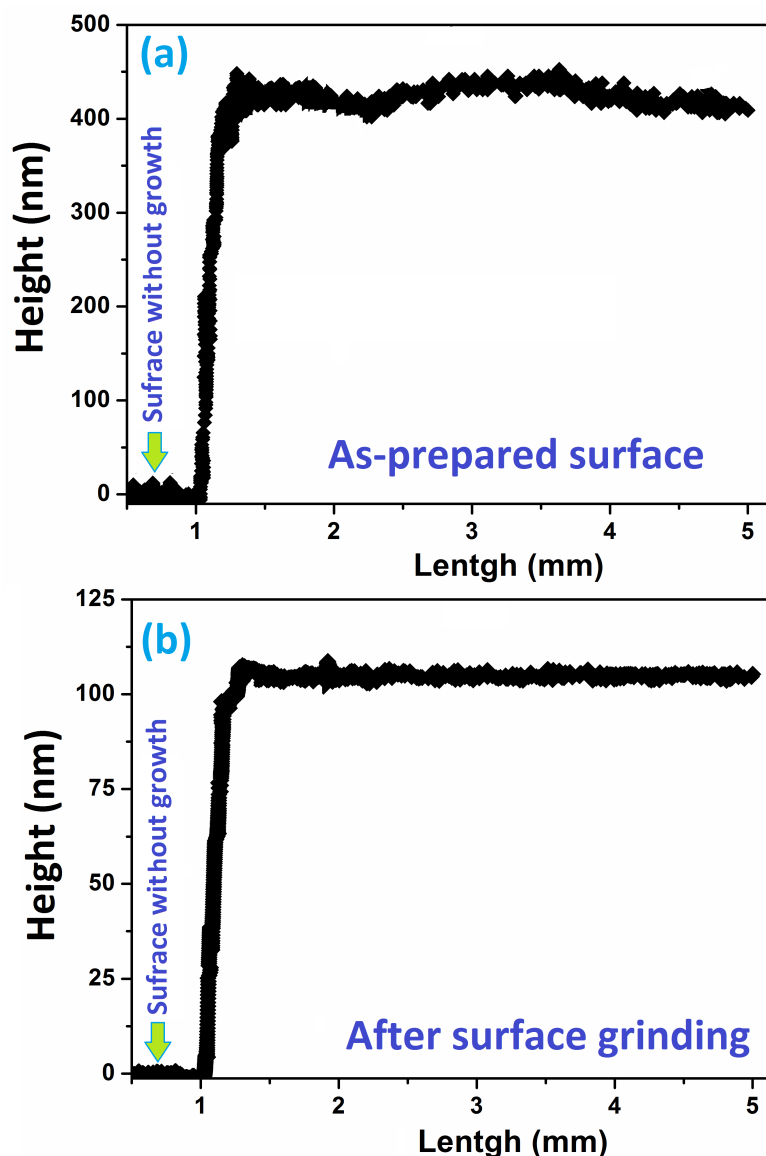


Figure 3.30: 2D surface roughness measurements of filled AAO membrane; (a) as-prepared, (b) after grinding treatment.

Roughness measurements with the profilometer were carried out on the sample that presents the best magnetic properties, i.e. the magneto-electrodeposited and cooled sample at 0.6 T. A first profilometry measurement showed a very high roughness around 400

nm (Fig.3.30.a). The substrate required grinding and polishing in order to obtain an acceptable surface state for a copper deposit. This measurement performed after grinding and polishing is presented in Fig.3.30.b. It can be seen that the roughness decreases from a few hundred nanometers to 100 nm. Consequently, the surface is ready for copper deposition via *rf* sputtering.

### Chapter 3: Summary

In this chapter, we firstly focused on the determination and optimization of the electrochemical conditions to be employed in order to obtain the spinel phase of  $CoFe_2O_4$  on FTO substrates via electrodeposition process. Next, we studied the physico-chemical properties of  $CoFe_2O_4$  nano-crystallites electrochemically embedded in AAO membranes with different pore diameters (20, 100 and 200 nm) via various techniques (CV, CA, FTIR, XRD, SEM, AFM, SQUID-VSM, SP). More precisely, we have chosen to study the effect of pore diameters and deposition potential on the formation of  $CoFe_2O_4$  deposit. The results show that the 20nm-nanowires exhibit very interesting magnetic properties. Then, we investigated the magnetic field effect during the electrochemical process. We emphasized that the presence of the magnetic field affects the nucleation and the electrochemical growth by changing the filling time of the AAO membrane pores. On the other hand, the convective effect of the magnetic field influences the morphology of  $CoFe_2O_4$  deposits. The magnetic characterization of  $CoFe_2O_4$  nanowires revealed that the magnetic field leads to a significant enhancement of the squareness ratio and coercive field. Moreover, the magnetic measurements have indicated that the magnetic field cooling produces a self-polarized magnetic nanocomposite with an internal magnetic field of 1.52 T. Finally, the profilometry measurements have confirmed that the surface state of the nanocomposite substrate is suitable for the copper deposition used in the etching of the microwave structure.

# Bibliography

- [1] J. S. Santos, R. Matos, F. Trivinho-Strixino, E. C. Pereira, Effect of temperature on Co electrodeposition in the presence of boric acid. *Electroch. Acta*, 53 (2007) 644-649.
- [2] M. F. Ashby, D. R. H. Jones, Engineering Materials 1: An Introduction to Properties, Applications and Design, Elsevier, 4th edn, 2012.
- [3] M. S. Kilic, M. Z. Bazant, A. Ajdari, Steric effects in the dynamics of electrolytes at large applied voltages. I. Double-layer charging. *Phys. Rev. E*, 75 (2007) 021502.
- [4] A. C. Nawle, A. V. Humbe, M. K. Babrekar, K. M. Jadhav, Deposition and microstructure of cobalt ferrite thin film prepared by spray pyrolysis technique. *I. J. C. P. S.*, 7 (2018) 602–606.
- [5] S. Velumani, X. Mathew, P. J. Sebastian, S. K. Narayandass, D. Mangalaraj, Thickness dependent properties of hot wall deposited CdSe films. *J. Mater. Sci. Lett.*, 22 (2003) 25-28.
- [6] G. Riveros, H. Gómez, A. Cortes, R. E Marotti, E. A. Dalchiele, Crystallographically-oriented single-crystalline copper nanowire arrays electrochemically grown into nanoporous anodic alumina templates. *Appl. Phys. A*, 81 (2005) 17-24.
- [7] N. Labchir, A. Hannour, A. A. Hssi, D. Vincent, J. P. Chatelon, D. Dufeu, M. Sajieddine, Microwave response of coplanar waveguide based on electrodeposited  $CoFe_2O_4$  nanowires. *J. Magn. Magn. Mater.*, 510 (2020) 166952.
- [8] T. M. Whitney, P.C. Searson, J.S. Jiang, C.L. Chien, Fabrication and magnetic properties of arrays of metallic nanowires. *Science*, 261 (1993) 1316.
- [9] R. Ferré, K. Ounadjela, J.M. George, L. Piraux, S. Dubois, Magnetization processes in nickel and cobalt electrodeposited nanowires. *Phys. Rev. B*, 56 (1997) 14066.
- [10] S. Karim, K. Maaz, Magnetic behavior of arrays of nickel nanowires: effect of microstructure and aspect ratio. *Mater. Chem. Phys.*, 130 (2011) 1103-1108.
- [11] M. S. Kilic, M.Z. Bazant, A. Ajdari, Steric effects in the dynamics of electrolytes at large applied voltages I. Double-layer charging, *Phys. Rev. E*, 75 (2007) 021502.
- [12] A. Franco, F. L.A. Machado, V. S. Zapf, Magnetic properties of nanoparticles of cobalt ferrite at high magnetic field, *J. Appl. Phys.*, 110 (2011) 053913.
- [13] C. H. Chia, S. Zakaria, M. Yusoff, S. C. Goh, C. Y. Haw, S. Ahmadi, H. N. Lim, Size and crystallinity-dependent magnetic properties of  $CoFe_2O_4$  nanocrystals. *Ceram. Int.*, 36 (2010) 605-609.

- [14] Z. Wu, P. Niu, B. Yang, R. Yu, Effect of aspect ratio on microstructure and magnetic properties of spinel  $CoFe_2O_4$  nanowire arrays. *Appl. Phys. A*, 105 (2011) 177.
- [15] V. Laur, G. Vérissimo, P. Quéffélec, L. A. Farhat, H. Alaaeddine, E. Laroche, J.P. Ganne, Self-biased Y-junction circulators using lanthanum-and cobalt-substituted strontium hexaferrites, *IEEE. Trans. Microw. Theory. Tech*, 63 (2015) 4376–4381.
- [16] O. Aaboubi, A. Y. Ali-Omar, A. Franczak, K. Msellak, Investigation of the electrodeposition kinetics of Ni–Mo alloys in the presence of magnetic field, *J. Electroanal. Chem*, 737 (2015) 226–234.
- [17] K. L. Rabah, J. P. Chopart, H. Schloerb, S. Saulnier, O. Aaboubi, M. Uhlemann, J. Amblard, Analysis of the magnetic force effect on paramagnetic species. *J. Electroanal. Chem*, 571 (2004) 85–91.
- [18] V. Ganesh, D. Vijayaraghavan, V. Lakshminarayanan, Fine grain growth of nickel electrodeposit: effect of applied magnetic field during deposition. *Appl. Surf. Sci*, 240 (2005) 286–295.
- [19] G. Ji, S. Tang, B. Xu, B. Gu, Y. Du, Synthesis of  $CoFe_2O_4$  nanowire arrays by sol–gel template method. *Chemical physics letters. Chem. Phys. Lett*, 379 (2003) 484–489.
- [20] Y. Xu, D. S. Xue, D. Q. Gao, J. L. Fu, X. L. Fan, D. W. Guo, W. B. Sui, Ordered  $CoFe_2O_4$  nanowire arrays with preferred crystal orientation and magnetic anisotropy. *Electrochim. Acta*, 54 (2009) 5684–5687.
- [21] J. J. Yuan, Q. Zhao, Y. S. Xu, Z. G. Liu, X. B. Du, G. H. Wen, Synthesis and magnetic properties of spinel  $CoFe_2O_4$  nanowire arrays. *J. magn. magn. mater*, 321 (2009) 2795–2798.
- [22] S. R. Naik, A. V. SalKer, Change in the magnetostructural properties of rare earth doped cobalt ferrites relative to the magnetic anisotropy. *J. Mater. Chem*, 22 (2012) 2740–2750.
- [23] I. C. Nlebedim, D. C. Jiles, Thermal effects on the magnetic properties of titanium modified cobalt ferrite. *J. Appl. Phys*, 117 (2015) 17A506.
- [24] R. H. Kodama, A. E. Berkowitz, Surface spin disorder in  $NiFe_2O_4$  nanoparticles. *Phys. Rev. Lett*, 77(1996) 394
- [25] L. Ajroudi, N. Mliki, L. Bessais, V. Madigou, S. Villain, C. Leroux, Magnetic, electric and thermal properties of cobalt ferrite nanoparticles. *Mater. Res. Bull*, 59 (2014) 49–58.
- [26] A. A. Bagade, V. V. Ganbavle, S.V. Mohite, T. D. Dongale, B. B. Sinha, K.Y. Rajpure, Assessment of structural, morphological, magnetic and gas sensing properties of  $CoFe_2O_4$  thin films. *J. Colloid. Interface. Sci*, 497 (2017) 181.
- [27] A. J. Franco, V. Zapf, Temperature dependence of magnetic anisotropy in nanoparticles of  $Co_xFe(3-x)O_4$ . *J. Magn. Magn. Mater*], 320 (2008) 709–713.
- [28] K. Maaz, A. Mumtaz, S.K. Hasanain, A. Ceylan, Synthesis and magnetic properties of cobalt ferrite ( $CoFe_2O_4$ ) nanoparticles prepared by wet chemical route. *J. Magn. Mater*, 308 (2007) 289–295.

- [29] X. Fan, J. Guan, X. Cao, W. Wang, F. Mou, Low-temperature synthesis, magnetic and microwave electromagnetic properties of substoichiometric spinel cobalt ferrite octahedra. *Eur. J. Inorg. Chem.*, 3 (2010) 419–426.
- [30] S. Tomita, P. E. Jonsson, K. Akamatsu, H. Nawafune, H. Takayama, Controlled magnetic properties of Ni nanoparticles embedded in polyimide films. *Phys. Rev. B*, 76 (2007) 174432.

# Chapter 4

## Modeling of $CoFe_2O_4$ nanocomposite permeability - Application to coplanar Y Circulator

### Contents

---

2.1	Introduction . . . . .	54
2.2	Electrochemistry: basic concepts . . . . .	54
2.3	Magneto-electrodeposition . . . . .	58
2.4	Magneto-electrochemical synthesis of $CoFe_2O_4$ . . . . .	61
2.5	Characterization techniques . . . . .	65

---

### 4.1 Introduction

After outlining in the previous chapters the state of the art of the different types of circulators and improving the magnetic properties of  $CoFe_2O_4$  nanocomposite synthesized by the magneto-electrodeposition technique, we are going to focus now on the analytical modeling and electromagnetic simulation of the Y-junction circulator. We introduce the theoretical model used to predict the permeability tensor of  $CoFe_2O_4$  nanocomposite. Tests under MATLAB software will be performed using different squareness ratios ( $m$ ) for  $CoFe_2O_4$  nanocomposite. Afterwards, we will discuss more concretely the phenomena involved in the circulator. We note that the circulator has been primarily studied in its stripline configuration by Bosma (1962) [1] and followed by the study of Fay and Comstock [2]. In our work, we will start from the theoretical study of the stripline circulator based on Bosma's formulas using the theoretical model adopted for the magnetic permeability. The expressions of the electromagnetic fields present in the stripline will be discussed, leading to the dimensioning of the component. Then, the calculation of the S-parameters, taking into account the different loss factors, will make it possible to evaluate the performance of the circulator and to transpose its dimensions towards the coplanar topology. On the other hand, a protocol of integration for the theoretical model of the magnetic permeability in the Ansoft HFSS commercial software will be followed in order to numerically simulate the structure previously studied in an analytical approach. Indeed, the 3D electromagnetic simulation enables the ferrite thickness to be taken into account, which is not the case

in the first analytical modeling. Finally, based on the results obtained with the stripline circulators, we will model with HFSS a coplanar structure (-line and circulator) and we will also conduct a parametric study in order to optimize the performance of the component. The best resulting design will be used for the manufacturing of prototypes.

## 4.2 Permeability model of $CoFe_2O_4$ nanocomposite

### Permeability tensor

As in the behavioural models, we sought to determine the tensor permeability of the material by examining the response of the nanowired ferrimagnetic composite with their magnetic characteristics such as  $M_s$ ,  $M_r/M_s$ ,  $H_i$  and geometrical ones such as the porosity  $p$  and the filling rate  $h_w$  of the AAO membrane pores. The permeability tensor  $\mu$  of the composite magnetic substrate has been determined using the modified Irashagi model detailed in chapter 1.

$$\hat{\mu}_{wire} = \hat{\mu} = \begin{pmatrix} \mu & -j\kappa & 0 \\ +j\kappa & \mu & 0 \\ 0 & 0 & \mu_z \end{pmatrix} \quad (4.1)$$

where

$$\mu = 1 + 2\pi\mu_o M_s \gamma p h_w (f_r + jf\alpha) ((f_r + jf\alpha)^2 - f^2)^{-1} (m^2 + 1) \quad (4.2)$$

$$\kappa = 4\pi\mu_o M_s \gamma p h_w f ((f_r + jf\alpha)^2 - f^2)^{-1} m \quad (4.3)$$

$$\mu_z = 1 + 2\pi\mu_o M_s \gamma p h_w (f_r + jf\alpha) ((f_r + jf\alpha)^2 - f^2)^{-1} (1 - m^2) \quad (4.4)$$

By way of illustration, consider the following conditions:  $\mu_o M_s = 0.18 T$ ,  $f_r = 42 GHz$ ,  $\alpha = 0.017$ ,  $p = 50 \%$  and  $h_w = 100 \%$ .

Some results of this model with an orientation of magnetic crystallite moments varying from 30 % to 100 % have been studied. Fig.4.1, Fig.4.2 and Fig.4.3 show the variations of the components of  $\mu$ ,  $\kappa$  and  $\mu_z$  corresponding to the permeability tensor as a function of the moments orientation ( $m = M_r/M_s$ ) of the  $CoFe_2O_4$  nano-crystallites.

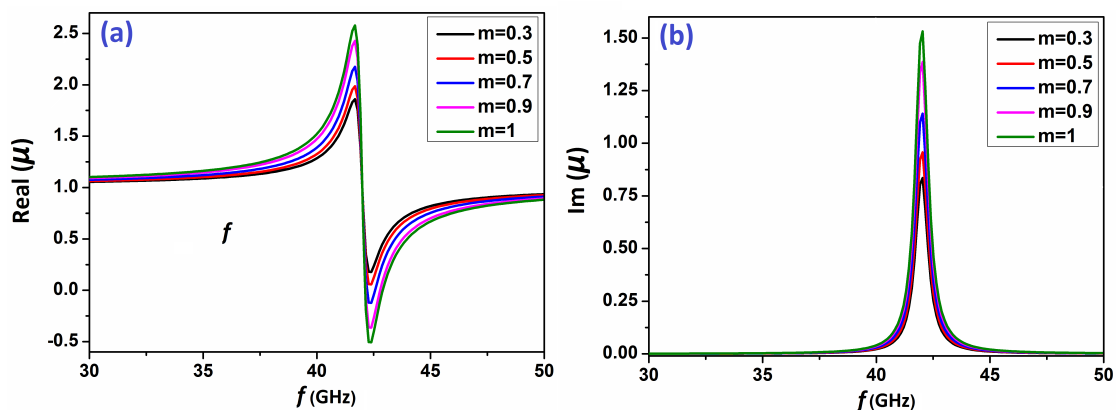


Figure 4.1: Evolution of  $\mu$  components as a function of  $CoFe_2O_4$  nano-crystallites orientation.

As shown in the obtained results, by increasing the orientation of the nano-crystallites

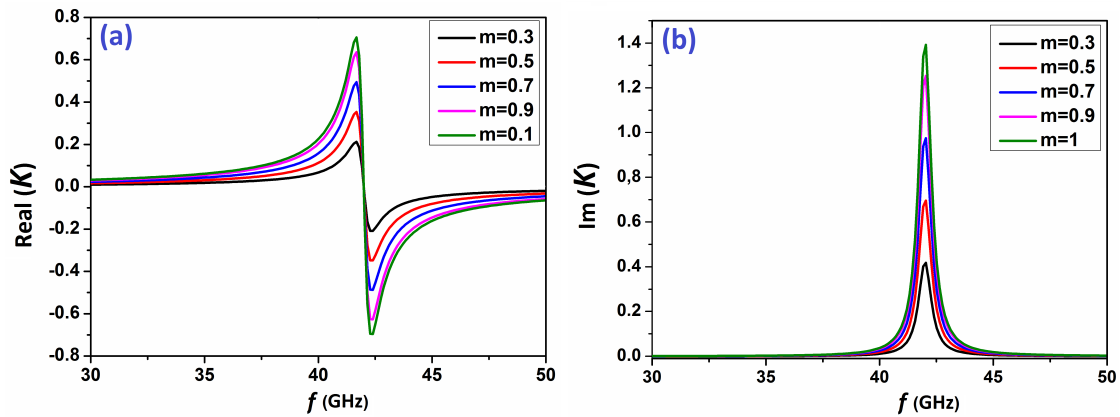


Figure 4.2: Evolution of  $\kappa$  components as a function of  $\text{CoFe}_2\text{O}_4$  nano-crystallites orientation.

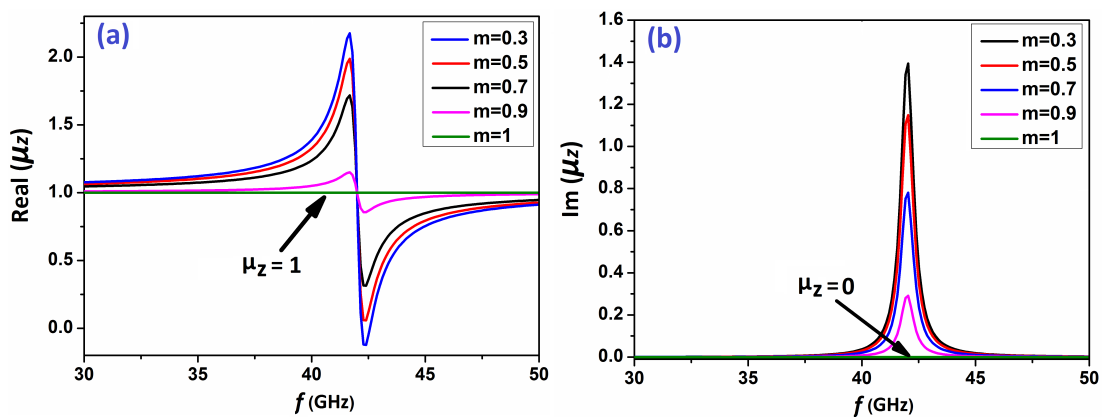


Figure 4.3: Evolution of  $\mu_z$  components as a function of  $\text{CoFe}_2\text{O}_4$  nano-crystallites orientation.

from 30 % to 100%, the two elements  $\mu$  and  $\kappa$  increase at the resonance while for the element  $\mu_z$  the real part tends towards 1 and the imaginary part becomes zero for an orientation of 100 % magnetic material. As a result, the adopted model converges well towards the Polder model in the saturated case. The resonance frequency remains practically unchanged. For more accurate results, we think that a new model has to be developed taking into account the crystallite size and the domain size of the ferrite nanowires, especially for partial magnetized states. This part was out of this Ph.D. work.

Based on the present model, simulations on Matlab software of a Bosma circulator have been carried out with encouraging initial results. We can nevertheless give some preliminary results in the next paragraph.

## 4.3 Electromagnetic analysis approaches of the circulator

### 4.3.1 Theoretical modeling (Bosma model)

The Y-junction stripline circulator designed by Bosma [1] is the most widely used in theoretical studies of circulators. The core of this circulator in stripline technology



consists of three access lines oriented at  $120^\circ$  to each other and connected to a central metal disk. This conductor is inserted between two ferrite cylinders with the same shape as the central disk, in order to ensure the homogeneity of the transverse structure. The stripline structure is sandwiched by two ground planes above and below the ferrite disks. Two permanent magnets located on each side of the structure create a static magnetic polarization field that magnetizes the ferrimagnetic material along the axis of the magnetic cylinders (Fig.4.4).

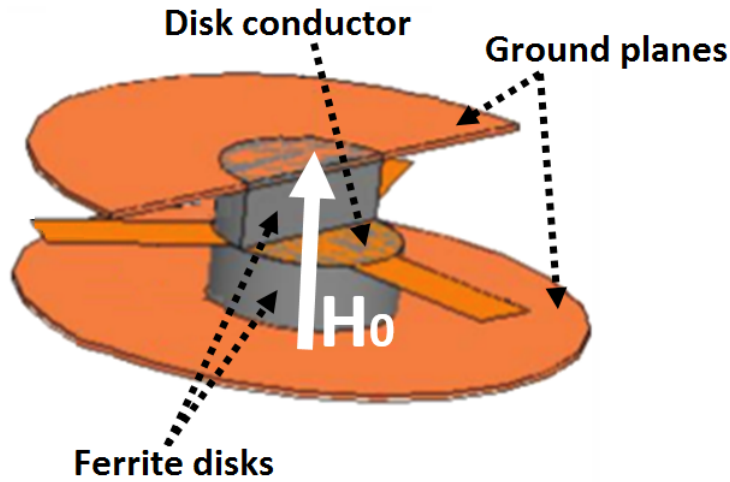


Figure 4.4: Structure of the Y-junction stripline circulator.

### 4.3.2 Electric and magnetic fields

Fay and Comstock [2] have shown that the ferrite disks can be considered as resonant cavities. In the absence of an internal polarization ( $H_i = 0$ ), the cavities have a single resonant mode and there is a standing wave pattern within the structure (Fig.4.5).

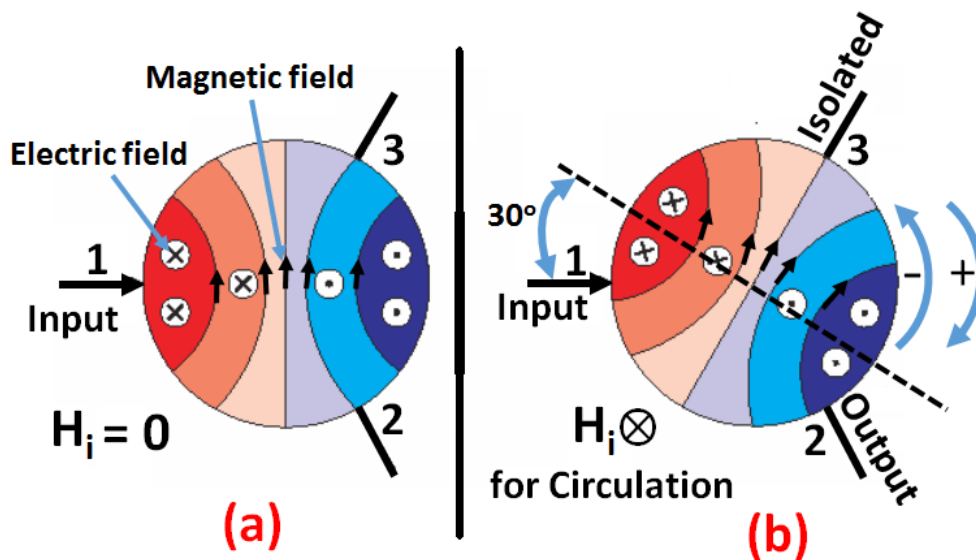


Figure 4.5: Ferrite junction circulation; (a) unmagnetized ferrite, (b) magnetized ferrite.

As shown in Fig.4.5.a, the electric field is oriented perpendicularly to the plane of the conductors. Moreover, the electric field located at ports 2 and 3 is in the opposite direction,

with an amplitude approximately half the electric field's one at port 1. Thus the energy present at the input port is equally distributed over the other two ports. When a static magnetic polarization field is applied along the axis of the ferrite disks, the standing wave pattern can be rotated by  $30^\circ$  (see Fig.4.5.b), which is an optimal angle for observing the circulation phenomenon. The electric field at port 1 has the same amplitude but in the opposite direction to that at port 2, and the electric field at port 3 is zero. Thus, the energy present at the input port (port 1) is transferred to the output port (port 2) and the third port (port 3) is isolated. It should be noted that if the polarization field is in the opposite direction, the circulation of the EM waves is in the opposite direction.

In his works, Bosma assumes that the resonant cavities (ferrite junction) are considered to have electrical walls on the upper and lower sides. The periphery ( $r = R$ ) of the ferrite disks is considered to form a magnetic wall except at the access lines. Thus, the  $E_r$  and  $E_\phi$  components are zero, and the height of the ferrite disks is considered to be sufficiently small so that electromagnetic fields are supposed to be constants along z-direction. In addition, since the  $E_z$  component is antisymmetric on each side of the central conductor, it is possible to consider only one ferrite disk to establish the expressions of the electromagnetic fields. The figure below, which illustrates the structure of the central conductor in the cylindrical coordinates, is used to define the notations that will be further used.

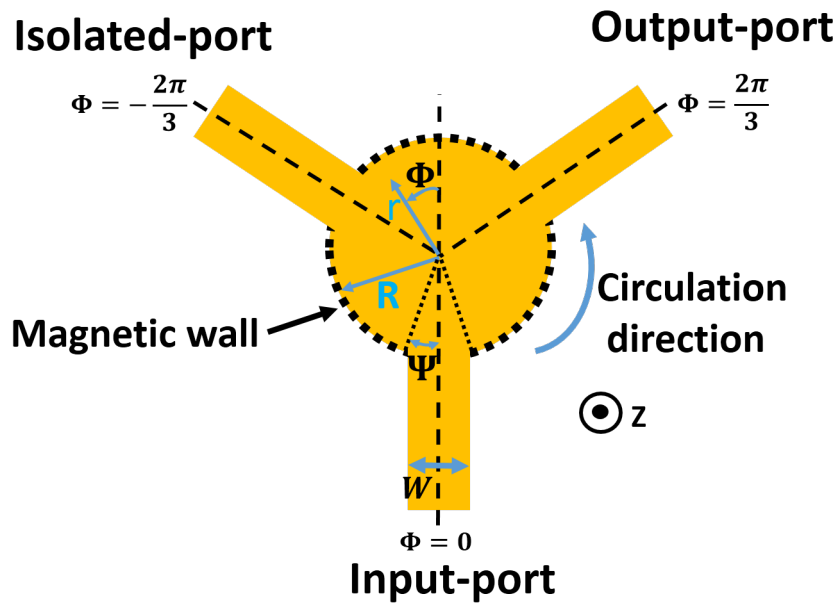


Figure 4.6: *Design of the central conductor in cylindrical coordinates.*

In order to determine the expressions of electromagnetic fields, it is necessary to write the Maxwell's fundamental equations:

$$\vec{rot} \vec{E} = j\omega\mu_o\hat{\mu}\vec{H} \quad (4.5)$$

$$\vec{rot} \vec{H} = -j\omega\varepsilon_o\varepsilon_f\vec{E} \quad (4.6)$$

where  $\varepsilon_f$  is the permittivity of the ferrite material. In the cylindrical coordinate system, the right-hand side of Eq.4.5 can be written:

$$j\omega\mu_o\hat{\mu}\vec{H} = j\omega\mu_o \begin{bmatrix} \mu & -j\kappa & 0 \\ +j\kappa & \mu & 0 \\ 0 & 0 & \mu_z \end{bmatrix} \vec{H} \Rightarrow j\omega\mu_o \begin{cases} \mu H_r - j\kappa H_\Phi \\ j\kappa H_r + \mu H_\Phi \\ \mu_z H_z \end{cases} \quad (4.7)$$

The left-hand side of Eq.4.5 can be written as follows:

$$\vec{rot} \vec{E} = \begin{cases} \frac{1}{r} \frac{\partial E_z}{\partial \Phi} - \frac{\partial E_\Phi}{\partial z} \\ \frac{\partial E_r}{\partial z} - \frac{\partial E_z}{\partial r} \\ \frac{1}{r} \frac{\partial}{\partial r} (r E_\Phi) - \frac{1}{r} \frac{\partial E_r}{\partial \Phi} \end{cases} \quad (4.8)$$

The previous expression will be simplified since, as a first approximation, only the z component of the electric field is not zero and the electromagnetic fields have no variation along z. By introducing these results into Eq.4.5, we obtain:

$$\begin{cases} \frac{1}{r} \frac{\partial E_z}{\partial \Phi} = j\omega\mu_o(\mu H_r - j\kappa H_\Phi) \\ -\frac{\partial E_z}{\partial r} = j\omega\mu_o(j\kappa H_r + \mu H_\Phi) \\ 0 = \mu_z H_z \end{cases} \quad (4.9)$$

It is therefore possible to express the components according to r and  $\Phi$  of the magnetic field as follows:

$$H_\Phi = \frac{1}{j\omega\mu_o\mu_{eff}} \left[ \frac{\partial E_z}{\partial r} + j \frac{\kappa}{\mu} \frac{1}{r} \frac{\partial E_z}{\partial r} \right] \quad (4.10)$$

$$H_r = \frac{1}{j\omega\mu_o\mu_{eff}} \left[ \frac{1}{r} \frac{\partial E_z}{\partial \Phi} + j \frac{\kappa}{\mu} \frac{\partial E_z}{\partial r} \right] \quad (4.11)$$

where

$$\mu_{eff} = \frac{\mu^2 - \kappa^2}{\mu} \quad (4.12)$$

This parameter is called the effective permeability and is it calculated from the permeability tensor elements of the ferrimagnetic material. As before, if the two members of Maxwell's second equation are expanded and it is taken into account that  $H_z = E_r = E_\Phi = 0$ , then the following relationship will be derived:

$$\frac{1}{r} H_\Phi + \frac{\partial H_\Phi}{\partial r} - \frac{1}{r} \frac{\partial H_r}{\partial \Phi} = j\omega\epsilon_o\epsilon_f E_z \quad (4.13)$$

If one introduces into the latter result the expressions of the magnetic field components (Eq.4.10 and Eq.4.11), one can finally obtain the following equation known as the Helmholtz equation:

$$\left( \frac{\partial^2}{\partial r^2} + \frac{1}{r} \frac{\partial}{\partial r} + \frac{1}{r^2} \frac{\partial^2}{\partial \Phi^2} + \omega^2 \mu_o \mu_{eff} \epsilon_o \epsilon_f \right) E_z = 0 \quad (4.14)$$

This equation adopts a general solution as follows:

$$E_{zn} = [A_{+n} e^{jn\Phi} + A_{-n} e^{-jn\Phi}] J_n(Kr) \quad (4.15)$$

where

$$K = \omega \sqrt{\mu_o \mu_{eff} \varepsilon_o \varepsilon_{eff}} \quad (4.16)$$

Here  $K$  is referred to the wave number and  $J_n(Kr)$  the  $n$ -order Bessel function of the first kind.

The solution given in Eq.4.15 corresponds to the  $n$ th transverse magnetic (TM) mode of ferrite resonance. Introducing this solution into Eq.4.10, we obtain:

$$H_{\Phi n}(\Phi, r) = jY_{eff} \left[ A_{+n} e^{jn\Phi} \left( J_{n-1}(Kr) - \frac{nJ_{n-1}(Kr)}{Kr} \left( 1 + \frac{\kappa}{\mu} \right) \right) + A_{-n} e^{-jn\Phi} \left( J_{n-1}(Kr) - \frac{nJ_{n-1}(Kr)}{Kr} \left( 1 - \frac{\kappa}{\mu} \right) \right) \right] \quad (4.17)$$

where

$$Y_{eff} = \sqrt{\frac{\varepsilon_o \varepsilon_{eff}}{\mu_o \mu_{eff}}} \quad (4.18)$$

$Y_{eff}$  represents the effective wave admittance of the ferrite material. In order to determine the resonance modes occurring in the junction, it is necessary to consider the boundary conditions. Bosma assumes that at the periphery of the ferrite disks exists a magnetic wall, which implies the following condition:

$$H_{\Phi}(r = R) = 0 \quad (4.19)$$

He also stipulates the assumptions given below (see Eq.4.20 and Eq.4.21). The magnetic wall condition at the periphery of the ferrite disks is valid except at the access ports. Moreover, in order to simplify the analytical calculation, the component according to  $\Phi$  of the magnetic field is considered constant over the entire width of the access lines. Since the input port is located at  $\Phi = 0$ , the output port at  $\Phi = \frac{2\pi}{3}$  and the isolated port at  $\Phi = -\frac{2\pi}{3}$ , it comes, for  $r = R$ :

$$\left\{ \begin{array}{ll} -\Psi < \Phi < \Psi, & H_{\Phi 1} = H_1 \\ \frac{2\pi}{3} - \Psi < \Phi < \Psi + \frac{2\pi}{3}, & H_{\Phi 1} = H_1 \\ -\frac{2\pi}{3} - \Psi < \Phi < \Psi - \frac{2\pi}{3}, & H_{\Phi 1} = 0 \\ \text{Otherwise,} & H_{\Phi 1} = 0 \end{array} \right. \quad (4.20)$$

$$\left\{ \begin{array}{ll} \Phi = 0, & E_{z1} = E_1 \\ \Phi = \frac{2\pi}{3}, & E_{z1} = -E_1 \\ \Phi = -\frac{2\pi}{3}, & E_{z1} = 0 \end{array} \right. \quad (4.21)$$

In the previous expressions, as a first approximation, only the resonance mode of  $n=1$  has been retained because this mode is the fundamental mode. Considering the conditions outlined above, it is possible to determine the expressions of the coefficients  $A_+$  and  $A_-$  of Eq.4.15. It becomes:

$$A_{\pm} = \frac{E_1}{2J_1(KR)} \left( 1 \pm \frac{j}{\sqrt{3}} \right) \quad (4.22)$$

Thus, introducing this result into Eq.4.15, the electric field is expressed as follows:

$$E_z = E_1 \frac{J_1(Kr)}{J_1(KR)} \left( \cos(\Phi) - \frac{\sin(\Phi)}{\sqrt{3}} \right) \quad (4.23)$$

The amplitude of the electric field at the input port is set to an arbitrary value, e.g.  $E = 1 \text{ V/m}$ , in order to plot the evolution of the  $z$  component of the electric field at the periphery of the ferrite discs (i.e.  $r = R$ ) as a function of the considered angle (see Fig.4.7).

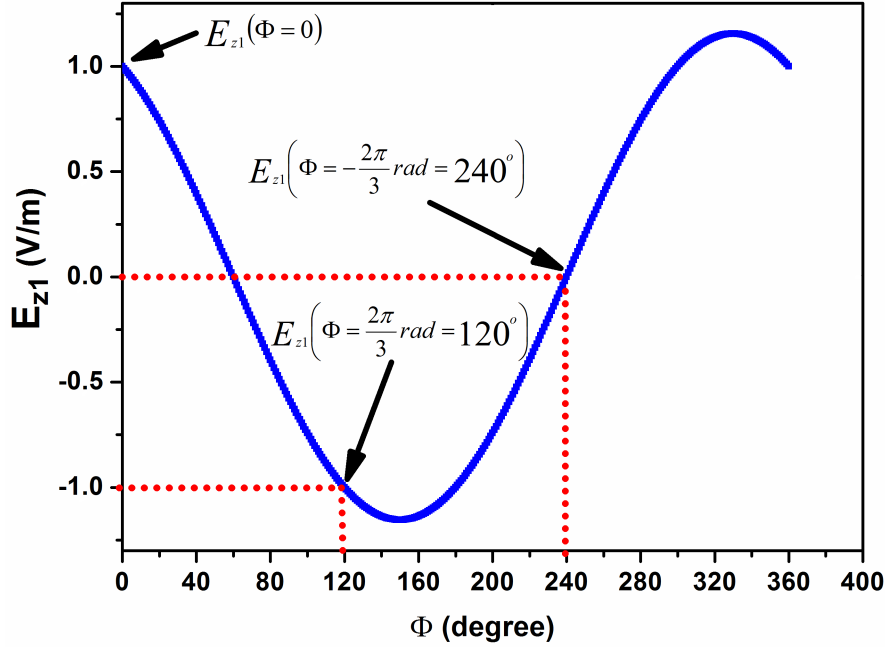


Figure 4.7: Evolution of the electric field along  $z$  for  $r = R$  and  $n = 1$  as a function of  $\Phi$ .

According to Fig.4.7, the amplitude of the electric field present in the input port for  $\Phi = 0$  is identical to that of the electric field (with a  $180^\circ$  phase shift) present in the output port located at  $\Phi = -\frac{2\pi}{3}\text{rad} = 120^\circ$ . Finally, the electric field is zero in the output port located at  $\Phi = -\frac{2\pi}{3}\text{rad} = 240^\circ$ . The general characteristics of the circulator outlined at the beginning of this section are validated.

Likewise, by inserting the Eq.4.22 into Eq.4.17, it comes to :

$$H_{\Phi 1}(\Phi, r) = jY_{eff} \frac{E_1}{2J_1(Kr)} \left[ \left( 1 + \frac{j}{\sqrt{3}} \right) \left[ J_0(Kr) - \frac{J_1(Kr)}{Kr} \left( 1 + \frac{\kappa}{\mu} \right) \right] e^{j\Phi} + \left( 1 - \frac{j}{\sqrt{3}} \right) \left[ J_0(Kr) - \frac{J_1(Kr)}{Kr} \left( 1 - \frac{\kappa}{\mu} \right) \right] e^{-j\Phi} \right] \quad (4.24)$$

In order to make this expression compatible with the conditions specified in Eq.4.19, the Eq.4.19 is developed in Fourier series:

$$H_{\Phi} = H_1 \left[ \frac{2\Psi}{\pi} + \sum_{n=1}^{\infty} \frac{\sin(n\Psi)}{n\pi} \cos(n\Phi) + \sqrt{3} \frac{\sin(n\Psi)}{n\pi} \sin(n\Phi) \right] \quad (4.25)$$

For the mode  $n = 1$ , one can write:

$$H_{\Phi 1}(\Phi, r) = \frac{-j\sqrt{3}H_1 \sin(\Psi)}{2\pi} \left[ \left( 1 + \frac{j}{\sqrt{3}} \right) e^{j\Phi} - \left( 1 - \frac{j}{\sqrt{3}} \right) e^{-j\Phi} \right] \quad (4.26)$$

To equalize Eq.4.26 with Eq.4.24, the following conditions are required :

$$J_1'(KR) = J_0(KR) - \frac{J_1(KR)}{KR} = J_0(x) - \frac{J_1(x)}{x} = 0 \quad (4.27)$$

$$\frac{Y_{eff}E_1}{KR} \frac{\kappa}{\mu} = \frac{\sqrt{3}H_1 \sin(\Psi)}{\pi} \quad (4.28)$$

where:

$$x = KR = \omega \sqrt{\mu_o \mu_{eff} \varepsilon_o \varepsilon_f} R \quad (4.29)$$

Several solutions exist for the Eq.4.27 through the properties of Bessel functions. The most commonly adopted solution is the solution  $x_{1,1} = 1.84$ . The radius of the central conductor of the circulator can be determined from the Eq.4.29. It depends on the desired operating frequency and the selected magnetic material. The second condition given in Eq.4.28 is useful to define the coupling angle  $\Psi$  between the junction and the circulator access lines (see Fig.4.6). If the coupling angle is small, it comes:

$$\Psi \simeq \sin(\Psi) = \frac{\pi}{\sqrt{3}KR} \frac{Y_{eff} \kappa}{Y_d \mu} \quad (4.30)$$

where

$$Y_d = \frac{H_1}{E_1} = \frac{\sqrt{\varepsilon_o \varepsilon_d}}{\mu_o} = \frac{\sqrt{\varepsilon_d}}{120\pi} \quad (4.31)$$

where  $\varepsilon_d$  is the relative permittivity of the dielectric material surrounding the ferrite disks. It is possible to determine the width ( $W$ ) of the access lines as a function of the coupling angle and the radius of the central conductor disk as follows (see Fig.4.6):

$$W = 2R \sin(\Psi) \quad (4.32)$$

After establishing the expressions that enable the dimensioning of the Y-junction stripline circulator, the performance of such device is then evaluated.

### 4.3.3 Analytical calculation of the S-parameters

In order to evaluate the performance presented by the Y-junction stripline circulator, it is required to establish the S-parameters that characterize its operation. We have presented in the first chapter that the S-parameters matrix of the circulator can be expressed as follows:

$$[S] = \begin{bmatrix} S_{11} & S_{12} & S_{13} \\ S_{21} & S_{22} & S_{23} \\ S_{31} & S_{32} & S_{33} \end{bmatrix} \quad (4.33)$$

where the parameters  $S_{ii}$ ,  $S_{ij}$  and  $S_{ji}$  represent the reflection, direct transmission and reverse transmission coefficients, respectively. The three ports are assumed to be identical and therefore:  $S_{11}=S_{22}=S_{33}$ ,  $S_{12}=S_{23}=S_{31}$  and  $S_{21}=S_{13}=S_{32}$ . As a first approximation, the electromagnetic fields are assumed to have no variation along z, so the ferrite thickness is excluded in the calculation of the S-parameters. The components  $E_z$  and  $H_\Phi$  are coupled by the impedance matrix expressed as follows:

$$[Z] = [E_z] [H_\Phi]^{-1} = \begin{bmatrix} Z_{11} & Z_{12} & Z_{13} \\ Z_{21} & Z_{22} & Z_{23} \\ Z_{31} & Z_{32} & Z_{33} \end{bmatrix} \quad (4.34)$$

The expressions that relate the incident fields (index  $i$ ) and the reflected fields (index  $r$ ) are presented as follows:

$$[E_z] = [E_{zi}] + [E_{zr}] \quad (4.35)$$

$$[E_{zr}] = [S] [E_{zi}] \quad (4.36)$$

$$[H_\Phi] = [H_{\Phi i}] + [H_{\Phi r}] \quad (4.37)$$

$$[H_{\Phi r}] = -[S] [H_{\Phi i}] \quad (4.38)$$

$$[E_{zi}] = [Z_d] [H_{\Phi i}] \quad (4.39)$$

where  $Z_d$  is a diagonal matrix which can be derived from Eq.4.31 as follows:

$$Z_d = \frac{120\pi}{\sqrt{\varepsilon_d}} \quad (4.40)$$

From these definitions, the following relationship is achieved:

$$[S] = \left[ [Z] + [Z_d] \right]^{-1} \left[ [Z] - [Z_d] \right] \quad (4.41)$$

After a development by using the relationships mentioned above, the coefficients  $S_{11}$ ,  $S_{21}$  and  $S_{31}$  can be represented by the following formulas:

$$S_{11} = 1 + \frac{2Z_d(Z_{21}Z_{31} - (Z_{11} + Z_d)^2)}{(Z_{11} + Z_d)^3 + Z_{21}^3 + Z_{31}^3 + Z_{21}Z_{31}(Z_{11} + Z_d)} \quad (4.42)$$

$$S_{21} = \frac{2Z_d(Z_{21}(Z_{11} + Z_d) - Z_{31}^2)}{(Z_{11} + Z_d)^3 + Z_{21}^3 + Z_{31}^3 + Z_{21}Z_{31}(Z_{11} + Z_d)} \quad (4.43)$$

$$S_{31} = \frac{2Z_d(Z_{31}(Z_{11} + Z_d) - Z_{21}^2)}{(Z_{11} + Z_d)^3 + Z_{21}^3 + Z_{31}^3 + Z_{21}Z_{31}(Z_{11} + Z_d)} \quad (4.44)$$

By setting the following simplified expressions:

$$C_1 = \frac{j\pi}{2Z_{eff}}(Z_{11} + Z_d) \quad (4.45)$$

$$C_2 = \frac{j\pi}{2Z_{eff}}Z_{21} \quad (4.46)$$

$$C_3 = \frac{j\pi}{2Z_{eff}}Z_{31} \quad (4.47)$$

where  $Z_{eff}$  is the effective wave impedance corresponding to the admittance  $Y_{eff}$  defined in Eq.18, one finally obtains:

$$S_{11} = 1 + \frac{\pi Z_d(C_1^2 - C_2C_3)}{jZ_{eff}(C_1^3 + C_2^3 + C_3^3 - 3C_1C_2C_3)} \quad (4.48)$$

$$S_{21} = \frac{\pi Z_d(C_3^2 - C_1C_2)}{jZ_{eff}(C_1^3 + C_2^3 + C_3^3 - 3C_1C_2C_3)} \quad (4.49)$$

$$S_{31} = \frac{\pi Z_d (C_2^2 - C_1 C_3)}{j Z_{eff} (C_1^3 + C_2^3 + C_3^3 - 3C_1 C_2 C_3)} \quad (4.50)$$

The expressions of the S-parameters given above correspond to the findings of Wu and Rosenbaum [3] as well as Neidert and Phillips [4]. Moreover, the theoretical results obtained by Bosma [1] enable to express the  $E_z$  component as a function of the  $H_\Phi$  component by introducing a Green's function:

$$E_z(r, \Phi) = \int_{-\pi}^{\pi} G(r, \Phi; R, \Phi') H_\Phi(R, \Phi') d\Phi' \quad (4.51)$$

where  $\Phi'$  defines the position of the source, the input port, and  $\Phi$  is the position of the considered port. It is reminded that the input port is located at  $\Phi = 0$  rad, the output port at  $\Phi = \frac{2\pi}{3}$  rad and the isolated port at  $\Phi = -\frac{2\pi}{3}$  rad.

The Green's function will have the following expression [1]:

$$G(r, \Phi; R, \Phi') = \frac{j J_0(Kr)}{2\pi Y_{eff} J'_0(KR)} - \frac{1}{\pi Y_{eff}} \times \sum_{n=1}^{\infty} \frac{\frac{\kappa}{\mu} \frac{n J_n(Kr)}{KR} \sin n(\Phi - \Phi') - j J'_n(kR) \cos n(\Phi - \Phi')}{(J'_n(kR))^2 - \left(\frac{\kappa}{\mu} \frac{n J_n(kR)}{kR}\right)^2} \quad (4.52)$$

It is possible to determine the parameters of the impedance matrix from the Green's function.

$$Z_{11} = \frac{E_{z1}}{H_{\Phi 1}} \Big|_{H_{\Phi 2}=H_{\Phi 3}=0} = \int_{-\Psi}^{\Psi} G(0; \Phi') d\Phi' \quad (4.53)$$

$$Z_{21} = \frac{E_{z2}}{H_{\Phi 1}} \Big|_{H_{\Phi 2}=H_{\Phi 3}=0} = \int_{\frac{2\pi}{3}-\Psi}^{\frac{2\pi}{3}+\Psi} G\left(\frac{2\pi}{3}; \Phi'\right) d\Phi' \quad (4.54)$$

$$Z_{31} = \frac{E_{z3}}{H_{\Phi 1}} \Big|_{H_{\Phi 2}=H_{\Phi 3}=0} = \int_{-\frac{2\pi}{3}-\Psi}^{-\frac{2\pi}{3}+\Psi} G\left(-\frac{2\pi}{3}; \Phi'\right) d\Phi' \quad (4.55)$$

At first approximation, the Green's function is considered as being constant over the entire width of the access lines. Therefore, the previous expressions are written as follows:

$$Z_{11} = 2G(0; 0) \quad (4.56)$$

$$Z_{21} = 2G\left(\frac{2\pi}{3}; 0\right) \quad (4.57)$$

$$Z_{31} = 2G\left(-\frac{2\pi}{3}; 0\right) \quad (4.58)$$

By substituting these equations into Eq.4.45 to Eq.4.47, the expressions of the coefficients  $C_1$ ,  $C_2$  and  $C_3$  become finally:

$$C_1 = \frac{j\pi Z_d}{2Z_{eff}} + \frac{j\pi}{Z_{eff}} \Psi G(0; 0) \quad (4.59)$$

$$C_2 = \frac{j\pi}{Z_{eff}} \Psi G\left(\frac{2\pi}{3}; 0\right) \quad (4.60)$$

$$C_3 = \frac{j\pi}{Z_{eff}} \Psi G\left(-\frac{2\pi}{3}; 0\right) \quad (4.61)$$

By knowing the expressions of  $C_1$ ,  $C_2$  and  $C_3$ , it is then possible to calculate the S coefficients in order to estimate the performance of the Y-junction stripline circulator.



### 4.3.3.1 Loss-related calculation of the S-parameters

In order to accurately estimate the expected performance of the Y-junction stripline circulator, it is necessary to take the losses into account in the calculation of the S-parameters. For this purpose, the works of Neidert and Phillips [4] are studied. There are three types of losses in the circulator: magnetic and dielectric losses, as well as the losses that arise from the conductors.

The magnetic losses are introduced by taking into consideration the damping factor  $\alpha$  in the model of the magnetic material. Consequently, the quantities  $\mu$  and  $\kappa$  of the magnetic permeability tensor will be complex. Indeed, the imaginary parts will represent the losses. It comes:

$$\begin{cases} \mu = \mu' - j\mu'' \\ \kappa = \kappa' - j\kappa'' \end{cases} \quad (4.62)$$

The dielectric losses are introduced in the calculation of the S-parameters by writing the dielectric constant in the complex form. It is given by:

$$\begin{cases} \varepsilon_r = \varepsilon_r' - \varepsilon_r'' \\ \varepsilon_r'' = \varepsilon_r' \tan \delta \end{cases} \quad (4.63)$$

where  $\tan \delta$  is the dielectric loss tangent of the magnetic material. One will choose similarly the dielectric loss tangent of the dielectric material (substrate) surrounding the ferrite disks.

Since the conductors are not perfect at the ferrite-conductor interface, in addition to the normal electric field component and the tangential component of the magnetic field, there is a small tangential component of the electric field, and a small normal component of the magnetic field. To consider these conductors losses, one denotes  $G_B$  as Bosma's Green's function of Eq.4.52 and the new Green's equation is written [4]:  $G_N = G_B - G_{N1} - G_{N2}$ ; where  $G_{N1}$  and  $G_{N2}$  are the new terms given by:

$$G_{N1} = -\frac{(1+j) J_0'(kr)}{2\pi\sigma\delta} \frac{J_0'(x)}{J_0'(x)} + \frac{(1-j)}{\pi\sigma\delta} \times \sum_{n=1}^{\infty} \frac{(ad-bc) \sin n(\Phi - \Phi') - j(ac-bd) \cos n(\Phi - \Phi')}{c^2 - d^2} \quad (4.64)$$

$$G_{N2} = \frac{(1-j) \kappa J_0'(Kr)}{2\pi\sigma\delta} \frac{J_0'(x)}{\mu J_0'(x)} + \frac{(1+j)}{\pi\sigma\delta} \times \sum_{n=1}^{\infty} \frac{(ed-gc) \sin n(\Phi - \Phi') - j(ec-gd) \cos n(\Phi - \Phi')}{c^2 - d^2} \quad (4.65)$$

where

$$\left\{ \begin{array}{l} x = Kr \\ a = J'_n(Kr) \\ b = \frac{\kappa}{\mu} n \frac{J_n(Kr)}{kr} \\ c = J'_n(x) \\ d = \frac{\kappa}{\mu} n \frac{J_n(x)}{x} \\ e = \frac{\kappa}{\mu} J'_n(Kr) \\ g = n \frac{J_n(Kr)}{kr} \end{array} \right. \quad (4.66)$$

The introduction of two additional terms to the initial Green's function is not sufficient to correctly model the losses generated by the conductors. The attenuation produced by the conductors should be calculated. By analogy to TEM waves between two parallel conductors [4], the attenuation constant is expressed as :

$$Attenuation(dB) = \frac{8.686R_s l}{Z_{eff} h} \quad (4.67)$$

where  $R_s = (\sigma\delta)^{-1}$  is the surface resistance,  $Z_{eff}$  the wave impedance of the effective medium present between the two parallel planes and  $h$  the height of the ferrite disc. In the expression of  $R_s$ ,  $\sigma$  refers to the conductivity and the skin depth  $\delta$  is calculated as follows:

$$\delta = \frac{1}{\sqrt{\pi f \mu \sigma}} \quad (4.68)$$

$\mu$  represents the conductor permeability, and  $f$  is the operating frequency.

For the circulator, the length  $l$  corresponds to the distance between two successive ports, i.e.  $l = \frac{2\pi}{3}$ . In addition, an ideal (perfectly matched) circulator can be considered as a device with only two ports, one input port and one output port. Since the electric fields at the input and output ports are dephased by  $180^\circ$ , and the distance between them is  $l = \frac{2\pi}{3}$ . Moreover, the guided wavelength  $\lambda_g$  can be expressed as follows:

$$\lambda_g = \frac{4\pi R}{3} \quad (4.69)$$

Furthermore, the wave impedance of the effective medium present between the two parallel planes is expressed by:

$$Z_{eff} = \frac{120\pi}{\sqrt{\varepsilon_{reff}}} \quad (4.70)$$

where

$$\sqrt{\varepsilon_{reff}} = \frac{C}{f\lambda_g} \quad (4.71)$$

where  $\varepsilon_{reff}$  is the effective relative permittivity and  $C$  is the speed of light in vacuum. The attenuation induced by the conductors should be included in the S-parameters corresponding to the insertion losses in order to properly model the losses introduced by the

conductors. For example, if the EM wave circulates from port 1 to port 3 and then to port 2, the insertion loss parameter  $S_{31}$  will be corrected as follows:

$$S_{31} = 20 \log \left[ \frac{\pi Z_d (C_2^2 - C_1 C_3)}{j Z_{eff} (C_1^3 + C_2^3 + C_3^3 - 3 C_1 C_2 C_3)} \right] + \text{Attenuation}(dB) \quad (4.72)$$

Conversely, if the electromagnetic circulation occurs in the direction  $1 \rightarrow 2 \rightarrow 3$  then it is the parameter  $S_{21}$  that represents the insertion losses.

$$S_{21} = 20 \log \left[ \frac{\pi Z_d (C_3^2 - C_1 C_2)}{j Z_{eff} (C_1^3 + C_2^3 + C_3^3 - 3 C_1 C_2 C_3)} \right] + \text{Attenuation}(dB) \quad (4.73)$$

In addition, it should be noted that the ferrite thickness  $h$  is not taken into account in the calculation of the S-parameters of the circulator although the losses due to the conductors are taken into consideration.

#### 4.3.4 Stripline circulator based on $CoFe_2O_4$ nanocomposite

As a first approach, we determined the effective permeability of the nanowired  $CoFe_2O_4$  composite. In our study, we considered that we have  $CoFe_2O_4$  nanowires oriented along the wire axis. Thus, the magnetic substrate has a saturation magnetization  $M_s$  of 0.18 T and an internal static magnetic field  $H_i$  of 1.52 T (it is the sample electrodeposited and cooled under a magnetic field of 0.6 T).

The evolution of the effective permeability (Eq.4.12) of the  $CoFe_2O_4$  nanowires as a function of frequency was modelled using the modified Irashagi model (Fig.4.8).

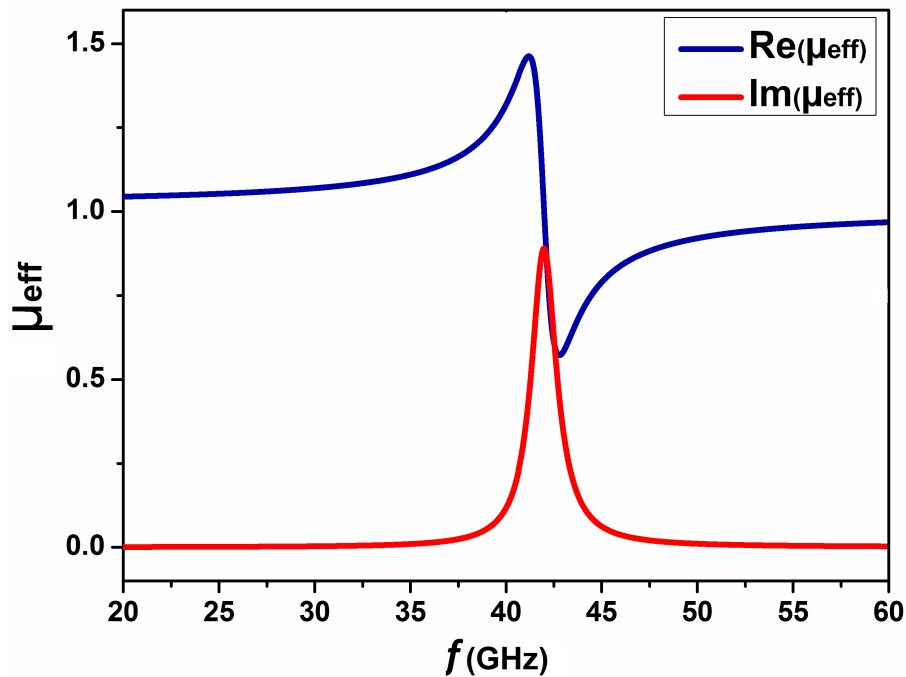


Figure 4.8: Evolution of the effective permeability for  $CoFe_2O_4$  nanocomposite as a function of frequency.

The resonance phenomenon of the effective permeability, when the internal field is fixed at 1.52 T, appears at a frequency of 42 GHz. Our objective is to realize a circulator that should operate around 40 GHz. However, this component does not operate at resonance; the circulator operates either below or above resonance. The operation of the circulator known as above and below resonance are understood to be in field, i.e. when the internal field is respectively higher or lower than the field required for the resonance. The geometrical parameters of the central conductor of the circulator have been determined using the formulas (Eq.4.29 and Eq.4.32), which depend on the effective permeability of the  $CoFe_2O_4$  nanowires. The estimations provide a radius  $R$  of the central conductor disk of  $475 \mu m$ , and an access line width  $W$  of  $72 \mu m$ .

Once the effective ferrite permeability has been evaluated, the values of the S-parameters between two consecutive ports of the circulator, as a function of frequency, can be analytically determined from the theoretical analysis performed previously. The conductor material is the copper. The dielectric material is the alumina surrounding the ferrite disks, which has a relative permittivity of ( $\epsilon_d = 10$ ). The permittivity of cobalt ferrite is fixed at 13. A dielectric loss tangent ( $\tan \delta = 10^{-2}$ ) has been taken into account in the analytical calculation. As can be shown in Fig.4.9, the modelled circulator using Matlab (Bosma) software operates at frequency of  $35.8 GHz$  (below resonance).

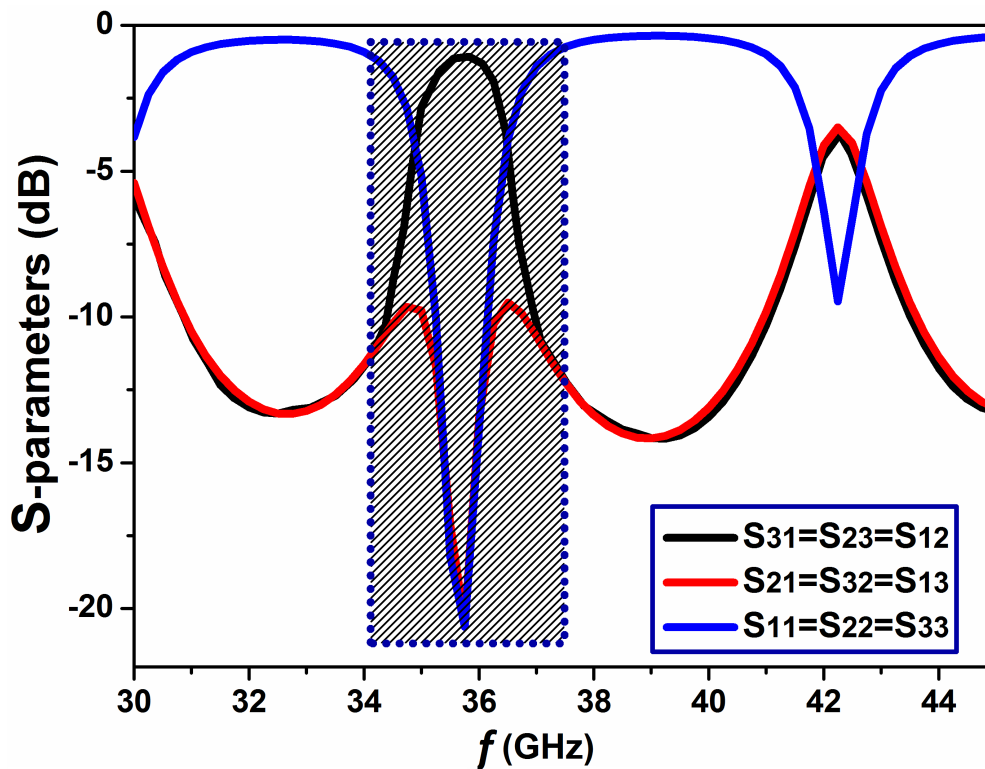


Figure 4.9: *The S-parameters as a function of frequency for the stripline circulator; analytical calculation.*

According to the evolution of the S-parameters as a function of frequency, the reflection is  $-20.45 dB$ , the isolation is  $-20.64 dB$  and the insertion loss is  $-0.98 dB$ . This is the best result obtained with the parameters already described.

As the structure concerned in our work is the coplanar topology, it does not correspond exactly to the one studied by Bosma, even though the operation principle remains the

same. Therefore, the optimized geometrical parameters ( $R, W$ ) will be maintained in the coplanar structure for the next analysis.

### 4.3.5 Numerical modeling and simulation

In this section we will firstly present the importance of the numerical simulation for our study, followed by a brief presentation of the used simulator. Then, we will evoke the protocol followed for the integration of the magnetic permeability tensor in the simulator.

#### 4.3.5.1 The selected numerical simulator

A numerical simulation tool is almost indispensable for our study. We have chosen this approach because it is less costly, it allows to gain a lot of time and offers the possibility to vary various parameters on the structure in order to study their influence without much difficulty. For the present study, the selected simulator is a commercial software developed by the company ANSYS called HFSS (High Frequency Structure Simulator) [5]. The HFSS simulator, as its name indicates, is a software used in the RF-HF electronics to study the electromagnetic behavior of microwave components.

The HFSS provides many options to study different electromagnetic behaviors and to perform many tasks such as:

- ▷ The determination of the S-parameters;
- ▷ The evaluation of the 3D mapping for the electric and magnetic field;
- ▷ The determination of the current density in a conductor ( $J_{vol}/J_{surf}$ );
- ▷ The determination of the admittance and impedance parameters ( $Y_{ij}$  or  $Z_{ij}$ );
- ▷ Etc.

A brief presentation of this simulator is outlined in the next paragraph.

#### Principle of the HFSS calculation

The HFSS calculates the electromagnetic fields using the Finite Element Method (FEM). Its principle of study consists in drawing at first the studied structure in 2D or 3D mode, and then to perform the field calculation by solving the Maxwell equations. A brief reminder of the principle of the FEM method used by HFSS is proposed in the coming paragraph. Fig.4.10 shows an interface image of the HFSS simulator.

**Finite Element Method (FEM):** the FEM is based on the resolution of the differential equations of the electromagnetic fields in the spectral domain [6-9]. It is therefore to solve a linear system of equations, the fields being the unknowns. The FEM allows to obtain a very accuracy results despite of a long calculation time, because the volume or surface to be analysed has to be entirely discretized into small elements or regions (see Fig.4.11). The small decomposed regions are called meshes.

**Meshed calculation in HFSS:** the calculation principle of the HFSS simulator is to excite the component using a source and then to calculate, for example, its S-parameters using the FEM. Therefore, the studied space being divided into a large number of elements or regions of small dimension (mesh), each element has several nodal points that form a tetrahedron (3D structure). However, the value of the S-parameters retained in each element is that obtained after an interpolation of all the other S-values at the center of each region. It is therefore important to mesh as finely as possible in order to obtain

a high accuracy of the final result. To make a mesh, HFSS uses the adaptive meshing

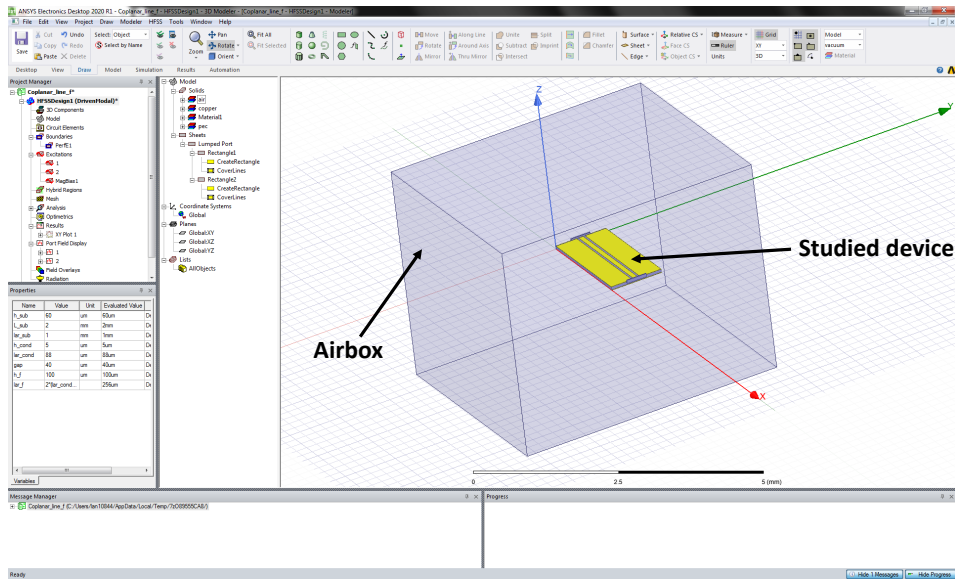


Figure 4.10: *Interface of the HFSS simulator.*

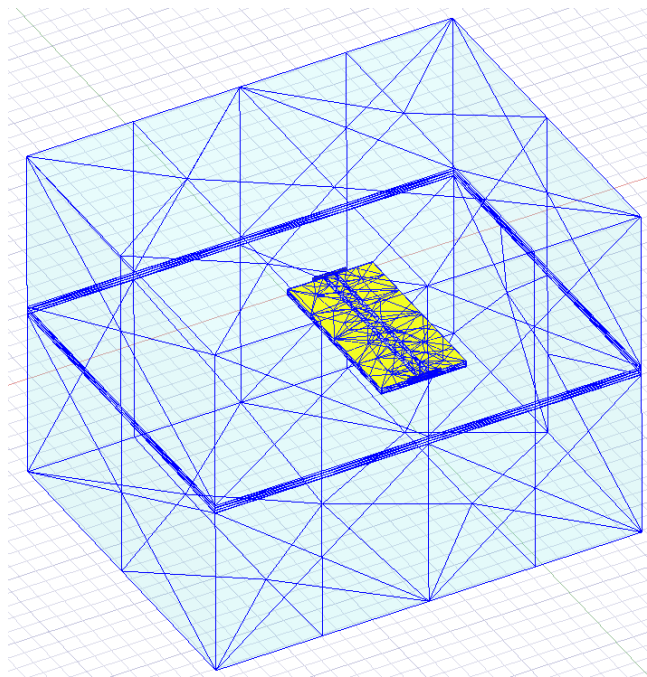


Figure 4.11: *Example of a meshed structure.*

method. This method consists in creating an assembly of elements at a single frequency defined by the user on the entire range of study. In our case, we have configured the adaptive meshing frequency at 40 GHz. Then, HFSS densifies the meshing in an iterative procedure especially in the space indicated by the user or by default in the areas that present large or complex errors. In order to densify a meshing or to stop it, the HFSS simulator compares two consecutive solutions resulting from the last two meshing. If the

difference satisfies to a certain condition defined by the user (as described later in this section), then the meshing process is finished. Otherwise, the domain is meshed more finely again. Moreover, the mesh size influences the accuracy of the simulation results. For our case study, we have taken into account the high frequency effects on the conductor part of the component to define a mesh size. A fine meshing is also required on the complex zones and on the surface of the component. The total number of meshes that one can have on such a structure can be of the order of 100 to 150 thousand tetrahedrons.

**Simulation condition:** when the simulation is finished, only one condition needs to be checked. It is the good convergence of the " $\Delta S_{max}$ " parameter. This condition is used to judge the stability of the calculations performed by the simulator. As the discretization of the studied space is carried out iteratively, HFSS compares the difference of the  $S_{ij}$  parameters calculated between 2 successive iterations (Pass) to a user-defined parameter. If the difference between two iterations is greater than  $\Delta S_{max}$ , the iterations must be continued, otherwise the solution is stable and the calculation is stopped (converged). The parameter  $\Delta S_{max}$  must be fixed to the smallest possible value in order to have an accurate and real solution. As a result, the more the convergence criterion ( $\Delta S_{max}$ ) is small, the more the calculation time will take a long time, and the more the necessary memory of the machine will be important, but the more the solution will be accurate and representative. For our case, we have imposed this value of the  $\Delta S_{max}$  parameter to  $10^{-3}$ . Fig.4.12 illustrates an example of a convergence curve obtained in a simulation. We can observe a very small variation of this curve when the target (the value of the parameter  $\Delta S_{max}$  imposed by the user) is reached.

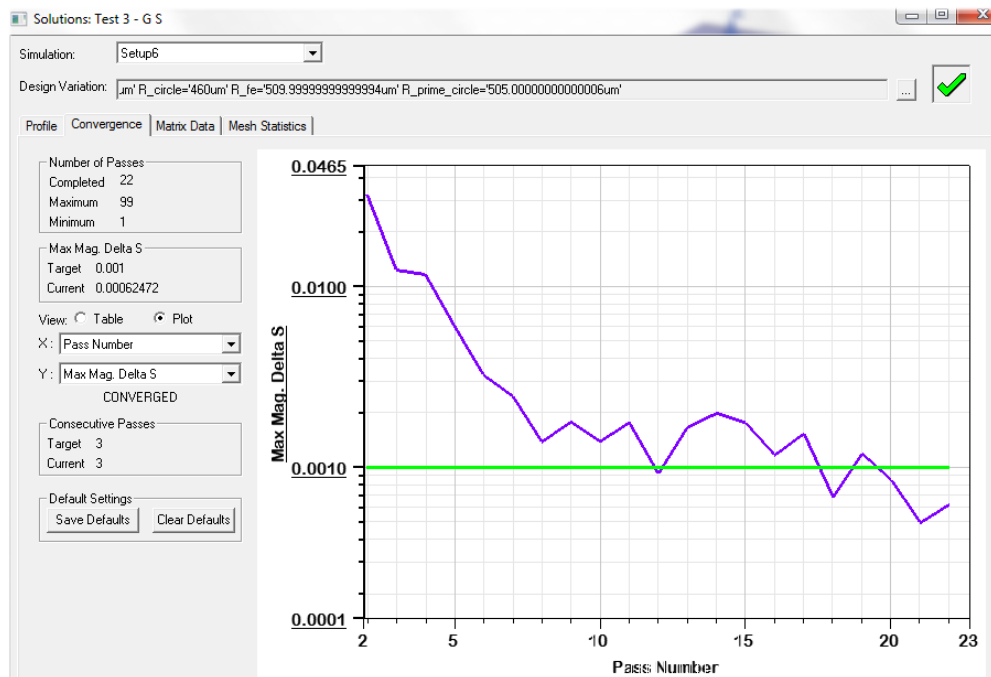


Figure 4.12: Example of a convergence curve.

In the next paragraph, we will present the main simulation steps that we have followed to carry out each component study.

## Simulation steps in HFSS

In this paragraph, we outline the different steps to be followed in order to simulate the electromagnetic response of an integrated component. These steps can be listed in the following chronological order:

- designing the structure in 3D mode on an air box. This box is designed and defined in the simulation tasks in order to limit the calculation space. When the dimensions are sufficiently large, the results are accurate and independent from the air box dimensions;
- assigning a material for the various objects that constitute the component. This step consists in assigning to each object a material with characteristics corresponding to its function in the component;
- defining the borders and boundary conditions. It consists in delimiting the studied space using an air box and defining boundary conditions at its edges. The accuracy of the results obtained at the end of a simulation depends on this step. A long study on the parameters of the boundary conditions was conducted in order to choose the optimal dimensions of the air box and the type of the boundary;
- defining a component excitation source. This step consists in selecting an excitation mode adapted to the conditions of the component study, and then to defining the power supply of the component;
- defining the simulation parameters such as the simulation frequency, a convergence criterion ( $\Delta S_{max}$ ), a maximum number of iterations, etc;
- running the simulation. The simulation duration depends on the structure and the simulation setting (which lead to accuracy results). Example: the simulation duration of a structure without ferrimagnetic nanocomposite is about 4 hours per sample while for structures based on magnetic material, the duration can be up to about 15 hours;
- processing the obtained results.

### 4.3.5.2 Integration of $CoFe_2O_4$ permeability tensor in HFSS

The anisotropic nature of the nanowires can be modeled using HFSS, either by using Polder formulations or by setting a user-defined permeability tensor. Conventionally, the Ansys HFSS uses the Polder model to calculate the components of the permeability tensor. As mentioned in chapter 2, the Polder model is only valid for the saturated state of the magnetic material.

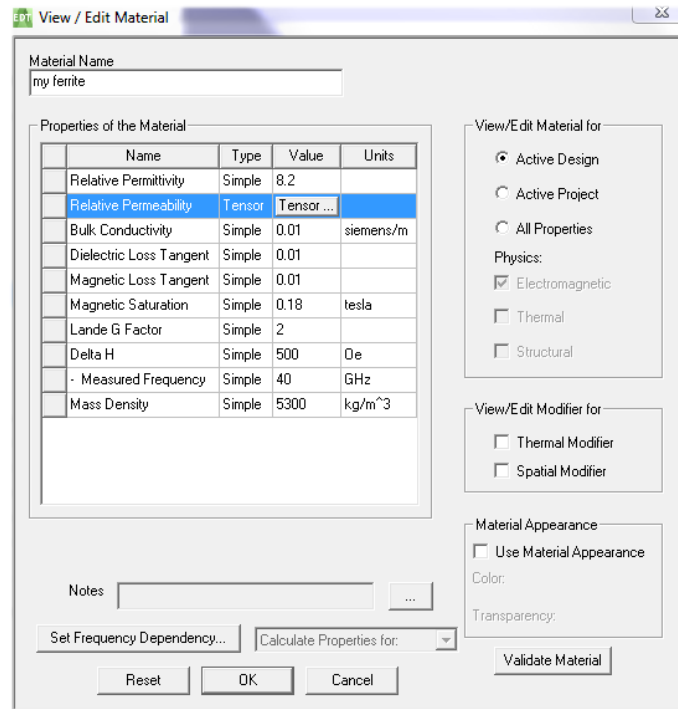
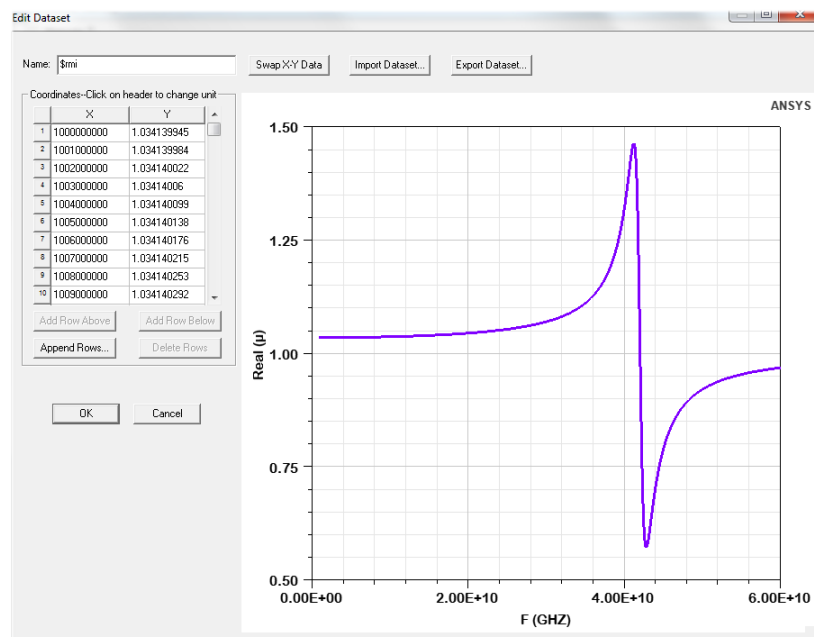
When the applied field is along z direction, the permeability tensor can be expressed as,

$$\hat{\mu} = \begin{pmatrix} \mu' - j\mu'' & -j(\kappa' - j\kappa'') & 0 \\ +j(\kappa' - j\kappa'') & \mu' - j\mu'' & 0 \\ 0 & 0 & \mu'_z - j\mu''_z \end{pmatrix} \quad (4.74)$$

Ansys Electronic Desktop Version 2017 and above offers the possibility to define the nine components of the permeability tensor as shown in Fig.4.13. This function allows the user to independently define the real and imaginary parts of the tensor elements. It is also possible to define these elements as frequency-dependent functions. This makes it possible to integrate our adopted model for the permeability of the  $CoFe_2O_4$  nanocomposite into HFSS, in order to accurately predict the microwave response of the targeted component.

As presented in Fig.4.14, HFSS has a function to define datasets with user-defined points,



Figure 4.13: *Material characteristics-HFSS.*Figure 4.14: *Definition of datasets into HFSS.*

each permeability tensor element can be defined as frequency dependent, using the data set inserted by the user as the first parameter of the piecewise linear interpolation function ( $pwl(\text{dataset} - \text{expression}, \text{variable})$ ). Thus, the frequency domain solver in HFSS must be able to quantify the expressions and calculate the value of the permeability tensor components at any desired frequency value. Our approach is based on the integration of the data points (calculated from the theoretical model in Matlab software) and on the proceeding of their linear interpolation into frequency dependent functions. The

permeability of materials is defined using the tensor function in HFSS. The real and imaginary parts of the permeability tensor components are imported as separate datasets into HFSS. Each dataset is interpolated into frequency-dependent functions using an intrinsic piecewise linear interpolation function. These frequency-dependent functions are then used to define the complex components of the permeability tensor.

#### 4.3.6 Simulation of a coplanar circulator based on $CoFe_2O_4$ nanocomposite

The circulator to be realized in this thesis is in its coplanar topology with a bottom ground plane as shown in Fig.4.15.a. The coplanar structure, as the name suggests, is a topology having its conductor planes in the same level separated by a small distance  $G$  (Fig.4.15.b).

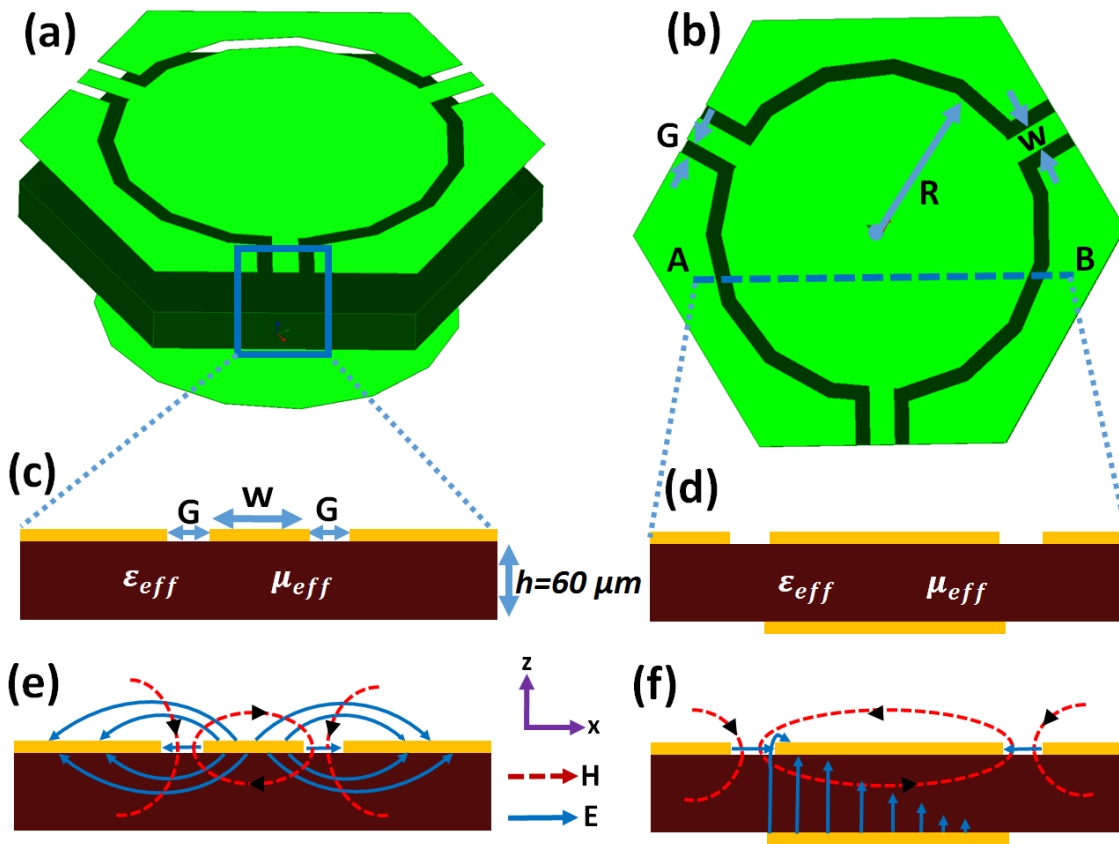


Figure 4.15: Coplanar topology; (a) coplanar circulator with a bottom ground plane, (b) top view of the coplanar circulator, (c) cross sectional view of the CPW of the circulator, (d) A-B cross-sectional view of the circulator with ferrimagnetic substrate, (e) schematic distribution of the RF fields for a CPW line, (f) field displacement in the center of the circulator with coplanar junction.

In order to form an idea of the operation of the coplanar circulator, one considers the coplanar access (CPW) of the circulator. As illustrated in Fig.4.15.c, the electric field  $E$  is stronger in the plane containing the line and the ground planes (horizontal direction). Then, the EM signal is transported towards the central conductor disk of the circulator via the CPW printed on the ferrimagnetic substrate. So, a bottom ground plane which is

not connected to the upper ground planes is patterned under the central disk (Fig.4.15.a, d). This ground plane provides a better transition of the EM signal propagated from the access line (horizontally) to the circular portion of the central conductor (vertically). As the center of the coplanar circulator is very similar to a stripline structure, the electric field must be modified. This, because, in the stripline structure (Fig.1.13), the electric field is stronger in the space sandwiched by the line and the ground planes (vertical direction). As result, the electric field displacement between the central conductor and the bottom ground plane facilitates the field transition between the CPW access and the central conductor disk of the circulator (Fig.4.15.f).

It should be noted that the access line width  $W$  and the radius  $R$  of the central disk have been theoretically optimized in the previous section. Moreover, the radius of the bottom ground plane disc is defined as the sum of the width of the central radius and the spacing gap  $G$  in order to improve the phenomenon of the electric field displacement at the central part of the circulator. So, the only remaining task is the optimization of  $G$ . To obtain the right  $G$ -value and to evaluate the performance of our ferrimagnetic nanocomposite, simulations of the CPW, which ensure the input and output of the EM signal to the circulator, were carried out.

The nanowired ferrimagnetic substrate employed in our work is an alumina membrane, electromagnetically charged by  $CoFe_2O_4$  nano-crystallites. Before proceeding to the HFSS simulation, we have used a simple law of proportionality in order to approximate the effective permittivity  $\varepsilon_{eff}$  of the nanocomposite, determined as a function of the nano-crystallites concentration and the AAO membrane pores filling coefficient [10, 11]:

$$\varepsilon_{eff} = (1 - p)\varepsilon_{AAO} + \rho_{CoFe_2O_4}p\beta\varepsilon_{CoFe_2O_4} \quad (4.75)$$

where  $p$  is the porosity of the AAO membrane,  $\beta$  the filling coefficient of the AAO membrane pores by  $CoFe_2O_4$  nano-crystallites,  $\rho_{CoFe_2O_4}$  the concentration of  $CoFe_2O_4$  nano-crystallites contained in the pores,  $\varepsilon_{AAO}$  the permittivity of alumina, and  $\varepsilon_{CoFe_2O_4}$  the permittivity of bulky  $CoFe_2O_4$ .

The typical characteristic properties of the ferrimagnetic nanocomposite are listed in Table.4.1.

Table 4.1: *Characteristics of  $CoFe_2O_4$  nanocomposite.*

$\beta$	$p$	$\rho_{CoFe_2O_4}$	$\varepsilon_{AAO}$	$\varepsilon_{eff}$	$\mu_o M_s(T)$	$\Delta H$ (Oe)	$\tan\delta$	$\alpha$	$\mu_o H_i(T)$
100%	50%	50%	10	8.2	0.18	284	$10^{-2}$	0.017	1.52

We must keep in mind that we used  $CoFe_2O_4$  nanowires in order to benefit from its strong magnetocrystalline anisotropy to prevent the application of an external field. Subsequently, the excitation field of the component is limited in our case to the anisotropy field of the  $CoFe_2O_4$  nanowires.

The coplanar line was simulated and adapted with HFSS software when no external magnetic field is applied (Fig.4.16). The simulation was performed by considering the saturation magnetization of the  $CoFe_2O_4$  nanocomposite and the effective internal field  $H_i$ . After several simulation tasks, a value of  $40 \mu m$  was estimated for spacing gap  $G$ . As displayed in Fig.4.17, the performed simulation has shown that the CPW exhibits a gyromagnetic resonance at a frequency of  $42 GHz$ .

In order to check the fidelity of the obtained result from HFSS, it is possible to deduce

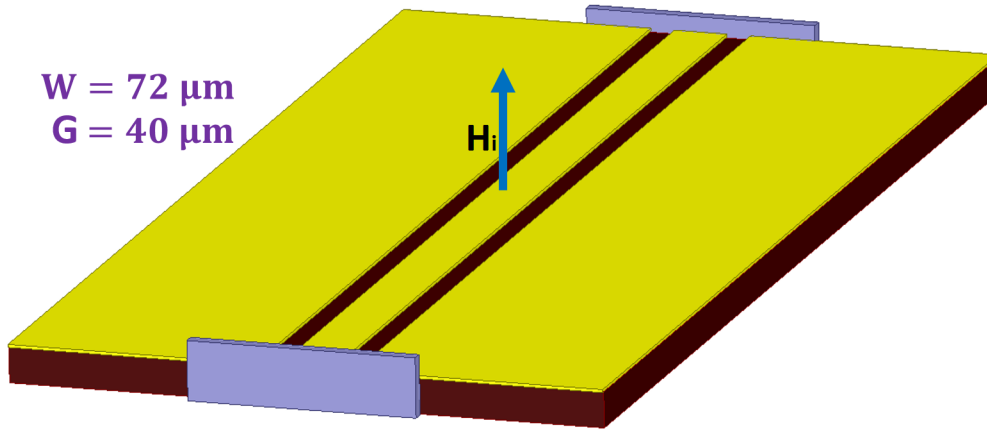


Figure 4.16: Simulated CPW based on the ferrimagnetic nanocomposite.

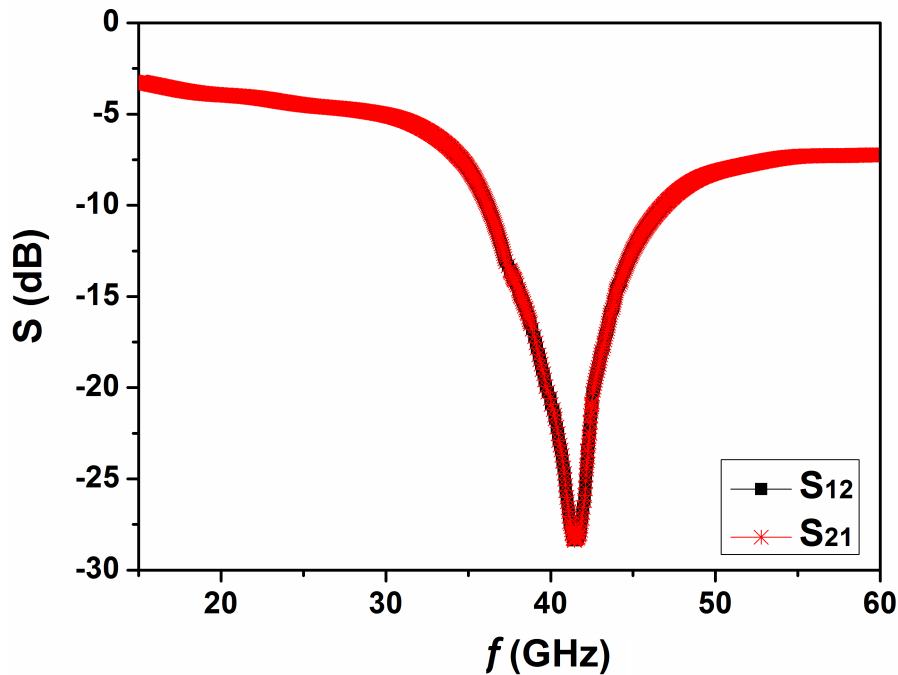


Figure 4.17: Simulated CPW based on the ferrimagnetic nanocomposite.

the effective internal magnetic field as a function of the resonance frequency value using the Kittel formula [12].

$$2\pi f_{res} = \gamma \times \mu_o H_i \quad (4.76)$$

where  $\gamma$  is the gyromagnetic ratio ( $\gamma = 2\pi \times 28 \text{ GHz}/T$ ).

The calculation gives an effective internal magnetic field close to  $1.52 \text{ T}$ , which is in good agreement with the experimental value deduced from the SQUID-VSM measurement. From these results, we decided to maintain the value of  $G$  ( $40 \mu\text{m}$ ) in the simulation of the coplanar circulator.

The coplanar circulator has been dimensioned according to the previously optimized values and then simulated on HFSS (Fig.4.18). The circulator was modeled and adapted to have the input impedance of the ports equal to  $50 \Omega$ . Fig.4.19 shows the simulation

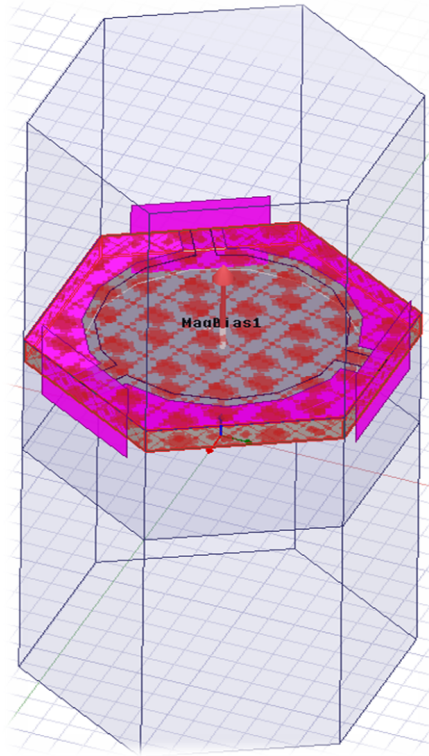


Figure 4.18: *Simulated coplanar circulator on HFSS .*

results of the designed circulator.

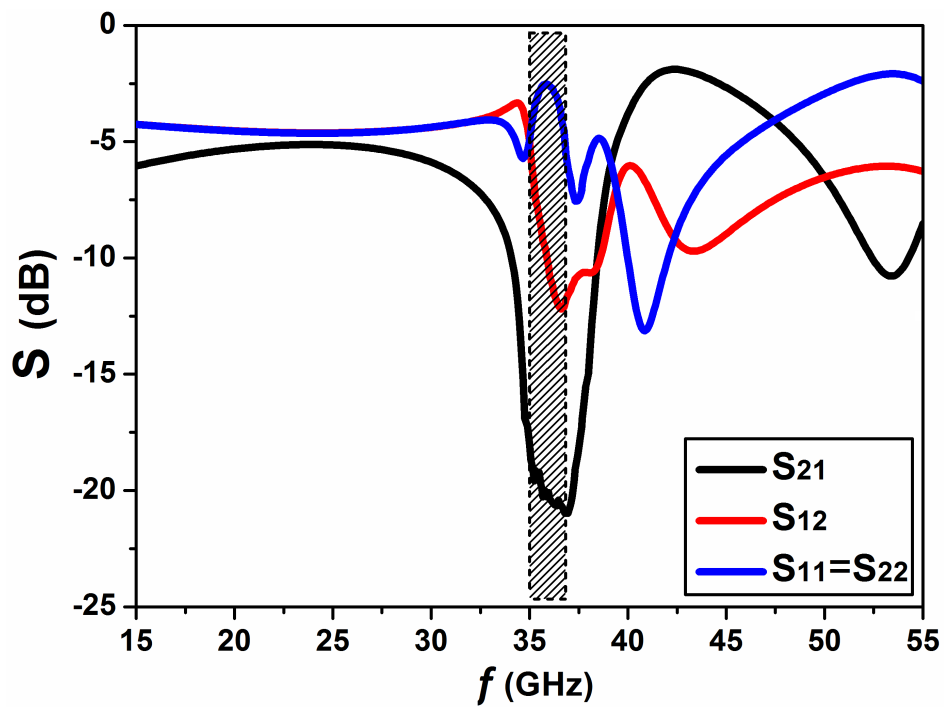


Figure 4.19: *Simulated S-parametres of the coplanar circulator.*

As shown in the simulation finding, one can observe a remarkable operation of the circulator around  $35.7\text{ GHz}$  for a bandwidth of  $1\text{ GHz}$ . In this band, the insertion losses

are  $-2.57$  dB, the insulation varies from  $-6$  to  $-10.33$  dB and the reflection coefficient is around  $-20.2$  dB. The present simulation shows that it is feasible to have a non-reciprocal effect of the circulator based on  $CoFe_2O_4$  nanocomposite. This requires the fabrication of the circulator as well as its microwave characterization.

## 4.4 Fabrication and microwave characterization of the CPW and Circulator

After designing and dimensioning the CPW and coplanar circulator through various analytical and numerical studies, prototypes were fabricated and characterized. The fabrication process and the different technological steps are exposed. The prototypes are then characterized using a microwave measuring bench consisting of a vector network analyzer (VNA) coupled with a probe tester. The measured S-parameters enable to conclude about the performance of the prototypes. No external magnetic field is applied during these experimental measurements. This makes it possible to check that the concept of self-biased circulator is achievable with our ferrimagnetic nanocomposite. In view of the experimental results, various suggestions are formulated and perspectives are envisaged in order to improve the performance of the targeted circulator.

### 4.4.1 Fabrication protocol of the circulator

The realization of the structures modeled under HFSS, requires many technological processes, which will be detailed in this section by presenting the equipment used in its fabrication.

The main technological steps followed for the fabrication of these structures can be summarized in three phases, which are:

- *Deposition of copper and preparation of substrate;*
- *Photolithography;*
- *Etching and tinning .*

#### 4.4.1.1 Deposition of copper and preparation of substrate

The preparation of the ferrimagnetic nanocomposite involves the deposition of copper, the sticking and the grinding processes.

A glass slide or insulator material (Alumina,...) serves as a mechanical carrier for the magnetic nanocomposite on which a  $5 \mu\text{m}$  layer of copper is deposited. This first layer of copper acts as a bottom ground plane of the circulator. The copper is deposited by the Radio-Frequency (RF) sputtering technique. This technique is a process that can be defined as the ejection of the superficial atoms of a material target to be deposited by ionized argon atoms, followed by the transfer of these ejected atoms onto a substrate to be covered with a thin film. This process takes place in a vacuum chamber in which the target and the substrate are placed, as shown in Fig.4.20.

Using a pumping unit (vane pump in series with a turbo-molecular pump) an ultimate vacuum between  $10^{-6}$  and  $10^{-7}$  mbar is reached. The bombardment ions are created from a neutral gas. The gas used is argon due to its high atomic mass and its chemical inertia. By applying a RF alternative voltage to the target, a plasma consisting of argon ions

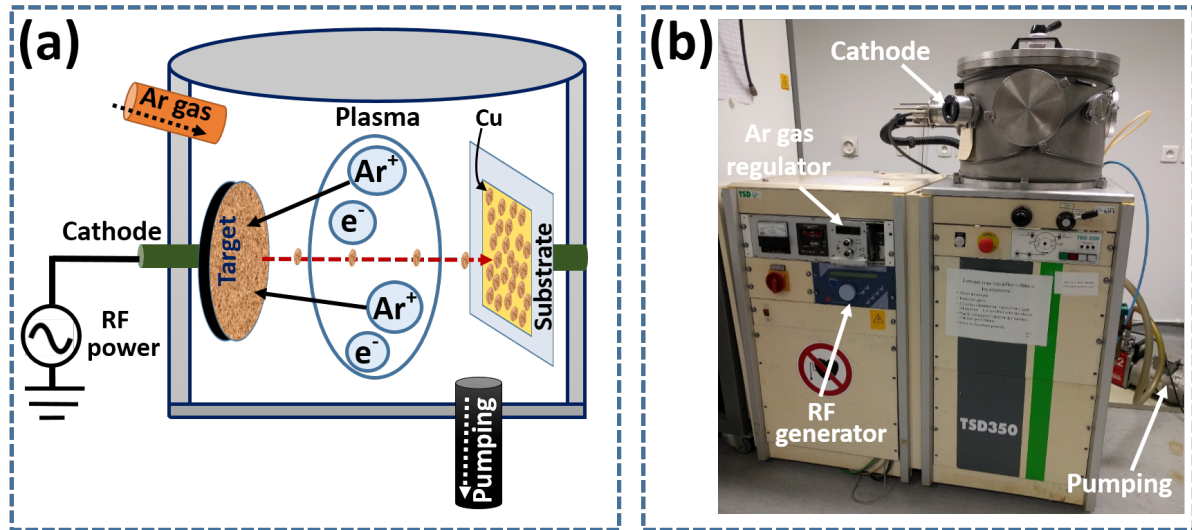


Figure 4.20: *Frame of TSD350 RF sputtering.*

and electrons is created, this brings the chamber pressure to a value between  $10^{-3}$  and  $10^{-1}$  *mbar* depending on the deposition parameters. The created ions are attracted to the negatively polarized electrode: the cathode where the target is located. The impact with the target will liberate atoms from the target and again electrons that will be able to ionize other gas atoms. The process is thus maintained. The ejection of the atoms is a purely mechanical effect due to the impact of the ions on the material to be deposited. The phenomenon involved is the transfer of the quantity of movement. The ejected atom will arrive on the substrate with certain energy, allowing it to be adhered on the substrate. The latter will gradually cover itself with a thin layer of the same material as the target by condensation. The formation of the thin film involves two stages: nucleation and growth. For all copper deposits performed at the LHC using the *TSD350* frame, we have implemented the following parameters: an Argon pressure of 20 *sccm* (standard cubic centimeters per minute), a distance between target and substrate equal to 6.7 *cm*, a frequency of 13.5 *MHz*, a deposition power of 300 *W* and a deposition pressure close to  $10^{-2}$  *mbar*. At these parameters, 30 minutes are sufficient to deposit 5  $\mu\text{m}$  of copper on the substrate.

The sticking of the ferrimagnetic nanocomposite on the metallized glass substrate enables to obtain a rigidity in order to manipulate it without damaging it. The sticking is carried out using the "Geo-fix" glue. The whole is placed on a heated plate at 70  $^{\circ}\text{C}$  for two hours with an imposed weight to apply pressure in order to decrease the thickness of the glue between the glass and the nanocomposite. Once glued, the ferrimagnetic substrate is polished with a very fine optical paper in order to obtain a roughness close to 100 *nm* which will favour a good adhesion of the copper that will be deposited to make the conductor and the top ground planes.

#### 4.4.1.2 Photolithography

The photolithography is a technique that leads to transfer a pattern from a mask on a substrate. The main photolithography steps performed in the clean room are:

- *Surface cleaning;*



- *Resin deposition and annealing 1*;
- *Resin insulation and annealing 2*;
- *Development of the insulated resin and annealing 3*.

#### i) Surface cleaning

The cleaning of the substrates is done in several steps. First, the substrate is rinsed with acetone and distilled water successively to remove the large dust grains and the protective resin deposited on the substrate. Next, the cleaning is continued in the Wet Bench where the cleaning process starts with 10 minutes of ultrasound in the acetone bath, followed by 10 minutes in the ethanol bath and finally 10 minutes in distilled water.

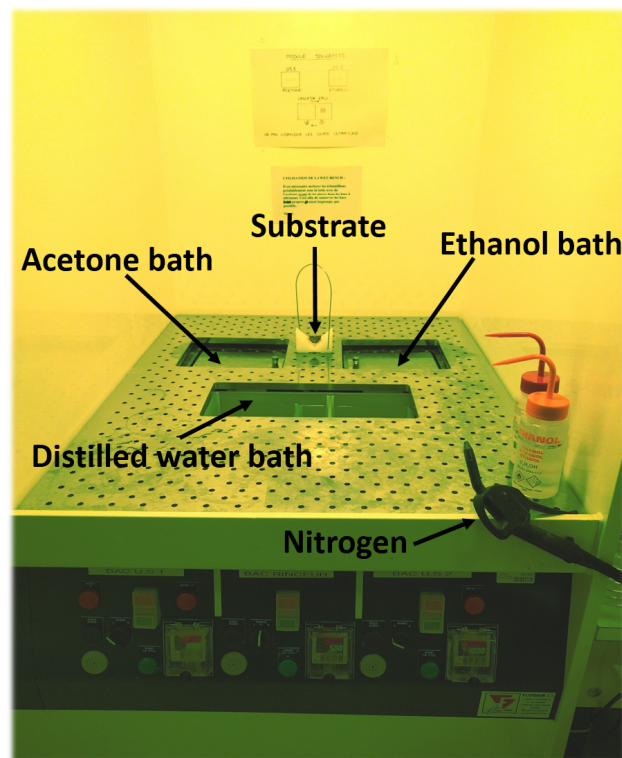


Figure 4.21: *Wet Bench in clean room.*

After these cleaning steps, the next step of the photolithography is initiated.

#### ii) Resin deposition and annealing 1

In order to obtain a better adhesion of the resin on the copper surface, it is recommended to deposit a SurPass 4000 layer, which is an advanced aqueous solution based on priming agents that ensures a maximum adhesion of a wide range of substrates. Thus, the substrate is placed on the spinner and a few drops of SurPass 4000 are injected. An aspiration system is required to fix the substrate on the spinner, which rotates at a speed of 5000 rpm for 30 seconds in order to obtain a very thin layer of SurPass. Then, some drops of the SPR 505 resin (positive resin) are added and the spinner is started (Fig.4.22). After finishing the deposition, the substrate is heated in the furnace at  $90\text{ }^{\circ}\text{C}$  for 90 s. This annealing step aims to evaporate quickly the solvents.



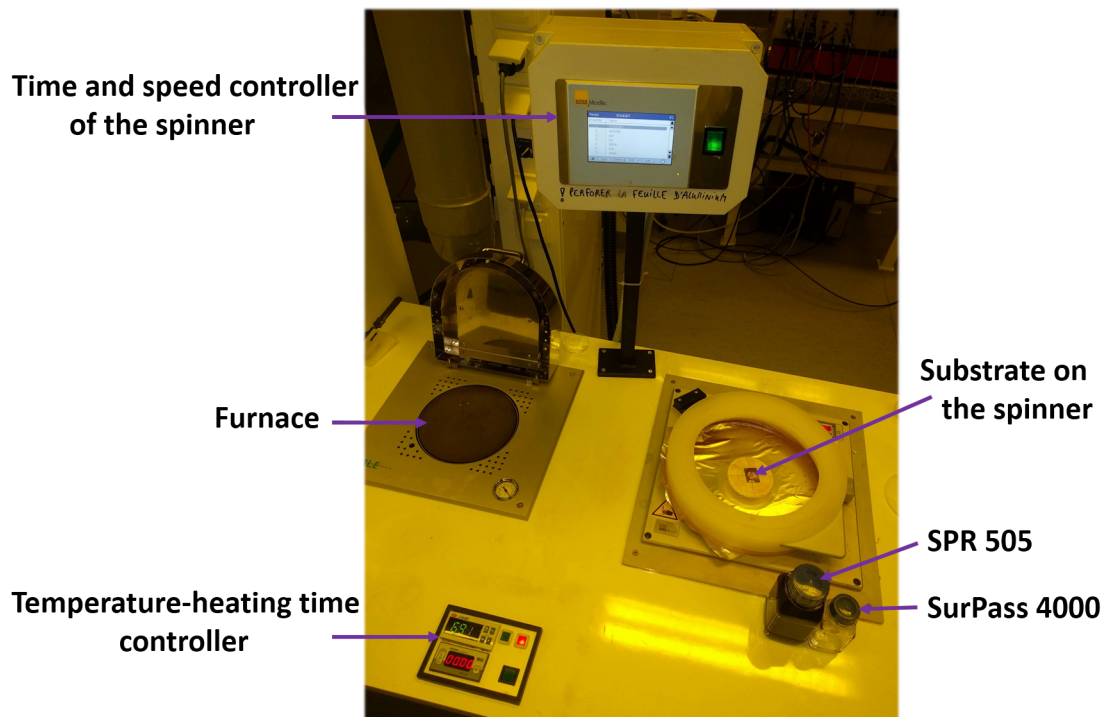


Figure 4.22: Resin deposition equipment used in the clean room.

### iii) Resin insulation and annealing 2

The resin-coated substrate is placed in a contact exposure machine presented in Fig.4.23.

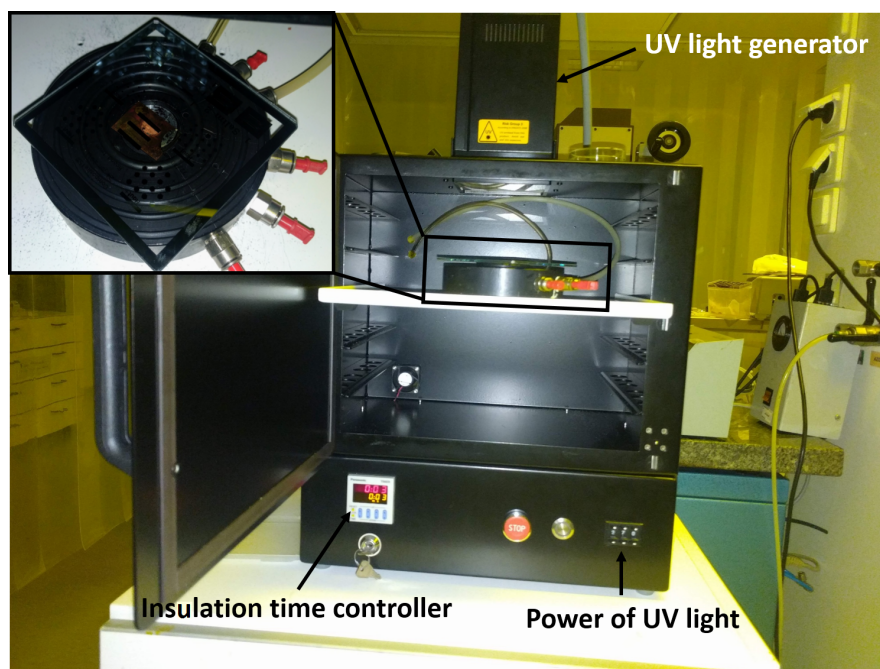


Figure 4.23: UV insulation machine.

Then, it is directly positioned below the chromium-glass pattern mask. When the posi-

tioning is satisfactory, the substrate is brought into contact with the mask by an aspiration system. The all are positioned in front of the Ultraviolet (UV) lamp of the machine. The substrate-mask contact must be perfect to avoid any diffraction phenomena. It is insulated by the UV light for 3 seconds with a power of 270 Watts. Finally, to activate the polymerization of the resin, a second annealing is carried out in the furnace at  $110\text{ }^\circ\text{C}$  for 90 s.

### iii) Development of the insulated resin and annealing 3

The UV-exposed resin is dissolved in the MF-319 developer and reveals the non-insulated resin. Once revealed, the substrate is rinsed slowly with distilled water and carefully dried again with nitrogen before proceeding to a final annealing at  $110\text{ }^\circ\text{C}$  for 4 min. This last heat treatment densifies the resin to prevent the penetration of the perchloride into the resin during the etching process. It also makes the resin mechanically more resistant.

#### 4.4.1.3 Etching and tinning

The photolithography step is followed by the chemical etching phase which consists on removing, using the iron perchloride, the copper that has not been protected by the resin. Before starting the procedure, a quantity of iron perchloride is diluted in water with a percentage of 50%-50% in order to not remove all the copper from the substrate. This solution is placed in a recipient which is itself placed in a water bath in order to accelerate the chemical reaction. Then, the substrate is placed in the diluted iron perchloride solution until the copper unprotected by the resin is removed. After, the substrate is rinsed with the distilled water to stop the reaction of the iron perchloride and make the conductive lines appear. In order to protect the copper and the etched circuit from oxidation and corrosion, it is necessary to tin it. The tinning at LHC is done chemically with a cold aqueous Tin (Sn) solution. It suffices to immerse the substrate in the solution for 1 minute at maximum in order to deposit a pure Sn layer on the etched pattern.

Fig.4.24 illustrates the different steps required to fabricate a coplanar circulator based on the ferrimagnetic nanocomposite.

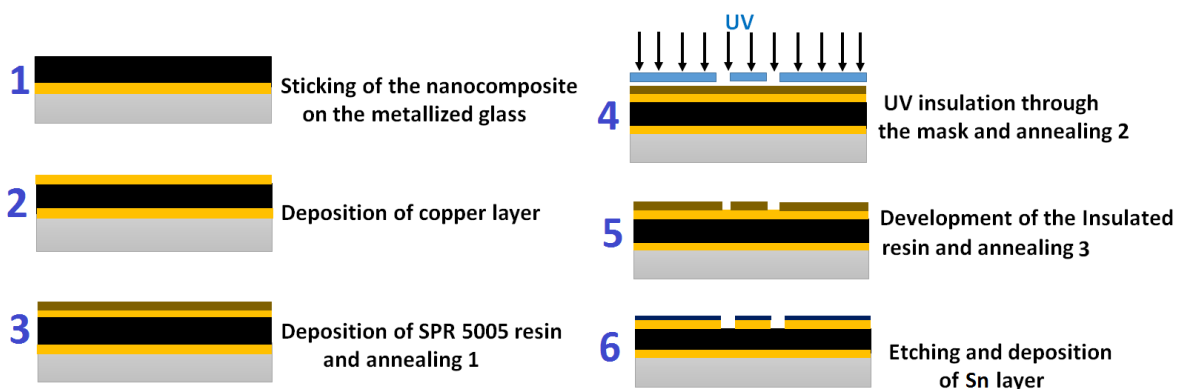


Figure 4.24: *Technological steps for the fabrication of the circulator.*

Fig.4.25 shows multiple coplanar circulators printed on the nanocomposite with the theoretically and numerically optimized dimensions.

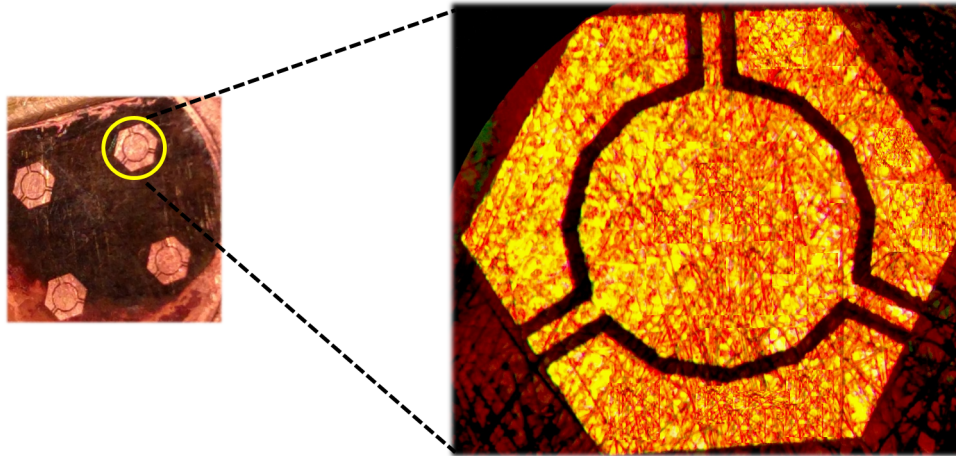


Figure 4.25: Printed coplanar circulators on the nanocomposite surface.

## 4.4.2 Microwave characterization

### 4.4.2.1 Characterization bench

The microwave characterization was carried out within LHC, in order to evaluate the performance of the fabricated prototypes. As shown in Fig.4.26.a, the measurement bench has a carrier for fixing the prototype using an aspiration system. Moreover, a two-ports vector network analyzer (VNA) operating in the  $40\text{ MHz} - 67\text{ GHz}$  band and equipped with three coplanar GSG (Ground-Signal-Ground) probes and its holders. A microscope is also associated with the measurement bench for positioning the probes on the millimeter-sized components. To measure the microwave response of the CPW, two coplanar probes are positioned oppositely to each other on the component as shown in Fig.4.26.b. Concerning the Y-junction circulator that has three access ports, it is necessary to have three points oriented at  $120^\circ$  (Fig.4.26.c). One of the third probes is connected to a load from  $50\ \Omega$  because even though the circulator is a 3-port component, it is possible to perform only 2-port measurements with our VNA. Before starting the measurements, an OSTL (Open-Short-Through-Load) calibration must first be performed for each port with a substrate suitable for the tips (calibration kit). This calibration will enable the analyzer to correct any systematic measurement errors, such as cable and connector errors. Afterwards, we can measure the  $S_{ij}$  parameters to visualize the gyromagnetic resonance phenomenon for the CPW and the circulation phenomenon for the circulator.

### 4.4.2.2 Measured S-parameters

Fig.4.27 present the collected S-parameters of the CPW based on the ferrimagnetic nanocomposite. For these measurements (Fig.4.27.a), we obtain a reciprocal behavior ( $S_{12} = S_{21}$ ), which was expected because the configuration adopted during the microwave measurements does not allow to observe the non-reciprocal effect. More precisely, in our realized structure the internal magnetic field  $H_i$  remaining along the  $CoFe_2O_4$  nanowires is perpendicular to the electric field existing on the copper lines, which prevents the birth of the field displacement phenomenon. The measurements show significant losses around  $41.2\text{ GHz}$  originated from the  $CoFe_2O_4$  nanowired nanocomposite. We can note a fairly broadband effect due to the gyromagnetic resonance of the ferrimagnetic  $CoFe_2O_4$  composite. For comparison, the simulated (HFSS) and measured (VNA) transmission



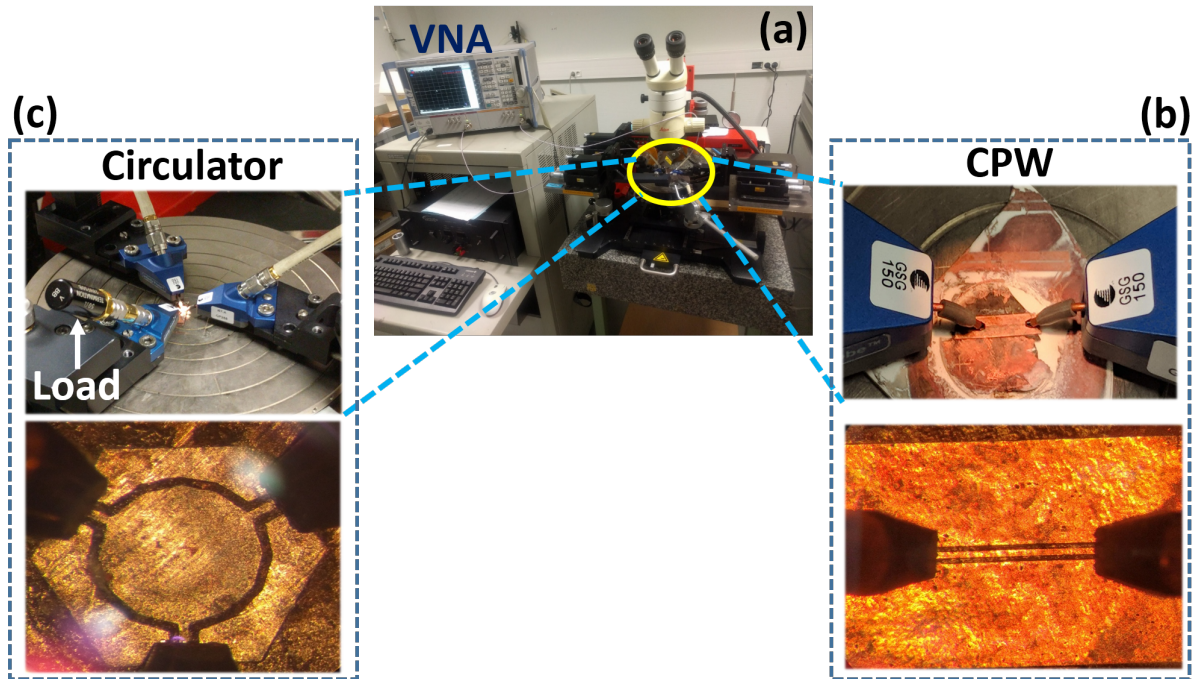


Figure 4.26: Microwave characterization bench; (a) measurement equipment, (b) probes configuration for the CPW structure, (c) probes configuration for the coplanar circulator.

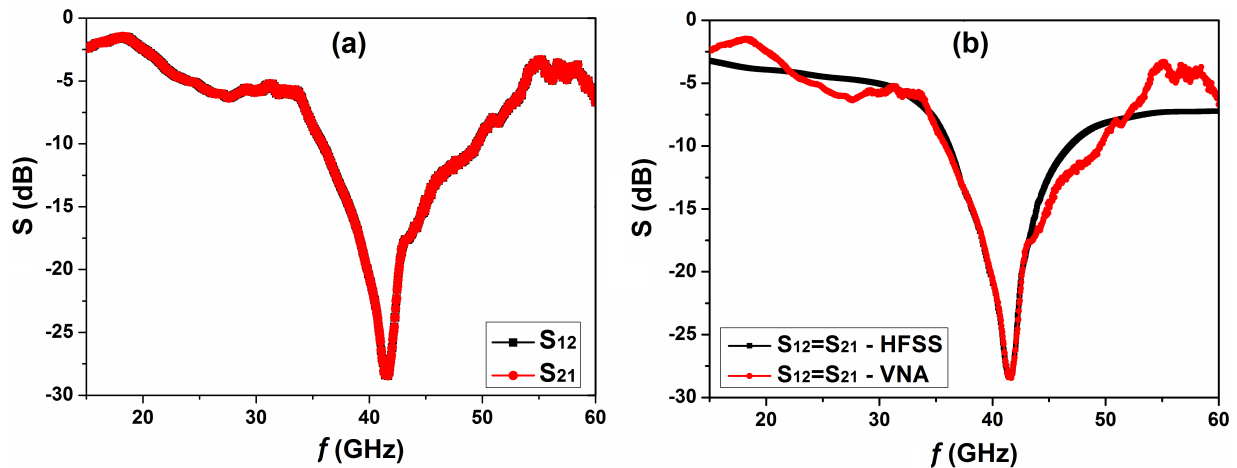


Figure 4.27: CPW S-parameters; (a) measured forward  $S_{12}$  and reverse  $S_{21}$  transmission coefficients, (b) comparison between HFSS and VNA results.

parameters  $S_{12}$  and  $S_{21}$  are plotted on the same graph (Fig.4.27.b). As a matter of fact, the experiment reproduces the simulation predictions that are based on the theoretical model of the permeability, which takes into account the moments orientation of  $CoFe_2O_4$  nano-crystallites inside the nanowires.

Fig.4.28 represents the S-parameters, measured on a frequency band from 15 to 65 GHz of the coplanar circulator made of the ferrimagnetic substrate, which has been separated into two components: reflection and transmission parameters. It should be noted that no magnetic field was applied during this phase. As shown in Fig.4.28, the reflection curves at port 1 ( $S_{11}$ ) and port 2 ( $S_{22}$ ) show a moderate adaptation in the measurement

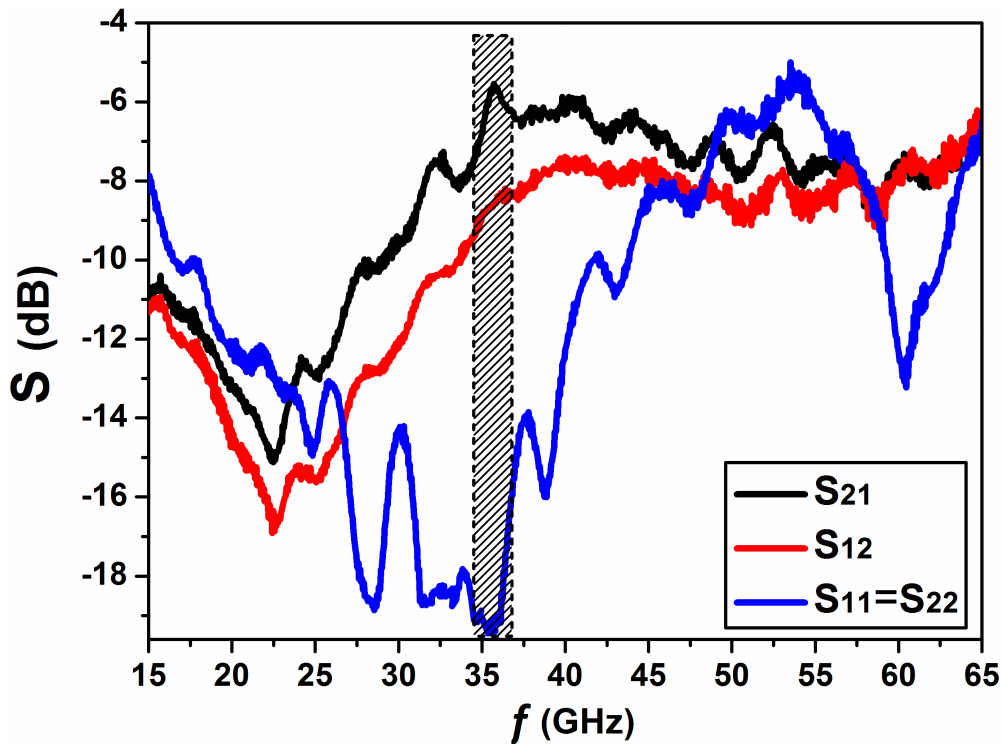


Figure 4.28: Measured  $S$ -parameters of the fabricated coplanar circulator.

frequency band. Moreover, the ferrimagnetic nanocomposite confers to the circulator its non-reciprocity. The reflection level is  $-19.3$  dB at 35 GHz. The transmission levels are  $-5.57$  and  $-8.59$  dB for the insertion ( $S_{21}$ ) and isolation  $S_{12}$  loss, respectively. The non-reciprocity is about 3 dB and the circulation phenomenon is observable around 35.5 GHz. The observed non-reciprocal effect ( $S_{12} \neq S_{21}$ ) appears to be small but is a first indication of the functioning of the constructed circulator. The achieved findings in our work are significantly more satisfactory than the results reported in chapter 1 for Ardaches et al. and Boyagin et al.

## Chapter 4: Summary

In this chapter, we have presented the theoretical model used to determine the permeability tensor of the ferrimagnetic nanocomposite. The general functioning and analytical modeling of the circulator in a stripline topology was demonstrated. This modeling leads to a preliminary rapid evaluation of the component's performance and its dimensioning before switching to the coplanar topology. To complete the dimensioning study of the coplanar circulator, several simulation tasks were carried out after the integration of the permeability tensor of the nanocomposite on HFSS software. Moreover, this chapter has summarized the etching stages of the CPW and circulator on the ferrimagnetic nanocomposite. Afterwards, a characterisation of the prototype components (CPW and Circulator) was performed using a vector network analyser. A non-reciprocal effect of 3 dB was observed for the constructed coplanar circulator. Moreover, our realized experiments in the synthesis of nanocomposite and fabrication in a clean room have enabled us to identify the technological obstacles and foresee new possibilities to develop magnetic nanocomposites applied to the design of self-biased circulator.

# Bibliography

- [1] H. Bosma, On stripline Y-circulation at UHF. *IEEE Trans. Microwave. Theory. Tech.*, 12 (1964) 61-72.
- [2] C. E. Fay, R. L. Comstock, Operation of the ferrite junction circulator. *IEEE Trans. Microwave Theory. Tech.*, 13 (1965) 15-27.
- [3] Y. S. Wu, F.J. Rosenbaum, Wide-band operation of microstrip circulators, *IEEE Trans. Microwave. Theory Tech.*, 22 1974 849-856.
- [4] R. E. Neidert, P. M. Phillips, Losses in Y-junction stripline and microstrip ferrite circulators. *IEEE. Trans. Microwave. Theory. Tech.*, 41 1993 1081-1086.
- [5] ANSYS. HFSS. Available at "<https://www.ansys.com/fr-fr/products/electronics/ansys-hfss>".
- [6] R. Vahldieck, and Wolfgang J. R. Hoefer, Electromagnetic modelling, Encyclopedia of RF and Microwave Engineering. John Wiley Sons, (2005) 1239-1240.
- [7] P. Silvester, Finite Element Analysis of Planar Microwave Networks, *IEEE Trans. Microw. Theory. Tech.*, 21 (1973) 104-108.
- [8] W. Rachowicz, L. Demkowicz, An hp-adaptive finite element method for electromagnetics-part II: A 3D implementation. *Int. J. Numer. Meth. Eng.*, 53 (2002) 147-180.
- [9] J. M. Jin, The Finite Element Method in Electromagnetics. John Wiley Sons, 2015.
- [10] M. Darques, J. De la Torre Medina, L. Piraux, L. Cagnon, I. Huynen, Microwave circulator based on ferromagnetic nanowires in an alumina template. *Nanotechnology*, 21 (2010) 145208.
- [11] A. Tchangoulian, E. Abou Diwan, D. Vincent, S. Neveu, F. Royer, J. P. Chatelon, R. Habchy, Realization of Unbiased Ferrite Cobalt Nano-Composite for Non-Reciprocal Microwave Components. *Mater. Sci. Eng. A*, 3 (2013) 751.
- [12] A. Hannour, D. Vincent, F. Kahlouche, A. Tchangoulian, S. Neveu, V. Dupuis, Self-biased cobalt ferrite nanocomposites for microwave applications. *J. Magn. Magn. Mater*, 353 (2014) 29-33.

# Conclusions and perspectives

The thesis project entitled "**Self-polarized magnetic nanocomposites based on ferrimagnetic nanowires for non-reciprocal microwave devices**" was done in collaboration between the LHC of Jean Monnet University in France and the LMER of Ibn Zohr University in Morocco for a duration of three years. The innovation of this work concerns the elaboration of self-polarized ferrimagnetic nanocomposite substrates and testing their feasibility to construct self-biased non-reciprocal coplanar circulator. The expected performance of the fabricated circulator is an insertion loss of less than  $-1$  dB, an insulation and reflections of more than  $-20$  dB.

A state of the art on magnetism was performed by presenting the various types of magnetic material and the different parameters that control their magnetic responses as well as their microwave characteristics. Afterwards, the different classes of ferrites and nanocomposite materials using ferrite nanoparticles were highlighted. These nanocomposite materials have for many years ensured a technological evolution in the field of microelectronics for the miniaturization of the electronic components. Many studies and works have been carried out on the ferrimagnetic nanocomposites in order to improve the performance, the miniaturization and their integration on the telecommunication devices. Their exploitation should make it possible to reduce the cost of components construction. Furthermore, the different models of permeability tensor were discussed.

A bibliographical study of circulators also provided a review of the different topologies of circulators. The coplanar structure was chosen due to its easy fabrication process and the convenience of interconnection with other microwave components. The requirement for miniaturization as well as high frequency operation led to the choice of "cobalt ferrite" as the magnetic material to be integrated in the constructed circulator. The  $CoFe_2O_4$  was chosen due to its strong anisotropy and its ability to ensure a self-polarization of the nanocomposite material. This nanocomposite can ensure the operation of the self-biased circulator.

The growth of  $CoFe_2O_4$  nano-crystallites into nanoporous templates has been the subject of a crucial part of this work. It was necessary to demonstrate the possibility of orienting the  $CoFe_2O_4$  nano-crystallites in AAO membranes with different pore diameters (200 nm, 100 nm, 20 nm) using the technique of electrodeposition under magnetic field. Numerous experiments have been performed to perfectly manage this manufacturing process. These experiments have contributed to the choice of the required conditions for the elaboration of  $CoFe_2O_4$  nanowires such as the deposition potential, the pore filling time, the annealing temperature,...etc. Several samples were elaborated by the magneto-electrodeposition. A series of structural (XRD), morphological (SEM, AFM) and magnetic (VSM-SQUID) characterizations were conducted in order

to investigate the physico-chemical properties of these nanocomposite substrates. These characterizations enabled us to select the ferrimagnetic nanocomposite ( $CoFe_2O_4$  magneto-electrodeposited in 20-nm AAO membrane and cooled at 0.6 T) to test it in the design of a self-biased circulator.

In parallel, the stripline circulator was analytically studied and modelled on MATLAB software due to the operation similarity of the stripline and coplanar circulators, this work provides the basic dimensions ( $R, W$ ) of the circulator as well as its performance by calculating the S-parameters. The numerical simulation part was carried out on the HFSS software which works by the Polder model designed for saturated materials. Since our nanocomposite is partially saturated, it was necessary to integrate into HFSS the model adopted in our work for the permeability tensor, in order to accurately estimate the microwave performances of the CPW and circulator. However, HFSS offers the possibility of integrating the permeability tensor data via linear interpolation functions as a function of frequency. Several CPWs were simulated for finding the optimum value of the spacing gap  $G$  between the access lines. Afterwards, the simulation of a coplanar circulator becomes accessible. The simulation of these components retains the adaptation of the ports to 50 *Ohms* and ensures the operation in the frequency band of 30 – 60 *GHz*.

The fabrication and the microwave characterization of these components are essential to validate the operation of the magnetic nanocomposite material at high frequencies. The different technological processes for manufacturing the prototypes such as copper deposition, clean room photolithography, and etching were presented. For the microwave characterization, a system equipped with coplanar probes was established to measure the S-parameters of the fabricated components. The measured S-parameters for the CPW have revealed that the nanocomposite exhibits a gyromagnetic resonance around 42 *GHz*. The circulator engraved on the  $CoFe_2O_4$  nanocomposite revealed a non-reciprocal effect of 3 *dB* with a correct adaptation. These performances are insufficient for such circulator industrialization.

According to the experimental work presented in this thesis, the microwave measurements have shown that the performance of the circulator needs to be improved. High insertion losses as well as low non-reciprocal effect have been observed. These can originate from several reasons, which will be discussed as perspectives:

As the non-reciprocal effect obtained is always weak, the improvement of the magnetic properties of the  $CoFe_2O_4$  nanocomposite is essential. On the other hand, the experimentally achieved squareness ratio ( $M_r/M_s = 0.6$ ) must be increased. Some orientation routes are envisaged.

- The electrodeposition of  $CoFe_2O_4$  in AAO membranes with a pore diameters of 10 – 8 *nm*, since it has been demonstrated that as the diameter decreases, the squareness ratio increases. In addition, the formation of agglomerations of particles is very likely and increases the interaction between them, which disturbs the orientation and reduces the global magnetization.
- The samples examined were made with an applied field of 0.6 *T*, which is probably not the sufficient value for orienting the  $CoFe_2O_4$  nano-crystallites within the AAO membrane pores. An electrodeposition under very intense magnetic fields (10 – 13 *T*) is desirable to force the orientation of  $CoFe_2O_4$  within the AAO membrane pores.



- Annealing of the ferrimagnetic substrate under magnetic field, this requires the development of an apparatus that includes a furnace surrounded by large coils.
- Elaborating a nanocomposite based on barium hexaferrite ( $BaFe_{12}O_{19}$ ), which is characterized by its high magnetocrystalline anisotropy.

Concerning the technological challenge, it is highly recommended to develop a grinding system more suitable for the filled AAO membranes in order to avoid the presence of the microcuts on the surface to obtain a homogeneous, flat and compact nanocomposite surface, that offers a better adhesion of copper. As a result, such stability of the fabrication and measurement processes and such reproducibility of the microwave measurements can be ensured.

# List of publications

- **N. Labchir**, A. Hannour, A. Ait hssi, D. Vincent, A. Ihlal, M. Sajieddine, Microwave response of coplanar waveguide based on electrodeposited  $CoFe_2O_4$  nanowires, *J. Magn. Magn. Mater.* 510 (2020) 166952, doi.org/10.1016/j.jmmm.2020.166952.
- **N. Labchir**, A. Hannour, D. Vincent, , D. Jamon, J. Y. Michalon, A. Ihlal, M. Sajieddine, Spontaneous Faraday rotation of  $Co_xFe_{3-x}O_4$  thin films electrodeposited under a static magnetic field, *J. Mater. Sci: Mater. Electron*, (2020), doi.org/10.1007/s10854-020-03652-9.
- **N. Labchir**, D. Vincent, A. Hannour, A. Ihlal, M. Sajieddine, (2019) Guide d'onde coplanaire à base de nanofils de  $CoFe_2O_4$ , In *JNM-2019*, 21<sup>èmes</sup> Journées Nationales Micro-Ondes.
- **N. Labchir**, A. Hannour, D. Vincent, A. Ihlal, M. Sajieddine, Magnetic field effect on electrodeposition of  $CoFe_2O_4$  nanowires, *Appl. Phys. A*, 125 (11) (2019) 748, doi.org/10.1007/s00339-019-3059-x.
- **N. Labchir**, E. Amaterz, A. Hannour, A. Ait hssi, D. Vincent, A. Ihlal, M. Sajieddine, (2019) Highly efficient nanostructured  $CoFe_2O_4$  thin film electrodes for electrochemical degradation of rhodamine B, *Water. Environ. Res*, doi.org/10.1002/wer.1272.
- **N. Labchir**, A. Hannour, D. Vincent, A. A. Hssi, M. Ouafi, K. Abouabassi, A. Ihlal, M. Sajieddine, Tailoring the optical bandgap of pulse electrodeposited  $CoFe_2O_4$  thin films, *J. Electron. Mater*, (2020) 1-7, doi: 10.1007/s11664-019-07923-y.
- **N. Labchir**, A. Hannour, D. Vincent, A. A. Hssi, A. Ihlal, M. Sajieddine, Magneto-electrodeposition of granular Co-Cu nanowire arrays, *Mater. Res. Express*, 6(11) (2019)11 50c3, doi. 10.1088/2053-1591/ab4d5a.
- **N. Labchir**, A. Hannour, A. A. Hssi, D. Vincent, K. Abouabassi, A. Ihlal, M. Sajieddine, Synthesis and characterization of  $CoFe_2O_4$  thin films for solar absorber application, *Mater. Sci. Semicond. Process*, 111 (2020) 104992, doi.org/10.1016/j.mssp.2020.104992.
- **N. Labchir**, A. Hannour, D Vincent, A. Ihlal, M. Sajieddine, Magneto-Electrodeposition of  $CoFe_2O_4$  Nanowire Arrays, *Proceedings of the Nanotech France*, International Conference Paris, France, 2019, doi: 10.26799/cp-nanotechfrance2019/9.
- A. A. Hssi, E. Amaterz, **N. Labchir**, L. Atourki, I. Y. Bouderbala, A. Elfanaoui, A. Benlhachemi, A. Ihlal, K. Bouabid, Electrodeposited ZnO nanorods as efficient photoanodes for the degradation of rhodamine B, *physica. status. solidi. a*, 2020, doi.org/10.1002/pssa.202000349.
- A. A. Hssi, L. Atourki, **N. Labchir**, M. Ouafi, K. Abouabassi, A. Elfanaoui, K. Bouabid, High-quality  $Cu_2O$  thin films via electrochemical synthesis under a variable applied potential, *J. Mater. Sci.: Mater. Electron*, 31(5) (2020) 4237-4244, doi.org/10.1007/s10854-020-02976-w.

- A. A. Hssi, L. Atourki, **N. Labchir**, K. Abouabassi, M. Ouafi, H. Mouhib, K. Bouabid, Structural and optical properties of electrodeposited  $Cu_2O$  thin films, *Materials Today: Proceedings*, 22 (2020) 89-92, doi.org/10.1016/j.matpr.2019.08.100.
- A. A. Hssi, L. Atourki, **N. Labchir**, M. Ouafi, K. Abouabassi, A. Elfanaoui, A. Ihlal, Optical and dielectric properties of electrochemically deposited  $p - Cu_2O$  films, *Mater. Res. Exp.*, 7 (2020) 016424, doi.org/10.1088/2053-1591/ab6772.
- A. A. Hssi, L. Atourki, **N. Labchir**, M. Ouafi, K. Abouabassi, A. Elfanaoui, A. Ihlal, K. Bouabid, Electrodeposition of oriented ZnO nanorods by two-steps potentiostatic electrolysis: Effect of seed layer time. *Solid. State. Sciences*, (2020) 106207, doi.org/10.1016/j.solidstatesciences.2020.106207.
- K. Abouabassi, M. Ouafi, A. A. Hssi, L. Atourki, H. Kirou, **N. Labchir**, L. Boulkaddat, E. Gilioli, A. Elfanaoui, K. Bouabid, A. Ihlal,  $CuSbSe_2$  thin films deposited from aqueous solution by electrodeposition in one step, *IEEE Xplore*, "7th International Renewable and Sustainable Energy Conference (IRSEC), Agadir, Morocco, (2019) 1-4, blue doi:10.1109/IRSEC 48032.2019.9078271.

# Abstract

---

This thesis work aim to develop a self-biased coplanar circulator. The chosen approach is based on the utilization of composite substrates based on self-polarized ferrimagnetic nanowires. It consists of integrating and orienting cobalt ferrite ( $CoFe_2O_4$ ) nano-crystallites in porous alumina membranes using the technique of electrodeposition under magnetic field. Ferrimagnetic  $CoFe_2O_4$  nanocomposites have been synthesized and characterized by several techniques. The performed SQUID-VSM measurements have revealed that the nanocomposite electrodeposited and cooled under a magnetic field of 0.6 T has the best magnetic properties, i.e. a large anisotropy field ( $H_a$ ), moderate coercive field ( $H_c$ ), and partial squareness ratio ( $M_r/M_s$ ). This nanocomposite is selected as an interesting candidate for the fabrication of a miniaturized self-biased circulator. The study has started with the implementation of an analytical dimensioning process based on Bosma's theory, in order to model a stripline circulator under MATLAB software. The main geometrical dimensions generated are then transposed to the 3D coplanar structure using the HFSS numerical simulator. Based on interesting simulation results, a first prototype was fabricated in the clean room and characterized at high frequencies. The measurements of the S-parameters have highlighted a circulation phenomenon, which remains very weak due to the imperfect orientation of the  $CoFe_2O_4$  nano-crystallites within the pores of the AAO membrane.

**Keywords:** Magneto-electrodeposition, self-polarized magnetic nanocomposite, Cobalt ferrite nanowires, nanoporous AAO membranes, gyromagnetic resonance, non-reciprocal self-biased circulator, telecommunication.

# Résumé

---

Ce travail de thèse a pour objectif de développer un circulateur coplanaire auto-polarisé. L'approche choisie est fondée sur l'utilisation de substrats composites à base de nanofils ferrimagnétiques auto-polarisés. Elle consiste à intégrer et orienter des nano-cristallites de ferrite de cobalt ( $CoFe_2O_4$ ) dans des membranes d'alumine poreuses par la technique de l'électrodéposition sous champ magnétique. Des nanocomposites ferrimagnétiques de  $CoFe_2O_4$  ont été élaborés et caractérisés par plusieurs techniques. Les mesures magnétiques de SQUID-VSM ont montré que le nanocomposite électrodéposé et refroidi sous champ magnétique de 0.6 T possède les meilleurs propriétés magnétiques, i.e. un grand champ d'anisotropie ( $H_a$ ), un champ coercitif modéré ( $H_c$ ), et un rapport partiel d'aimantations ( $M_r/M_s$ ). Ce nanocomposite est choisi comme un candidat intéressant pour la fabrication d'un circulateur miniaturisé auto-polarisé. L'étude présentée débute par la mise en place d'un processus analytique de dimensionnement basé sur les travaux de Bosma, afin de modéliser sous MATLAB un circulateur triplaque. Les principales dimensions géométriques obtenues sont ensuite transposées vers la structure coplanaire en 3D à l'aide du simulateur numérique HFSS. Suite à des résultats de simulation intéressants; un premier prototype a été fabriqué dans la salle blanche et caractérisé en hautes fréquences. Les mesures de paramètres S ont montré un phénomène de circulation, qui reste très faible en raison de l'orientation imparfaite des nano-cristallites de  $CoFe_2O_4$  à l'intérieur des pores de la membrane.

**Mots clés:** Magnéto-électrodéposition, nanocomposite magnétique auto-polarisé, nanofils de ferrite de Cobalt, membranes d'alumine nanoporeuses, résonance gyromagnétique, circulateur non-réciproque autopolarisé, télécommunication.

---

Laboratory of Hubert Curien (LHC)

UMR-CNRS-5516, UNIVERSITY OF LYON - UNIVERSITY OF JEAN MONNET, FRANCE

Laboratory of Materials and Renewable Energies (LMER)

UNIVERSITY OF IBN ZOHR, FACULTY OF SCIENCES, MOROCCO

---